Université de Sherbrooke
Faculté de génie
Département de génie civil et de génie du bâtiment

Numerical Simulation of Self-Consolidating Concrete Flow as Homogeneous Fluid(s) and Heterogeneous Material During Pumping Process

Simulation Numérique de l'écoulement du Béton Autoplaçant en tant que Fluide(s) Homogène(s) et Matériel Hétérogène Pendant le Processus de Pompage

Thèse de doctorat
Spécialité : Génie civil

Tooran TAVANGAR

A dissertation submitted in partial fulfillment of the requirements for the degree of Doctor of Philosophy in Civil Engineering

(Thèse présentée au département de génie civil et de génie du bâtiment en vue de l'obtention du grade Docteur en philosophie en génie)

Jury:	Ammar Yahia	Director
	Kamal H. Khayat	Co-director
	Jeffrey S. Marshall	Collaborator
	Sébastien Poncet	Reporter
	Geert De Schutter	Evaluator
	Viktor Mechtcherine	Evaluator

Sherbrooke (Québec), Canada   March 2023

To my mother, Kimia, who taught me how to love

and my father, Mohammadreza, who taught me how to fight

ABSTRACT

Pumping is one of the most commonly used methods to transport self-consolidating concrete (SCC). The prediction of pumping pressure drop is of particular interest to properly design the pumping circuits for successful pumping process given the application on hand. This is necessary to fulfil the targeted flow rate and ensure homogeneity of concrete during and after pumping, respectively. During the pumping process, a thin layer of highly fluid fine mortar enriched with high volume of cement paste and fine particles, namely lubrication layer (LL), is formed in vicinity of the pipe walls. It is revealed in literature that concrete pumpability is significantly controlled by the LL characteristics, in terms of thickness and flow properties, as well as the rheological properties of the bulk concrete (BC). This study firstly aims to predict the pressure required to pump SCC and to characterize the LL in large-scale pipelines using computational fluid dynamics (CFD). Although the concrete pumping process seems conceptually simple, the challenge underlying material physics is complex and covers a broad range of time and length scales. Another challenge comes from the interaction between suspending fluid phase (mortar) and diversity of particle sizes (aggregate) in concrete matrix, causing heterogeneous rheological behavior across the pipe section, and formation of the LL. The main mechanisms of LL formation, including the shear-induced particle migration (SIPM) and wall effects, were also simulated using multiphasic simulation techniques, including discrete element method (DEM) and coupled CFD-DEM.

First, a comprehensive literature review on numerical methodologies used to model concrete pipe flow as well as their advantages and disadvantages was presented. In addition, potential solutions were introduced to predict concrete pipe flow given an application on hand in reasonable time and precision. This study was conducted in two complementary phases. The Phase 1 included developing computational models to predict the pressure loss in a full-scale concrete pumping circuit, as a function of the pipes' geometry, rheological properties of BC, and the LL characteristics. Two novel tri-viscous models were developed to simulate the presence of the LL and BC as a homogeneous fluid with variable rheological properties across the pipe, corresponding to the BC and LL, using OpenForam software.

In the second phase, the main mechanisms of LL formation, including the wall effect and SIPM, were simulated using DEM and coupled CFD-DEM approaches. The pipe flow of concrete was simulated as a biphasic suspension to evaluate the coupled effect of characteristics of the suspended

particles (i.e., granular skeleton) and the suspending cement paste/mortar matrix. The interaction of the suspended particles and suspending fine mortar was simulated by considering the collision of particles with different particle-size distributions (PSD) and concentrations (and pipe wall), as well as the suspending fluid's drag force. A multiscale soft-sphere discrete element method (DEM) and its four-way CFD-DEM coupling were employed in Phase 2 to simulate the rheological heterogeneity across the pipe and formation of the LL. Accordingly, the coupled effect of PSD, concentration, and mean diameter of particles, as well as the rheological properties of the suspending fluid and flow Reynolds number on wall effect, SIPM, and rheological heterogeneities across the pipe was evaluated. The LL of the investigated mixtures were eventually characterized in terms of the thickness and rheological properties.

Keywords: Computational fluid dynamics; Concrete pumping; Discrete element method; Lubrication layer; Numerical simulation; Particle-size distribution; Plug flow; Pressure loss; Rheology; Self-consolidating concrete; Shear-induced particle migration (SIPM).

RÉSUMÉ (en français)

Le pompage est l'une des méthodes les plus couramment utilisées pour transporter le béton auto-plaçant (BAP). La prédiction de la baisse de pression de pompage est d'un intérêt particulier pour concevoir correctement les circuits de pompage et assurer un processus de pompage réussi compte tenu de l'application en cours. Cela est nécessaire pour répondre aux exigences de coulage, y compris le débit ciblé et l'homogénéité du béton respectivement pendant et après le pompage. Cette étude visait à prédire la pression requise pour pomper le BAP avec la caractérisation de la couche de lubrification formée près de la paroi du tuyau en utilisant des méthodes numériques. Bien que le processus de pompage du béton semble conceptuellement simple, le défi sous-jacent de la physique des matériaux est complexe et couvre une large gamme d'échelles de temps et de longueurs. Un autre défi vient de l'interaction entre la phase fluide et la diversité des tailles de particules dans le mélange de béton, ce qui résulte en différentes propriétés rhéologiques dans le béton à travers la section du tuyau.

Cette étude a été menée en deux phases différentes et complémentaires. La phase 1 avait pour objectif principal de développer un modèle de calcul pour comprendre le circuit de pompage du béton en grandeur réelle. La perte de pression en fonction de la géométrie des tuyaux, des propriétés rhéologiques du béton et des caractéristiques d'écoulement de la couche de lubrification sont présentées et discutées. La méthode de dynamique des fluides computationnelle (CFD) a été utilisée pour prédire la pompabilité du béton et évaluer l'importance des paramètres d'influence, y compris les caractéristiques de la phase en suspension (c'est-à-dire le squelette granulaire), les propriétés rhéologiques de la matrice de pâte de ciment/mortier en suspension et les nombres de Reynolds de l'écoulement et des particules solides. Deux nouveaux modèles ont été introduits pour prédire la pompabilité des mélanges de béton et la caractérisation de la couche de lubrification et des zones de bouchage. De plus, une revue complète de la littérature sur les méthodologies numériques utilisées pour modéliser l'écoulement des tuyaux en béton a été effectuée, avec une comparaison des avantages et des inconvénients de ces différentes approches. En outre, des solutions potentielles ont été présentées pour les méthodes numériques les plus efficaces et les plus fiables pour prédire l'écoulement de béton dans des tuyaux.

Les modèles informatiques basés sur la méthode des éléments discrets (DEM) et le couplage CFD-DEM ont été développés lors de la Phase 2. La migration de particules induite par cisaillement

(SIPM), principal phénomène physique conduisant à la formation de la couche de lubrification, a été également étudiée. En conséquence, l'effet couplé de la distribution de taille des particules (PSD), de la concentration et du diamètre moyen des particules en tant que paramètres d'influence sur la couche limite, le SIPM et les hétérogénéités rhéologiques à travers le tuyau ont été étudié. Outre l'évaluation des paramètres d'influence sur la migration des particules, cette étude à plusieurs échelles a permis de proposer une bonne estimation de l'épaisseur de la couche de lubrification ainsi que des propriétés rhéologiques, y compris sa viscosité et son seuil d'écoulement.

Mots-clés : Pompage de béton; Perte de pression; Propriétés rhéologiques; Migration de particules induite par cisaillement (SIPM); Modélisation numérique.

ACKNOWLEDGEMENT

First, I would like to genuinely express my gratitude to my supervisor Prof. Ammar Yahia for granting me his confidence, continuous support, and patience through all those years. All his guidance, patience, and encouragement are highly appreciated. I have always learned from him, especially having perseverance during good and not-so-good days. The PhD journey for me was one of those good memories I will always remember, and I will be proud to be one of his scholars.

I would also like to thank my co-supervisor, Prof. Kamal Khayat, for his continuous guidance, advice, and motivation that he has provided throughout my Ph.D. experience. I would like to thank him for being always supportive to me. It was a pleasure to collaborate with him in my PhD from whom I learned a lot.

I would also like to thank Prof. Jeffrey S. Marshall, for his endless support during my PhD for the modeling part. I would like to thank him for having me in his group at US during my MITAC internship, his big help for computational aspects, and providing me his original DEM code and scientific materials to advance in my project. It was a great honor for me to collaborate with him and learned a lot from him.

I would also wish to thank Dr. Masoud Hosseinpoor for his collaboration and endless support during this project. He always pushed me forward with enthusiasm which is much appreciated. Thanks to all the professors of Civil and Building Engineering Department at Université de Sherbrooke, research assistants, technicians, and our research group members and colleagues. Also, special thanks to industrial partners participating in the NSERC Industrial Chair on Fluid Concrete with Adapted Rheology for their financial support for this project. The author is also thankful to the members of the dissertation committee for their valuable comments and advices.

Last but not least, special thanks to my parents, Kimiya and Mohammad, and my brother, Tooraj, for their continuous encouragement, care and love during this journey. Thanks for having confidence in me and raising me to be the person I am today.

Tooran Tavangar

March 2023

Table of Content

List of Figures

List of Tables

List of symbols

a	[m]	Radius of contact region
a_{ij}	[-]	Loosening effect
A	[-]	Amplitude of cloud
a_p	[m]	Particle radius
$Avg(\varphi)_{Z1-4}$	[-]	Average of the total particles' concentrations in radial zones Z1-4
b	[-]	Wall effect for particles
$c(x,t)$	[-]	Local concentration
$COV(\varphi)$	[-]	Coefficient of variation of particles' concentrations (φ) in different
d	[m]	Diameter
e	[m]	Thickness
D_{pipe}	[m]	Pipe diameter
e	[-]	Coefficient of restitution
E	[$Kg^1\ m^{-1}\ s^{-2}$]	Effective elastic modulus of colliding particles
$f(\boldsymbol{x} - \boldsymbol{x}_n , R_n)$	[-]	Weighting function for particle cloud
F	[$Kg\ m\ s^{-2}$]	Force
f_{DF}	[]	Drag force correction factor
L$_{e\text{-}Laminar}$	[m]	Hydrodynamic entry length
L_{pipe}	[m]	Pipe length
m	[Kg]	Mass of a particle
M	[$Kg\ m^2\ s^{-2}$]	torque
N	[-]	Number of particles
N	[-]	Number of mesh in y direction
n	[-]	Unit normal connecting the centroids of two particles
n	[-]	Total number of particles
n	[-]	Pseudoplasticity index (Herschel-Bukley model) (chapters 4-5)
n	[-]	Unit normal connecting the centroids of two particles (chapters 6-7)
N_c	[-]	Particle time step/collision time step ratio
$N_{collision}$	[-]	Collision flux
N_p	[-]	Fluid time step/particle time step ratio

P	[Kg m^{-1} s^{-2}]	Pumping pressure
Q	[m^3 s^{-1}]	Flow rate
r	[m]	Radial distance to the pipe center
R^2	[-]	Coefficient of determination
Re	[-]	Suspending-fluid flow Reynolds number
Re	[-]	Reynolds number of concrete pipe flow
r_e	[m]	Effective radius of colliding particles
Re_p	[-]	Particle Reynolds number
r_i	[m]	Vector from particle "i" centroid to contact point
R_n	[m]	Radius of particle cloud n
T	[Kg m^{-1} s^{-2}]	Stress tensor
t	[s]	Time
t$_R$	[-]	Direction of particle rolling velocity
t$_S$	[-]	Direction of particle sliding velocity
U	[m/s]	Mean fluid velocity
u	[m/s]	Flow velocity
v	[m/s]	Particle velocity
V$_P$	[m/s]	Flow velocity at plug zone
w_0	[m/s]	Measure of particle relative collision velocity
w/b	[-]	Water-to-binder ratio
X	[m, m, m]	Position vector
x	[m]	Centroid position
y$_{critical}$	[m]	Critical distance of lubrication layer to the center axis

Abbreviations

BC	Bulk concrete
CA1-3	Three classes of coarse aggregate
CFD	Computational fluid dynamics
CFD-DEM	Coupled CFD and DEM approach
CPP	Cumulative passing percentage of aggregate from each sieve

CPSD	Coarse PSD
CSA	Canadian Standards Association
CVC	Conventional vibrated concrete
DEM	Discrete element modelling
DIP	Digital image processing
FPSD	Fine PSD
FVM	Finite Volume Method
H-B	Herschel-Bulkley rheological model
HC	High concentration (40%)
HWC	Highly workable concrete
LC	Low concentration (10%)
LL	Lubrication layer
LVG$_{LL}$	Linear velocity gradient
min	Minimum
max	Maximum
MPSD	Medium PSD
MC	Medium concentration (25%)
P1-5	Five different subclasses of spherical particles
PISO	Pressure-Implicit with Splitting of Operators
PMA	Phenomenological multiphasic approach
PSD	Particle-size distribution
RMSD	Root-mean squared difference
RMSE	Root-mean squared error
RVF	Remaining volumetric fraction of aggregate on each sieve
SCC	Self-consolidating concrete
SIDM	Shear-induced diffusion model
SIMPLE	Semi-Implicit Method for Pressure Linked Equations
SIPM	Shear-induced particle migration
SPH	Smoothed particle hydrodynamics
SPM	Single-phase modelling
UPV	Ultrasonic pulse velocimetry

VOF		Volume of fluid method
UPV		Ultrasonic pulse velocimetry
VHI		Viscosity-heterogeneity index
VOF		Volume of fluid method
WE		Wall effect
WEI		Wall-effect index
YSHI		Yield stress-heterogeneity index
Z1		Radial zone corresponding to radial range of 0-0.5R
Z2		Radial zone corresponding to radial range of 0.5R-0.75R
Z3		Radial zone corresponding to radial range of 0.75R-0.875R
Z4		Radial zone corresponding to radial range of 0.875R-R

Greek Letters

α	[-]	A 6th-degree polynomial function of restitution coefficient (e)
$\boldsymbol{\alpha}$	[-]	Fluid volume fraction
α_i	[-]	Highest packing density amongst all possible lattice packings of spherical particles of subclass 'i'
β	[-]	Re_p-dependent index
$\dot{\gamma}$	[s^{-1}]	Shear rate
$\Delta COV\ (t)$	[-]	Variation of *COV* values calculated at time step "t", relative to their initial values (at $t = 0$)
$\boldsymbol{\Delta P}$	[Kg m^{-1} s^{-2}]	Pressure loss
$\boldsymbol{\Delta p}$	[Kg m^{-1} s^{-2}]	Total pressure loss through a unit length of pipe
ΔT	[s]	Time step
δ_N	[m]	Normal overlap of particles
$\boldsymbol{\varepsilon}$	[-]	Simulation error
$\boldsymbol{\eta}$	[Kg^1 m^{-2} s^{-1}]	Viscous constant
$\boldsymbol{\eta_N}$	[Kg^1 m^{-1} s^{-1}]	Newtonian viscosity in bi-viscous rheological model
η_N	[Kg s^{-2}]	Normal dissipation coefficient
η_T	[Kg s^{-2}]	Tangential dissipation coefficient

μ	$[\text{Kg}^1\,\text{m}^{-1}\,\text{s}^{-1}]$	Suspending-fluid viscosity
μ_f	[-]	Friction coefficient
$\mu_p(0)$	$[\text{Kg}^1\,\text{m}^{-1}\,\text{s}^{-1}]$	Plastic viscosity of the suspending fluid
$\mu_p(\varphi)$	$[\text{Kg}^1\,\text{m}^{-1}\,\text{s}^{-1}]$	Plastic viscosity ($\mu_p(\varphi)$) of the suspensions of the reference mixtures and different radial zones
$\mu_{p\text{-}r\text{-}i}$	$[\text{Kg}^1\,\text{m}^{-1}\,\text{s}^{-1}]$	Relative plastic viscosity of the suspensions of the reference mixture and radial zone "*i*", to those of the suspending fluid
$\boldsymbol{\mu_0}$	$[\text{Kg}^1\,\text{m}^{-1}\,\text{s}^{-1}]$	Artificial viscosity
$\boldsymbol{\mu_{app}}$	$[\text{Kg}^1\,\text{m}^{-1}\,\text{s}^{-1}]$	Apparent viscosity
$\boldsymbol{\mu_{p\text{-}C}}$	$[\text{Kg}^1\,\text{m}^{-1}\,\text{s}^{-1}]$	Plastic viscosity of concrete
$\boldsymbol{\nu}$	$[\text{m}^2\,\text{s}^{-1}]$	Kinematic viscosity
$\boldsymbol{\nu_0}$	$[\text{m}^2\,\text{s}^{-1}]$	Kinematic artificial viscosity
$\boldsymbol{\nu_p}$	$[\text{m}^2\,\text{s}^{-1}]$	Kinematic plastic viscosity of lubrication layer
$\boldsymbol{\rho}$	$[\text{Kg}\,\text{m}^{-3}]$	Density
$\boldsymbol{\sigma}$	[-]	Surface tension constant
$\sigma(\varphi)$	[-]	Standard deviation the total particles' concentrations
σ	[-]	Poisson's ratio
$\boldsymbol{\tau}$	$[\text{Kg}\,\text{m}^{-1}\,\text{s}^{-2}]$	Shear stress
$\boldsymbol{\tau_0}$	$[\text{Kg}\,\text{m}^{-1}\,\text{s}^{-2}]$	Yield stress
$\tau_0(0)$	$[\text{Kg}\,\text{m}^{-1}\,\text{s}^{-2}]$	Yield stress of the suspending fluid
$\tau_0(\varphi)$	$[\text{Kg}\,\text{m}^{-1}\,\text{s}^{-2}]$	Yield stress of the suspensions of the investigated reference mixtures and different radial zones
$\tau_{0\text{-}r\text{-}i}$	$[\text{Kg}\,\text{m}^{-1}\,\text{s}^{-2}]$	Relative yield stress of the suspensions of the reference mixture and radial zone "*i*", to those of the suspending fluid
φ	[-]	Total particle concentration
φ_i	[-]	Concentration of particles in the reference mixtures (whole pipe domain) and given radial zone "*i*"
φ_{max}	[-]	Packing density of particles
$\varphi_{max\text{-}i}$	[-]	Packing density of the spherical particles in the reference mixtures "*i*" (whole pipe domain) or given radial zone "*i*"
$\boldsymbol{\omega}$	$[\text{s}^{-1}]$	Fluid vorticity at the particle centroid position

$\mathbf{\Omega}$	[rad/s]	Angular velocity of a particle
Ω_T	[rad/s]	Relative twisting rate
$\dot{\mathbf{\gamma}}_{\mathbf{c}}$	[s^{-1}]	Critical shear rate value
d/dt	[s^{-1}]	Derivative following particle
∇	[-]	Del operator

Subscripts

C	Contact
c	Bulk concrete
crit	Critical tangential
exp	experimental
i	particles of subclass 'i'
j	particles of subclass 'j'
ij	particles of subclass 'i' due to the influence of particles of subclass 'j'
LL	Lubrication layer
LL-100 mm	lubrication layer in 100-mm diameter pipe
LL-125 mm	lubrication layer in 125-mm diameter pipe
max	Maximum
min	Minimum
n	Particle n
p	particle
$plug$	Plug
r	Rolling
R	Rolling
sim	*Numerical*
t	twisting
$t\text{-}crit$	Critical twisting
T	Tangential
w	Wall

Z1-4   Radial zones Z1-4

Superscripts

F	Fluid
n	Normal direction
nd	Normal damping
ne	Normal elastic
s	tangential direction

CHAPTER 1. INTRODUCTION

1.1 Synopsis

Due to its higher flowability compared to conventional concrete, self-consolidating concrete (SCC) is gaining market acceptance for various applications, including highrise building and pumping. In Canada, the construction industry has extensively employed SCC (Self-Consolidating Concrete) for the repair of numerous bridges and structures. This advanced concrete technology has proven to be highly effective in patching and refacing tasks involving piers, abutment walls, deck soffits, and girders (see Fig. 1.1). Its successful application in these areas has contributed to its widespread adoption within the industry [1].
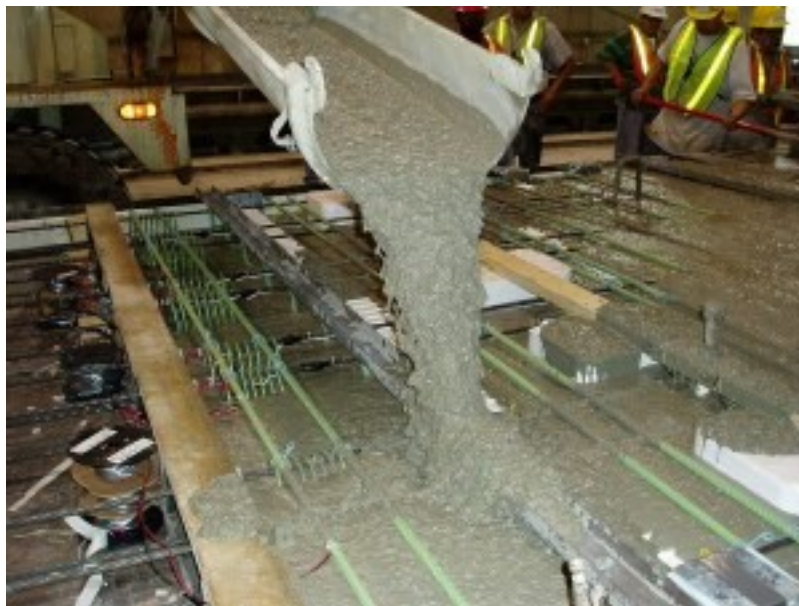
Fig. 1.1. The process of pouring SCC into forms for a full-depth precast bridge deck panel [1].

While it is generally anticipated that the use of SCC would result in lower pressure loss, there are some situations where SCC led to higher pressure loss. It was shown in literature that the pumpability of SCC can be affected by the availability of residual superplasticizer in the mixing water. Lower yield stress and plastic viscosity of SCC can lead to higher risk of segregation. This can result in pipe blockage and higher pumping pressure loss. On the other hand, larger portion of SCC is sheared due to its lower rheological properties which required higher energy to be pumped compared to conventional concrete. Therefore, in order to reach an accurate prediction of SCC

behavior, it is essential to investigate the rheological variation of SCC through pumping process [2].

SCC can be considered as a multiphase mixture of aggregate suspended in a homogeneous and highly-flowable cement paste/mortar matrix. The flow properties of SCC during pumping are thus influenced by the characteristics of both solid (aggregate) and liquid (mortar) phases. Due to high fluidity of the mortar matrix of SCC compared to that of conventional vibrated concrete (CVC). Although, particle migration is an essential tool to make all types of concrete flowable, the mechanism causing to aggregates movement is different in CVC and SCC. Wall effect and shear-induced particle migration phenomena are the main reason in particle migration for CVC and SCC, respectively. This can negatively affect the adequacy of rheological measurements for this highly-flowable construction material [3–6]. In the case of CVC, high concentration of the granular skeleton can limit the movement of particles toward the pipe center. On the other hand, high yield stress of the CVC mixtures can limit the shear rare magnitude existing during the pipe flow. These can limit the shear-induced particle migration for CVC. Therefore, the wall effect is the most significant mechanism leading to formation of the LL for CVC. However, higher suspending paste volume, lower concentration of aggregate, and typically low yield stress of SCC lead to higher shear rate magnitudes and, consequently, higher possibility of shear-induced migration, resulting to formation of the LL in vicinity of the pipe walls for SCC pumping.

Feys and Khayat [6] and Feys et al. [7] reported that due to the dynamic segregation and migration of coarse aggregate during pumping process, a fine mortar layer is created in the highest shear-rate zone located close to the pipe walls, namely the lubrication layer (LL). The characteristics of the LL, in terms of thickness and rheology, were shown to significantly control the required pumping pressure [7–10]. On the other hand, the coarse aggregate move towards the pipe center (low shear-rate) until they reach their closest packing density (Fig. 1.2) which can alter the rheological properties of pumped concrete across the pipe and affect the pumping pressure. However, in the case of SCC whereby the bulk concrete (BC) is also sheared, concrete always tries to reach an equilibrium between increasing the aggregate packing and the formation of the LL with different characteristics (i.e., thickness and rheological properties). In order to better understanding the mechanisms leading to the formation of the LL during pumping process, it is necessary to

investigate the flow performance of SCC as a multiphase suspension of aggregate (fine and coarse aggregate) in a non-Newtonian suspending fluid (cement paste or fine mortar) during pipe flow (i.e., under shear and frictional stresses).

Several studies showed the significant effect of the characteristics of lubrication layer on pumpability of concrete [4, 7–9]. For example, increasing the plastic viscosity and yield stress, and reducing the thickness of the lubrication layer can result in higher pressure loss for a given pumping distance [7]. However, due to the confined flow type during pumping and opaque nature of concrete, it is difficult to extract the lubrication layer during or after pumping. For the first time, Haustin et al [10] conducted a PulsaCoP set-up to measure rheology variation of concrete during pumping process using an artificial transparent suspension. However, it is still hard to experimentally determine the composition and measure the thickness and rheological properties of the LL.
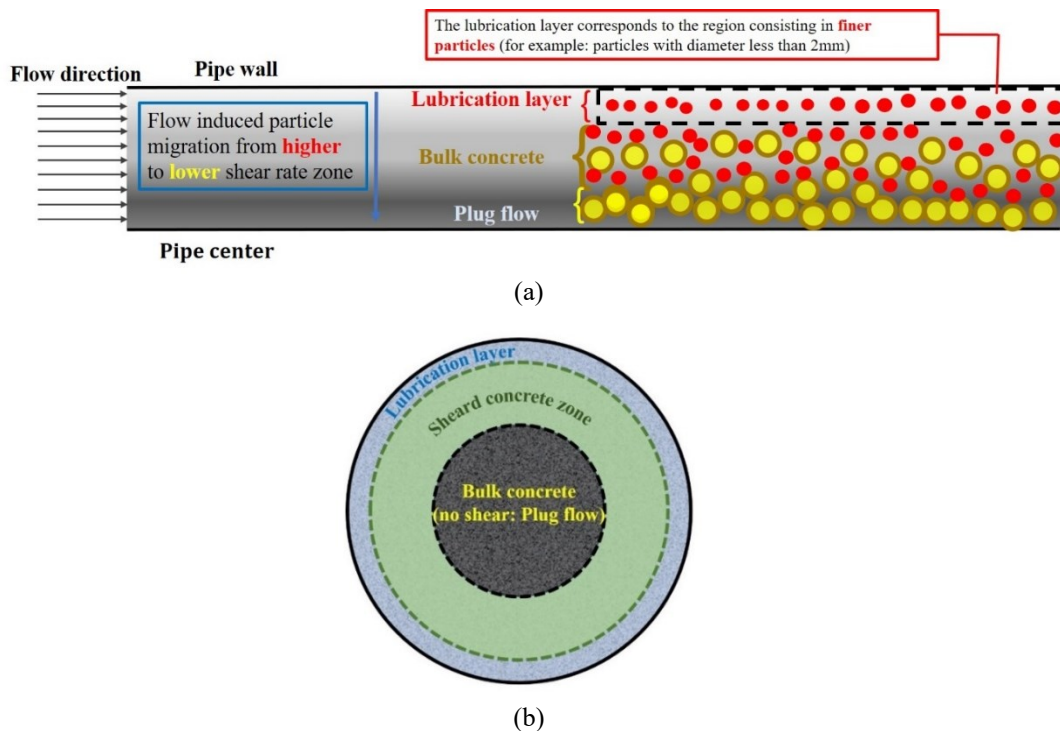
Fig. 1.2. Formation mmechanism of lubrication layer during pumping process: (a) migration of coarse aggregate from high- to low-shear rate zones, and (b) different regime zones in a pumping tube.

Therefore, it is necessary to develop theoretical tools to allow simulating the mechanisms of LL formation and predict its effect on pumpability of SCC. Several analytical methods were proposed

in literature to predict concrete pumpability, including flow rate, pumping pressure, and pumpable distance [9]. For example, Kaplan et al. [11] established a model to predict the pumping pressure as a function of the geometry of the pipe and pumping flow rate, thickness and rheological properties of the LL, and rheological properties of concrete pumped, as shown in Eq. 1.1:

$$\Delta P_{tot} = \frac{2L}{R} \left(\frac{\frac{Q}{3600\Pi R^2 K_r} - \frac{R}{4\mu_p}\tau_{0,ll} + \frac{R}{3\mu_p}\tau_0}{1 + \frac{R}{4\mu_p}\eta_{ll}} \eta_{ll} + \tau_{0,ll} \right) \tag{1.2}$$

where ΔP is the pressure drop (Pa), Q is the flow rate (m^3/h), L is the pipe length (m), R is the pipe diameter (m), k_r is the non-dimensional filling coefficient of pump cylinders, τ_0 and $\tau_{0,ll}$ are the yield stresses of concrete and LL (Pa), respectively, μ_p is the concrete plastic viscosity (Pa s), and η_{ll} is the viscous constant (Pa s/m) of LL. It is worthy to mention that η_{ll} ($\eta_{ll} = \frac{\mu_p}{e_{ll}}$) is defined as the plastic viscosity-to-thickness ratio of the LL, where μ_p and e_{ll} denote the plastic viscosity and thickness of the lubrication layer, respectively. Considering the challenging measurement of the LL thickness using a slipper and interface rheometer, the viscous constant can characterize the LL. This parameter can help to predict the pressure loss using analytical models, such as those of Kaplan. However, unlike the standard rheological tests, it is not feasible to calculate the shear rate magnitudes in an interface rheometer due to the unknown thickness of the LL. Additionally, there are limitations in employing flow equations based on rheological properties and thickness of the LL. In order to better control the pumping process, it is necessary to consider the viscous constant, yield stress, viscosity, and thickness of both LL and bulk concrete [12].

As it can be observed in Fig. 1.3, there is a very good agreement between pressure loss calculated using Kaplan et al. [11] model, and those experimentally measured by Khatib [13] for a large-scale pipeline.
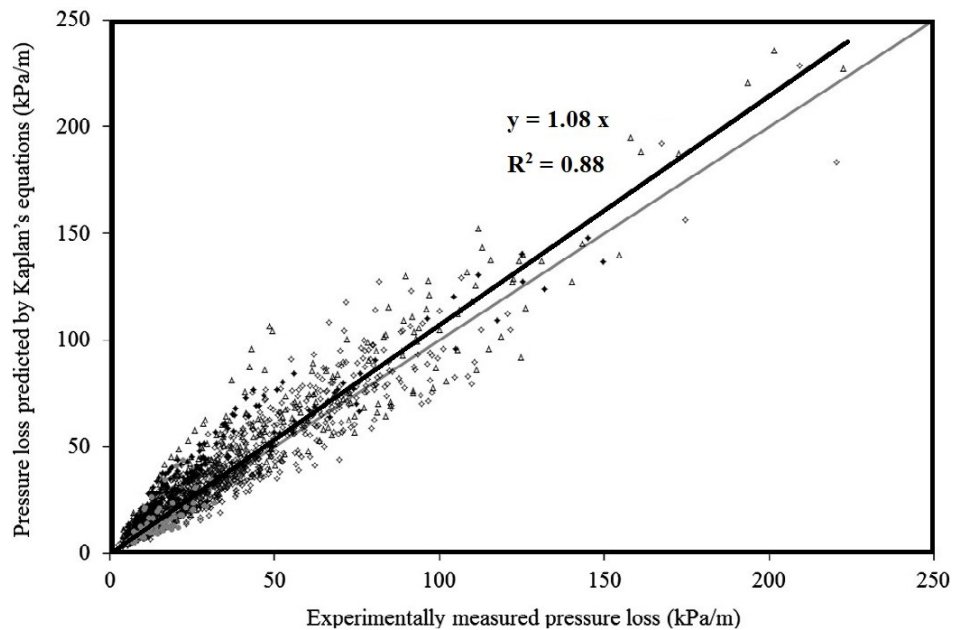
Fig. 1.3. Comparison between pressure loss obtained using Kaplan et al. [11] model and experimental measurement by Khatib [13].

However, these models only consider the rheological properties and thickness of the LL and BC after the formation of slip layer. Therefore, the accuracy of these models is strongly dependent on the adequacy of the initial assumptions of thickness and rheological properties of the BC and its corresponding LL. The interface rheometers, namely tribometers, are usually used to estimate the LL properties. However, due to lack of enough shear rate and pressure compared to real concrete pipe flows, the tribometer results could not be realistic. Indeed, there is a distinction in aggregate migration between tribometers and pipes. In a pipe, aggregates tend to move inward to a more confined space, while in an interface rheometer, their movement is outwarded to a less confined space. Therefore, the characteristics of the LL formed in an interface rheometer can differ from those created in a pipe. The LL in an interface rheometer may be larger compared to that observed in a pipe. The contrasting movement and confinement conditions give rise to variations in the properties and behavior of the LL in the tribometers and realisic pipe flow [12].

 Numerical simulations have been recently used [8,9,14] to predict the pumpability of concrete in large-scale pipelines or different pipe segments. However, the previous numerical studies did not consider the mechanism of formation of the LL, neither the shear-induced variation of rheological properties of concrete across the pipe [8,9,14] for realistic PSDs of aggregate and mortar rheology. Therefore, it is necessary to develop tools to accurately predict the pumping pressure in reasonable

time for a given application on hand, characterize the LL, and understand the mechanism of formation of the LL.

1.2 Research objectives

The main objectives of this study include developing numerical models to predict the concrete pressure loss and simulate the heterogeneous concrete pipe flow behavior, including the mechanism of formation of the LL in the vicinity of the pipe walls during pumping process. The specific objectives include:

1) Simulate the pumping behavior of 19 different SCC mixtures through a 30-m pumping circuit (Fig. 1.4), experimentally measured by Khatib [14], including the prediction of the pumping pressure loss in pipes with different diameter and under different flow rates;

2) Characterize the LL and plug zones using CFD tools for the pumping experiments carried out by Khatib [14] (Fig. 1.4);

3) Develop new viscosity models to consider the rheological variations across the pipe for large-scale pumping simulations using homogeneous-fluid numerical approach.

4) Develop numerical models to simulate the heterogeneous flow performance of concrete suspension during pumping (i.e., under pressure, shear, and friction), including the shear-induced particle migration of coarse aggregate towards the center of the pipe and formation of the LL close to the pipe walls.

5) Evaluate the coupled effect of wide PSD and concentration of solid particles and rheological properties of suspending mortar on pumping-induced heterogeneities across the pipe using particle-based computational models.
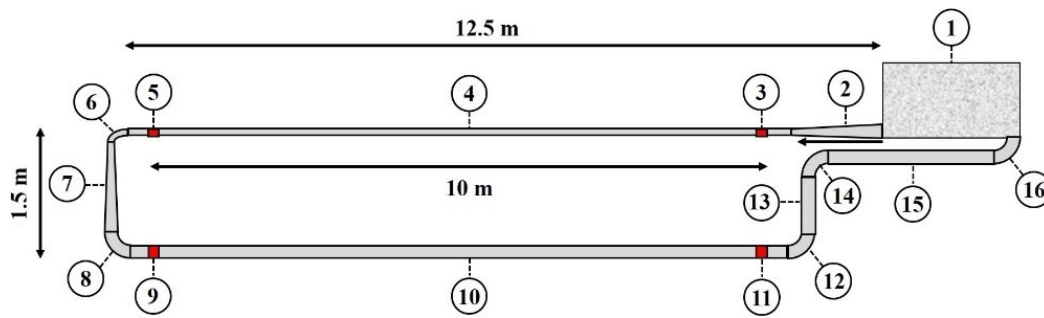
Lay-out of circuit:
<u>1</u>: **Pump**
<u>2 and 7</u>: **Reducer**
<u>3, 5, 9, and 11</u>: **Pressure sensors and strain gauges**
<u>4</u>: **Horizontal section, 100-mm diameter pipes**
<u>6</u>: **90° elbow, 100-mm diameter**
<u>8, 12, 14, and 16</u>: **90° elbow, 125-mm diameter**
<u>10</u>: **Horizontal section, 120-mm diameter pipes**
<u>12-16</u>: **Inclined part of the loop**

Fig. 1.4. Schematics of the pumping circuit developed by Khatib [14].

In this study, two main approaches, including the homogenous and heterogenous analyses, are carried out to simulate the SCC pipe flow behavior. Through the homogeneous-analysis phase, new viscosity models are developed to consider the presence of the LL with different rheological properties compared to the BC and reduce the calculation cost for large-scale pumping circuits. Therefore, instead of considering two different fluids corresponding to the BC and LL, a single-fluid approach, but with variable viscosity across the pipe, is employed. Furthermore, fitting with the experimental data, the LLs of the carried-out experiments are characterized with higher precision compared to the tribological measurements. Moreover, the plug flow zones are also characterized using the simulation results. The coupled effect of rheological properties of BC, LL, and plug zone characterized using the simulation results on pumping pressure loss values of SCC through a large-scale pumping circuit is evaluated with a minimized calculation time.

Through the heterogenous-analysis approach, pumped concrete is assumed as a diphasic suspension of solid particles in a suspending fluid, corresponding to aggregate and mortar matrix, respectively. Accordingly, the shear-induced particle migration of aggregate during concrete pipe flow is simulated taking into account their collisions (and with pipe wall), in addition to the interaction between the particles and the suspending mortar. The heterogenous phase aims to simulate the mechanisms leading to the formation of the LL, considering the aggregate with wide PSDs and concentrations, as well as suspending fluid with different rheological properties

(Reynolds number). Therefore, multi-scale computational approaches, including DEM and 4-way coupled CFD-DEM, are employed to highlight the effect of full consideration of the interaction between the suspended aggregate and suspending mortar. The pumping-induced rheological heterogeneity across the pipe is simulated using the particle-based computational approaches and the LL is characterized in terms of thickness and rheological properties using the numerical results.

1.3 Scientific contribution and originality

The results of the homogenous study represent a step towards the understanding of the concrete pipe flow behavior to reduce the cost of pumping process at large scale. Novel viscosity models are proposed to accurately predict the pressure required to pump SCC with wide range of rheological properties through different pipe diameters and under wide range of flow rates. The proposed models lead to higher precision and significantly shorter calculation time to simulate large-scale pumping experiments compared to existing numerical models. Moreover, they lead to evaluate the characteristics of the LL, BC, and plug flow zones rather than tribological measurements. On the other hand, the proposed numerical approach in the heterogenous-analysis phase can be used as a comprehensive multi-scale model to understand the multiphasic phenomena, including the formation of the LL, occurring during pipe flow for wide range of PSD and concentration of particles and mortar rheology. The obtained results can help to improve the SCC formulation protocol to facilitate pumping in complex projects. Although, it has been noted that a few studies have been carried out to model the flow of concrete within pipes, however, none of the previous research have specifically investigated the mechanisms leading to the formation of the LL in concrete mixtures containing aggregate of varying sizes at the different length and time scales. This novel investigation in the concrete field provides an innovative computational technique to evaluate shear-induced particle migration and pumping-induced rheological heterogeneities occurred during concrete pipe flow. This can lead to design successful pumping process.

The investigation extends on fully coupling continuum-discrete approach also allows to investigate the effect of aggregate on suspending fluid flow, and vice-versa. The coupled effect of different multiphasic parameters, such as mortar rheology, PSD, packing density, and concentration of aggregate on the variation of radial heterogeneities of concrete pipe flow is investigated. The

obtained results confirm the importance of full aggregate-mortar coupling approach to evaluate the heterogeneous flow behavior of concrete flow in pipes. The LL is fully characterized in terms of its rheological properties and thickness for typical concrete mixtures. This can lead to achieve accurate and realistic prediction of the shear-induced rheological heterogeneities of concrete during pumping process.

1.4 Outline of the thesis

This thesis is organized into eight chapters that are summarized, as follows:

Chapter 1 presents an overview of the project contexts and research problems, followed by the objectives of the research activities carried out in this study. The major scientific contributions and originality of this study are presented in this chapter as well.

Chapter 2 provides a comprehensive literature review on the topic. The advantages and disadvantages of different analytical and numerical methods to simulate concrete pipe flow are discussed. A practical guideline has been proposed to choose an appropriate computational approach dependent on the pumping application in hand. The single fluid simulation, DEM, and CFD-DEM coupling approach are also introduced and discussed along with their potential challenges through a comprehensive state-of-the art on the concrete pumping simulation.

Chapter 3 presents a summary of the methodologies employed in this study, including the continuum, discrete, and coupling continuum-discrete approaches. This chapter is an introduction of the following chapters addressing the objectives mentioned in Chapter 1.

Chapter 4 presents a new tri-viscous model to simulate the pipe flow of various SCC and highly-workable concrete mixtures, experimentally carried out by Khatib at the University of Sherbrooke, developed using CFD. Two fluids and the novel tri-viscous approaches are applied to consider the coupled effect of the LL characteristics, concrete rheology, pipe diameter, and pumping flow rate on the pumping pressure loss. The tri-viscous model simulates the radial variation of rheological properties of concrete, as a single fluid, across the pipe as a function of the radial distance to the

pipe center. The LL and plug flow zones are characterized in terms of their radial position, thickness, and rheological properties.

Chapter 5 extends the study on prediction of the pressure drop in large-scale pumping circuits using CFD and single-fluid approach. A novel tri-viscous model is proposed to consider the radial variation of rheological properties of pumped concrete as a function of the shear-rate magnitudes across the pipe. The pressure drops of highly flow rate experiments carried out by Khatib [14] at the University of Sherbrooke are well predicted using the novel shear-rate dependent viscosity model. The LL and plug flow zones are characterized for high flow rate pumping experiments. Furthermore, the shear-rate gradients occurred during concrete process are obtained to better understand the concrete flow regime through pumping process. The coupled effect of the characteristics of different pipe flow zones and critical shear rate on pumping pressure drop is successfully evaluated.

Chapter 6 deals with the heterogeneity behavior of concrete pipe flow. The shear-induced particle migration (SIPM) and wall effect phenomenon as the main mechanisms leading to the formation of the LL are modelled using discrete element method (DEM). A soft-sphere DEM approach is implemented to simulate the particle collisions (and pipe wall) and effect of suspending mortar on particle motions to better understanding the mechanisms of LL formation in the vicinity of pipe walls. Initially, the variation of particles concentration at different radial zones across the pipe for nine typical concrete suspensions is evaluated over the simulation time. Secondly, the coupled contribution of particle concentration and size distribution on radial heterogeneities across the pipe is also investigated.

Chapter 7 extends the study on modeling the mechanism of the formation of the LL using a four-way CFD-DEM coupling method to consider the effects of both suspending fluid on particles motion and particles on suspending fluid flow. The coupling approach is proposed to provide more realistic understanding of pumping-induced particle migration for concrete suspensions. The coupled effect of PSD and concentration of particles, as well as the rheological properties of suspension mortar, reflected by the Reynolds number, on the formation of LL and pumping flow

rate is evaluated. The radial rheological heterogeneities across the pipe are evaluated using the numerical results.

The importance of considering the effect of particles on suspending fluid flow is highlighted by comparing the results with those obtained using the 1-way DEM approach, as explained in Chapter 6.

Chapter 8 provides a summary of the main findings and concluding remarks of this study. Furthermore, perspectives for future work are also presented in this chapter.

It is important to mention that Chapters 2, and 4-7 correspond to the five review and research papers published or submitted for publication in highly impact factor scientific journals in the concrete and construction fields. Chapter 2 provides a comprehensive review paper published in the ACI Material Journal. This entitled "Computational investigation of concrete pipe flow: A critical review". Chapter 4 includes a scientific article published in Cement and Concrete Composites journal. This article is entitled "Novel tri-viscous model to simulate pumping of flowable concrete through characterization of lubrication layer and plug zones" published in 2022. Chapter 5 corresponds to the second scientific paper (Numerical simulation of flowable concrete pumping using a novel shear-rate dependent tri-viscous mode) submitted to Cement and Concrete Research journal. In Chapter 6, the published scientific article (Discrete-element modeling of shear-induced particle migration during concrete pipe flow: Effect of size distribution and concentration of aggregate on formation of lubrication layer) in Cement and Concrete Research Journal is presented. Chapter 7 presented the paper entitled "Four-way CFD-DEM coupling to simulate concrete pipe flow: Mechanism of formation of lubrication layer" submitted for possible publication in Cement and Concrete Research Journal.

REFERENCES

[1]   Website: Canada ConstructConnect, Title: "Self-consolidating concrete continues to gain traction across the country", Accessed: [June 2023].

[2]   D. Feys, G.D. Schutter, K.H. Khayat, R. Verhoeven, Changes in rheology of self-consolidating concrete induced by pumping, Materials and structures, 49 (2016) 4657– 4677. https://doi.org/10.1617/s11527-016-0815-7

[3]   K.H. Khayat, Workability, Testing, and Performance of Self-Consolidating Concrete, ACI materials journal (1999) 346-353.

[4]   D. Feys, K.H. Khayat, R. Khatib, How do concrete rheology, tribology, flow rate and pipe radius influence pumping pressure?, Cement and concrete composites, 66 (2016) 38–46. https://doi.org/10.1016/j.cemconcomp.2015.11.002.

[5]   N. Roussel, (2011), Understanding the Rheology of Concrete, Elsiver Science, (2011) ISBN 9780857095282.

[6]   D. Feys, K.H. Khayat, Particle migration during concrete rheometry: How bad is it?, Materials and structures, 50 (2017) 1–13. https://doi.org/10.1617/s11527-016-0992-4.

[7]   D. Feys, K.H. Khayat, A. Perez-Schell, R. Khatib, Development of a tribometer to characterize lubrication layer properties of self-consolidating concrete, Cement and concrete composites, 54 (2014) 40–52. https://doi.org/10.1016/j.cemconcomp.2014.05.008.

[8]   E. Secrieru, J. Khodor, C. Schröfl, V. Mechtcherine, Formation of lubricating layer and flow type during pumping of cement-based materials, Construction and building materials. 178 (2018) 507–517. https://doi.org/10.1016/j.conbuildmat.2018.05.118.

[9]   S.H. Kwon, K.P. Jang, J.H. Kim, S.P. Shah, State of the Art on Prediction of Concrete Pumping, International Journal of concrete structures and materials, 10 (2016) 75–85. https://doi.org/10.1007/s40069-016-0150-y.

[10]   M.A. Haustein, M.N. Kluwe, R. Schwarze, Experimental investigation of the pumping of a model-concrete through Pipes, Materials (Basel), 13 (5) (2020) 1161. https://doi.org/10.3390/ma13051161.

[11]   D. Kaplan, F. De Larrard, T. Sedran, Design of concrete pumping circuit, ACI materials journals. 102 (2005) 110–117. https://doi.org/10.14359/14304.

[12]   D. Feys, G.D. Schutter, S. Fataei, N.S. Martys, V. Mechtcherine, Pumping of concrete:

Understanding a common placement method with lots of challenges, Cement and concrete researh, 154 (2022) 106720. https://doi.org/10.1016/j.cemconres.2022.106720.

[13]   R. Khatib, Analysis and Prediction of Pumping Characteristics of High-Strength Self-Consolidating Concrete, Ph.D. Thesis, Universit´e de Sherbrooke, 2013. http://hdl.handle.net/11143/6634

[14]   V.N. Nerella, V. Mechtcherine, Virtual Sliding Pipe Rheometer for estimating pumpability of concrete, Construction and building materials, 170 (2018) 366–377. https://doi.org/10.1016/j.conbuildmat.2018.03.003.

CHAPTER 2. Literature review "Computational investigation of concrete pipe flow: A critical review"

Authors and affiliations

Tooran Tavangar: Ph.D. candidate, Cement and Concrete Research Group, Department of Civil and Building Engineering, Université de Sherbrooke, Sherbrooke, Québec, J1K 2R1, Canada.

Masoud Hosseinpoor: Post-Doc, Cement and Concrete Research Group, Department of Civil and Building Engineering, Université de Sherbrooke, Sherbrooke, Québec, J1K 2R1, Canada.

Ammar Yahia: Professor, Cement and Concrete Research Group, Department of Civil and Building Engineering, Université de Sherbrooke, Sherbrooke, Québec, J1K 2R1, Canada.

Kamal H. Khayat: Professor, Department of Civil, Architectural and Environmental Engineering, Missouri University of Science and Technology, Rolla, MO 65409-0710, USA.

Abstract

The prediction of concrete pumpability is of particular interest to properly design pumping circuits and select suitable pumps for successful processing of concrete. A critical review of empirical, analytical, and numerical models is carried out to predict concrete pumpability as a function of pipeline geometry, rheological properties of the bulk concrete, and the characteristics of the lubrication layer. The main mechanisms leading to the formation of the lubrication layer, including the wall effect, Reynolds dilatancy, and shear-induced particle migration (SIPM), are discussed. The main phenomenological models governing SIPM are formulated in terms of spatial variations of particles' interaction frequency and viscosity. In addition to the single-phase methodology, new computational approaches on SIPM in pipe flow of solid/liquid suspensions are discussed. The coupled CFD-DEM and SPH methods are recommended as the most precise and realistic approaches to simulate concrete pipe flow compared to the DEM and single-phase modellings.

Keywords: discrete element method; lubrication layer; pumpability; Reynolds dilatancy; rheology; shear-induced particle migration; smoothed particle hydrodynamics

2.1 Introduction

Concrete pumping is one the most frequently used construction methods to place concrete given its significant ability to provide a continuous supply of material, higher casting rate, lower construction cost, and ease of accessibilities on jobsites [1]. The flow properties of concrete suspension in pipes are influenced by the characteristics of the solid and liquid phases of the material. These include the volumetric content, morphology, and particle-size distribution of granular skeleton and rheological properties of cement paste/mortar matrices. Due to the shear-induced particle migration (SIPM) of coarse aggregate, a thin layer enriched with cement paste and fine sand particles is created in the highest shear-rate zone located close to the pipe walls; this zone is referred to as the lubrication layer (LL) [1-6]. The coarse aggregates move towards the pipe center until they reach their highest packing density [2,3]. The resulting radial distribution of aggregate can lead to nonuniform rheological behavior and, consequently, dissimilar flow velocity and shear-rate profiles in different zones of the pipe section. Understanding these complex flow behaviors of fresh concrete in pipes is therefore essential to avoid pumping failure risks, such as

pipe blockage. Therefore, it is necessary to develop theoretical tools to predict the pumpability of concrete given their rheological properties and compositions, as well as flow rate, pipe geometry, and presence of bends and reducers. Moreover, investigating the heterogeneous mechanisms inducing LL formation during pumping process is important.

Despite the use of concrete pumping for almost one century, it is only in the last couple of decades that more scientific investigations were carried out on this topic [4,5]. Several analytical methods were proposed to predict concrete pumpability in terms of pumping pressure, flow rate, pump diameter, and pumping distance [5]. Computational tools were recently employed to comprehensively investigate the complex multiphasic behavior of concrete under pumping conditions [6].

In this study, a critical comprehensive review of empirical, analytical, and numerical methods to predict concrete pumpability is presented. The main mechanisms leading to LL formation are introduced. Furthermore, new analytical and computational studies on SIPM during pressure-driven flow of solid/liquid suspensions are introduced. These models can predict concrete flow behavior during pumping and simulate the formation of the LL.

2.2 Research significance

Comprehensive understanding of the mechanisms leading to the formation of the LL is necessary to achieve successful pumping process. Analytical and numerical modelling of concrete pipe flow using a single-phase material can lead to faster and reliable predictions. However, this methodology is incapable to evaluate the heterogeneous flow behavior of concrete pipe flow. The proposed approaches in this study allow to evaluate the SIPM in pipe flow, hence supporting the hypothesis behind the formation of the LL. The coupled CFD-DEM and SPH methods that consider the multiphasic interactions of aggregate and cement paste/fine mortar matrices are recommended to predict pumpability.

2.3 Analytical investigation of concrete pipe flow

As reported by Browne and Bamforth [7], the stress transfer during the movement of concrete in pipes depends on the cement paste content. When the paste content is sufficient, the shear stress can take place in the cement paste and direct contact between aggregate particles and the pipe wall

can be avoided. Therefore, the stress transfer is hydrodynamic in nature, and pressure in pipe can linearly decrease (ΔP) with the pipe length (L). The required pumping pressure (P) increases linearly with the flow rate (Q). A thin layer of cement paste or fine mortar, namely the LL, is created at the interface with the pipe wall, which reduces the frictional interaction [8,9]. The ΔP-L and P-Q relationships are dependent on the ability to form this LL.

The first attempt to establish an analytical relationship between the ΔP (Pa) and Q (m^3/s) values as a function of concrete yield stress τ_0 (Pa) and plastic viscosity μ_p (Pa.s) and pipe geometry, radius R (m) and length L (m), was proposed using the Buckingham-Reiner equation [10] for pipe flow of Bingham fluids. The analytical relationship is as follows:

$$Q = \pi \frac{3\Delta P^4 R^4 + 16\tau_0{}^4 L^4 - 8\tau_0 L R^3 \Delta P^3}{24\Delta P^3 \mu_p L} \tag{2.1}$$

However, the use of Buckingham-Reiner equation for concrete pumping resulted in significant overestimation of ΔP (2-10 times higher) compared to experimental values [1,9,11,12]. This is due to the assumption that the concrete remains homogeneous during pumping, hence denying the formation of the LL and neglecting its effect in Eq. 2.1. This discrepancy was corrected in the analytical models proposed by Kaplan et al. [1,11]. These models predict ΔP in the cases where the bulk concrete (BC) does not undergo any shear (plug flow in Eq. 2.2) and when both the LL and some of the BC undergo some shearing during flow (Eq. 2.3).

$$\Delta P = \frac{2L}{R}\left(\frac{Q}{3600\pi R^2 k_r} \times \frac{\mu_{p,LL}}{e_{LL}} + \tau_{0,LL}\right) \tag{2.2}$$

$$\Delta P = \frac{2L}{R}\left(\frac{\dfrac{Q}{3600\pi R^2 k_r} - \dfrac{R}{4\mu_P}\tau_{0,LL} + \dfrac{R}{3\mu_P}\tau_0}{1 + \dfrac{R}{4\mu_P} \times \dfrac{\mu_{p,LL}}{e_{LL}}} \times \frac{\mu_{p,LL}}{e_{LL}} + \tau_{0,LL}\right) \tag{2.3}$$

where k_r, $\tau_{0,LL}$ (Pa), $\mu_{p,LL}$ (Pa.s), and e_{LL} (m) are the filling coefficient of piston pumps' cylinders, yield stress, plastic viscosity, and thickness of the LL, respectively. Considering the linear increase of shear stress in pipes, from zero at the central axis to its maximum value at the wall of the pipe, when the maximum shear stress τ_w (Pa) (Eq. 2.4) is smaller than the yield stress of concrete ($\tau_w < \tau_0$), the BC is not sheared, and Eq. 2.2 applies. Otherwise (i.e., $\tau_w > \tau_0$), ΔP (Pa) can be predicted using Eq. 2.3 for partially sheared concrete in the pipe.

$$\tau_w = \frac{\Delta P.R}{2L} < \tau_0 \tag{2.4}$$

The radius of the un-sheared concrete zone, namely plug radius R_P (m), can be calculated, as follows:

$$R_P = \frac{2\tau_0.L}{\Delta P} \tag{2.5}$$

Assuming that the BC and LL behave as Bingham materials, the flow velocity profiles in different zones of the pipe section, including LL, sheared concrete, and plug zones (Fig. 2.1), and, consequently, the total flow rate can be evaluated, as follow [13]:

$$V_{LL} = \frac{1}{\mu_{p,LL}} \left(\frac{\Delta P_L(R^2 - r^2)}{4} - \tau_{0,LL}(R - r) \right) \text{ for } R_{LL} \leq r \leq R \tag{2.6}$$

$$V_{SC} = \frac{1}{\mu_{p,LL}} \left(\frac{\Delta P_L(R^2 - R_{LL}{}^2)}{4} - \tau_{0,LL}(R - R_{LL}) \right) + \frac{1}{\mu_p} \left(\frac{\Delta P_L(R_{LL}{}^2 - r^2)}{4} - \tau_0(R_{LL} - r) \right) \text{ for } R_P \leq r \leq R_{LL} \tag{2.1}$$

$$V_P = \frac{1}{\mu_{p,LL}} \left(\frac{\Delta P_L(R^2 - R_{LL}{}^2)}{4} - \tau_{0,LL}(R - R_{LL}) \right) + \frac{1}{\mu_p} \left(\frac{\Delta P_L(R_{LL}{}^2 - R_P{}^2)}{4} - \tau_0(R_{LL} - R_P) \right) \text{ for } 0 \leq r \leq R_P \tag{2.8}$$

$$Q = 2\pi \left(\int_{R_{LL}}^R V_{LL} dr + \int_{R_P}^{R_{LL}} V_{SC} dr + \int_0^{R_P} V_P dr \right) = \frac{150\pi}{\mu_p \cdot \mu_{p,LL}} \left[3\mu_p \Delta P_L (R^4 - R_{LL}{}^4) - 8\tau_{0,LL}\mu_p (R^3 - R_{LL}{}^3) + 3\mu_{p,LL}\Delta P_L (R_{LL}{}^4 - R_P{}^4) - 8\tau_0\mu_{p,LL}(R_{LL}{}^3 - R_P{}^3) \right] \tag{2.9}$$

where V_{LL}, V_{SC}, and V_P are concrete flow velocity (m/s) at radial distance r (m) from the central axis, located at the LL, sheared concrete zone, and plug zone, respectively. Moreover, ΔP_L (Pa/m) $= \Delta P/L$ is the total pressure loss through a unit length of pipe. As shown in Fig. 1, the parameters R, R_P, and R_{LL} (m) correspond to the pipe radius, and the radial positions where the sheared concrete and LL zones start, respectively.
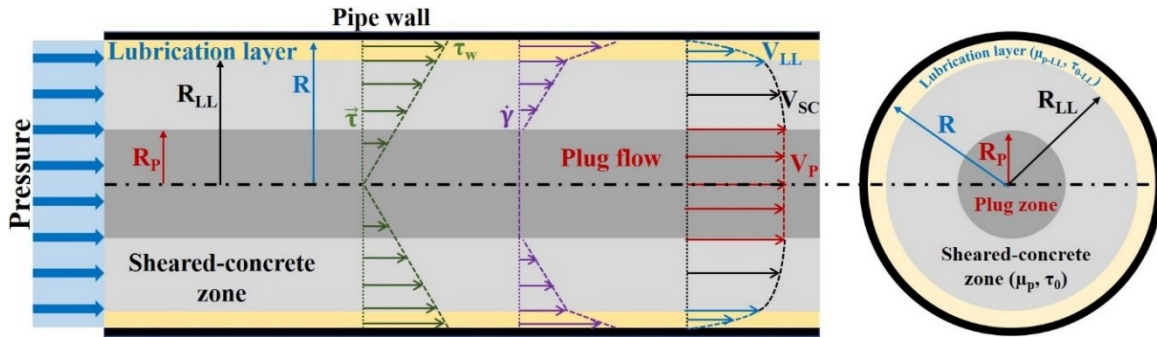
Fig. 2.1. Schematic representation of concrete pipe flow under pressure: velocity profiles and shear stress and shear-rate distributions in different flow zones over pipe cross-section, including LL, sheared-concrete, and plug flow zones [1,8,13]

As expressed in Eqs. 2.2-2.9, in addition to the rheological properties of the bulk concrete, the thickness of the LL ($e_{LL} = R - R_{LL}$) and its rheological properties ($\tau_{0,LL}$ and $\mu_{p,LL}$) can significantly influence the concrete pumpability. Rheological properties of concrete can be evaluated using different types of rheometers [14]. However, precise evaluation of LL characteristics is also necessary to predict concrete pumping characteristics. Due to the confined pipe-flow conditions, it is quite complex to evaluate the thickness of LL and take a representative sample for rheological measurements. Various experimental methods were employed to evaluate the thickness and composition of LL, such as ultrasonic pulse velocimetry (UPV) [15,16] and image analysis of the cut sections of hardened concrete in pipes [17]. However, the use of such methods can lead to more complexities, such as sophisticated noisy data processing [15,16]. Furthermore, as reported in literature, there is no uniform agreement on LL thickness, since it can vary between 1-10 mm for different concrete types [17-20]. It is reported in literature that LL is generally composed of a fine mortar with a maximum particle size of around 2 mm [21-23].

In order to evaluate the rheological properties of the LL, several frictional rheometers, referred to also as tribometers, were developed [2,5]. Feys et al. [2] developed a new coaxial-cylinders tribometer for highly workable concrete (HWC). The authors identified the radius and shear stress of the plug and sheared concrete zones in order to evaluate more precisely the rheological properties of the LL in terms of $\tau_{0,LL}$ and viscous constant. The viscous constant ($\eta_{LL} = \mu_{p,LL}/e_{LL}$) is measured as an interdependent characteristic of the LL to its plastic viscosity and thickness. Mechtcherine et al. [24] developed a sliding pipe rheometer, called Sliper, consisting of a fixed pipe containing the concrete sample and a sliding pipe. The authors proposed an experimental methodology to evaluate the rheological properties of LL created at the sliding pipe walls by correlating the measured pressure and sliding velocity values.

The measured characteristics of the LL can be successfully integrated in the analytical models (Eqs. 2.2-2.9) to predict the pumpability of different types of concrete in large-scale pipelines [1,13,24-26]. The analytical models revealed that for a given flow rate, lower η_{LL} values (i.e., lower $\mu_{p,LL}$ or higher e_{LL}) can lead to lower ΔP. However, due to the high shear-rate values in the LL zone, the shear stress exceeds its yield value and, therefore, $\tau_{0,LL}$, having very small values on the order of 1 Pa, does not significantly affect concrete pumpability.

It is important to note that the tribometer set-ups cannot guarantee an accurate simulation measurement of the thickness and plastic viscosity of the LL during pipe flow. Due to the absence of pressure and lower applied shear-rate in the tribometer, the flow conditions in a tribometer are quite different than those in pipes. Moreover, the concrete sample is not sheared in the Sliper set-up where only the sliding pipe moves on the interface. Thus, the measured shear stress and pressure loss values are not representative of the pumping of HWC or self-consolidating concrete (SCC) where the bulk concrete is mostly sheared.

According to the analytical models (Eqs. 2.2,2.3), precise evaluation of thickness, and rheological properties of the LL is highly important to accurate prediction of pressure loss. However, as discussed earlier, the tribometer and Sliper set-ups cannot simulate the realistic pipe-flow conditions leading to create the LL. In order to better understanding the flow behavior and characterization of the LL, the main mechanisms leading to the formation of the LL during pipe flow (i.e., pressure-driven shearing under confined condition) should be investigated.

2.4 Mechanisms leading to formation of LL during pumping

The main mechanisms leading the formation of the LL during pumping can be described by three following phenomena:

2.4.1 Wall effect

During pipe flow, the aggregate cannot cross the pipe walls, and the radial displacements of aggregate are limited. This reduces the concentration of coarse aggregate and creates a thin layer of finer particles at the concrete-pipe interface. As reported by Vand [27] (Fig. 2.2), the minimum thickness of this layer corresponds to the half of the maximum size of aggregate (i.e., $D_{max}/2$).
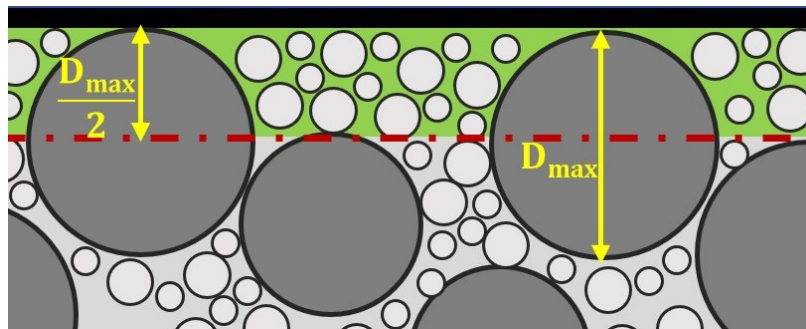
Fig. 2.2. The wall effect on formation of LL [27].

2.4.2 Reynolds dilatancy

The shear-induced volumetric change of granular dispersions is referred to as the Reynolds dilatancy [28-30]. Due to Reynolds dilatancy, when a loosely-packed granular suspension is subjected to shear flow, the granular system is compacted (Fig. 2.3), hence the solid concentration and pore pressure increase [29]. The increase in the pore pressure can lead to displacement of the suspending fluid from the voids. This can partially explain the mechanism of the LL formation during concrete pumping [2]. Moreover, concrete always tends to find an equilibrium between increasing the aggregate packing in the bulk concrete and forming of the LL close to the pipe walls [2,3]. In the case of HWC and SCC mixtures, whereby the bulk concrete is also sheared, the Reynolds dilatancy can prevent the maximum packing of aggregate.
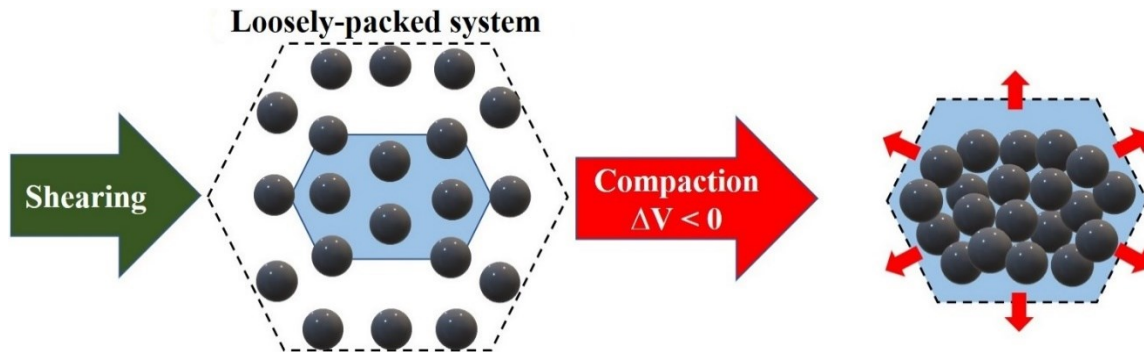
Fig. 2.3. Shear-induced volumetric change of an assembly of particles: compaction from loosely-packed to closely-packed arrangement, pushing out the suspending matrix from the voids [28-30].

Hosseinpoor et al. [30] investigated the volumetric changes of different SCC mixtures under shear in a coaxial-cylinders tribometer (Fig. 4) using 3D-image analysis techniques. Due to Reynolds dilatancy, the fine mortar portion of the concrete moves towards the highest shear-rate zone (rotating cylinder in tribometer set-up) and creates the LL. The LL thickness in the tribometer set-up is estimated using the ratio of the total shear-induced volumetric changes of the sample-to-the surface area of the inner cylinder. This is estimated in the range of 0.1-0.9 mm for SCC [30]. However, these values are underestimated compared to those reported for pumping processes [17-20]. This can be explained by the absence of pressure in tribological tests, despite the real pipe-flow conditions. Indeed, the presence of pressure can increase the particle migration and, consequently, the thickness of the LL compared to those created in tribological test set-ups.

Fig. 2.4. Shear-induced volumetric change of an assembly of particles: compaction from loosely-packed to closely-packed arrangement, pushing out the suspending matrix from the voids [28-30].

2.4.3 Shear-induced particle migration (SIPM)

When the pipe flow is well developed and equilibrium state is reached, the relative concentration of solid particles located at the center of pipe increases but decreases in the vicinity of the pipe wall compared to the homogeneous mixture before pumping. This is referred to the shear-induced particle migration (SIPM) of coarse aggregate during pipe flow. SIPM leads to un-uniform concentration of aggregate and, consequently, dissimilar rheological properties across the pipe section. An investigation of the SIPM mechanisms of concrete in pipes is necessary to predict the thickness and rheological characteristics of the LL.

Leighton et al. [31,32] proposed two phenomenological models to describe SIPM in heterogeneous suspensions as a consequence of spatial variations in particles' interaction frequency and effective viscosity. Phillips et al. [33] modified these models to develop a diffusion equation describing the evolution of particle concentration profiles in a pressure-driven pipe flow due to two following phenomena:

2.4.3.1 Spatially varying particles' interaction frequency

In a heterogeneous suspension subjected to shear, the particles irreversibly move from their original streamline due to the interparticle collisions. According to Phillips et al. [33], the particles located in more concentrated zone experience a higher frequency of collisions and can migrate towards the lower collision frequency (i.e., lower concentration) and normal to their shear surface. As shown

by Phillips et al. [33], the flux N_c caused by the spatially varying interaction frequency of particles can be expressed, as follows:

$$N_c = -K_c a^2(\varphi^2 \nabla\dot{\gamma} + \varphi\dot{\gamma}\nabla\varphi) \qquad (2.10)$$

where a (m) and φ are the radius and concentration of solid particles, respectively, $\dot{\gamma}$ (s^{-1}) is shear-rate, and K_c is a constant that should be identified using the experimental data fitting. The $\varphi^2\nabla\dot{\gamma}$ term emphasizes that even in the absence of any initial concentration gradient (i.e., initial homogeneous distribution of particles: $\nabla\varphi = 0$), the shear-rate gradient results in particle migration from the higher (close to pipe walls) to lower shear-rate zones (pipe axis). Indeed, the higher shear-rate values lead to higher number of interparticle interactions. Moreover, the second term $\varphi\dot{\gamma}\nabla\varphi$ implies that any gradient in particle concentrations (i.e., heterogeneous distribution: $\nabla\varphi \neq 0$) results in spatial variation in the frequency of interactions.

2.4.3.2 *Spatially varying viscosity*

The particle interactions can also be affected by the spatially varying apparent viscosity. Any gradient in the particle concentrations can lead to variation of viscosity, described by the existing models (i.e., $\mu_{app}(\varphi)$) [34]. Therefore, at the collision moment, the existing viscosity gradient leads to different resistances against the movement of particles located in different viscosity zones. This consequently results in different centers of rotation of the particles to be displaced from their initial position, in the absence of any viscosity gradient, toward the higher viscosity. Therefore, the particles are displaced towards the lower viscosity zones. The particle flux due to the spatial variation of μ_{app} was expressed by Philips et al. [33], as follows:

$$N_\mu = -K_\mu \dot{\gamma}\varphi^2 \left(\frac{a^2}{\mu_{app}}\right)\frac{d\mu_{app}}{d\varphi}\nabla\varphi \qquad (2.11)$$

where K_μ is a constant determined by experimental data fitting. For pipe flow, $\frac{\partial}{\partial z} \ll \frac{\partial}{\partial r}$, $u_{zr} \ll u_z$, $u_z = u_z(r, z)$, and p = p(z), where z and r are the direction of pumping flow and radial directions related to pipe axis, respectively, u (m/s) is the velocity and p (Pa) is the pressure [35]. These assumptions can simplify the conservation equations for steady and incompressible flow, as follows:

$$\frac{\partial p}{\partial z} - \frac{1}{r}\frac{\partial}{\partial r}\left(r\mu_{app}\frac{\partial u_z}{\partial r}\right) = 0 \text{ and } Q = 2\pi \int_0^R r.\,u_z dr \tag{2.12}$$

Lam et al. [35] proposed the governing equation of SIPM for suspension pipe flow by combining Eqs. 2.10-2.12, as follows:

$$\frac{\partial \varphi}{\partial t} + \frac{\partial(u_z\varphi)}{\partial z} = \nabla.\left[a^2 K_c\varphi\nabla\left(\varphi\frac{\partial u_z}{\partial r}\right) + K_\mu\varphi^2 a^2\frac{\partial u_z}{\partial r}\frac{\nabla\mu_{app}}{\mu_{app}}\right] \tag{2.13}$$

The schematics of the elaborated SIPM mechanisms is presented in Fig. 5. Three main boundary conditions can be considered for a pipe flow. These include no slip (u = 0) and no particle flux at the pipe walls (r = R), and homogeneous distribution of particles at the pipe entrance (z = 0), as follows:

$$\begin{cases} u = 0, & \text{for } r = R \\ \left[K_c\varphi\nabla\left(\varphi\frac{\partial u_z}{\partial r}\right) + K_\mu\varphi^2\frac{\partial u_z}{\partial r}\frac{\nabla\mu_{app}}{\mu_{app}}\right].n = 0, & \text{for } r = R \\ \varphi = \varphi_0, & \text{for } 0 \le r \le R \text{ at } z = 0 \end{cases} \tag{2.14}$$

The relationship between the shear stress and shear-rate values in concrete can be expressed by an appropriate rheological model (e.g., Bingham fluid). Moreover, the variation of viscosity and yield stress values can be described as functions of aggregate concentration and rheological properties of cement paste. The aggregate concentration can be evaluated during the pumping process using the SIPM's Eqs. 2.13-2.14. As reported in [23], after a certain amount of time, an equilibrium is achieved, and the concentration gradient of particles remains constant. The thickness and rheological properties of the LL can then be evaluated at this state.
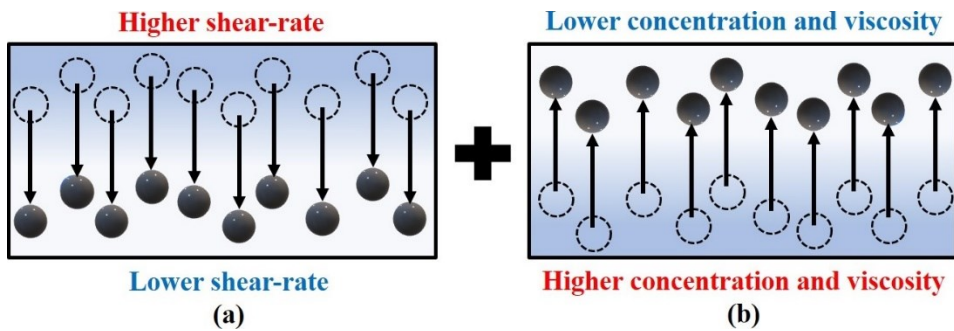
Fig. 2.5. Schematics of SIPM mechanism, migration from (a) higher shear-rate zones to low shear-rate ones, and (b) higher-concentration (higher viscosity) zones to low-concentration (lower viscosity) ones [31-33].

2.5 Numerical investigation of concrete pipe flow

Due to the opaque nature of concrete, the visual identification of a threshold to accurately measure the LL thickness during pumping is not reliable. Moreover, the alternative empirical methods, such as tribometers, cannot fully simulate the flow conditions during pumping procedure, due to their shear-rate limit and also lack of pressure [26]. Furthermore, due to assuming concrete as a single fluid, evaluating the effect of the multiphasic mechanisms that can cause the formation of the LL were neglected in the various analytical models (Eqs. 2.2-2.9). The analytical models cannot neither evaluate the effect of different pipeline segments, such as bends and reducers on concrete flow behavior. Moreover, concrete is typically pumped by using double piston pumps. The pulsation of pumping pressure showed significant effect on the SIPM and flow behavior of suspensions during pumping [36-38]. Pressure pulsation can keep the concrete in a permanent acceleration and deceleration (i.e., non-constant flow velocity), unlike the force equilibrium assumption of the analytical models [38]. This can lead to an additional force exerted on concrete in the pipe according to the 2nd Newton's law (i.e., $\Sigma F = m.dv/dt$). The variable flow velocity can alter the shear rate values. As explained earlier, this can thus affect the SIPM and Reynolds dilatancy of pumped concrete, as the main mechanisms leading to formation of the LL, during pulsating pumping flow. Snook et al. [36] reported the migration of particles toward the pipe center for volume fractions larger than 10% (e.g., concrete) under an oscillatory pumping regime.

Furthermore, rheological properties of concrete are changed through the long pumping lines. Feys et al. [39] reported that increasing pumping time and flow rate can substantially decrease the concrete viscosity due to additional shearing, hence leading to additional dispersion of cement particles. The air-void system also varies under pumping process, which can significantly change the rheological properties of the pumped concrete [39].

However, these effects cannot be taken into consideration using the analytical models. In order to provide more realistic prediction of concrete pipe flow, the computational techniques must be employed to consider the physical interaction between the solid and liquid phases of concrete under pipe-flow conditions.

Such tools are developed to describe the flow of concrete in a pipeline under pressure where different materials can exist. Selection of an appropriate numerical methodology can lead to an adequate prediction, given the pumping condition. The following section discusses recent

numerical studies that have been carried out on concrete pumping. The advantages and disadvantages of these numerical approaches are subsequently discussed in "Discussions and Recommendations" section.

2.6 Numerical approaches to simulate concrete pipe flow

The computational modelling techniques to simulate the concrete pipe flow can be discussed in four main categories, as follow:

2.6.1 Single-phase modelling

In this approach, concrete is assumed as a continuous medium, and its rheological properties correspond to an equivalent single fluid, thus neglecting the presence of aggregate. Due to this simplification, this approach is frequently used to simulate the concrete flow in large scale casting. Several computational fluid dynamic (CFD) methods, such as Volume of Fluid (VOF) [40], were employed to simulate the concrete flow as a single-phase [6]. The flow domain is initially discretized in various mesh-cells, and then the incompressibility and no-slip boundary conditions are applied.

2.6.1.1 Single-phase modelling schema

Fresh concrete flow as a single-phase was modelled using the mass and momentum conversation equations for incompressible fluid, steady and laminar flow. The Navier-Stokes equations in the discretized version of an integral representation were implemented as a constitutive equation to evaluate the concrete flow as a single-phase [41,42], as follows:

$$\frac{\partial \rho}{\partial t} + \frac{\partial}{\partial x_i}(\rho . u_i) = 0 \tag{2.15}$$

$$\frac{\partial}{\partial t}(\rho . u_i) + \frac{\partial}{\partial x_j}(\rho . u_j . u_i) = -\frac{\partial P}{\partial x_i} + \frac{\partial}{\partial x_j}\left[\mu . \left(\frac{\partial u_i}{\partial x_j} + \frac{\partial u_j}{\partial x_i}\right)\right] \tag{2.16}$$

where ρ (kg/m^3), u (m/s), P (Pa), and μ (Pa.s) are the concrete density, flow velocity, pressure, and concrete viscosity, respectively. It is worthy to mention that at the right side, the negative term represents the normal stresses and the last term refers to the shear stresses. The most frequent codes used to simulate the fresh concrete as a single phase include OpenFOAM, ANSYS Fluent, and FLOW-3D.

2.6.1.2 *Examples of single-phase modellings of concrete pumping*

Various numerical studies carried out on single-phase modelling of concrete pumping are reported in the literature [8,17,19,22,42-44]. Using single-phase approach, the computational domain of pipe section is usually divided in two zones corresponding to the bulk concrete and LL zones. The rheological properties of each zone are independently assigned using the rheological and tribological measurements. The numerical predictions, established assuming either in the absence or presence of different LL thicknesses, can be compared to the experimental pumping pressure and flow velocity measurements in full-scale pipelines [8,17,22,42]. Moreover, the predicted LL thicknesses can be compared to those measured using image analyses of the cut pipe sections [17]. The numerical results revealed that assuming a LL thickness of almost 2 mm (1.5-3.5 mm) led to good agreements with the experimental ΔP measurements. However, neglecting the LL resulted in significant overestimation and underestimation of pumping pressure [42,43] and flow rate [19], respectively. This can highlight the significant effect of LL on concrete pumpability.

The most recent studies on single-phase modelling of concrete pumping were carried out in Germany [8,22,43-44]. These include the experimental and numerical investigations of concrete pipe flow in both laboratory and jobsite scales using a bi-viscous approach and the ANSYS Fluent software. The presence of LL was considered using a modified viscosity model. The studies indicated that the rheological properties of the concrete vary according to the radial position of each computational cell. Moreover, the employed bi-viscous approach was described by combining the Newtonian and Bingham models. Accordingly, for shear-rates less than a critical value ($\dot{\gamma} < \dot{\gamma}_c$), fresh concrete behaves as a Newtonian fluid with a higher initial viscosity ($\eta_N = 100$ Pa.s) than the bulk concrete. On the other hand, when $\dot{\gamma} > \dot{\gamma}_c$, the rheological properties of either the bulk concrete or LL were allocated depending on the radial position of the mesh-cells. Several assumptions were then considered for the LL thicknesses in the models based on either the experimental tribometer and Sliper results, analytical solutions for pipe flow and tribometers, or initial assumptions (2-8 mm) [8]. The LL thickness corresponding to the numerical simulations with the best fit with the experimental measurements of pumping pressure was finally reported as an optimized value. It is worthy to mention that the main finding regarding thickness of LL was between 2 and 4 mm for highly flowable (such as SCC) and conventional vibrated concrete (CVC), respectively [8].

Nerella and Mechtcherine [43] established a numerical model to simulate the flow behavior of various mixtures in the Sliper set-up. Secrieru et al. [44] simulated a small-scale pipeline of 36-mm diameter and 3.4-m length using the bi-viscous approach. Secrieru et al. [8] also simulated the pipe flow of different types of concrete in a 160-m pipeline, having 100- and 125-mm diameter, bents, and reducers. The Sliper test was also numerically simulated assuming different LL thicknesses (2-8 mm). The LL thicknesses resulted in the best agreement with the experimental Sliper pressure values, including 4 mm for CVC (Fig. 2.6a) and 2 mm for SCC (Fig. 2.6b) mixtures, were then applied in the numerical simulations of the full-scale pipelines. The numerical simulations were found in good agreements with the pressure values and LL thicknesses, evaluated using either the analytical models (Eqs. 2.2-2.3) or experimental measurements (Figs. 2.6c and 2.6d).
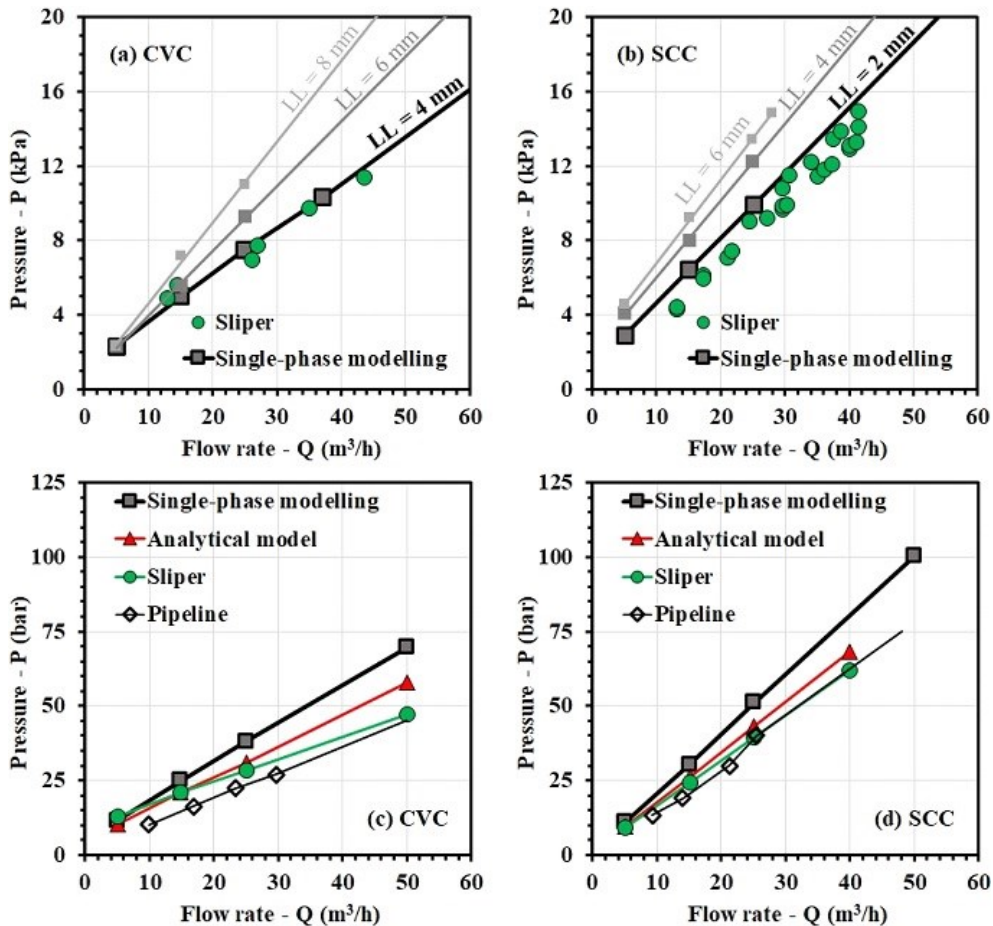
Fig. 2.6. Pressure (P)-flow rate (Q) graphs established for (a and b) calibration of the single-phase modelling with respect to LL thickness based on Sliper results, as well as (c and d) comparison between different experimental, analytical, and computational results obtained for full-scale pumping of CVC and SCC mixtures (adapted from [8])

2.6.2 *Phenomenological multiphasic approach (PMA)*

Few numerical investigations were carried out on concrete pumping using the phenomenological multiphasic approach (PMA) [15,45-46]. In this approach, the fresh concrete is considered as a suspension of fine and coarse aggregate in a suspending fluid (cement paste or mortar matrix). These studies employed the SIPM governing equation (Eq. 2.13) to simulate the suspension pipe flow. Assuming that the fresh concrete behaves according to the Bingham model, the apparent viscosity in Eq. 2.13 can be expressed, as $\mu_{app} = \mu_p + \frac{\tau_0}{\dot{\gamma}}$. The plastic viscosity μ_p and yield stress τ_0 of concrete are then defined as functions of the rheological properties of cement paste (μ_{p-p} and τ_{0-p}), volumetric fraction (φ), and packing density (φ_m) of fine (FA) and coarse aggregate (CA) [14,47-48], as follow:

$$\frac{\mu_p}{\mu_{p-p}} = \left(1 - \frac{\varphi_{FA}}{\varphi_{m-FA}}\right)^{-\eta^*_{FA}\cdot\varphi_{m-FA}} \cdot \left(1 - \frac{\varphi_{CA}}{\varphi_{m-CA}}\right)^{-\eta^*_{CA}\cdot\varphi_{m-CA}} \tag{2.17}$$

$$\frac{\tau_0}{\tau_{0-p}} = \sqrt{\frac{1 - \varphi_{FA}}{\left(1 - \frac{\varphi_{FA}}{\varphi_{m-FA}}\right)^{\eta^*_{FA}\cdot\varphi_{m-FA}}}} \cdot \sqrt{\frac{1 - \varphi_{CA}}{\left(1 - \frac{\varphi_{CA}}{\varphi_{m-CA}}\right)^{\eta^*_{CA}\cdot\varphi_{m-CA}}}} \tag{2.18}$$

where η^* is the shape-dependent intrinsic viscosity of solid particles (e.g., $\eta^* = 2.5$ for spheres). Consequently, the concentration profiles of aggregate across the pipe sections can then be estimated using the conservation equations for steady and incompressible pipe flow (Eq. 2.12), SIPM governing equation (Eq. 2.13), and appropriate boundary conditions (Eq. 2.14).

Jo et al. [45], Choi et al. [15], and Choi [46] employed the same PMA methodology to simulate the concrete pipe flow. A given length of pipe was modeled and discretized using quadrangular mesh cells, with finer sizes close to the pipe wall (LL zone). The authors used Fluent software to calculate the flow properties (i.e., pressure, velocity, shear-rate, etc.). Moreover, a subroutine program was coded to solve the SIPM equations (Eqs. 2.13-2.14), assuming $K_c = 0.3$ and $K_\mu = 0.6$ values, according to Phillips et al. [33]. Depending on the targeted multiphasic scale in numerical simulations, the established codes considered the yield stress and plastic viscosity relationships with solid dispersions (Eqs. 2.17-2.18), as well as the shape and size characteristics of the solid suspended particles to determine η^* values.

Jo et al. [45] carried out a parametric analysis to determine the effect of various influencing parameters, such as coarse aggregate size, water-to-binder ratio, and pipe diameter, on LL formation in a pipe model with 100-125-mm diameter and 1.5-m length. The authors assumed a spherical shape of the particles by setting the intrinsic viscosity $\eta^* = 2.5$ and $\varphi_m = 0.60$ values, according to Ferraris and Brower [14]. Similarly, Choi et al. [15] and Choi [46] evaluated the effect of shape and size of aggregate, respectively, on LL formation, velocity, and flow rate during pumping process. The circularity of fine and coarse aggregate particles was evaluated using the image analyses to estimate their intrinsic viscosity values using the empirical model proposed by Szecsy [49]. Accordingly, the obtained η^* values of 3.5-6 were used in the PMA simulations for different fine and coarse aggregate classes. For the experimental verification, 125-mm diameter pipelines of 170-m and 1000-m length were employed by Choi et al. [15] and Choi [46], respectively. UPV was also used to measure the velocity profile of concrete in the investigated pipelines. A numerical pipe model of 10-m length and 125-mm diameter was established. Considering the effect of particles morphology in estimating the rheological properties of suspensions significantly enhanced the precision of the established simulations. PMA resulted in accurate prediction of pumping pressures and velocity profiles compared to the experimental measurements.

The numerical results revealed that PMA is capable to evaluate the radial variation of rheological properties across the pipe section. According to the numerical PMA simulations, significantly lower aggregate concentration and rheological properties, as well as higher velocity and shear-rate values were obtained in a thin layer close to the pipe wall, referring to LL.

2.6.3 Discrete element method (DEM)

DEM was initially proposed for granular flow modellings [50,51]. In this approach, the problem is generally discretized by circular or spherical particles in 2D and 3D models, respectively. The interaction between the modelled particles and rheology of the suspending matrix are controlled using appropriate constitutive relationships. Accordingly, the elastic, viscous, and frictional components of particle-particle interactions are represented by virtual rheological elements consisting of springs, dashpots, and sliders, respectively. The spring constant (shear elasticity modulus "G") corresponds to the elastic state. Once the forces exerted on the particle exceed the yield stress τ_0 (threshold value) of the slider model, the plastic state of the flow is initiated with a μ_p (plastic viscosity) constant displacement rate of the modelled dashpots (Fig. 2.7). The properties

of the model material should then be calibrated using the experimental or theoretical algorithms [52,53]. The force-displacement law is then used to update the contact force arising from the relative motion at each contact. The motion law is again applied to the particles to update their velocity and position. This is based on the resultant force and momentum arising from the contact forces and gravity acting on the body. Numerical simulation of concrete flow using DEM led to develop valuable information of the flow properties of suspension, such as tracking of aggregate displacements, blocking, and segregation [52,53]. Moreover, DEM showed more accurate predictions of final spread compared to single-phase CFD models [54].
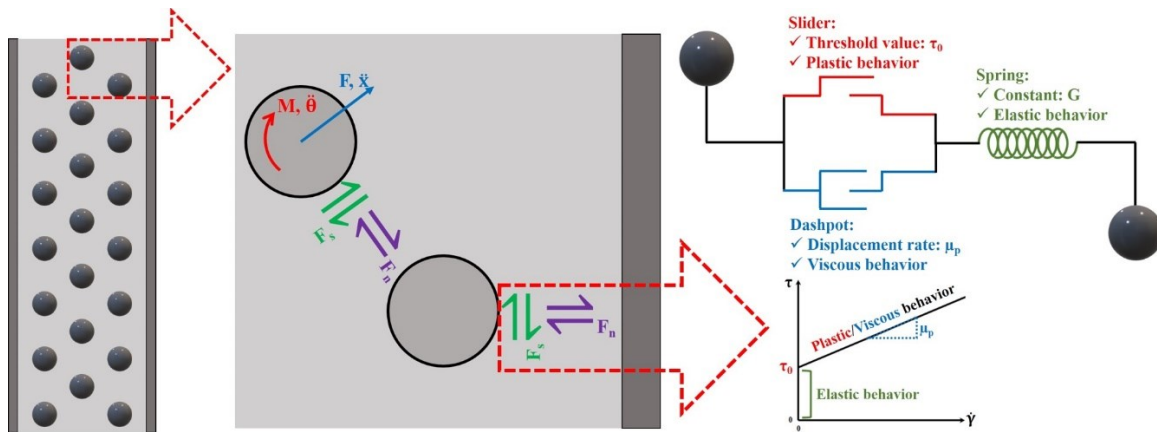
Fig. 2.7. Description of a visco-elastoplastic (Bingham) model by DEM method [52,53,55]

The motion of particles in DEM is controlled by the Newton's second law; i.e., $F = m\ddot{x}$ and $M = I\ddot{\theta}$, where $\ddot{x}$ and $\ddot{\theta}$ are the translational and angular acceleration vectors of a specific particle, m and I stand for mass and momentum of inertia, and F and M are the total force and momentum vectors, respectively. The F and M parameters correspond to the constitutive behavior at contact and external body force, such as gravity [55]. The translational ($\dot{x}$) and angular velocity ($\dot{\theta}$) are computed as the integration of the acceleration vectors over time. Similarly, the position and orientation of particles can be updated using the updated velocity vectors. This information is then used to evaluate the relationships between different contact entities, including the particles, obstacles, and wall boundaries, and eventually calculate the contact forces by the constitutive contact laws. Appropriate contact-models should be selected to describe the normal and shear components of the contacts. As shown in Fig. 2.7, the Bingham model is frequently used to describe the contact behavior.

Haustein et al. [37] employed DEM method by means of MercuryDPM software to simulate the effect of particle-size distribution and Coulomb's friction coefficient on the SIPM of bidisperse

particles under pulsating pumping regime. The numerical results successfully revealed three different regions across the pipe section of pulsating pumped granular flow with different solid contents and rheological properties, including the bulk, boundary, and buffer layers. The particles in the bulk layer at the pipe center were found to be near the random-close packing (high viscosity) and long-lasting frictional contacts. On the contrary, the materials in the boundary layer were shown to be sheared and thus loosened up (medium to high viscosity). Finally, the buffer layer consists in lower concentration of loosened particles under shear (low viscosity) and shorter interparticle frictional contacts. These layers correspond to the plug, sheared-concrete, and lubrication layers formed during concrete pipe flow, respectively.

Zhan et al. [55] carried out a parametric study to evaluate the effect of various parameters influencing the pumpability of concrete using DEM approach by means of PFC 5.0 code. The authors used the linear parallel bond model to describe the contact between the aggregate and pipe walls, consisting of pair of tensile and shear springs. The established aggregate-aggregate and aggregate-wall interactions consist of linear contact, dashpot, and parallel components. It is worthy to mention that all the defined parameters describing the contact-model are not equivalent to the conventional macroscopic properties which can be experimentally measured. In order to determine these contact parameters, a calibration process must be performed. Accordingly, some simple flow cases can be simulated with an initial assumption of a given set of contact parameters. Using the inverse analysis, the contact parameters are adjusted to achieve reasonable simulation results compared to the experimental ones. Zhan et al. [55] optimized the contact-model parameters by carrying out the slump-flow and V-Funnel tests. Then, they simulated the concrete flow in different representative straight pipe and elbow segments of 1-m length and 100-200-mm diameter. For example, under a pumping velocity = 0.3 m/s, pressure drop values of 0.035 and 0.012 MPa/m were obtained for the vertical and horizontal pipe segments for 150-mm diameter pipelines, respectively. The total pressure loss ΔP_{total} (MPa) of a full-scale pumping system was estimated as follows:

$$\Delta P_{total} \approx 0.035 \times H_{vertical} + 0.012 \times L_{horizontal} \tag{2.19}$$

where $H_{vertical}$ and $L_{horizontal}$ are the total pumping height and length of horizontal pipeline, respectively, in meter. The pressure results of the established DEM simulations were reasonably comparable to those measured at different well-known projects, such as Burj Khalifa ($H_{vertical}$ =

576 m and $L_{horizontal}$ = 83 m) and Shanghai ($H_{vertical}$ = 582 m and $L_{horizontal}$ = 150 m) towers [55]. Accordingly, Eq. (19) led to ΔP_{total} values of 21.15 and 22.17 MPa which are 23% higher and 5% smaller than values reported for Burj Khalifa (17.1 MPa) and Shanghai (23.4 MPa) towers, respectively.

2.6.4 Smoothed particle hydrodynamics (SPH)

Smoothed particle hydrodynamics (SPH) is an interpolation method to approximate values and derivatives of continuous field quantities by using discrete sample points [56]. These are identified as smoothed particles that carry concrete entities, including mass, position, and velocity. The particles can also carry estimated physical field quantities, such as mass-density, pressure, etc. SPH can approximate the derivatives of continuous fields using analytical differentiation on arbitrary-located particles. Each particle occupies a fraction of the discretized space [56]. As can be observed in Fig. 8, the SPH quantities are obtained as the weighted averages from the adjacent particles. The integral interpolant of any quantity function $f_i(x)$ is defined over all the space Ω, as follows:

$$f_s(x) = \sum_j f_j \frac{m_j}{\rho_j} W(x - x_j, h) \tag{2.20}$$

where W is the weighting kernel function, and h is the smoothing distance, which determines the interaction degree of a particle with its neighboring particles. Considering the conservation equations and density calculation, the integration/differential formats are changed to summation SPH discretized equations. For example, continuity equation can be changed to Eq. 21, where V and ρ denote velocity and density, respectively.

$$\frac{D\rho}{Dt} = -\rho\nabla.V \implies \frac{\partial\rho_i}{\partial t} = -\rho_i \sum_j \frac{m_j}{\rho_j} (V_i^\alpha - V_j^\alpha)\nabla_i^\alpha W_{ij} \tag{2.21}$$

Recently, there are several studies carried out on flow simulation of cement-based materials using SPH method [57,58]. Although SPH showed a considerable potential to simulate the heterogeneous phenomenon during concrete flow, the use of this method to simulate concrete pumping has been quite limited. Martys et al. [59] simulated the pipe flow of spherical suspended particles in a power-law rheology suspending fluid using SPH. The authors simulated the pipe flow of suspensions containing different concentrations of 1-mm spherical particles in three different suspending fluids

corresponding to Newtonian, shear-thinning, and shear-thickening types. The SPH simulations revealed that the shear-thinning and shear-thickening suspending fluids showed more flattened velocity profile than the Newtonian one. In the case of shear-thinning suspending fluid, a significant effective slip was observed near the pipe wall, despite the no-slip boundary assumption. This can be explained by the very high shear-rate values close to the wall, which leads to very low viscosity in the case of shear-thinning fluids. Therefore, the particles can easily move near the wall appearing as a slip effect. According to Martys et al. [59], in the case of concrete pumping and 3D printing applications, the shear-thinning behavior of the suspending matrix of concrete can lead to significantly facilitate the pumping process by providing higher flow velocity (flow rate) and lower pumping pressure.
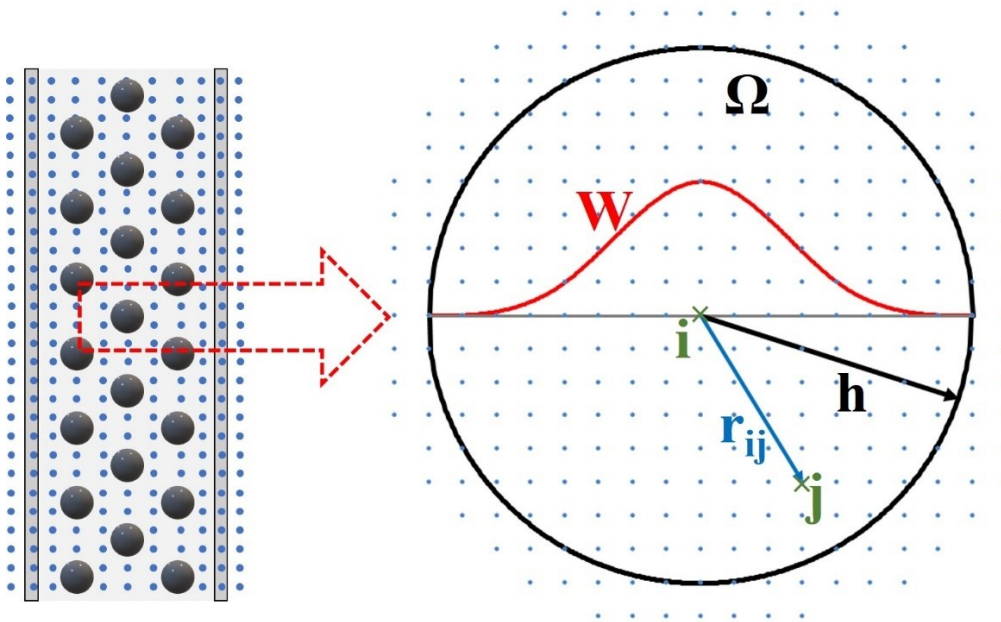
Fig. 2.8. Schematics of a typical SPH particle and its adjacent particles [56]

Most recently, Tran-Duc et al. [60] employed the SPH approach to evaluate the effect of different volumetric fractions (0-30%) and particle-size distributions of coarse aggregate (0.5, 8, 10, 16, and 20 mm) on pumpability of mortar and SCC. The mortar flow simulations showed identical flow velocity profiles with those obtained using the analytical solutions. On the other hand, SPH simulations revealed that, under a given pressure gradient (1.7 kPa/m), increasing the volumetric fraction (up to 30%) and size of coarse aggregate (up to 20 mm) can lead to lower (up to 47%) and higher (up to 24%) flow rates when pumping SCC, respectively.

2.7 Discussions and recommendations

The main advantages and disadvantage of the numerical methods to simulate the concrete pipe flow are discussed in this section.

2.7.1 Single-phase approach

In the case of single-phase approach, the calculation time is significantly reduced due to the absence of aggregate. However, the results of this approach are significantly sensitive to the mesh settings. Any small variation of the cells' sizes can considerably affect the accuracy of the numerical simulations to consider the shear conditions in different zones. A mesh-sensitivity analysis should then be performed to validate the robustness of the numerical solutions. On the other hand, despite the good agreements with the experimental measurements, the single-phase approach is not capable to simulate pipe blockage and different multiphasic mechanisms of LL formation. This is due to the fact that the fresh concrete is considered as a single phase without the presence of aggregate. Other multiphasic approaches were thus proposed to simulate the heterogeneous flow behavior of concrete in pipes [31-33,35].

2.7.2 Phenomenological multiphase approach (PMA)

PMA was shown to successfully simulate the main phenomena governing the shear-induced particle migration (SIPM). PMA helped to understand why and in which conditions the aggregate migrate from the higher to lower shear-rate zones of the pipe. In addition, the particle migration from the zones of higher viscosity and solid concentration toward those with lower values was also evaluated. The use of SIPM governing equation led to successfully simulate the equilibrium state when the final concentration profile of aggregate was achieved and, hence, the thickness and rheological properties of LL were estimated.

However, PMA is very dependent on appropriate assumption of the phenomenological constants K_c and K_μ. Moreover, the selection of the multiphasic scale of concrete suspension is debatable. Accordingly, based on a chosen size threshold, fresh concrete can be considered as a suspension of either fine and coarse aggregate in cement pastes, or coarser aggregate in fine mortars. The choice of this threshold that identifies the suspended particles and suspending phase can significantly affect the precision in predicting the solid concentrations of LL and bulk concrete. Moreover, the accuracy and computational time of PMA models are considerably dependent on

the size and number of the mesh-cells. The mesh-sensitivity should be thus evaluated to achieve robust numerical results. Furthermore, the PMA models can only predict the equilibrium state, hence the direct physical and hydrodynamic interactions between the aggregate and suspending fluid cannot be quantitatively simulated. Furthermore, the physical evaluation of inertia, particles' collisions, drag, surface tension, and surface roughness of aggregate and pipe cannot be considered in PMA. The physical interactions between solid and liquid phases of fresh concrete can be modelled using particle-based methodologies, such as DEM and SPH.

2.7.3 Discrete element method (DEM)

DEM showed a great potential to evaluate various heterogeneous phenomena during pumping, such as blocking, by simulating the displacement, velocity, and forces of individual particles. A proper assumption of aggregate grading or size thresholds to define the suspending and suspended phases can help to simulate LL formation using DEM. However, from physical point of view, it is difficult to define the direct contact between the modelled particles representing the suspending mortar and coarse aggregate. The experimental evaluation of the contact parameters is also impossible. On the other hand, simulating the motion of a huge number of particles in full-scale pipelines using DEM is almost impossible because of the limitation of the commonly used CPUs to do it in a reasonable calculation time. Furthermore, the complex secondary flows in the vicinity of wall and aggregate cannot be modelled using DEM.

In order to take into consideration such phenomena and reduce the calculation time, it is recommended to combine DEM with CFD analyses [61]. Accordingly, the influence of the suspending fluid can be simulated using a CFD code. The dynamics of aggregate in the established parallel DEM code can then be updated using the calculated hydrodynamic forces by means of the CFD model [61]. This is called coupled CFD-DEM modelling [61]. A comprehensive review on the basic method, progresses, and recent applications of CFD-DEM modelling approach is recently given by Kieckhefen et al. [61].

Zhou et al. [62] simulated the vertical pumping of biphasic suspensions of ceramic particles in water using CFD-DEM approach. The results were successfully validated by experimental measurements on suspensions made with 2.7%-10% solid particles measuring 2.32-3.82 mm in diameter that were pumped with different mass flow rates of 1.469 and 1.723 kg/s in a vertical pipe measuring 30.6-mm diameter and 2.2-m length. According to the numerical simulation results,

higher pressure drops were obtained with the increase in solid fraction. It was also revealed that considering the lift force in the estimation of the pressure loss can indeed enhance the accuracy of the numerical simulations. Accordingly, the simulations conducted with lift force led to prediction errors of 0.8%-17.9%, 2.0%-41.0%, and 5.0%-35.9% for liquid velocity, solid concentration, and solid velocity, respectively. The CFD-DEM simulations showed that the maximum particle concentration and flow velocity are obtained in the pipe center, which gradually decline in radial direction toward the wall. However, when the lift force is omitted, the tendency of the solid particles toward the center axis could not be reproduced.

As an example for concrete pipe flow modelling, Tan et al. [63] successfully employed the coupled CFD-DEM method to investigate the wear mechanism of the pipe elbows. The simulated elbow consisted of 100-mm diameter pipes including a 1.6-m horizontal part, 0.6-m vertical part, and a 90° circular bend with almost 0.628-m length, 0.3, and 0.4-m inner and outer radii, respectively. The concrete was modelled as a suspension of 25% cement paste (suspending fluid), 49% fine aggregate (2 mm), and 26% coarse aggregate (15 mm). The kinematics and trajectory of the particles impacting on the bended pipe were simulated to investigate the wear mechanism of the elbow. Accordingly, the location of the maximum erosive wear damage in the elbow was successfully found in agreement with that observed in actual pumping process. It was revealed that rather other parts of pipeline, the wall of the elbow would suffer more severe friction.

Most recently, Jiang et al. [64] optimized the layout and structural parameters of conveying pipes of pump truck using CFD-DEM simulations of concrete pipe flow through straight, inclined, reducer, and bend pipe segments, as well as their combination. The optimization parameters included the length and inclination of straight pipes, as well as the curvature radius and bending angle of the bend segments. The yield stress and plastic viscosity values of the investigated concrete mixtures ranged from 221.9 to 300.8 Pa and from 7.7 to 12.7 Pa.s, respectively. The authors reported a 5.5% reduction in pressure loss of the optimized model compared to the initial layouts. As expected, according to the numerical results, coarse aggregate was found more concentrated near the pipe center. The average velocity of the coarse aggregate of the optimized model was lower than that of the initial layout, hence improving the wear of the conveying pipes.

2.7.4 Smoothed particle hydrodynamics (SPH) method

Simulating the interactions between the aggregate, suspending paste/mortar matrix, and pipe walls using SPH can predict different heterogeneous mechanisms inducing LL formation. Considering different interparticle forces in a SPH model can result in more realistic predictions compared to DEM. However, the following challenges can be addressed to use SPH for modelling of concrete pipe flow:

- The large number of particles in SPH simulation, especially in the case of large-scale pipelines, can significantly increase the calculation time.

- A calibration step is essential to choose and optimize the appropriate weighting functions W (Eqs. 20-21).

- The optimization algorithms are required to discretize the suspending fluid, aggregate, and pipe wall boundaries by the computational particles to achieve robust numerical solutions. These optimizations can be expressed in terms of number, shape, diameter, size, spatial distribution, and layers number of the modelled particles.

2.8 Overall recommendation

According to the critical review presented in this paper, a guideline can be offered to select the appropriate computational method according to a given pumping application that needs to be simulated. The guideline attempts to strike a balance between the quality of the calculated information and complexity of the modeling and rapidity of calculation time.

- A relatively quick estimate of pressure-loss in large scale pipeline applications can be achieved using the single-phase approach that can result in the lowest calculation time.

- In order to evaluate the LL characteristics in terms of thickness and rheological properties in large scale pumping applications, the PMA approach is suggested to simulate the aggregate concentration profiles across the pipe section in an equilibrium state.

- For the prediction of the heterogeneous flow phenomena in the vicinity of bend and reducer segments, such as pipe blockage, which require shorter time intervals to simulate, the particle-based methods are recommended. Such methods include the DEM and SPH methods.

- The coupled CFD-DEM method is recommended as the most precise numerical approach by considering the physical interactions between the aggregate, suspending matrix, and pipe wall boundaries that lead to the formation of the LL, wear mechanisms of the piping wall, and pipe blockage.

2.9 Conclusions

Simulating concrete pumpability is of particular interest to properly design the pumping circuits for successful pumping process given the application on hand. In this paper, a comprehensive review of empirical, analytical, and numerical methodologies that can be used to assess concrete pumpability was presented. Different heterogeneous flow behaviors of concrete in pipes were presented and analyzed. Based on the critical review presented herein, the following concluding remarks can be drawn:

1) Numerical prediction tools can be successfully employed to overcome the complexities in experimentally characterizing the LL, in terms of rheological properties and thickness, during pumping.

2) The main mechanisms that can lead to the formation of the LL include the wall effect, Reynolds dilatancy, and shear-induced particle migration (SIPM). Reynolds dilatancy can partially explain the mechanism of LL formation. However, the absence of pressure leads to underestimating the LL thickness induced by Reynolds dilatancy compared to real pumping processes. Taking into consideration the main pipe flow conditions, including pressure, shear, and pipe confinement, as well as the interaction between solid and liquid phases of the concrete material, the SIPM can better be used to evaluate the LL formation compared to the other two influencing mechanisms.

3) Two main phenomenological models governing SIPM were formulated in terms of spatial variations of particles' interaction frequency and suspension viscosity. The SIPM governing equations were properly established to simulate the variation of aggregate concentration through the pipe diameter and better predict the characteristics of the LL.

4) Unlike the analytical models, numerical simulations can consider the multiphasic interactions of aggregate and cement paste/fine mortar matrices during pipe flow. Four different numerical methods were employed to simulate concrete pumpability and LL formation. This included single-phase, phenomenological multiphase (PMA), discrete

element method (DEM), and smoothed particle hydrodynamic (SPH) approaches. The single-phase modelling is the quickest approach to predict concrete pumpability in terms of pressure loss and flow velocity profiles, but this approach is unable to simulate the heterogeneous flow behavior of concrete pipe flow, including the formation of the LL.

5) Phenomenological multiphase approach can simulate the mechanisms of the LL formation using the SIPM governing equation. However, this approach cannot directly evaluate the physical interactions of aggregate and cement paste during pipe flow.

6) Simulating the interparticle interactions and displacements of individual particles, the DEM showed a great potential to predict the heterogenous flow behavior of concrete in pipes. However, it is difficult to experimentally characterize the physical contact parameters between the modelled particles.

7) The DEM can require extensive computational time to simulate the flow in a full-scale pipeline. The combination of DEM with CFD analyses was shown to enhance the accuracy of prediction and reduce the calculation time.

8) The SPH resulted in more realistic and physically-meaningful consideration of the interactions between the suspended particles, suspending fluid, and pipe wall, compared to the DEM. The main challenges to simulate concrete pipe flow using SPH were addressed in this study.

9) According to this critical review, a guideline was proposed to select appropriate numerical methods to simulate concrete pumping. Accordingly, the coupled CFD-DEM approach is recommended as the most precise and realistic computational approach to model concrete flow in pipes.

2.10 Acknowledgement

REFERENCES

[1]   D. Kaplan, F. De Larrard, and T. Sedran, Design of concrete pumping circuit, ACI Materials Journal, 102 (2) (2005)110-117.

[2]   D. Feys, K.H. Khayat, A. Perez-Schell, R. Khatib, Development of a tribometer to characterize lubrication layer properties of self-consolidating concrete, Cement & Concrete Composites, 54 (2014) 40-52. doi: 10.1016/j.cemconcomp.2014.05.008.

[3]   D. Feys, K.H. Khayat, Particle migration during concrete rheometry: How bad is it?, Materials and Structures, 50 (2017) 122. doi: 10.1617/s11527-016-0992-4.

[4]   D. Feys, How much is bulk concrete sheared during pumping?, Construction and Building Materials, 223 (2019) 341-351. doi: 10.1016/j.conbuildmat.2019.06.224.

[5]   S.H. Kwon, K.P. Jang, J.H. Kim, , S.P. Shah, State of the art on prediction of concrete pumping, International Journal of Concrete Structures and Materials, 10 (3) (2016) S75-S85.

[6]   M. Choi, C.F. Ferraris, N.S. Martys, D. Lootens, V.K. Bui, , H.R.T Hamilton, Metrology needs for predicting concrete pumpability, Advances in Materials Science and Engineering, (2015) 456238. doi: 10.1155/2015/456238.

[7]   R.D. Brown, P.B. Bamforth, Tests to establish concrete pumpability, ACI Journal Proceedings, 74 (5) (1977) 193-203.

[8]   E. Secrieru, W. Mohamed, S. Fataei, V. Mechtcherine, Assessment and prediction of concrete flow and pumping pressure in pipeline, Cement and Concrete Composites, V. 107, 2020, 103495. doi: 10.1016/j.cemconcomp.2019.103495.

[9]   D. Feys, G. De Schutter, , R. Verhoeven, Parameters influencing pressure during pumping of self-compacting concrete, Materials and Structures, 46 (2013) 533-555. doi: 10.1617/s11527-012-9912-4.

[10]   E. Buckingham, On plastic flow through capillary tubes, Proc Am Soc Test Mater, 21 (1921), 1154-1161.

[11]   D. Kaplan, De Larrard, T. Sedran, M. Vachon, G. Machese, Forecasting pumping parameters, In: Proc. of the 2nd Int RILEM symp. on self-compacting concrete, Tokyo, (2001) 556-564.

[12]   G. De Schutter, D. Feys, Pumping of fresh concrete: Insights and challenges", RILEM Technical Letters, V. 1, 2016, pp. 76-80. doi:10.21809/rilemtechlett.2016.15

[13]   S.H. Kwon, S.D. Jo, C.K. Park, J.H. Jeong, S.H. Lee, Prediction of concrete pumping: Part II-analytical prediction and experimental verification, ACI Materials Journal, 110 (6) (2013) 657-668.

[14]   C.F. Ferraris, L.E. Brower, Comparison of concrete rheometers: international tests at MB (Cleveland OH, USA) in 2003, *National Institute of Standards and Technology Interagency Report*, NISTIR 7145, 2003.

[15]   M.S. Choi, Y.J. Kim, S.H. Kwon, Prediction on pipe flow of pumped concrete based on shear-induced particle migration, Cement and Concrete Research, 52 (2013) 216-224. doi: 10.1016/j. cemconres.2013.07.004.

[16]   K.P. Jang, W.J. Kim, M.S. Choi, S.H. Kwon, A new method to estimate rheological properties of lubricating layer for prediction of concrete pumping, Adv. Concr. Constr., 6 (5) (2018) 465-483.

[17]   L. Chen, G. Liu, , W. Cheng, G. Pan, Pipe flow of pumping wet shotcrete based on lubrication layer, SpringerPlus 5, 945 (2016).

[18]   S. Jacobsen, L. Haugan, T.A. Hammer, E. Kalogiannidis, Flow conditions of fresh mortar and concrete in different pipes, Cement and Concrete Research, 39 (11) (2009) 997-1006. doi:10.1016/j.cemconres.2009.07.005.

[19]   H.D. Le, E.H. Kadri, S. Aggoun, J. Vierendeels, P. Troch, G. De Schutter, Effect of lubrication layer on velocity profile of concrete in a pumping pipe, Materials and Structures, 48 (2015) 3991-4003. doi: 10.1617/s11527-014-0458-5.

[20]   E. Secrieru, S. Fataei, C. Schröfl, V. Mechtcherine, Study on concrete pumpability combining different laboratory tools and linkage to rheology, Construction and Building Materials, 144 (2017) 451-461. doi: 10.1016/j.conbuildmat.2017.03.199.

[21]   T.T. Ngo, E.H. Kadri, R. Bennacer, F. Cussigh, Use of tribometer to estimate interface friction and concrete boundary layer composition during the fluid concrete pumping, Construction and Building Materials, 24 (7) (2010) 1253-1261. doi: 10.1016/j.conbuildmat.2009.12.010.

[22]   E. Secrieru, Pumping behaviour of modern concretes – Characterisation and prediction, Ph.D. Dissertation, Technische Universität Dresden, (2018).

[23]   A. Salinas, D. Feys, Estimation of lubrication layer thickness and composition through reverse engineering of interface rheometry tests, Materials, 13 (8) (2020) 1799. doi: 10.3390/ma13081799

[24]   V. Mechtcherine, V.N. Nerella, K. Kasten, Testing pumpability of concrete using Sliding Pipe

Rheometer, Construction and Building Materials, 53 (2014) 312-323. doi: 0.1016/j.conbuildmat.2013.11.037

[25]   S.H. Kwon, S.D. Jo, C.K. Park, J.H. Jeong, S.H. Lee, Prediction of concrete pumping: Part I-development of new tribometer for analysis of lubrication layer, ACI Materials Journal, 110 (6) 647-656.

[26]   D. Feys, K.H. Khayat, A. Perez-Schell, R. Khatib, Prediction of pumping pressure by means of new tribometer for highly-workable concrete, Cement and Concrete Composites, 57 (2015). doi: 10.1016/j.cemconcomp.2014.12.007

[27]   V. Vand, Viscosity of solutions and suspensions. I. Theory, J. Phys. Colloid Chem., 52 (1948) 277-299. doi: 10.1021/j150458a001

[28]   O. Reynolds, LVII. On the dilatancy of media composed of rigid particles in contact. With experimental illustrations, The London, Edinburgh, and Dublin Philosophical Magazine and Journal of Science, 20 (127) 1885 469-481. doi: 10.1080/14786448508627791

[29]   X. Meng, Y. Wang, Modeling dynamic flows of grain–fluid mixtures by coupling the mixture theory with a dilatancy law, Acta Mechanica, 229 (6) (2018) 2521-2538. doi: 10.1007/s00707-018-2111-9.

[30]   M. Hosseinpoor, B.I.O. Koura, A. Yahia, New methodology to evaluate the Reynolds dilatancy of self-consolidating concrete using 3D image analysis – Coupled effect of characteristics of fine mortar and granular skeleton, Cement and Concrete Composites, 108 (2020) 103547. doi: 10.1016/j.cemconcomp.2020.103547.

[31]   D. Leighton, A. Acrivos, Measurement of shear-induced self-diffusion in concentrated suspensions of spheres, J. Fluid. Mech., 177 (1987) 109-131. doi: 10.1017/S0022112087000880.

[32]   D. Leighton, A. Acrivos, The shear-induced migration of particles in concentrated suspensions, J. Fluid. Mech., 181 (1987) 415-439. doi: 10.1017/S0022112087002155.

[33]   R.J. Phillips, R.C. Armstrong, R.A. Brown, A.L. Graham, J.R. Abbott, A constitutive equation for concentrated suspensions that accounts for shear-induced particle migration, Phys. Fluids A: Fluid Dynamics 4, 30 (1992) 30-40.

[34]   I.M. Krieger, T.J. Dougherty, A mechanism for non-Newtonian flow in suspensions of rigid spheres, Transaction of the Society of Rheology, 3 (1959) 137-152. doi: 10.1122/1.548848.

[35]   Y.C. Lam, X. Chen, K.W. Tan, J.C. Chai, S.C.M. Yu, Numerical investigation of particle migration

in Poiseuille flow of composite system, Composites Science and Technology, 64 (7-8) (2004) 1001-1010. doi: 10.1016/j.compscitech.2003.08.005.

[36] B. Snook, J.E. Butler, É. Guazzelli, Dynamics of shear-induced migration of spherical particles in oscillatory pipe flow, Journal of Fluid Mechanics, 786 (2016) 128-153. doi: 10.1017/jfm.2015.645.

[37] M.A. Haustein, G. Zhang, R. Schwarze, Segregation of granular materials in a pulsating pumping regime, Granular Matter, 21 (2019) 111. doi: 10.1007/s10035-019-0967-6.

[38] M.A. Haustein, R. Schwarze, Experimental investigation of the pumping of a model-concrete through pipes, Materials, 13 (5) (2020) 1161. doi: 10.3390/ma13051161.

[39] D. Feys, G. De Schutter, K.H. Khayat, R. Verhoeven, Changes in rheology of self-consolidating concrete induced by pumping, Materials and Structures, 49 (2016) 4567-4677. doi: 10.1617/s11527-016-0815-7.

[40] C.W. Hirt, B.D. Nichols, Volume of fluid (VOF) method for the dynamics of free boundaries, Journal of Computational Physics, 39 (1) (1981) 201-225. doi: 10.1016/0021-9991(81)90145-5.

[41] R. Schwarze, CFD-Modellierung: Grundlagen und Anwendungen bei Strömungsprozessen, Springer-Verlag, Berlin/Heidelberg, 2013.

[42] M. Choi, N. Roussel, Y. Kim, J. Kim, Lubrication layer properties during concrete pumping, Cement and Concrete Research, 45 (2013) 69-78. doi: 10.1016/j.cemconres.2012.11.001.

[43] V.N. Nerella, V. Mechtcherine, Virtual Sliding Pipe Rheometer for estimating pumpability of concrete, Construction and Building Materials, 170 (2018) 366-377. doi: 10.1016/j.conbuildmat.2018.03.003

[44] E. Secrieru, J. Khodor, C. Schröfl, V. Mechtcherine, Formation of lubrication layer and flow type during pumping of cement-based materials, Construction and Building Materials, 178 (2018) 507-517. doi: 10.1016/j.conbuildmat.2018.05.118

[45] S.D. Jo, C.K. Park, J.H. Jeong, S.H Lee, S.H. Kwon, A computational approach to estimating a lubricating layer in concrete pumping, Computers Materials and Continua, 27 (3) (2012) 189-210.

[46] M.S. Choi, Numerical prediction on the effects of the coarse aggregate size to the pipe flow of pumped concrete, Journal of Advanced Concrete Technology, 12 (2014) 239-249. doi:10.3151/jact.12.239

[47] H. Hafid, G. Ovarlez, F. Toussaint, P.H. Jezequel, N. Roussel, Estimating measurement artifacts in

concrete rheometers from MRI measurement on model materials, In Proceedings of SCC2010, 2010, Montreal, Canada, 127-137.

[48]   X. Chateau, G. Ovarlez, K.L. Trung, Homogenization approach to the behavior of suspensions of noncolloidal particles in yield stress fluids, Journal of Rheology, 52 (2) (2008) 489-506. doi:10.1122/1.2838254

[49]   R.S. Szecsy, Concrete Rheology, Ph.D thesis, Urbana, Illinois, 1997.

[50]   P.A. Cundall, A computer model for simulating progressive, large-scale movement in blocky rock system, Proceedings of the International Symposium on Rock Mechanics, Nancy, France, 4-6 October 1971.

[51]   P.A. Cundall, O.D.L. Strack, A discrete numerical model for granular assemblies, *Géotechnique*, 29 (1) (1979) 47-65. doi:10.1680/geot.1979.29.1.47

[52]   N. Roussel, M.R. Geiker, F. Dufour, L.N. Thrane, P. Szabo, Computational modeling of concrete flow: General overview, Cement and Concrete Research, 37 (9) (2007) 1298-1307. doi: 10.1016/j.cemconres.2007.06.007

[53]   N. Roussel, A. Gram, M. Cremonesi, L. Ferrara, K. Krenzer, V. Mechtcherine, S. Shyshko, J. Skocec, J. Spangenberg, O. Svec, L.N. Thranse, K. Vasilic, Numerical simulations of concrete flow: A benchmark comparison, Cement and Concrete Research, 79 (2016) 265-271. doi: 10.1016/j.cemconres.2015.09.022.

[54]   A. Gram, J. Silfwerbrand, Numerical simulation of fresh SCC flow: applications, Materials and Structures, 44 (4) (2011) 805-813. doi: 10.1617/s11527-010-9666-9.

[55]   Y. Zhan, J. Gong, Y. Huang, C. Shi, Z. Zuo, Y. Chen, Numerical study on concrete pumpability behavior via local flow simulation with discrete element method, Materials, 12 (9) (2019) 1415. doi: 10.3390/ma12091415.

[56]   G.R. Liu, M.B. Liu, Smoothed particle hydrodynamics: A Meshfree Particle Method, World Scientific Printers CO. Pte. Ltd., Singapore, ISBN 981-238-456-1.

[57]   M.S.A. Dhaheer, S. Kulasegaram, B.L. Karihaloo, Simulation of self-compacting concrete flow in the J-ring test using smoothed particle hydrodynamics (SPH), Cement and Concrete Research, 89, (2016) 27-34. doi: 10.1016/j.cemconres.2016.07.016.

[58]   T. Tran-Duc, T. Ho, N. Thamwattana, A smoothed particle hydrodynamics study on effect of coarse

aggregate on self-compacting concrete flows, International Journal of Mechanical Sciences, 190 (2021) 106046. doi: 10.1016/j.ijmecsci.2020.106046.

[59]   N.S. Martys, W.L. George, R.P. Murphy, K.M. Weigandt, Pipe flow of sphere suspensions having a power-law dependent fluid matrix, Journal of Rheology, 64 (2) (2020) 445-457. doi: 10.1122/1.5131021.

[60]   T. Tran-Duc, T. Ho, N. Thamwattana, A smoothed particle hydrodynamics study on effect of coarse aggregate on self-compacting concrete flows, International Journal of Mechanical Sciences, 190 (2021) 106046. doi: 10.1016/j.ijmecsci.2020.106046.

[61]   P. Kieckhefen, S. Pietsch, M. Dosta, S. Heinrich, Possibilities and limits of computational fluid dynamics–discrete element method simulations in process engineering: A review of recent advancements and future trends, Annual Review of Chemical and Biomolecular Engineering, 11 (2020) 397-422. doi: 10.1146/annurev-chembioeng-110519-075414

[62]   M. Zhou, S. Wang, S. Kuang, K. Luo, J. Fan, A. Yu, CFD-DEM modelling of hydraulic conveying of solid particles in a vertical pipe, Powder Technology, 354 (2019) 893-905. doi: 10.1016/j.powtec.2019.07.015.

[63]   Y. Tan, H. Zhang, D. Yang, S. Jiang, J. Song, Y. Sheng, Numerical simulation of concrete pumping process and investigation of wear mechanism of the piping wall, Tribology International, 46 (1) 2(012) 137-144.

[64]   S. Jiang, X. Chen, G. Cao, Y. Tan, X. Xiao, Y. Zhou, S. Liu, Z. Tong, Y. Wu, Optimization of fresh concrete pumping pressure loss with CFD-DEM approach, Construction and Building Materials, 276 (2021) 122204. doi: 10.1016/j.conbuildmat.2020.122204.

CHAPTER 3. METHODOLOGY

3.1 Introduction

Since the thesis follows an article-based structure, the methodology employed is detailed in each chapter. However, in this chapter, the methodologies employed, the objectives of this study, as well as the logic behind the selection of the numerical modeling algorithm are presented.

3.2 Simulation approaches

In this study, the flow behavior of concrete during pumping process is modeled. Different numerical methodologies were employed to evaluate the effect of rheological properties of concrete, as well as the characteristics of the lubrication layer (e.g., thickness and tribological properties) on the pumpability of SCC (i.e., pressure loss). Moreover, the mechanisms of the formation of lubrication layer was modeled as a heterogeneous phenomenon. This study was conducted in two main phases (See Fig. 3.1):

1. **Phase 1** is focused on homogenous analysis of pipe flow of various highly-flowable concrete mixtures in a large-scale pumping circuit. New tri-viscous models were proposed to simulate concrete pipe flow as a single fluid with radially variable rheological properties across the pipe, corresponding to the LL, BC, and the plug flow zones. The CFD models were established to predict the pressure loss of the pumping experiments. The LL and plug flow zones were characterized in terms of rheological properties and thickness. The coupled effect of the characteristics of different radial zones, flow rate, and pipe diameter on pumping pressure loss were investigated.

2. **Phase 2** involves modeling the heterogeneous phenomenon leading to the formation of the LL. The pipe flow of the concrete is simulated as a diphasic suspension of aggregate with different PSDs and concentrations in suspending mortar matrix with different rheological properties. The shear-induced particle migration and wall effect phenomenon were modeled using particle-based methods, including DEM and coupled CFD-DEM. The heterogeneous analyses were carried out in aggregate scales with wide size distribution to facilitate the pumping procedure by better understanding the LL formation mechanisms. Contribution of the key factors are highlighted to estimate the heterogenous rheological behavior of concrete across the pipe.
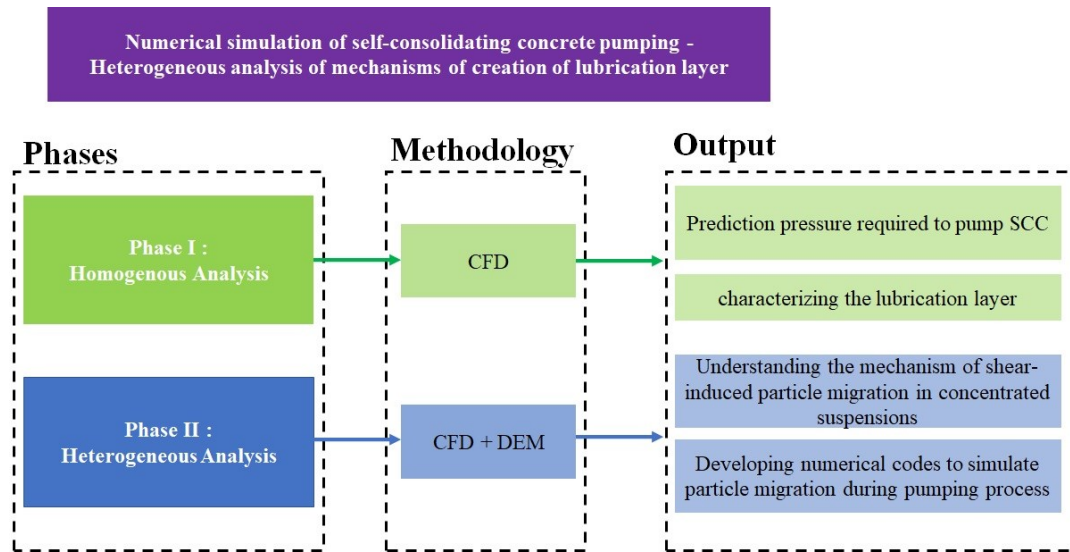
Fig. 3.1. Methodology of this study, including homogenous and heterogeneous analyses of concrete pipe flow.

3.2.1 Phase 1: Homogenous modeling of concrete flow

In this section, computational fluid dynamic (CFD) was applied to predict the pressure needed to pump fluid concrete given the pumping circuit. The pipe flow of 22 highly-flowable concrete mixtures with different rheological properties, including four highly-workable concrete (HWC) and 18 SCC, through a 30-m circuit were considered (Fig. 1.2). The pipe flow behavior of the investigated mixtures was simulated using CFD for two 10-m horizontal segments of the circuit with different pipe diameters of 100 and 125 mm under different flow rates. The rheological properties of the LL and reference mixtures were experimentally measured at the Université de Sherbrooke (Canada) in 2013 [1]. The pumping measurements repeated either four, five, or six times in 30-min intervals depending on the workability of mixtures and pump power. The rheological properties and compositions of the investigated mixtures are presented in Table 3.1.

The concrete pipe flow was simulated as single or two fluids without considering the presence of particles. The challenge was how to consider the presence of the LL with different rheological properties compared to the BC. Due to the formation of the LL, three regions with different rheological properties are developed in the pipe; one corresponding to the LL in vicinity of the pipe wall, and second one corresponds to the sheared BC with greater rheological properties than those of the LL, and the third refers to the plug flow zone in pipe center with higher plastic viscosity and yield stress than those of BC and LL. In this phase, three different

methodologies were developed based on two fluid and single fluid approaches to model the radial variation in rheological properties of concrete across the pipe, which were explained in detail in the following sections. By applying these proposed methodologies, three different regions, including the plug flow, BC, and LL zones, can be distinguishable using the velocity profiles obtained using the simulation results. The characteristics of different pipe flow zones were also evaluated in terms of thickness and rheological properties.

The simulation results were validated with experimental values reported in Reference [2]. Several parameters, including the pumping pressure, flow rate, rheological, tribological, and workability properties of the investigated mixtures were measured over time. The experiments were carried out under different flow rate magnitudes ranging from 4 to 20 L/s. Detailed information regarding the experimental set-up and measurement procedures can be found in Ref. [1].

Table 3.1. Fresh density, rheological, and tribological properties of the investigated mixtures [3,4].

Mix		Test 1	Test 2	Test 3	Test 4	Test 5	Test 6
HWC1	ρ (kg/m³)	2373	2391	2367	2381	-	-
	$\tau_{0\text{-}C}$ (Pa)	188	146	330	518	-	-
	$\mu_{p\text{-}C}$ (Pa.s)	99	96	92	89	-	-
	$\tau_{0\text{-}LL}$ (Pa)	59	76	89	151	-	-
	η_{LL} (Pa.s.m⁻¹)	2591	3549	2572	2563	-	-
HWC2	ρ (kg/m³)	2347	2374	2370	2369	-	-
	$\tau_{0\text{-}C}$ (Pa)	99	119	128	239	-	-
	$\mu_{p\text{-}C}$ (Pa.s)	86	89	87	99	-	-
	$\tau_{0\text{-}LL}$ (Pa)	38	96	89	88	-	-
	η_{LL} (Pa.s.m⁻¹)	2682	3377	3396	2979	-	-
HWC3	ρ (kg/m³)	2360	2364	2373	2359	2363	-
	$\tau_{0\text{-}C}$ (Pa)	121	169	213	358	838	-
	$\mu_{p\text{-}C}$ (Pa.s)	56	55	65	59	56	-
	$\tau_{0\text{-}LL}$ (Pa)	4	73	83	67	129	-
	η_{LL} (Pa.s.m⁻¹)	2117	1689	1464	2674	2680	-
HWC4	ρ (kg/m³)	2340	2361	2362	2372	2359	-
	$\tau_{0\text{-}C}$ (Pa)	52	48	69	64	79	-
	$\mu_{p\text{-}C}$ (Pa.s)	62	62	60	57	57	-
	$\tau_{0\text{-}LL}$ (Pa)	44	77	65	54	62	-
	η_{LL} (Pa.s.m⁻¹)	2607	1603	1576	2627	2007	-
SCC1	ρ (kg/m³)	2424	2434	2435	2401	2380	-
	$\tau_{0\text{-}C}$ (Pa)	35	40	29	45	35	-
	$\mu_{p\text{-}C}$ (Pa.s)	52	47	47	50	58	-
	$\tau_{0\text{-}LL}$ (Pa)	29	20	29	13	72	-
	η_{LL} (Pa.s.m⁻¹)	2223	1714	1778	2023	2577	-
SCC2	ρ (kg/m³)	2404	2398	2423	2343	2306	-
	$\tau_{0\text{-}C}$ (Pa)	37	35	30	86	381	-
	$\mu_{p\text{-}C}$ (Pa.s)	40	39	40	44	50	-
	$\tau_{0\text{-}LL}$ (Pa)	0	46	51	76	105	-
	η_{LL} (Pa.s.m⁻¹)	1860	1627	1632	1729	3001	-
SCC3	ρ (kg/m³)	2377	2370	2340	2384	-	-
	$\tau_{0\text{-}C}$ (Pa)	23	48	92	138	-	-
	$\mu_{p\text{-}C}$ (Pa.s)	37	35	40	40	-	-
	$\tau_{0\text{-}LL}$ (Pa)	18	51	39	69	-	-
	η_{LL} (Pa.s.m⁻¹)	1844	2058	1451	2399	-	-

Table 3.1. Continued

Mix		Test 1	Test 2	Test 3	Test 4	Test 5	Test 6
SCC4	ρ (kg/m^3)	2397	2438	2412	2442	2430	-
	τ_{0-C} (Pa)	59	32	48	68	47	-
	μ_{p-C} (Pa.s)	52	43	39	37	36	-
	τ_{0-LL} (Pa)	39	38	24	31	16	-
	η_{LL} (Pa.s.m^{-1})	1754	1570	1611	1388	2167	-
SCC5	ρ (kg/m^3)	2359	2367	2348	2307	2372	-
	τ_{0-C} (Pa)	27	20	15	11	10	-
	μ_{p-C} (Pa.s)	33	30	27	27	26	-
	τ_{0-LL} (Pa)	0	4	4	11	0	-
	η_{LL} (Pa.s.m^{-1})	700	381	402	414	995	-
SCC7	ρ (kg/m^3)	2407	2444	2395	2465	-	-
	τ_{0-C} (Pa)	84	66	89	80	-	-
	μ_{p-C} (Pa.s)	76	63	62	69	-	-
	τ_{0-LL} (Pa)	19	49	35	49	-	-
	η_{LL} (Pa.s.m^{-1})	2330	2723	2567	1720	-	-
SCC8	ρ (kg/m^3)	2451	2442	2371	2436	2424	-
	τ_{0-C} (Pa)	46	38	37	40	40	-
	μ_{p-C} (Pa.s)	55	63	61	59	57	-
	τ_{0-LL} (Pa)	0	9	17	24	52	-
	η_{LL} (Pa.s.m^{-1})	2463	2027	1847	1776	2525	-
SCC9	ρ (kg/m^3)	2355	2350	2374	2387	-	-
	τ_{0-C} (Pa)	38	28	19	19	-	-
	μ_{p-C} (Pa.s)	29	29	27	27	-	-
	τ_{0-LL} (Pa)	18	7	7	18	-	-
	η_{LL} (Pa.s.m^{-1})	490	240	252	326	-	-
SCC10	ρ (kg/m^3)	2255	2255	2265	2357	-	-
	τ_{0-C} (Pa)	41	49	41	54	-	-
	μ_{p-C} (Pa.s)	50	43	43	46	-	-
	τ_{0-LL} (Pa)	24	2	4	18	-	-
	η_{LL} (Pa.s.m^{-1})	1247	1372	1427	1334	-	-
SCC11	ρ (kg/m^3)	2335	2348	2335	2327	2325	-
	τ_{0-C} (Pa)	31	34	28	76	107	-
	μ_{p-C} (Pa.s)	33	30	31	35	46	-
	τ_{0-LL} (Pa)	6	9	13	27	54	-
	η_{LL} (Pa.s.m^{-1})	948	1279	1299	1024	3395	-
SCC12	ρ (kg/m^3)	2343	2338	2354	2315	-	-
	τ_{0-C} (Pa)	90	120	255	652	-	-
	μ_{p-C} (Pa.s)	83	97	102	104	-	-
	τ_{0-LL} (Pa)	70	121	93	171	-	-
	η_{LL} (Pa.s.m^{-1})	3714	4366	3279	2901	-	-
SCC13	ρ (kg/m^3)	2215	2256	2247	2258	2288	
	τ_{0-C} (Pa)	37	38	36	56	52	-
	μ_{p-C} (Pa.s)	46	40	41	39	41	-
	τ_{0-LL} (Pa)	17	37	37	24	26	-
	η_{LL} (Pa.s.m^{-1})	1424	1084	1083	729	1207	-
SCC14	ρ (kg/m^3)	2282	2279	2308	2315	-	-
	τ_{0-C} (Pa)	25	27	20	19	-	-
	μ_{p-C} (Pa.s)	38	28	29	32	-	-
	τ_{0-LL} (Pa)	37	19	21	10	-	-
	η_{LL} (Pa.s.m^{-1})	629	531	536	431	-	-
SCC15	ρ (kg/m^3)	2361	2345	2371	2357	2358	-
	τ_{0-C} (Pa)	64	53	59	46	73	-
	μ_{p-C} (Pa.s)	57	49	48	48	46	-
	τ_{0-LL} (Pa)	23	14	11	54	29	-
	η_{LL} (Pa.s.m^{-1})	1543	1720	1713	1767	1368	-

Table 3.1. Continued

Mix		Test 1	Test 2	Test 3	Test 4	Test 5	Test 6
SCC16	ρ (kg/m^3)	2346	2369	2386	2383	2365	-
	$\tau_{0\text{-}C}$ (Pa)	51	47	53	67	99	-
	$\mu_{p\text{-}C}$ (Pa.s)	59	49	61	54	55	-
	$\tau_{0\text{-}LL}$ (Pa)	1	36	38	8	42	-
	η_{LL} (Pa.s.m^{-1})	2652	1913	1635	2118	1415	-
SCC17	ρ (kg/m^3)	2363	2366	2377	2373	2363	
	$\tau_{0\text{-}C}$ (Pa)	30	25	41	48	58	-
	$\mu_{p\text{-}C}$ (Pa.s)	48	41	43	50	42	-
	$\tau_{0\text{-}LL}$ (Pa)	12	49	34	24	8	-
	η_{LL} (Pa.s.m^{-1})	1360	1539	1424	1484	2051	-
SCC18	ρ (kg/m^3)	2414	2411	2407	2389	2391	2391
	$\tau_{0\text{-}C}$ (Pa)	48	54	59	81	84	165
	$\mu_{p\text{-}C}$ (Pa.s)	65	65	67	73	69	88
	$\tau_{0\text{-}LL}$ (Pa)	11	39	35	17	11	37
	η_{LL} (Pa.s.m^{-1})	2493	2456	2386	1728	1940	2753
SCC19	ρ (kg/m^3)	2419	2420	2425	2398	2424	-
	$\tau_{0\text{-}C}$ (Pa)	84	91	138	138	476	-
	$\mu_{p\text{-}C}$ (Pa.s)	149	129	145	164	192	-
	$\tau_{0\text{-}LL}$ (Pa)	120	231	254	301	291	-
	η_{LL} (Pa.s.m^{-1})	5365	7893	6668	6983	6003	-

The Reynolds number of the investigated mixtures in the pumping circuit is less than 10 and the hydrodynamic entry length is less than 0.04. Therefore, the investigated pipe flows were considered to be in laminar and fully developed flow regimes. Therefore, the simulations were carried out in two dimensions and 1-m pipe length to reduce the calculation time.

The numerical simulations were carried out using OpenFOAM as an open-source software. The FOAM stands for Open-Source Field Operation and Manipulation. OpenFoam is an object-oriented software developed in C++ which benefits from a set of precompiled libraries which are provided as source code. It allows the users to conveniently customize their library to create their own model. Therefore, besides cost benefit, the time for coding is saved. Moreover, the powerful libraries and solvers of OpenFoam allow to solve almost any CFD problem [4].

Regarding the abovementioned advantages, the behavior of pumped concrete can be modeled by choosing proper solver and viscosity models in OpenFoam. Since none of the existing viscosity models in OpenFoam can correctly take in to account the behavior of concrete in pipes, three different viscosity models were developed and two of them were added to the OpenFoam libraries. The first method was established based on two fluids, corresponding to the LL and BC, while the second and the third ones were based on a single fluid flow with radially variable rheological properties across the pipe. By implementing the developed viscosity models, the effect of the LL on the pressure loss can be predicted. Therefore, the presented CFD models can result in higher accuracy in comparison with the previous single-

phase CFD models in literature. The explanation, advantages, and disadvantages of each model were explained in the following sections.

3.2.1.1 Two-phase approach (Double-Bingham Model)

In this approach, two different Bingham fluid phases correspond to the BC and LL. The interFoam, as one of the standard solvers for two incompressible and isothermal immiscible fluids in OpenFoam, was used [5]. The two immiscible fluids were separated by introducing the parameter α, namely the volume fraction which was explained in the following sections.

3.2.1.1.1 Governing equations of InterFoam

InterFoam solves following transport phase and Navier-Stokes equations using PISO algorithm (Pressure-Implicit with Splitting of Operators) for pressure-velocity coupling and applying volume of fluid (VOF) method to model the interface between two incompressible, isothermal, and immiscible fluids. InterFoam uses a numerical technique namely finite volume method (FVM) to solve the problems [5–9]. In FVM, the geometry is discretized in the first step to finite volumes. This method transforms the partial differential equations into discrete algebraic equations over finite volumes. By integrating the extracted differential equations over the discretized elements, they are transformed into algebraic equations. The Governing equations for interFoam solver are written, as follows [5,9]:

Continuity equation: $\nabla \cdot u = 0$ (3.1)

Transport phase equation (interface): $\frac{\partial \alpha}{\partial t} + \nabla \cdot (u\alpha) = 0$ (3.2)

Momentum equation: $\frac{\partial(\rho u)}{\partial t} + \nabla \cdot (\rho uu) = -\nabla p + \nabla \cdot T + f_\sigma$ (3.3)

where u is the velocity and α represents the volume fraction, which equals 1 in the region of the first phase, 0 in the region of second phase, and between 0 and 1 in the interface region (Table 3.2). T implies the stress tensor which has two components, including turbulent and viscous stress. The surface tension force is shown by f_σ and is obtained by Eq. 3.7. The pressure can be decomposed into two terms including hydrostatic and dynamic pressure as presented in Eq. 3.6, where g and x are gravitational acceleration and position vectors, respectively. Density and viscosity are calculated according to the volume fraction of each phase, as shown in Eqs. 3.4 and 3.5.

$$\rho = \alpha\rho_1 + (1 - \alpha)\rho_2 \tag{3.4}$$

$$\mu = \alpha\mu_1 + (1 - \alpha)\mu_2 \tag{3.5}$$

$$P_d = P - \rho gx \tag{3.6}$$

$$f_\sigma = \sigma k\nabla\alpha \tag{3.7}$$

$$k = -\nabla.\left(\frac{\nabla\alpha}{|\nabla\alpha|}\right) \tag{3.8}$$

where σ and k are surface tension constant and curvature, respectively. By substituting Eqs. 3.4-3.6 and 8-7 to Eq. 3.3, this provides Eq. 3.9 [9].

$$\frac{\partial(\rho u)}{\partial t} + \nabla.(\rho uu) = -\nabla p_d + \nabla.T - \rho g.x + \sigma k\nabla\alpha \tag{3.9}$$

Tracking interfaces between phases is usually one of the critical challenges to solve multi-phase problems. For this purpose, VOF method is used in interFoam [10,11]. To avoid numerical smearing of the interface, an interfacial compression flux term is added to the equation. The VOF method captures the interface, by which the surface cannot be tracked as by the techniques based on the interface tracking methods and the position of the surface is estimated by a phase fraction function. This method assumes that a continuous velocity field prevails along all the interfaces. This complies with the interface boundary conditions in the physics of fluids which means that the relative velocity between phases is zero. In VOF method, the additional transport equation Eq. 3.2 is added, which is solved simultaneously with Navier-Stokes equation to obtain the volume fraction of one phase at each time step. This transport equation is only solved in the interface region where there is a gradient in the phase fraction as presented in Table 3.2. The volume fraction (α) varies between 0 and 1 at interface between two phases[10]. While the volume fraction is either zero or one in the region of each phase.

Table 3.2. The variation of volume fraction parameter (α).

	Volume fraction
Phase 1	$\alpha = 1$
Interface between two phases	$0 < \alpha < 1$
Phase 2	$\alpha = 0$

Since the pressure term does not exist in the continuity equation, a suitable approach should be implemented to solve the coupling between pressure and velocity. As mentioned earlier, applying PISO procedure, the pressure-velocity coupling is solved in InterFoam. This method

is established based on the predictor and corrector step. The pressure and flux at previous iteration are used to approximate velocity field in the momentum equation, which is called momentum predictor. Then, the pressure is calculated based on the predicted velocity. Next, the new value flux is obtained using the calculated pressure. At the corrector stage, the velocity field is corrected based on updated pressure and flux. More information about PISO algorithm are explained in reference [12].

At the first step, initial value and boundary conditions should be set up for variables. Then the solver starts to investigate the variables at new time step using their values at the pervious time step. Following that, the predicted value of velocity based on the momentum predictor stage is calculated. The PISO loop continues until the tolerance for pressure-velocity system is satisfied. At this point, the updated values for velocity and pressure and conservative fluxes at new time step are obtained. According to the updated values, all other equations in the system are solved [12].

3.2.1.1.2 Geometry

The 2-D geometry of two-phase model of concrete pumping in the pipes with different diameters was developed in OpenFoam using blockMesh with a total length of 1 m and width values of 0.05 m and 0.0625 m. While the whole domain was divided into two blocks, the first block corresponded to the bulk flow, and the second block corresponded to the initial thickness of the LL, as presented in Fig. 3.2a. The initial value of α determined in the setFields dictionary, divided the region in two domains corresponding to the volume fraction of each phase in each domain.

3.2.1.1.3 Initial boundary conditions

The boundary conditions for velocity were fixed value at the inlet and zero-gradient at the outlet for both phases, including BC and LL. Furthermore, for both phases, the pressure boundary conditions were set to ZeroGradient at the inlet and a fixed value at the outlet for both phases [13].

The recent experimental studies have primarily focused on the characterization of the LL and have not taken into account the possibility of slippage in the interface rheometers [14]. The assumption of a no-slip and symmetry boundary conditions were applied for walls and the center axis of pipe, respectively [15,16] (Fig. 3.2).

The boundary conditions for α were similar to the velocity boundary conditions, i.e., fixed value at the inlet and zero-gradient at the outlet.
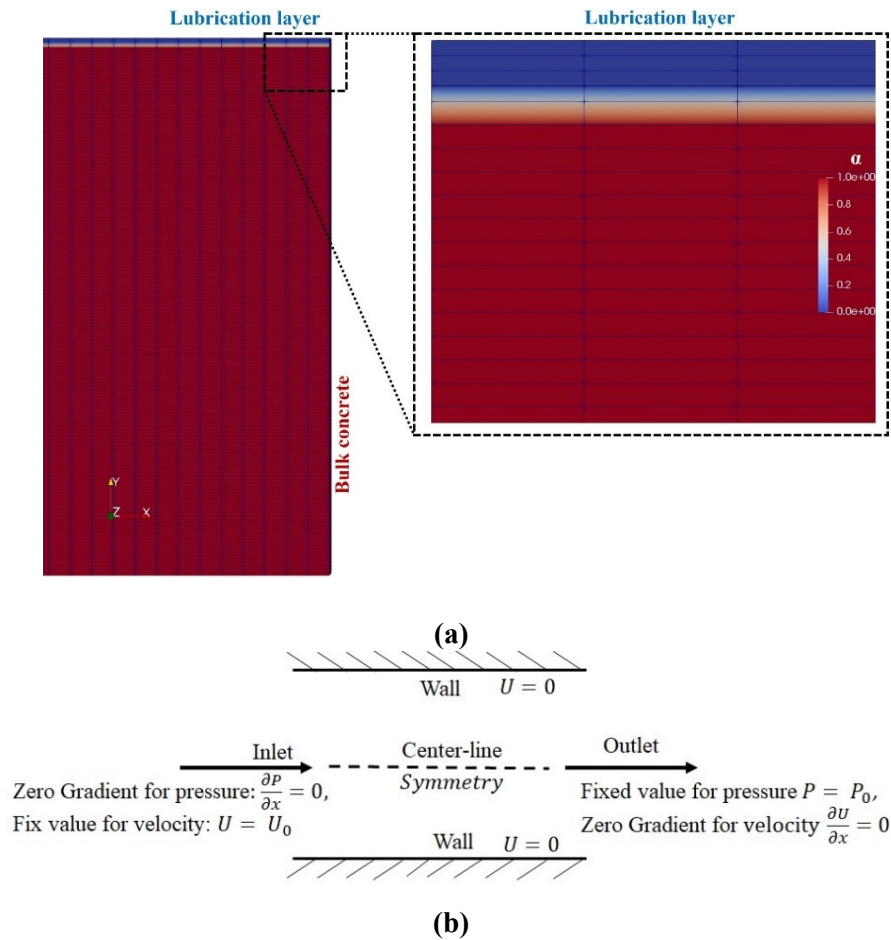
(b)
Fig. 3.2. (a) Pipe modelling and **(b)** boundary conditions for numerical simulations.

It is worthy to mention the InterFoam solver is a transient solver, meaning that the variables evolve over time until reaching a stable state. To achieve stability and ensure a smooth interface between the two phases, the thickness of the LL gradually increases over time to prevent potential disturbances caused by sudden viscosity changes at the interface between the LL and the bulk concrete. Therefore, the initial thickness should be less than 2 mm to reach about 2-mm thickness in the steady state. Simulating different cases, it was found that the initial thickness of around 0.5 mm enables us to reach appropriate results.

3.2.1.1.4 Viscosity model

In total, five different viscosity models are available in OpenFoam V6 to describe the rheological behavior of modelled fluids, including Bird-Carreau, Cross-Power Law, Hershel-Bulkley, Power-Law, and Newtonian models [13]. The interFoam solver enables us to consider two different rheological models for both phases (i.e., BC and LL). In the two-phases approach,

the Herschel-Bulkley (H-B) model was employed to describe the flow behavior of the BC and LL. The H-B model consists of a power-law relationship between the shear stress (τ) and shear rate ($\dot{\gamma}$), considering a yield value (yield stress: τ_0), consistency (k), and pseudoplasticity (n) indices, as follows:

$$\tau = \tau_0 + k\dot{\gamma}^n \tag{3.10}$$

However, by considering n = 1, Eq. 3.10 turns to the Bingham model (See Eq. 3.11 and Fig. 3.3), which is used in two-fluid approach to simulate the rheological behavior of the BC and LL phases in interFoam.

$$\tau = \tau_0 + \mu_p\dot{\gamma} \tag{3.11}$$

$$\mu_{app} = \frac{\tau_0}{\dot{\gamma}} + \mu_p \tag{3.12}$$

where μ_p is the plastic viscosity of the investigated fluid. The apparent viscosity (μ_{app}) is the ratio of shear stress to shear rate, as presented in Eq 3.12.
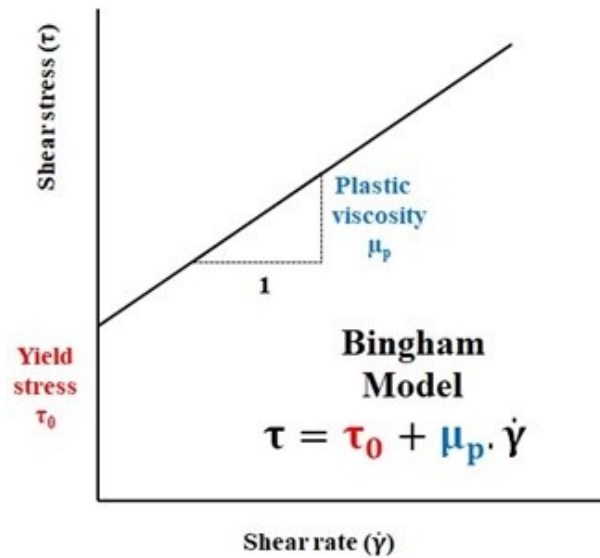
Fig. 3.3. Schematics of the Bingham rheological model.

The Bingham fluid can show two different behaviors depending on the value of applied shear stress. When the magnitude of the applied shear stress is lower than the yield stress, the deformation equals zero. This behavior means that the viscosity of flow approaches infinity and this part of flow refers to the unsheared bulk flow. On the other hand, Bingham fluid behaves as a Newtonian fluid with a plastic viscosity μ_p if the magnitude of the applied shear stress is higher than the yield stress. Through the simulation, the modeling of unsheared bulk flow having an infinity viscosity causes disconvergences of the solution. This problem is solved

by using bi-viscous model which is a combination of both Newtonian and Bingham models [16,17].

To prevent the aforementioned disconvergency, a critical value of shear rate ($\dot{\gamma}_c$) was defined in the Viscosity-Model class of OpenFOAM which its beyond (i.e., $\dot{\gamma} \geq \dot{\gamma}_c$), the flow follows the Bingham model of the investigated BC (Eq. 3.11). Moreover, for the shear rate values lower than the critical value (i.e., $\dot{\gamma} < \dot{\gamma}_c$), corresponding to the un-sheared zone, the fluid acts like a Newtonian fluid with a relatively high viscosity of μ_0, namely the artificial viscosity. Due to the use of two different values of viscosity (μ_0, μ_p) to describe the flow behavior of concrete across the pipe, this is referred to the bi-viscous model [17,18], which is schematically presented in Fig. 3.4.
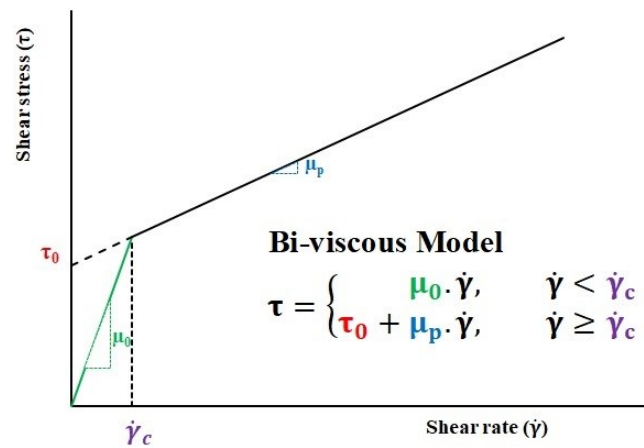
Fig. 3.4. Relationships between the shear stress and shear rate values in Bi-viscous rheological model considering the critical shear rate ($\dot{\gamma}_c$) and artificial viscosity (μ_0) values.

In OpenFoam [13], the bi-viscous model was applied using a loop in a whole domain. The loop allows to calculate the apparent viscosity for each cell using the Eq. 3.12, then the apparent viscosity of each cell was updated according to the minimum value between the artificial and calculated apparent viscosity, as written in Eq. 3.13.

$$\mu_{app} = \min(\mu_0, \frac{\tau_0}{\dot{\gamma}} + \mu) \qquad (3.13)$$

where μ_0 and μ_{app} imply the artificial and updated apparent viscosity values, respectively. Although μ_0 cannot be infinity, it should be large enough to capture the un-sheared zone of Bingham fluid. For cells with shear rate lower than its critical value ($\dot{\gamma}_c$), the magnitude of their calculated apparent viscosities becomes higher than infinity viscosity, therefore, after the comparison step in the loop, the updated apparent viscosity becomes equivalent to the value of

artificial viscosity [13]. While for other points, the apparent viscosity was considered equal to the calculated one. It avoids infinity value for apparent viscosity in points where the shear rate is lower than the critical value. At this stage, the value of apparent viscosity for each cell is updated [13].

3.2.1.1.5 Inputs for the Transport properties

The value for surface tension between two phases (σ) and rheological parameters, including the yield stress (τ_0), artificial (μ_0), and plastic viscosity (μ_p) values, of each phase should be defined by the user in the transport file of interFoam solver. The dimension of each variable was determined by seven scalars between two brackets in which each scalar represents the power of its base unit. Table 3.3 shows the basic unit of each number in the SI system [13].

Table 3.3. Definition of the units of different physical properties.

No.	Property	SI unit
1	Mass	kilogram (kg)
2	Length	meter (m)
3	Time	second (s)
4	Temperature	Kelvin (K)
5	Quantity	mole (mol)
6	Current	ampere (A)
7	Luminous intensity	candela (cd)

For example, [0 1 -1 0 0 0 0] corresponds to m/s. It is worthy to mention that the magnitudes and dimensions of parameters in OpenFOAM incompressible solvers, such as interFoam, are scaled by the constant density of simulated fluid.

The interface rheometers allow to evaluate the yield stress and viscous constant of the LL. It is important to note that the viscous constant represents both the viscosity and thickness of the LL. However, it is experimentally impossible to measure these two parameters separately. This causes a challenge to model its presence. Therefore, the viscosity of the LL can be calculated indirectly by a pre-assumed thickness and its viscous constant. Assuming an initial thickness of 2 mm, the viscosity of the LL has been calculated by multiplying the viscous constant, obtained using the tribological measurement, by 0.002 m.

The applied algorithm in two-phase approach (double-Bingham model) is shown in Fig. 3.5. As can be seen, the problem was solved based on a trial-and-error procedure. The error (ε) is defined by Eq. 3.14.

$$\varepsilon = \frac{\left|\Delta P_{sim} - \Delta P_{exp}\right|}{\Delta P_{exp}} \tag{3.14}$$

where ΔP_{exp} and ΔP_{sim} are the experimentally and numerically pressure drops, respectively.

When the difference between experimental and numerical pressure drop becomes smaller than 5% ($\varepsilon < 5\%$), the simulation stops. It is worthy to mention that reaching the simulation results with physical meaning as well as the error less than 5% was not possible for all the cases. In this case, by changing the values of the viscosity (v_{ll}) of LL, infinity viscosity of the LL (v_{0-ll}) and bulk concrete (v_{0-b}), size of mesh in y direction (N), and initial LL thickness (e), an attempt was done to achieve physically meaningful results with minimized error as well.

During the simulation, the LL thickness was increased as the interFoam is an unsteady solver. At the end of pipe flow period, the final thickness of LL was considered. Next, the simulated viscous constant values of the LL were calculated by dividing the LL viscosity to its final thickness at the end of pipe flow period and compared with those obtained experimentally.

It is reported in literature that the LL characteristics significantly influence the concrete pumpability [2,19, 20]. One of the important issues in the modeling of concrete pumping is to apply proper viscosity models to properly simulate the radial variation in rheological properties of concrete across the pipe, hence allowing to achieve accurate results. The proper viscosity model should capture three different regions in the cross section of pipe, including the sheared bulk flow, plug flow, and LL. In the double-Bingham approach which decomposes the whole region in two different Bingham-models, all three regions can be modeled. Applying interFoam solver with two H-B model in OpenFOAM enables us to define three different regions in the cross section of the pipe. Accordingly, the effect of the LL characteristics on the pressure drop of flow can be investigated. Also, the result of tribometer can be compared with the simulation results which helps us to understand the different conditions of concrete flow through the real pumping process and empirical tribology measurements. However, implementing the two-phase solver needs more computational time comparing to the single-phase solver. In the following section, the concrete flow was simulated using the single-fluid approach but with variable viscosity across the pipe, implemented through adding new viscosity models in OpenFoam called Tri-viscous.
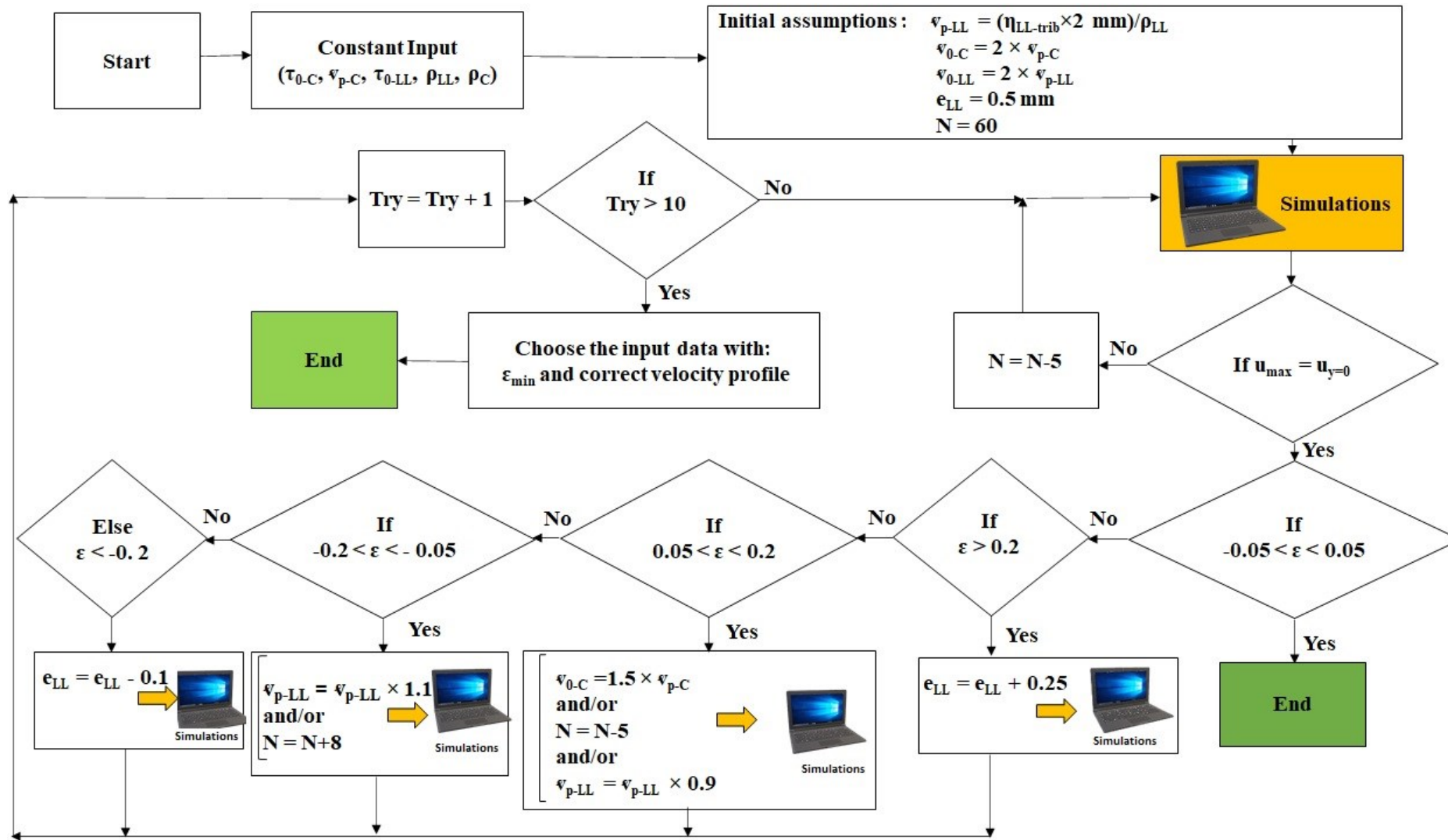
Fig. 3.5. Schematics of the algorithm applied for two-fluids approach (Double-Bingham model).

3.2.1.2   Single-phase approach (Tri-viscous Model)

Herein, the flow of the investigated concrete mixtures with different rheological properties was considered as a single fluid which experience a laminar and fully developed flow in the pumping circuit with pipe's diameters of 100 mm and 125 mm and under different flow rates, as summarized in Table 3.1. To model the flow using the single-phase approach, simpleFoam as a steady-state solver, was applied [13,20]. It solves the Navier–Stokes equations for incompressible fluid, using SIMPLE (Semi-Implicit Method for Pressure Linked Equations) algorithm to solve the pressure-velocity coupling. In SIMPLE technique, the discretized momentum equations were solved using the initial values of pressure and velocity [22,23]. The variables are corrected using the pressure correction equation and applying the under-relaxation factor which plays an important role to reach stability and convergency, defined by the user in the Control-Dict file [13,24].

3.2.1.2.1   Governing equations

In SimpleFoam, the continuity and momentum equations were solved for one-fluid at steady-state. Due to constant density of incompressible fluids, the continuity and momentum equations were written, as follow [21]:

Continuity equation: $\nabla.\,u = 0$ (3.35)

Momentum equation: $\frac{\partial(\rho u)}{\partial t} + \nabla.\,(\rho uu) = -\nabla p + \nabla.\,T + f_\sigma$ (3.16)

where u and T represent the velocity and the stress tensor, respectively. The stress tensor is a combination of turbulent and viscous stresses. As simpleFoam is made for incompressible fluid, the Navier-Stokes equations' parameters are divided by the density. Therefore, the input values and dimensions for variables, such as viscosity and yield stress, should be divided by the density value and its dimension.

3.2.1.2.2   Boundary conditions

The no-slip and symmetry conditions were considered for the wall and center axis of the pipe, respectively. The inlet boundary conditions for velocity and pressure were fixed value and zero gradient, respectively [13, 15, 16]. While, for the outlet boundary conditions, a constant value for pressure and zero gradient for velocity were applied, as shown in Fig. 3.2.a.

3.2.1.2.3 Tri-Viscous model

As explained earlier, the shear-induced particle migration and formation of the LL lead to radial variations in the rheological properties of pumped concrete across the pipe [25]. The use of single-fluid approach to simulate this behavior results in solving a single Navier-Stokes equation, rather than two in the case of the two-fluid approach (double-Bingham model). Moreover, there is no need to solve Eq. 3.2 to consider the interaction between the multi-phases using "α" parameter. Using single-fluid approach results in lower calculation time and computational costs comparing to double-Bingham approach. However, according to the changes in properties of flow close to wall, a discontinuity in velocity of fluid at interface is caused, and the continuity assumption should be checked [26].

In order to simulate these rheological variations using the single-fluid approach, the employed model should allow to simulate the variations of the rheological parameters of concrete across the pipe. These variations can be considered as functions of either the radial distances of each cell (cell's center point) to the center axis (i.e., y coordinate) or the shear-rate magnitudes (i.e., $\dot{\gamma}$). Since, the 5 existing viscosity models in OpenFOAM [13] are unable to consider the variations in their rheological parameters (i.e., fixed value during simulation), new viscosity models were then required to be established.

In order to develop a new model, a proper criterion should be selected to determine the transition point in the rheological parameters from those of the BC (i.e., $\tau_{0\text{-b}}$ and $\nu_{\text{p-b}}$) to those corresponding to the LL (i.e., $\tau_{0\text{-ll}}$ and $\dot{v}_{\text{p}-\text{ll}}$), in a single viscosity model. Accordingly, two new approaches were proposed in this study to define these criteria, as follow:

Tri-Viscous model I: in this model, the rheological parameters of the modeled fluid vary as a function of the radial distance to the center axis: A critical distance to the center axis (i.e., "y_{critical}" coordinate) was thus selected which its beyond the viscosity model follows the rheological parameters of the LL (i.e., $\tau_{0\text{-ll}}$ and $\nu_{\text{p-ll}}$). On the other hand, the rheological properties of the cells with y < y_{critical} coordinates correspond to the BC (i.e., $\tau_{0\text{-b}}$ and $\nu_{\text{p-b}}$).

Tri-Viscous model II: In this model, the rheological parameters of the modelled fluid vary due to the shear rate magnitudes: A critical value of shear rate (i.e., "$\dot{\gamma}_{\text{critical}}$") was defined which corresponds to the minimum shear rate value in the LL. Therefore, the shear rate values of each cell in each time step were compared to this critical value. The Bingham yield stress and plastic viscosity values of the cells with higher shear rates than $\dot{\gamma}_{\text{critical}}$ were then set to those of the LL

(i.e., $\tau_{0\text{-}ll}$ and $\nu_{p\text{-}ll}$). On the other hand, the rheological parameters of the lower shear rate cells (i.e., $\dot{\gamma} < \dot{\gamma}_{critical}$) correspond to those of the BC (i.e., $\tau_{0\text{-}b}$ and $\nu_{p\text{-}b}$).

3.2.1.2.4 Tri-Viscous model I: Radius-dependent viscosity

The first model was developed based on H-B viscosity model of OpenFoam and the criterion corresponded to the radial position of the BC and LL in the pipe. Assuming the LL as a very thin layer with a constant thickness formed near the pipe wall, if the cell center was located in a distance less than the thickness of LL from the wall, the rheological behavior of the fluid in the cell is governed by the LL properties. Otherwise, the viscosity behavior should follow the BC's properties. The concept of this model is schematically presented in Fig. 3.6.
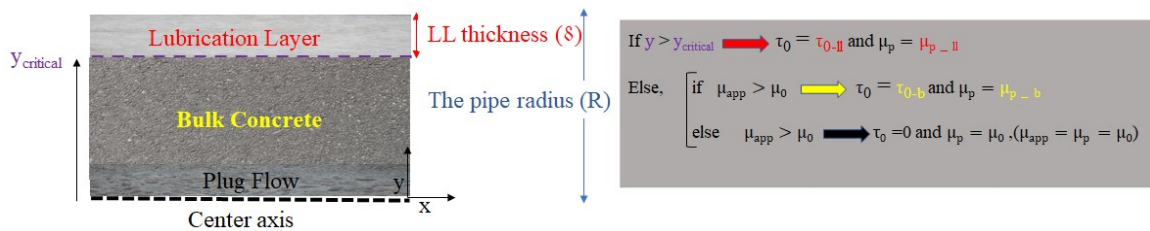
Fig. 3.6. The separation between LL and bulk flow based on if-statement of Tri-Viscous model I.

This model predicts the variation of rheological properties of concrete by comparing the vertical distance of each cell center (i.e., "y" coordinate) from the centerline of the pipe and the critical distance (i.e., "$y_{critical}$" coordinate), which is calculated as

$$y_{critical} = R - \delta \tag{3.14}$$

where R and δ represent the radius of the pipe and thickness of the LL, respectively. For example, assuming the formation of 2-mm LL in the pipe with 100-mm diameter, the $y_{critical}$ is set to 0.048 m. For each point, the y component is checked, and if it is smaller than 0.048 m, the rheological properties of the cell correspond to those of the BC (i.e., $\tau_{0\text{-}b}$ and $\nu_{p\text{-}b}$). Otherwise, the rheological properties of LL (i.e., $\tau_{0\text{-}ll}$ and $\nu_{p\text{-}ll}$) are set to those cells.

For applying this model in OpenFoam, the H-B viscosity class was copied with adding if-statement inside a loop which controls the y component of each cell, as presented in Fig. 3.7.
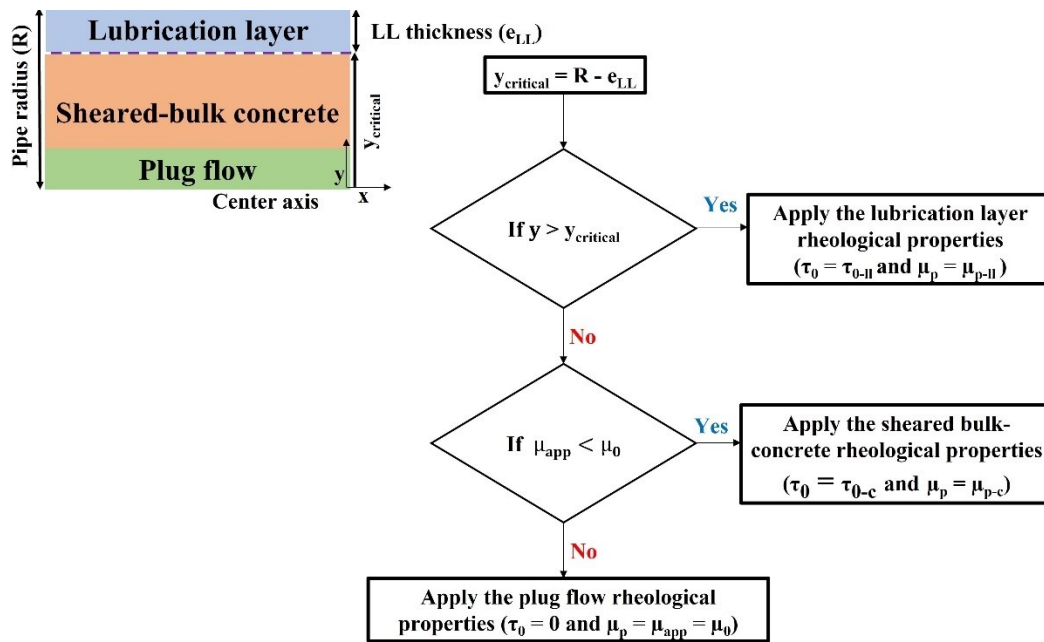
Fig. 3.7. Schematics of if-statement applied in Tri-Viscous model I to separate between the LL and bulk concrete.

The transport properties file of this model needs 8 parameters as inputs, including n, $\tau_{0\text{-}b}$, $v_{p\text{-}b}$, v_0, $\tau_{0\text{-}ll}$, $v_{p\text{-}ll}$, $v_{0\text{-}ll}$, and y_{critical}. Where v_0 is the artificial viscosity of the un-sheared zone as explained in the double-Bingham model, which was used to solve disconvergence problem resulted from infinity viscosity of the un-sheared zone. As applying two plastic viscosities corresponded to the BC and LL plus one artificial viscosity, it is called tri-viscous model.

The algorithm used to model concrete flow was shown in Fig. 3.8. To simulate concrete by this approach, an initial assumption of LL thickness was required to calculate not only the plastic viscosity of LL based on the tribometer data, but also the value of y_{critical} which depends on the thickness of LL and the radius of pipe.
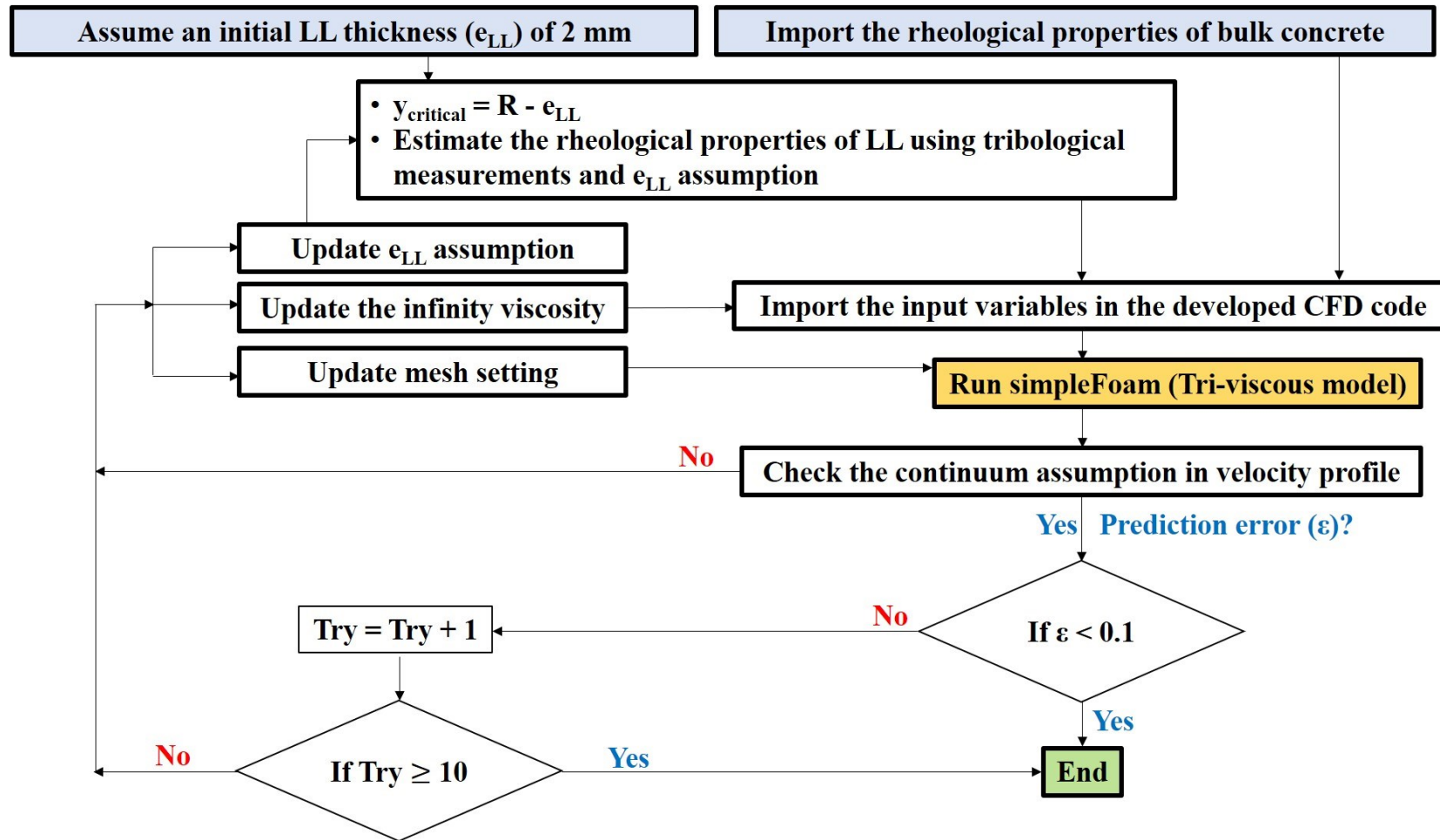
Fig. 3.8. Schematics of the algorithm applied in the Tri-Viscous model I.

3.2.1.2.5 Tri-Viscous model II: Shear rate-dependent viscosity

In this model, the H-B viscosity model was chosen as the base class and the changes were applied by adding the if-statement inside a loop to control the value of shear rate in each cell. The threshold between the BC and LL zones was distinguished according to the shear-rate values (Fig. 3.9). It means that the $\dot{\gamma}_{critical}$ was defined by the user and if the value of calculated shear rate in each cell is greater than the critical one, the rheological properties of the LL (i.e., τ_{0-ll} and ν_{p-ll}) is set to the calculated cell.

As mentioned earlier, the shear-rate in the LL zone is higher than the one in the bulk flow which means that the transition point can be defined by the minimum shear-rate in the LL or the maximum shear-rate in the bulk flow. The point in which has a minimum value of shear-rate in the LL represents the onset of bulk flow which indicates that increasing the $\dot{\gamma}_{critical}$ means the thinner LL. In other words, the LL thickness was calculated based on the value of $\dot{\gamma}_{critical}$. The geometric schematic of this model can be drawn, as follows:
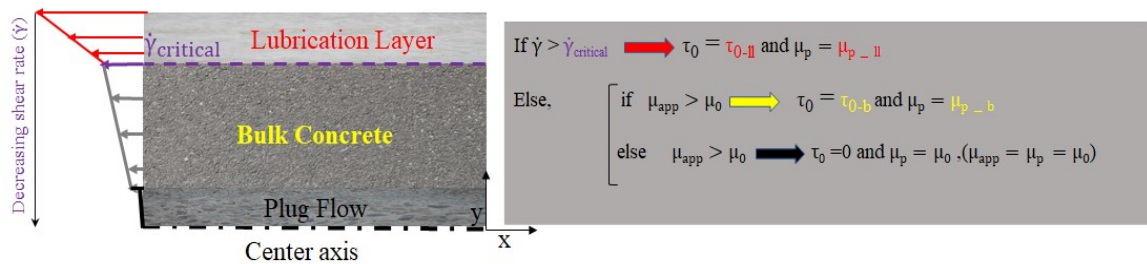
Fig. 3.9. The separation between LL and bulk flow based on if-statement of Tri-Viscous model II.

This model needs 8 parameters including n, τ_{0-b}, ν_{p-b}, ν_0, τ_{0-ll}, ν_{p-ll}, ν_{0-ll}, and $\dot{\gamma}_{critical}$ as inputs which are defined by the user in the transport properties file. Similarly, to the pervious approach, this approach is identified by three viscosities including two plastic viscosities of the BC and LL, as well as the artificial viscosity, which was used to simulate the un-sheared zone. Therefore, this method is called tri-viscous model, as shown schematically in Fig. 3.10. The difference between these two methods is the criteria of the transition point from the LL and BC.
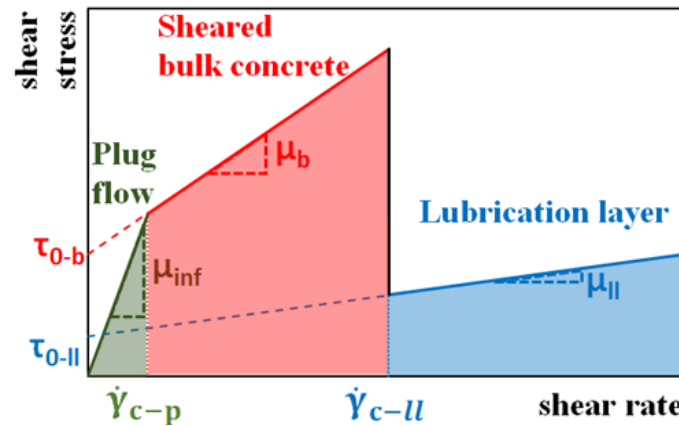
Fig. 3.10. Shear-stress vs shear rate relationship in tri-viscous model II.

As can be observed in Fig. 3.11, some initial assumption, such as critical shear rate ($\dot{\gamma}_{critical}$), the mesh size in y direction (N), initial viscosity of LL (v_{ll}) and infinity viscosity (v_0) were varied to achieve the physically meaningful results with a minimum error, compared to the experimental measurements. It is worthy to mention that in all these three models, the parameter called "Try" was defined which prevents doing simulation for more than 10 times, as can be seen in Figs. 3.6, 3.8, and 3.11.

In this study, after creating these new models, the library has been compiled with "wamke" commend and added into the available viscosity model classes in OpenFoam. In order to recognize these two new viscosity models with simpleFoam or other solvers of OpenFOAM, the created library were added in Control-Dict file. Using OpenFOAM, these two models were applied to consider the effect of LL on the pumping process. More detailed information about how new libraries can be added in OpenFoam is provided in [27].

Applying these three models in Phase 1 of this study, the effect of rheological and tribological properties on concrete pumpability was studied. Different pipe flow zones, including the LL, sheared BC, and plug zone, were identified and characterized. The simulated LL characteristics were compared to the experimental measurements obtained using the tribometer. After highlighting the significance of the LL characteristics on concrete pumpability, the mechanism of formation of LL were modeled in Phase 2. Accordingly, the concrete pipe flow, as a heterogeneous suspension of aggregate and suspending mortar, has been simulated in the next phase to simulate the main mechanisms leading to the formation of LL.
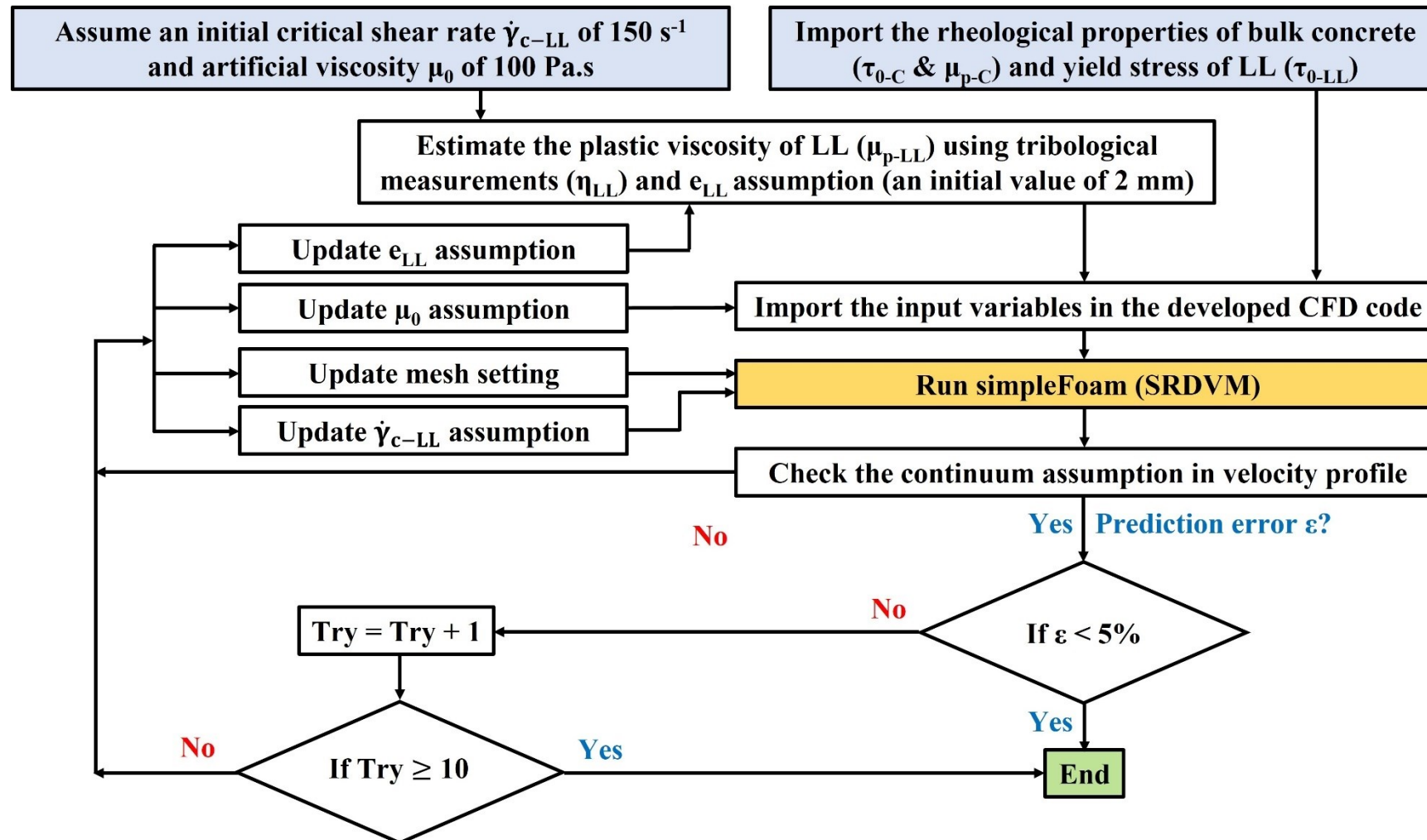
Fig. 3.11. Schematics of tri-viscous model II.

3.2.2 Phase 2: Heterogeneous modeling of concrete flow - Coupling fluid and solid phases

In order to better understanding the concrete behavior during pumping and capture the mechanism of particle migration and the formation of LL, the concrete flow was modelled as a biphasic suspension of aggregate (solid phase) and mortar (liquid phase). The coupled effect of wide PSD and concentration of particles, mortar rheology, and pipe flow regime (Reynolds number) on pumping-induced rheological heterogeneities across the pipe has been evaluated using these heterogeneous approaches. This phase was divided into two sub-phases, which are explained below:

I. **DEM phase:** The computations were conducted using the multiple time-step soft-sphere DEM approach, which was described by Marshall [28]. A Cartesian grid was used for the computations, and an interpolation scheme was used to detect interparticle and particle-wall collisions using a level-set approach [29]. The DEM algorithm employed an efficient multi-timescale approach that included fluid, particle, and collision timescales, each with corresponding time steps, as shown in Fig. 3.14. The largest time step (ΔT_f) was used for the fluid motion and was also used to update lists of local particles. Particle motion was described using the particle time step (ΔT_p), during which collisions were detected. Colliding particles were resolved using a smaller time step called the collision time step (ΔT_c). All variables were non-dimensionalized using the pipe radius R as a length scale and mean fluid velocity U as a velocity scale. Time scales were non-dimensionalized using the convection time R/U. Particles were randomly initialized in the pipe using a generator function, and their positions were examined to avoid interparticle and particle-wall overlap in the initial positions. The generator subroutine was iterated until the desired concentration and PSD were achieved. (DEM). The schematics of algorithm applied in this sub-phase is shown in Fig. 3.14

II. **Coupled CFD-DEM:** In this study, the four-way coupled CFD-DEM method refers to the integration of two-way coupling between the fluid and particles in the DEM approach and the Navier-Stokes equations in the CFD approach. The multiple time-step soft-sphere DEM approach described earlier was used for particle motion and collisions, and the CFD solver was

based on the finite volume method. The two approaches were coupled using a drag force model based on the relative velocities between the fluid and particles, and the fluid velocity was updated using the momentum equation that incorporates the effects of particle-particle and particle-wall interactions, as well as the effect of the particles on the fluid motion and fluid motion on particles dynamics. The schematics of algorithm applied in this sub-phase is illustrated in Fig. 3.17.

3.2.2.1   *Governing equation for aggregate phase*

The particles advection and their interaction with the surrounding fluid, neighboring particles, and pipe wall were computed using a soft-sphere DEM model, originally introduced by Marshall [28]. The particles were modelled as spherical particles with different sizes, randomly generated through the pipe geometry in a descending order of particle size (i.e., larger particles were generated earlier). Considering the mass (m), translational ($\mathbf{v}$) and angular velocity ($\mathbf{\Omega}$), and inertia (I) of particles, their motions were evolved by conservation of linear and angular momentums [30, 28], given by

$$m\frac{d\mathbf{v}}{dt} = \mathbf{F}_F + \mathbf{F}_C \tag{3.58}$$

$$I\frac{d\mathbf{\Omega}}{dt} = \mathbf{M}_F + \mathbf{M}_C \tag{3.19}$$

where $\mathbf{F}_F$, $\mathbf{F}_C$, $\mathbf{M}_F$, and $\mathbf{M}_C$ imply the force and torques applied on particles from the suspending fluid and those induced by the particle (or wall) collisions, respectively. The suspending fluid mostly influences the particles advection by the drag force and viscous torque. It is worth mentioning that the Magnus, virtual mass, and Basset forces were neglected in this study due to low particle relaxation times caused by typically high viscosity of suspending matrix (mortar) in concrete suspensions. The drag force was computed using Stokes expression [31]. It was defined as a function of relative velocity between the particle ($\mathbf{v}$) and fluid ($\mathbf{u}_f$) at the centroid of particles, calculated by tri-linear interpolation from fluid velocity field at grid points [30, 28]. The crowding effect of surrounding particles on suspending fluid's drag force was applied as a correction factor f_{DF} defined by Di-Felice [31], given by

$$\mathbf{F}_F = -3\pi\, d\, \mu\, (\mathbf{v} - \mathbf{u}_f)\, f_{DF} \tag{3.20}$$

$$f_{DF} = (1 - c)^{-\beta} \tag{3.21}$$

where d, μ, and c are the particle diameter, fluid viscosity, and local particle concentration, respectively, and β is a function of the particle Reynolds number Re_p for a suspending fluid's kinematic viscosity υ, defined as

$$\beta = 2.7 - \frac{0.65}{\mathrm{Exp}\left[\frac{[1.5 - \ln(Re_p)]^2}{2}\right]} \tag{3.22}$$

$$Re_p = \frac{|\mathbf{v} - \mathbf{u}_f| d}{\upsilon} \tag{3.63}$$

A conservative particle blob method, introduced by Marshall [32], was employed to calculate the local concentration field. A 3D-Gaussian function (f) with a specific radius R_n and amplitude A_n was defined to distribute the particle volume onto the flow field [32]. The concentration at each point was then obtained using the effect of neighboring blobs, given by

$$c(\mathbf{x},t) = \sum_{n=1}^{N} A_n f(\mathbf{x} - \mathbf{x}_n, R_n) \tag{3.24}$$

$$f(\mathbf{x} - \mathbf{x}_n, R_n) = \frac{2}{3\pi R_n^3 \, \mathrm{Exp}\left(\frac{|\mathbf{x} - \mathbf{x}_n|^2}{R_n^2}\right)} \tag{3.25}$$

The viscous torque $\mathbf{M}_F$ acting on a particle is caused by the frictional drag of the fluid and is given by:

$$\mathbf{M}_F = \pi \mu d^3 \left(\frac{1}{2}\boldsymbol{\omega}\text{-}\boldsymbol{\Omega}\right) \tag{3.26}$$

where $\boldsymbol{\omega}$ represents the vorticity of the fluid evaluated at the position of the particle's center. In fluid flows where particles frequently collide with each other, the viscous torque exerted by the fluid plays a crucial role. Particle collisions can lead to significant rotation due to frictional forces, but this rotation is counteracted by the viscous torque imposed by the surrounding fluid.

3.2.2.2 Contact modeling

The interactions between particles during contact period can be categorized in four different types including: normal, sliding, twisting, and rolling which are shown schematically in Figs. 3.12a-d, respectively.

(a)   **(b)**   **(c)**   **(d)**
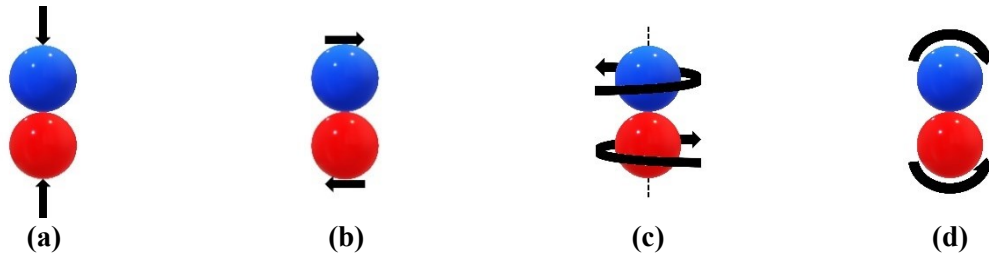
Fig. 3.12. Schematics of different contact types between particles, including **(a)** normal, **(b)** sliding, **(c)** twisting, and **(d)** rolling contacts [51].

In order to model the resistance of particles to the relative motions between two particles during collision and contact, as presented in Fig. 3.12, many rheological models are available [29]. Some of these models explain deformation and energy dissipation of particles using spring, damper and slider. In this study, the collision between particles was modeled using a spring-dashpot-slider system proposed by Cundall and Strack [33], schematically shown in Fig. 3.13.
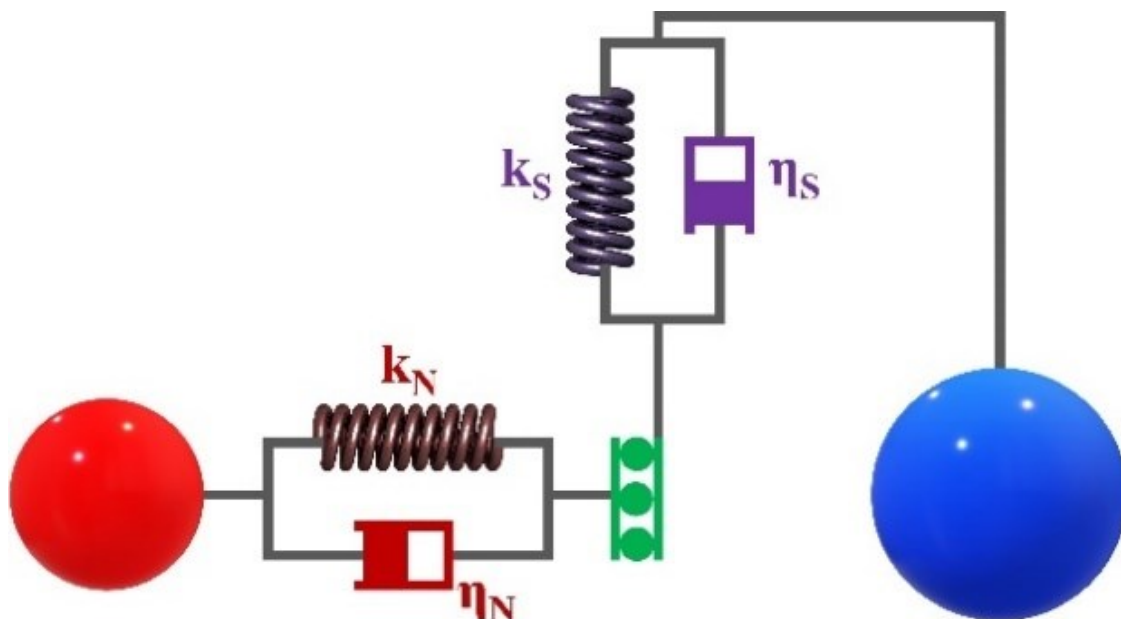
Fig. 3.13. . Schematic of contact models for the collision of particles [28].

Tables 3.4 and 3.5 provide a summary of the parameters and formulations utilized for modeling the contact forces and torques between two particles, i and j.

Table 3.4. Parameters of the contact model used in the employed DEM model.

Parameters	Symbol	Formulation
Particle radius	r	r_i and r_j
Vector from the particle centroid to the contact point	$\mathbf{r}$	$\mathbf{r}_i = r_i\mathbf{n}$ and $\mathbf{r}_j = -r_j\mathbf{n}$
Particle mass	m	m_i and m_j
Poisson's ratio of particle	σ	σ_i and σ_j
Shear modulus of particle	G	G_i and G_j
Centroid position of particle	$\mathbf{X}$	$\mathbf{X}_i$ and $\mathbf{X}_j$
Restitution coefficient	e	0.1
Effective radius	r_e	$\dfrac{1}{r_e} = \dfrac{1}{r_i} + \dfrac{1}{r_j}$
Effective elastic modulus	E	$\dfrac{1}{E} = \dfrac{1 - \sigma_i^{\,2}}{E_i} + \dfrac{1 - \sigma_j^{\,2}}{E_j}$
Effective shear modulus	G	$\dfrac{1}{G} = \dfrac{2 - \sigma_i}{G_i} + \dfrac{2 - \sigma_j}{G_j}$
Particle velocity at the contact surface	$\mathbf{v}_c$	$\mathbf{v}_c = \mathbf{v} + \mathbf{\Omega} \times \mathbf{r}$
Normal overlap	δ_N	$\delta_N = r_i + r_j - |\mathbf{x}_i - \mathbf{x}_j|$
Contact region radius	a	$a^2 = r_e\,\delta_N$

Table 3.5. Formulation of the contact forces and torques used in the DEM model.

Interaction	Symbol	Formulation	Direction	Variables
Normal force	$\mathbf{F}_{c,ij}^{\mathbf{n}}$	$k_N\,\delta_N - \eta_N \mathbf{v}_R.\mathbf{n}$	$\mathbf{n} = (\mathbf{x}_j - \mathbf{x}_i) / \lvert\mathbf{x}_j - \mathbf{x}_i\rvert$	$k_N = \frac{4}{3}E\,a(t)$ $\eta_N = \alpha\sqrt{m\,k_N}$ $\alpha = 1.2728 - 4.2783e + 11.087e^2 - 22.348e^3 + 27.467e^4 - 18.022e^5 + 4.821e^6$ $\mathbf{v}_R = \mathbf{v}_{ci} - \mathbf{v}_{cj}$
Sliding force	$\mathbf{F}_c^{\mathbf{s}}$ F_{crit}	$-k_T\left(\int_{t_0}^{t}\mathbf{v}_S(\zeta)\mathrm{d}\zeta\right).\mathbf{t}_S - \eta_T\mathbf{v}_S.\mathbf{t}_S$ $\mu_f\,\lvert F_n\rvert$	$\mathbf{t}_S = \mathbf{v}_S / \lvert\mathbf{v}_S\rvert$	$k_T = 8G\,a(t)$ $\mathbf{v}_S = \mathbf{v}_R - (\mathbf{v}_R.\mathbf{n})\mathbf{n}$ $\eta_T = \eta_N$ If $\lvert\mathbf{F}_c^{\mathbf{s}}\rvert > F_{crit}$; reset to $\mathbf{F}_c^{\mathbf{s}}$ $\mu_f = 0.3$
Twisting torque	M_t $M_{t\text{-}crit}$	$-\dfrac{k_T a^2}{2}\int_{t_0}^{t}\Omega_T(\tau)\mathrm{d}\tau - \dfrac{\eta_T a^2}{2}\Omega_T$ $\dfrac{2}{3}a\,F_{crit}$	$\Omega_T/\lvert\Omega_T\rvert$	$\Omega_T = (\mathbf{\Omega}_i - \mathbf{\Omega}_j).\mathbf{n}$ If $M_t > M_{t\text{-}crit}$; reset to M_t
Rolling torque	M_r	$-k_R\left(\int_{t_0}^{t}\mathbf{v}_L(\tau)\mathrm{d}\tau\right).\mathbf{t}_R - \eta_R\mathbf{v}_L.\mathbf{t}_R$	$\mathbf{t}_R = \dfrac{\mathbf{v}_L}{\lvert\mathbf{v}_L\rvert}$	$\mathbf{v}_L = -r_e\left(\mathbf{\Omega}_i - \mathbf{\Omega}_j\right)\times\mathbf{n} - \dfrac{1}{2}\left(\dfrac{r_j - r_i}{r_j + r_i}\right)\mathbf{v}_S$ $\eta_R = \mu_R\,\lvert F_{ne}\rvert$ $\mu_R = \dfrac{1 - e}{2.283w_0^{1.5}(K/m)^{2/5}}$ w_0: The relative velocity between two particles before the collision $K = \frac{4}{3}E\sqrt{r_e}$
Total torque exerted on particle i	M_C	$r_i\,F_S(\mathbf{n}\times\mathbf{t}_S) + M_r(\mathbf{t}_R\times\mathbf{n}) + \mathbf{M}_t.\mathbf{n}$	-	-

Fig. 3.14. The schematic illustration of the DEM multiscale algorithm applied in this study.

3.2.2.3 *Governing equation for the mortar phase*

The Navier-Stokes equations [27] were used to model the flow of the suspending mortar phase, as follow:

$$\frac{\partial}{\partial t}\left(c_v\rho_f\right)+\nabla.\left(c_v\rho_f\mathbf{u}_f\right) = 0 \tag{3.27}$$

$$\frac{\partial}{\partial t}\left(c_v\rho_f\mathbf{u}_i\right)+\frac{\partial}{\partial \mathbf{x}_j}\left(c_v\rho_f\mathbf{u}_i\mathbf{u}_j\right) = \frac{\partial}{\partial \mathbf{x}_j}\left[c_v\mu\left(\frac{\partial \mathbf{u}_i}{\partial \mathbf{x}_j}+\frac{\partial \mathbf{u}_j}{\partial \mathbf{x}_i}\right)\right] - c_v\frac{\partial \mathbf{p}}{\partial \mathbf{x}_i} - \mathbf{b}_i \tag{3.28}$$

The variables $\mathbf{u}_f$, $\mathbf{p}$, and ρ_f represent the velocity, pressure, and density of the suspending fluid, respectively. "b" represents the body force, including the drag force that the particles exert on the suspending fluid. c_v denotes the volumetric fraction of the suspending fluid. In this particular problem, it was assumed that the pressure term is constant across the pipe in the axial direction, which is typical for fully-developed laminar flow. The flow was also assumed to be axisymmetric, which means that the fluid velocity field depends only on the radius and time. To make the equations non-dimensional, the pipe radius (R_{pipe}) and mean fluid velocity (u_f) were used as the length and velocity scales, respectively. The non-dimensional mass and momentum equations are as follow:

$$\frac{\partial}{\partial t}(c_v)+\frac{\partial}{\partial \mathbf{r}}(c_v\mathbf{u}_f) = 0 \tag{3.29}$$

$$\frac{\partial}{\partial t}(c_v\mathbf{u}_f) = \frac{1}{Re}\frac{1}{\mathbf{r}}\frac{\partial}{\partial \mathbf{r}}(\mathbf{r}\,c_v\frac{\partial \mathbf{u}_f}{\partial \mathbf{r}}) - c_v\frac{4}{Re} - \mathbf{b} \tag{3.30}$$

where the suspending fluid Reynolds number Re is given by

$$Re = \frac{\rho_f u_f D_{pipe}}{\mu} \tag{3.31}$$

3.2.2.4 *Splitting algorithm*

Due to wide variety of particle sizes in concrete suspension (from 1 up to 20 mm), solid particles may be larger than the fluid mesh cells. In order to reduce the noises, especially for fine fluid mesh cells [34], it is important to calculate the volumetric fraction of particles, occupied in each fluid cell. The volume of a spherical particle with radius r_p, located at distance $|\mathbf{r}|$ between its centroid to the pipe center, and enclosed between two planes with distances a and b ($a < b$) to the pipe center, corresponding to the inner and outer boundaries of a suspending fluid mesh cell, respectively, can be estimated as follows:

$$V = \pi \left[r_p{}^2 (b-a) - \frac{(b-|\mathbf{r}|)^3 - (a-|\mathbf{r}|)^3}{3} \right] \qquad (3.32)$$

It is worth mentioning that for simplification, the curvature of the fluid meshes was not taken into account and it was assumed that particles were enclosed between two straight surfaces. In this study, the pipe geometry was discretized in 21 cylindrical meshes with identical length of the pipe L_{pipe}, where the inner and outer boundaries of the ir^{th} mesh cell (ir starting from 0 to 20) are distanced by $(ir - 0.5)\Delta r$ and $(ir + 0.5)\Delta r$ to the pipe center ($\Delta r = R_{pipe}/20$). Accordingly, the 0th mesh cell refers to a cylindrical mesh of $D_{pipe}/20$ in diameter centered at the pipe axis. Also, the inner and outer radii of the 20th mesh cell measure $19.5 R_{pipe}/20$ and R_{pipe}, respectively. Considering the $ir_{first}{}^{th}$ and $ir_{last}{}^{th}$ cells, referring to the mesh cells which contain the points on the particle surface with the shortest ($|\mathbf{r}| - r_p$) and longest ($|\mathbf{r}| + r_p$) distances to the pipe center, respectively, as shown in Fig. 3.15, the particle is split in total N_{split} times ($N_{split} = ir_{last} - ir_{first}$). Therefore, four different scenarios can then happen depending on the size and location of the particles within the fluid mesh cells, as follow:

Scenario A: if $ir_{first} = ir_{last} = ir$, therefore the particle does not need to be split ($N_{split} = 0$). Therefore, the particle concentration in the ir^{th} mesh cell equals $\frac{4}{3}\pi r_p{}^3$.

Scenario B: The partial volume of the particle, enclosed in the $ir_{first}{}^{th}$ mesh cell can be estimated by setting $a = |\mathbf{r}| - r_p$ and $b = (ir_{first} + 0.5)\Delta r$ in Eq. (3.32).

Scenario C: The partial volume of the particle, enclosed in each of the ir^{th} mesh cell ($ir_{first} < ir < ir_{last}$) can be estimated by setting $a = (ir - 0.5)\Delta r$ and $b = (ir + 0.5)\Delta r$ in Eq. (3.32).

Scenario D: The partial volume of the particle, enclosed in the $ir_{last}{}^{th}$ mesh cell can be estimated by setting $a = (ir_{last} - 0.5)\Delta r$ and $b = |\mathbf{r}| + r_p$ in Eq. (3.32).

The abovementioned splitting scenario were examined for all the particles in each time step to calculate the total concentration of particles and volumetric fraction of the suspending fluid (c_v) in each fluid mesh cell and solve the Navier-Stokes equations (Eqs. (3.27)-(3.30)). Indeed, the particles' body force exerted on the volume of suspending fluid located in a given fluid cell depends on the total splitting volumes of particles in that cell.
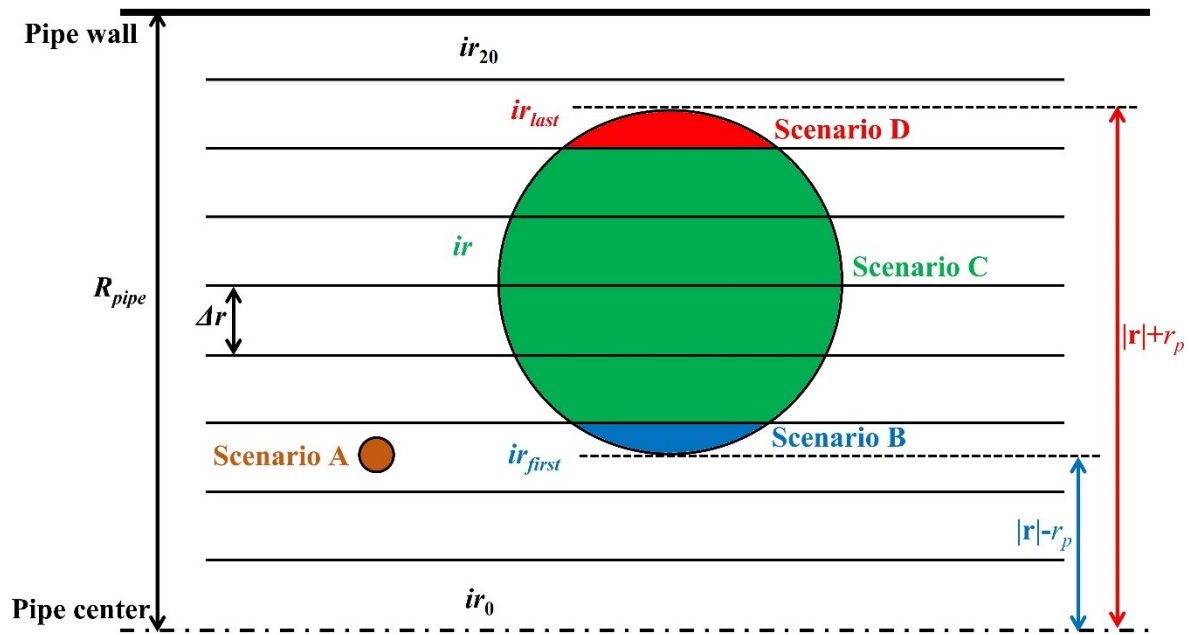
Fig. 3.15. The schematics of splitting method used to calculate the local particle concentration.

3.2.2.5 *Smoothing algorithm*

The Fourier-spectral filtering [36,37] was used as the smoothing method to prevent the instability of the results. The concentration field and body forces obtained using the DEM model at each node of the fluid domain were smoothed using Fourier series at each fluid time step [35,36]. The Fourier-series nodes were then extended double to create a period field. The Fourier-series coefficients were then multiplied by a factor g_n [37] which was calculated for each Fourier node n, as presented in Eq. 3.33, to develop the Fourier-expansion of the concentration field.

$$g_n = \frac{1 - \frac{1}{\exp\left(\frac{N_F^2 - n^2}{N_0^2}\right)}}{1 - \frac{1}{\exp\left(\frac{N_F^2}{N_0^2}\right)}} \tag{3.33}$$

where N_F and N_0 are the total number of Fourier nodes and an adjustable parameter, respectively. It was assumed that N_0 equals two times of N_F, as also did by Ghazi et al. [37]. An example for the pipe flow of a highly concentrated suspension (40%) across a 100-mm diameter pipe (R_{pipe} = 50 mm) is presented in Fig. 3.16. As shown for the original particle concentration profile obtained from the splitting algorithm, namely "Raw data", high frequency of noises can be observed in a central zone close to the pipe center which can cause instabilities in the CFD calculations. The concentration field was smoothed using two different N_F values of 10 and 20

in the employed spectral-filter method. As can be observed in Fig. 3.16, the choose of $N_F = 20$ led to higher precision compared to smoothing with 10 Fourier nodes, especially in the pipe center and the vicinity of the pipe wall, which are important to characterize the plug flow and LL, respectively. Therefore, in this study, the domain was divided into $N_F = 20$ Fourier nodes through the employed spectral-filter method.
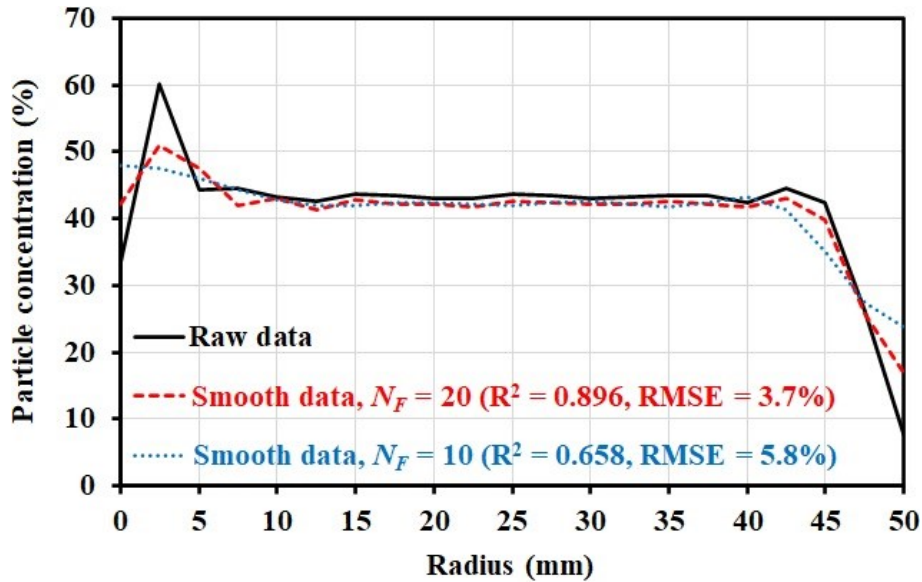
Fig. 3.16. Comparison between the smooth concertation profiles obtained using the spectral-filter method with different N_F of 10 and 20 and those originally obtained from the splitting algorithm (Raw data).

3.2.2.6 Coupling CFD and DEM models

The overall coupled CFD-DEM algorithm is schematically illustrated in Fig. 4. As can be observed, the coupling term between the particles and suspending fluid phases were firstly computed in terms of the concentration fields and body forces using an internal DEM algorithm, established as described earlier. Subsequently, the coupling term, calculated using the DEM model in cartesian system, was transmitted to the polar coordinates through the interface algorithm, established between the CFD and DEM solutions. The data were then smoothed through the spectral-filter method and introduced to the CFD model. The Navier-Stokes equations were then solved using the smooth data.
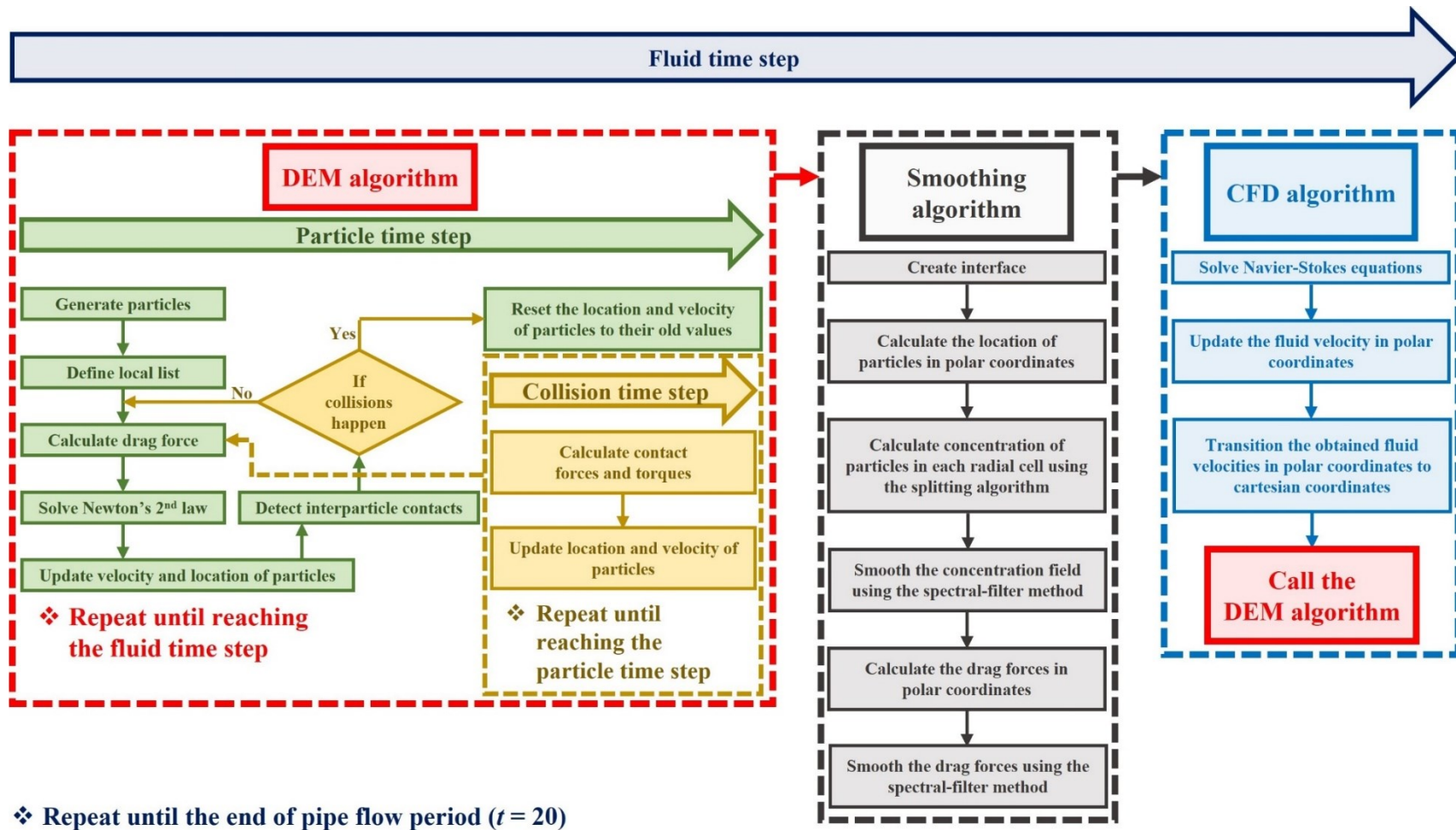
Fig. 3.17. The schematic illustration of the multiscale coupled CFD-DEM algorithm applied in this study.

3.2.2.7 *Specifications of the concrete pipe-flow models*

The concrete mixtures used in this phase consisted of one type of sand and three types of coarse aggregate, each with different size ranges corresponding to CA1 (2.5-10 mm), CA2 (5-14 mm), and CA3 (5-20 mm). The Canadian Standards Association has specific guidelines, outlined in the CSA A23.1:19/CSA A23.2:19 standards, for the PSD of aggregate used in concrete. Table 3.6 shows these recommended limits for different classes of aggregate. To conform to these limits, the cumulative passing percentages of the investigated aggregate models were selected as the average of the minimum (*min*) and maximum (*max*) allowed limits for each standard-sieve size, ($CPP = (min + max)/2$), which is shown in Table 3.7. The remaining volumetric fractions of each type of sand and coarse aggregate on each sieve were then calculated and presented in the Table 3.7.

Table 3.6. Grading limits for different classes of fine (sand) and coarse aggregate (CA1-3), recommended by CSA A23.1:19/CSA A23.2:19 standard [37] in terms of the minimum (*min*) and maximum (*max*) allowed cumulative passing percentages (%) from each standard sieve.

Standard sieve size (mm)	Sand (0-5 mm)		CA1 (2.5-10 mm)		CA2 (5-14 mm)		CA3 (5-20 mm)	
	min	*max*	*min*	*max*	*min*	*max*	*min*	*max*
28					-	-	100	100
20	-	-	-	-	100	100	85	100
14			100	100	90	100	50	90
10	100	100	85	100	45	75	25	60
5	95	100	10	30	0	15	0	10
2.5	80	100	0	10	0	5	0	5
1.25	50	90	0	5				
0.630	25	65						
0.315	10	35	-	-	-	-	-	-
0.160	2	10						
0.080	0	3						

Table 3.7. PSDs of the modelled sand and coarse aggregate (CA1-3), in terms of *CPP* (vol.%) and *RVF* (vol.%) on each standard sieve, conforming to the CSA A23.1:19/CSA A23.2:19 standard [37].

Standard sieve size (mm)	Sand (0-5 mm)		CA1 (2.5-10 mm)		CA2 (5-14 mm)		CA3 (5-20 mm)	
	CPP (%)	RVF (%)	CPP (%)	RVF (%)	CPP (%)	RVF (%)	CPP (%)	RVF (%)
20			-	-	-	-	100	-
14	-	-			100		70	30
10			100		60	40	42.5	27.5
5	100		20	80	7.5	52.5	5	37.5
2.5	90	10	5	15	2.5	5	2.5	2.5
1.25	70	20	2.5	2.5				
0.630	45	25						
0.315	22.5	22.5				2.5		2.5
0.160	6	16.5	-	2.5 (< 1.25 mm)	-	2.5 (< 2.5 mm)	-	2.5 (< 2.5 mm)
0.080	1.5	4.5						
Base	-	1.5						

Table 3.8 displays the fine and coarse aggregate models, which consist of five subclasses of spherical particles, P1 (1 mm), P2 (3.5 mm), P3 (7.5 mm), P4 (12 mm), and P5 (17 mm), each

representing a specific sieve-size range, including 0-2.5, 2.5-5, 5-10, 10-14, and 14-20 mm, respectively. Table 3.9 shows the three different particle-size distributions (PSDs) of aggregate: fine, medium, and coarse PSDs. These PSDs consist of different volumetric fractions of four aggregate classes (sand and CA-3) and their corresponding five particle subclasses (P1-5), as listed in Table 3.8.

Table 3.8. Proportionings of the modelled sand and coarse aggregate (CA1-3), in terms of volumetric fractions (vol.%) of different particle subclasses of P1-5.

Particle subclasses		Sand	CA1	CA2	CA3
P1: 1 mm		90%	5%	2.5%	2.5%
P2: 3.5 mm		10%	15%	5%	2.5%
P3: 7.5 mm		-	80%	52.5%	37.5%
P4: 12 mm		-	-	40%	27.5%
P5: 17 mm		-	-	-	30%

Table 3.9 . Proportioning of the investigated PSDs of aggregate, in terms of volumetric fractions (vol.%) of 4 aggregate classes (sand and CA1-3) and their corresponding 5 particle subclasses (P1-5) in unit volume of aggregate.

PSD #	Aggregate classes (vol.%)				Particle subclasses (vol.%)				
	Sand	CA1	CA2	CA3	P1: 1 mm	P2: 3.5 mm	P3: 7.5 mm	P4: 12 mm	P5: 1 7mm
Fine	40	30	20	10	38	10	38	11	3
Medium	25	25	25	25	25	8	43	17	8
Coarse	10	20	30	40	12	7	47	23	12

In this study, the pipe flow of nine different suspensions were analyzed. These suspensions were made by combining three total particle concentrations (10%, 25%, and 40%) with three different particle-size distributions, as shown in Table 3.9. The mixture ratios for each suspension are presented in Table 3.10, which includes the total particle concentration, number of each particle class (P1-5), total number of particles, average diameter (D_{avg}), packing density (φ_{max}), and relative-solid packing fraction (φ/φ_{max}).

The simulations were performed in a cylindrical pipe with a 100-mm diameter (D_{Pipe}) or 50-mm radius (R) and 500-mm length (L_{Pipe}). The maximum allowed number of particles for the simulation was set to $n_{max} = 5 \times 10^5$ due to the computational limits of the employed code. Therefore, the L_{Pipe} values were adjusted for each suspension to avoid exceeding the n_{max} limit. The suspensions are labeled FPSD, MPSD, CPSD, LC, MC, and HC labels in Table 3.10 which correspond to the fine-, medium-, and coarse-PSDs, as well as low (10%), medium (25%), and high (40%) concentrations of aggregate, respectively.

Moreover, the virtual packing density (φ_{max}) of a polydisperse mixture of of five particle subclasses can be evaluated using the linear-packing model proposed by Stovall et al. [38] and de Larrard [38]. The formula for this calculation is as follows:

$$\varphi_{max} = \min_{i=1}^{5} \left[\frac{\alpha_i}{1 - (1 - \alpha_i) \sum_{j=1}^{i-1} a_{ij}\, \varphi_j - \sum_{j=i+1}^{5} b_{ij}\, \varphi_j} \right] \tag{3.34}$$

where $\alpha_i = \frac{\pi}{3\sqrt{2}}$, φ_j, a_{ij}, and b_{ij} are the highest packing density amongst all possible lattice packings of spherical particles of all subclasses 'i' = 1 to 5, volumetric content of subclass 'j', loosening (Eq. (3.35)), and wall effects (Eq. (3.36)) for particles of subclass 'i' (diameter d_i) due to the influence of particles of subclass 'j' (diameter d_j), respectively.

$$a_{ij} = \begin{cases} \sqrt{1 - \left(1 - \dfrac{d_j}{d_i}\right)^{1.02}}, & d_i > d_j \\ 0, & d_i \le d_j \end{cases} \tag{3.35}$$

$$b_{ij} = \begin{cases} 1 - \left(1 - \dfrac{d_i}{d_j}\right)^{1.50}, & d_j > d_i \\ 0, & d_j \le d_i \end{cases} \tag{3.36}$$

Additionally, the mean diameter of particles ($D_{avg\text{-}i}$) in each of the nine suspensions "i" (i = 1 to 9) was calculated by taking the volumetric-weighted arithmetic average of the diameters of the corresponding particle subclasses "j" (j = 1 to 5), as

$$D_{avg\text{-}i} = \frac{\sum_{j=1}^{5} \left(\varphi_{ji}\, d_j \right)}{\sum_{j=1}^{5} \varphi_{ji}} \tag{3.37}$$

where φ_{ji} represents the volumetric concentration of particle subclass "j" in a given suspension "i.

Table 3.10. Proportioning of the investigated suspensions, including total particle concentration (φ), number of each particle subclasses of P1-5, and total number of particles (n), as well as the D_{avg}, φ_{max}, and φ/φ_{max} of particles ($n_{max} = 5 \times 10^5$).

Model #	PSD	Concentration level	φ (%)	P1: 1 mm	P2: 3.5 mm	P3: 7.5 mm	P4: 12 mm	P5: 17 mm	n	D_{avg} (mm)	φ_{max}	$\dfrac{\varphi}{\varphi_{max}}$	$\dfrac{L_{Pipe}}{R}$
						Number of particles							
1-FPSD-LC	Fine			286 875	1 706	680	47	5	289 313	5.429	0.847	0.119	10.000
2-MPSD-LC	Medium	Low	10	187 500	1 421	756	73	11	189 761	6.990	0.858	0.116	10.000
3-CPSD-LC	Coarse			88 125	1 137	831	100	18	90 211	8.635	0.868	0.115	10.000
4-FPSD-MC	Fine			495 720	2 947	1 175	81	8	499 931	5.398	0.847	0.295	6.912
5-MPSD-MC	Medium	Medium	25	468 750	3 553	1 889	183	29	474 404	7.030	0.857	0.292	10.000
6-CPSD-MC	Coarse			220 313	2 843	2 078	250	46	225 530	8.657	0.868	0.288	10.000
7-FPSD-HC	Fine			495 720	2 947	1 175	81	8	499 931	5.398	0.847	0.473	4.320
8-MPSD-HC	Medium	High	40	494 025	3 745	1 991	193	30	499 984	7.016	0.857	0.466	6.587
9-CPSD-HC	Coarse			352 500	4 548	3 324	399	73	360 844	8.646	0.868	0.461	10.000

REFERENCES

[1]   R. Khatib, Analysis and prediction of pumping characteristics of high-strength self-consolidating concrete, Ph.D. Thesis, Université de Sherbrooke (2013) http://hdl.handle.net/11143/6634.

[2]   D. Feys, K.H. Khayat, R. Khatib, How do concrete rheology, tribology, flow rate and pipe radius influence pumping pressure?, Cement and Concrete Composites, 66 (2016) 38-46. https://doi.org/10.1016/j.cemconcomp.2015.11.002.

[3]   D. Feys, K.H. Khayat, A. Perez-Schell, R. Khatib, Prediction of pumping pressure by means of new tribometer for highly-workable concrete, Cement and Concrete Composites, 57 (2015) 102-115 https://doi.org/10.1016/j.cemconcomp.2014.12.007.

[4]   G. Chen, Q. Xiong, P.J. Morris, E.G. Paterson, A. Sergeev, Y.-C. Wang, OpenFOAM for Computational Fluid Dynamics, Not. Am. Math. Soc. 61 (2014) 354. https://doi.org/10.1090/noti1095.

[5]   S.S. Deshpande, L. Anumolu, M.F. Trujillo, Evaluating the performance of the two-phase flow solver interFoam, Comput. Sci. Discov. 5 (2012). https://doi.org/10.1088/1749-4699/5/1/014016.

[6]   V. Srinivasan, A.J. Salazar, K. Saito, Modeling the disintegration of modulated liquid jets using volume-of-fluid (VOF) methodology, Appl. Math. Model. 35 (2011) 3710–3730. https://doi.org/10.1016/j.apm.2011.01.040.

[7]   H. Jasak, Error analysis and estimation for finite volume method with applications to fluid flow, M (1996)..

[8]   P.T. Peeters, D. ir. B.W. van Oudheusden, CFD of multiphase pipe flow: a comparison of solvers, Aerodynamics. master (2016) 134.

[9]   G.H. Kim, S. Park, Development of a numerical simulation tool for efficient and robust prediction of ship resistance, Int. J. Nav. Archit. Ocean Eng. 9 (2017) 537–551. https://doi.org/10.1016/j.ijnaoe.2017.01.003.

[10]   G. Cerne, S. Petelin, I. Tiselj, Coupling of the Interface Tracking and the Two-Fluid Models for the Simulation of Incompressible Two-Phase Flow, J. Comput. Phys. 171 (2001) 776–804. https://doi.org/10.1006/jcph.2001.6810.

[11]   C.W. Hirt, B.D. Nichols, Volume of fluid (VOF) method for the dynamics of free boundaries, J. Comput. Phys. 39 (1981) 201–225. https://doi.org/10.1016/0021-9991(81)90145-5.

[12]   S.M. Damián, N.M. Nigro, An extended mixture model for the simultaneous treatment of small-scale and large-scale interfaces, Int. J. Numer. Methods Fluids. 75 (2014) 547–574. https://doi.org/10.1002/fld.3906.

[13]   C.J. Greenshields, OpenFOAM user guide version 6, OpenFOAM Found. Ltd. (2017) U-94. https://cfd.direct/openfoam/user-guide/.

[14]   D. Feys, G.D. Schutter, S. Fataei, N.S. Martys, V. Mechtcherine, Pumping of concrete: Understanding a common placement method with lots of challenges, Cement and concrete researh, 154 (2022) 106720. https://doi.org/10.1016/j.cemconres.2022.106720.

[15]   R.E. Denton, Y. Hu, Symmetry boundary conditions, J. Comput. Phys. 228 (2009) 4823–4835. https://doi.org/10.1016/j.jcp.2009.03.033.

[16]   S. Richardson, On the no-slip boundary condition, J. Fluid Mech. 59 (1973) 707–719. https://doi.org/10.1017/S0022112073001801.

[17]   J.D. Dent, T.E. Lang, A biviscous modified Bingham model of snow avalanche motion., Ann. Glaciol. 4 (1983) 42–46. https://doi.org/10.1017/S0260305500005218.

[18]   S.W. Jeong, Determining the viscosity and yield surface of marine sediments using modified Bingham models, Geosci. J. 17 (2013) 241–247. https://doi.org/10.1007/s12303-013-0038-7.

[19]   E. Secrieru, J. Khodor, C. Schröfl, V. Mechtcherine, Formation of lubricating layer and flow type during pumping of cement-based materials, Constr. Build. Mater. 178 (2018) 507–517. https://doi.org/10.1016/j.conbuildmat.2018.05.118.

[20]   H.D. Le, E.H. Kadri, S. Aggoun, J. Vierendeels, P. Troch, G. De Schutter, Effect of lubrication layer on velocity profile of concrete in a pumping pipe, Mater. Struct. Constr. 48 (2015) 3991–4003. https://doi.org/10.1617/s11527-014-0458-5.

[21]   M. Winter, Benchmark and Validation of open source CFD codes, with focus on compressible and rotating capabilities, Mycotoxin Res. 6 (2013) 100. http://www.ncbi.nlm.nih.gov/pubmed/21365933. 185–200.

[22]   H. Khawaja, M. Moatamedi, Semi-implicit method for pressure-linked equations (SIMPLE) ⇓ solution in MATLAB®, Int. J. Multiphys. 12 (2018) 313–325. https://doi.org/10.21152/1750-9548.12.4.313.

[23]   D. Feys, How much is bulk concrete sheared during pumping?, Constr. Build. Mater. 223 (2019) 341–351. https://doi.org/10.1016/j.conbuildmat.2019.06.224.

[24] J.H. Ferziger, M. Perić, R.L. Street, Computational Methods for Fluid Dynamics, Springer International Publishing (2020) 81-110. https://doi.org/10.1007/978-3-319-99693-6_4.

[25] J. Spangenberg, N. Roussel, J.H. Hattel, H. Stang, J. Skocek, M.R. Geiker, Flow induced particle migration in fresh concrete: Theoretical frame, numerical simulations and experimental results on model fluids, Cement and. Concrete research, 42 (2012) 633–641. https://doi.org/10.1016/j.cemconres.2012.01.007.

[26] P. Coussot, rheomtry of paste, suspension and grannular materials, John Wiley Sons. (2005) 291.

[27] H. Nilsson, How to implement a new boundary condition, Chalmers. (2014) 72–79.

[28] J.S. Marshall, Discrete-element modeling of particulate aerosol flows, Journal of Computational Physics, 228 (5) (2009) 1541-1561. https://doi.org/10.1016/j.jcp.2008.10.035.

[29] J.S Marshall, S. Li, (2014), Adhesive Particle Flow: A Discrete-Element Approach, Cambridge: Cambridge University Press, (2014) ISBN 9781139424547, https://doi.org/10.1017/CBO9781139424547.

[30] T. Tavangar, M. Hosseinpoor, A. Yahia, and K.H. Khayat, Discrete-element modeling of shear-induced particle migration during zones concrete pipe flow: Effect of size distribution and concentration of aggregate on formation of lubrication layer, Cement and Concrete Research, 166 107113 (2023). https://doi.org/10.1016/j.cemconres.2023.107113.

[31] Di Felice, The voidage function for fluid-particle interaction systems, International Journal of Multiphase Flow, 20 (1) (1994) 153-159. https://doi.org/10.1016/0301-9322(94)90011-6.

[32] J.S. Marshall, Comparison of methods for computing the concentration field of a particulate flow, International Journal of Multiphase Flow, 56 (2013) 4-14. https://doi.org/10.1016/j.ijmultiphaseflow.2013.05.009.

[33] P.A. Cundall, O.D.L. Strack, A discrete numerical model for granular assembles, Géotechnique, 29 (1) (1979) 47-65. https://doi.org/10.1680/geot.1979.29.1.47.

[34] B. Blais, F. Bertrand, CFD-DEM investigation of viscous solid-liquid mixing: Impact of particle properties and mixer characteristics, Chemical Engineering Research and Design, 118 (2017) 270-285. https://doi.org/10.1016/j.cherd.2016.12.018.

[35] F.F. Dizaji, J.S. Marshall, J.R. Grant, Collision and breakup of fractal particle agglomerate in a shear flow, Journal of Fluid Mechanics, 862 (2019) 592-623. https://doi.org/10.1017/jfm.2018.959.

[36] C.J. Ghazi, J.S. Marshall, A CO2 tracer-gas method for local air leakage detection and characterization, Flow Measurement and Instrumentation, 38 (2014) 72-81. https://doi.org/10.1016/j.flowmeasinst.2014.05.015.

[37] Canadian Standards Association CSA A23.1:19/CSA A23.2:19 standard, Concrete materials and methods of concrete construction/Test methods and standard practices for concrete, CSA Group (2019) SKU: 2425145.

[38] T. Stovall, F. de Larrard, M. Buil, Linear packing density model of grain mixtures, Powder Technology, 48 (1) (1986) 1-12. https://doi.org/10.1016/0032-5910(86)80058-4.

[39] F. de Larrard, Concrete mixture proportioning — a scientific approach, in: S. Mindess, A. Bentur (Eds.), Modern Concrete Technology Series No. 7, E&FN SPON, London (1999) ISBN 9780419235002.

Chapter 4. Novel tri-viscous model to simulate pumping of flowable concrete through characterization of lubrication layer and plug zones

91

CHAPTER 4. Novel tri-viscous model to simulate pumping of flowable concrete through characterization of lubrication layer and plug zones

Authors and affiliations

Tooran Tavangar: Ph.D. candidate, Cement and Concrete Research Group, Department of Civil and Building Engineering, Université de Sherbrooke, Sherbrooke, Québec, Canada, J1K 2R1.

Masoud Hosseinpoor: Research Assitance, Cement and Concrete Research Group, Department of Civil and Building Engineering, Université de Sherbrooke, Sherbrooke, Québec, Canada, J1K 2R1.

Ammar Yahia: Professor, Cement and Concrete Research Group, Department of Civil and Building Engineering, Université de Sherbrooke, Sherbrooke, Québec, Canada, J1K 2R1.

Kamal H. Khayat, Professor, Department of Civil, Architectural and Environmental Engineering, Center for Infrastructure Engineering Studies, Missouri University of Science and Technology, Rolla, MO, USA.

Abstract

In this study, computational fluid dynamics (CFD) was employed to simulate the pipe flow of 18 self-consolidating and four highly-workable concrete mixtures in a 30-m long pumping circuit. Pressure loss (ΔP) in 100- and 125-mm diameter (DP) pipelines was measured under low (1.2-6.2 l/s) and high (8.1-16.4 l/s) flow rates (Q). The numerical simulation was successfully carried out using a two-fluid model and a new variable-viscosity single-fluid approach, namely double-Bingham and tri-viscous models, respectively. The radial variation of rheological properties of the concrete across the pipe section, representing the plug flow, sheared concrete, and lubrication layer (LL) zones was successfully simulated based on a total of 404 pipe flow experiments. The relative LL viscous constant (η_{LL}) values obtained using numerical simulations-to-those obtained experimentally using a tribometer ranged between 30% to 200%. Moreover, the coupled effect of the characteristics of different flow zones, DP, and Q on ΔP was evaluated.

Keywords: Concrete pumping; Lubrication layer; Numerical simulation; Plug flow; Pressure loss; Rheology.

4.1 Analytical and empirical background of concrete pipe flow

Concrete pumping can significantly facilitate the casting process and shortens concrete construction duration [1]. However, successful pumping operations require good understanding of key parameters affecting concrete flowability and stability of concrete under pressure. The prediction of pumping pressure is of particular interest to properly design the pumping circuits and rheological properties of the concrete mixtures for successful pumping process given the application on hand. This is necessary to fulfil the casting demand, including the targeted flow rate and homogeneity of concrete during and after pumping, respectively [2-6].

4.1.1 Analytical models of concrete pipe flow

As reported by Browne and Bamforth [7], in the case of highly workable (HWC) and self-consolidating concrete (SCC) characterized by relatively high content of paste compared to conventional vibrated concrete (CVC), the cement paste is also subjected to the shear stress during concrete pipe flow. Thus, direct contact between aggregate particles and the wall of the pipe is

avoided. Therefore, the stress transfer is hydrodynamic, and the pressure decay (ΔP) is linear along the pipe length (L). The required pumping pressure (P) increases linearly with the flow rate (Q). Moreover, a micro-mortar thin layer, namely lubrication layer (LL), consisting of higher contents of water, cement paste, and fine particles relative to the bulk concrete (BC), is formed close to the pipe wall [3-6]. The main mechanisms of formation of the LL include the pipe-wall effect [8], Reynolds dilatancy of concrete [9,10], and shear-induced migration of coarse aggregate towards the central axis of the pipe [11,12]. These mechanisms were comprehensively discussed in Ref. [13]. Due to its lower plastic viscosity and yield stress relative to BC, the LL is sheared and, therefore, friction no longer governs the flow behavior of concrete in pipes [6,14]. The ΔP-L and P-Q relationships are thus dependent on the ability to form the LL. On the other hand, formation of LL results in nonuniform rheological behavior and, consequently, dissimilar flow velocity and shear-rate profiles in different zones of the pipe section. Several theoretical tools were developed during the last two decades to understand and predict such complex flow behavior of concrete in pipes and ensure efficient design of the pumping set-ups [13,15,16].

Analytical models were established to predict concrete pressure loss as a function of the rheological properties of concrete (i.e., yield stress $\tau_{0\text{-C}}$ and plastic viscosity $\mu_{p\text{-C}}$) and those of the LL ($\tau_{0\text{-LL}}$ and $\mu_{p\text{-LL}}$), as well as pumping flow rate Q and geometry of the pipes (i.e., radius R and length L) [1,17,18]. The Buckingham-Reiner equation [19] was initially proposed for pipe flow of Bingham fluids. However, its application for concrete pipe flow led to considerable overestimation (2 to 10 times higher) of pressure loss, due to neglecting the presence of the LL [1,14,18,20]. The most well-known analytical model was then proposed by Kaplan et al. [1,17,18] to predict ΔP. The proposed approaches considered two possible cases during concrete pipe flow, including: (1) when the total shear takes place only at LL while BC is unsheared; and (2) when both LL and some of BC undergo partial shearing during flow. The shear stress across the pipe section is assumed to linearly increase from zero at pipe center to its maximum value at pipe walls. Establishing a force equilibrium for a pressure-driven concrete pipe flow, the maximum shear stress at pipe walls can be calculated as $\tau_w = (\Delta P.R)/2L$. According to Kaplan et al. [1,17,18], when τ_w is smaller than the yield stress of concrete ($\tau_w < \tau_{0\text{-C}}$), the BC is not sheared, and Eq. (4.1) applies (1st case). Otherwise (i.e., $\tau_w > \tau_{0\text{-C}}$), ΔP can be predicted using Eq. (4.2) for partially sheared concrete in the pipe (2nd case), as follows:

Chapter 4. Novel tri-viscous model to simulate pumping of flowable concrete through characterization of lubrication layer and plug zones

94

$$\Delta P = \frac{2L}{R}\left(\frac{Q}{3600\pi R^2 k_r} \times \frac{\mu_{p-LL}}{e_{LL}} + \tau_{0-LL}\right) \tag{4.1}$$

$$\Delta P = \frac{2L}{R}\left(\frac{\frac{Q}{3600\pi R^2 k_r} - \frac{R}{4\mu_{p-C}}\tau_{0-LL} + \frac{R}{3\mu_{p-C}}\tau_{0-C}}{1 + \frac{R}{4\mu_{p-C}} \times \frac{\mu_{p-LL}}{e_{LL}}} \times \frac{\mu_{p-LL}}{e_{LL}} + \tau_{0-LL}\right) \tag{4.2}$$

where k_r, τ_{0-LL}, μ_{p-LL}, and e_{LL} are the filling coefficient of the piston pumps' cylinders, yield stress, plastic viscosity, and thickness of the LL, respectively. It is worthy to mention that k_r corresponds to the fraction of the piston pumps' cylinders filled by concrete at each pumping stroke and ranges between 0 and 1. The radius of the un-sheared concrete zone (plug radius r_{Plug}) can then be estimated, as follows:

$$r_{Plug} = \frac{2\tau_{0-C}}{\Delta p} \tag{4.3}$$

where $\Delta p = \Delta P/L$ is the total pressure loss through a unit length of pipe. Assuming the Bingham rheological model for BC and LL, the shear stress, flow velocity, and shear rate profiles in different zones across the pipe section is schematically illustrated in Fig. 4.1. As shown in Fig. 4.1 and Eqs. (4.4) to (4.7), VLL, VSC, and VP are flow velocity at distance r from the pipe center, located at the LL, sheared concrete zone, and plug zone, respectively, and Q is total flow rate, evaluated as follow [21]:

$$V_{LL} = \frac{1}{\mu_{p-LL}}\left(\frac{\Delta p(R^2 - r^2)}{4} - \tau_{0-LL}(R - r)\right) \text{ for } r_{LL} \leq r \leq R \tag{4.4}$$

$$V_{SC} = \frac{1}{\mu_{p-LL}}\left(\frac{\Delta p(R^2 - r_{LL}^2)}{4} - \tau_{0-LL}(R - r_{LL})\right) + \frac{1}{\mu_{p-C}}\left(\frac{\Delta p(r_{LL}^2 - r^2)}{4} - \tau_{0-C}(r_{LL} - r)\right)$$

$$\text{for } r_{Plug} \leq r \leq R_{LL} \tag{4.5}$$

$$V_P = \frac{1}{\mu_{p-LL}}\left(\frac{\Delta p(R^2 - r_{LL}^2)}{4} - \tau_{0-LL}(R - r_{LL})\right) + \frac{1}{\mu_{p-C}}\left(\frac{\Delta p(r_{LL}^2 - r_{Plug}^2)}{4} - \tau_{0-C}(r_{LL} - r_{Plug})\right)$$

$$\text{for } 0 \leq r \leq r\_Plug \tag{4.6}$$

$$Q = 2\pi \left(\int_{r_{LL}}^{R} V_{LL}.\,dr + \int_{r_{Plug}}^{r_{LL}} V_{SC}.\,dr + \int_{0}^{r_{Plug}} V_{P}.\,dr \right) \tag{4.7}$$

where r_{LL} is the radius where LL starts ($r_{LL} = R - e_{LL}$). According to Eqs. (4.1) to (4.7), the rheological properties of pumped concrete and its corresponding LL, as well as LL thickness (e_{LL}) must be precisely estimated to achieve an accurate evaluation of concrete pumpability. Concrete rheology can be measured using the existing rheometers [22]. However, due to confined condition of concrete pipe flow, taking samples from the LL zone and characterization of LL in terms of its thickness and rheological properties is practically problematic.
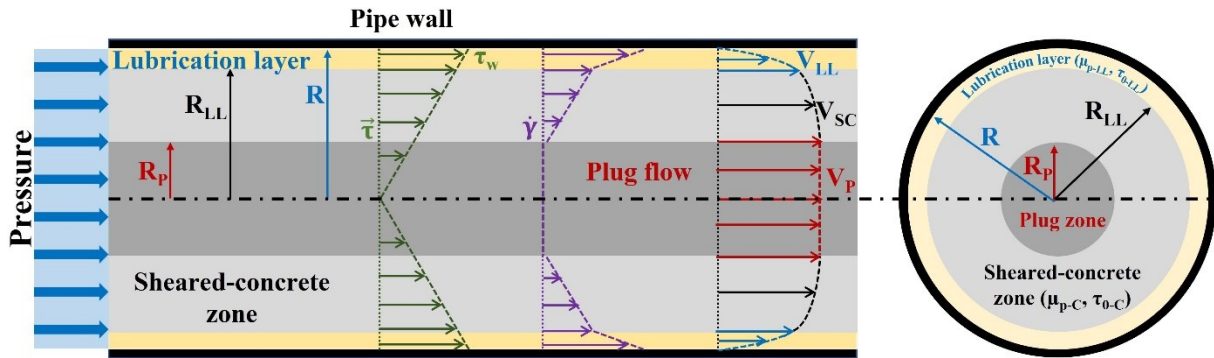
Fig. 4.1. Velocity profiles, shear stress, and shear-rate distributions in different flow zones over pipe cross-section, including LL, sheared-concrete, and plug flow zones [1,6,13,21].

4.1.2 Empirical evaluation of concrete tribology

Various empirical methods were employed to evaluate the LL thickness, such as image analysis of the cut sections of hardened concrete in pipes [23] and ultrasonic pulse velocimetry (UPV) [24,25]. However, the evaluated values using these methods are uncertain due to their technical complexities, (e.g., noisy data processing). On the other hand, no uniform agreement was found on LL thickness that it can vary between 1 to 10 mm for different types of concrete [24-29].

Frictional rheometers, including sliding rheometers and tribometers, were developed to simulate the concrete flow in pipes and estimate the rheological properties of the LL formed at the interface of concrete and the measuring unit. For instance, the Sliper was developed to measure the rheological properties of the LL using a sliding pipe [30]. This was obtained by correlating different measured pressure and sliding velocity values. It is worthy to mention that in the Sliper set-up the pipe wall is moved, and the investigated concrete is stationary. Hence, the concrete in

pipe section is not sheared and only plug and LL zones are formed. Therefore, the Sliper is not quite representative for highly flowable mixtures, such as HWC and SCC, where the BC is mostly sheared. Moreover, the thickness of the created LL cannot be directly evaluated.

On the other hand, rotational tribometers consist in coaxial-smooth cylinders which exert shear on the concrete sample located at their gap to simulate the concrete flow across the pipes [1,31-33]. Most recently, Feys et al. [33] developed a coaxial-cylinders tribometer adapted for HWC and SCC mixtures. The authors established a methodology to determine the plug radius and the shear stresses at the sheared-BC and LL. Consequently, the created LL can be characterized in terms of yield stress ($\tau_{0\text{-}LL}$) and viscous constant (η_{LL}). The viscous constant is an interdependent property of LL defined as its plastic viscosity-to-thickness ratio ($\eta_{LL} = \mu_{p\text{-}LL}/e_{LL}$). It is worth mentioning that the tribometers cannot evaluate the thickness of LL, independent to their rheological properties. By considering the LL characteristics, obtained using tribological measurements, in analytical models, Kaplan et al. [1] showed good agreements with experimental pressure loss values in large-scale concrete pipelines. However, tribometers cannot perfectly simulate the flow conditions of concrete during pumping procedures. This is due to the absence of pressure and significantly lower shear-rate values occurring during tribological tests compared to those in concrete pipe flow. Hence, in terms of rheological properties and thickness, the characteristics of the LL formed in tribometer cannot represent those formed at vicinity of the pipe walls during concrete pumping.

4.1.3 Research significance of numerical simulation of concrete pipe flow

In addition to the straight horizontal pipes, a typical pipeline consists of different segments, such as vertical and inclined straight pipes, as well as bends and reducers. The analytical models were originally developed for horizontal straight pipes, thus they cannot evaluate the concrete pumpability through such complementary geometries. Moreover, the concrete mixtures were shown to be subjected to time- and shear-dependent variations of rheological properties [34-37] and air-void system [37-39] during pumping process. As reported in literature [34-37], concrete viscosity decreases after pumping due to increase in temperature and additional dispersion of cement particles and superplasticizer action, induced by the additional shearing in pipes. The proposed analytical solutions cannot consider these variations in rheological properties of both BC and LL. This can negatively affect their precision to predict the concrete pumpability.

As discussed above, the analytical and empirical methods cannot reflect the realistic pressure-driven flow conditions of concrete in pipes. Computational techniques were then employed to simulate the physical interactions between different solid and liquid phases of concrete and pipe wall, as well as variation of concrete properties across the pipe (i.e., formation of LL, sheared BC, and plug zones). They can also simulate the time- and shear-dependent changes in rheological behavior of concrete, hence leading to more precise prediction of concrete pipe flow behavior. The main computational methods to simulate the concrete flow during pumping process can be classified in five different categories: phenomenological multiphasic approach (PMA); discrete element modelling (DEM); smoothed particle hydrodynamics (SPH); coupled computational fluid dynamics (CFD) and DEM approach (CFD-DEM); and single-phase modelling (SPM) using CFD [13]. These numerical approaches are further discussed in the section below.

4.2 Numerical simulation of concrete pipe flow

The selection of an appropriate computational approach is essential to secure adequate prediction of concrete pumpability, given the pumping conditions. A comprehensive review on the existing computational approaches and their applications for numerical simulation of concrete pumping was presented in Ref. [13]. The phenomenological multiphasic approach (PMA) is conducted by the governing equations for shear-induced particle migration (SIPM) in pipes. These equations were proposed by Lam et al. [11] based on diffusion equations describing the evolution of particle concentration in a pressure-driven pipe flow. The diffusion equations were developed by Philips et al. [40] due to spatially varying in both particles' interaction frequency and viscosity. The PMA was successfully employed to simulate the aggregate concentration across the pipe section at an equilibrium state, hence evaluating the LL thickness and rheological properties for large-scale pumping set-ups [24,41,42]. However, the accuracy of PMA simulations is highly dependent on the selection of the phenomenological coefficients of employed diffusion equations, as well as the shape-dependent intrinsic viscosity of the solid particles [13].

The particle-based methods, such as DEM [43,44] and SPH [45,46], were employed to take into consideration the physical interaction of solid particles and suspending paste/mortar, which cannot be directly simulated using the PMA. Using these approaches, concrete is simulated as computational particles. The particle interactions and their contacts in DEM are modelled using the virtual rheological elements, such as springs, dashpots, and sliders. On the other hand, the SPH

quantities, including the physical interaction of the particles corresponding to the solid and liquid phases, are obtained as the weighted averages from the adjacent particles. DEM showed a great potential to simulate the heterogeneous phenomena during pumping, such as pipe blockage and LL formation [44]. However, from a physical point of view, definition of the parameters describing the virtual contact models in DEM to represent the characteristics of solid and liquid phases is complicated [13]. Following an optimization process in terms of number, shape, diameter, size, spatial distribution, and layers number of the modelled particles, as well as the selection of the weighting functions, SPH led to more realistic consideration of solid-solid and solid-liquid interaction forces compared to DEM. However, both DEM and SPH methods require extensive computational time to simulate the concrete flow in full-scale pipelines. This has limited their applications to simulate the heterogenous flow behavior in vicinity of small-scale segments, such as bends and reducers which require shorter time intervals [13].

In the case of single-phase modelling (SPM) approach, concrete is simulated as a single fluid. The rheological properties of concrete are considered as the main inputs of the model, neglecting the presence of aggregate. Due to this simplification, SPM is recommended for simulation of concrete pumpability for large-scale pumping set-ups. Several CFD methods, such as Finite Volume Method (FVM), were used to solve the mass and momentum conversation equations for steady and incompressible flow. Accordingly, the Navier-Stokes equations were implemented as a constitutive equation to evaluate the concrete flow behavior as a single-phase in pipes [6,47,48], as follow:

$$\frac{\partial \rho}{\partial t} + \frac{\partial}{\partial x_i}(\rho.u_i) = 0 \tag{4.8}$$

$$\frac{\partial}{\partial t}(\rho.u_i) + \frac{\partial}{\partial x_j}(\rho.u_j.u_i) = -\frac{\partial P}{\partial x_i} + \frac{\partial}{\partial x_j}\left[\mu.\left(\frac{\partial u_i}{\partial x_j} + \frac{\partial u_j}{\partial x_i}\right)\right] \tag{4.9}$$

where ρ, u, P, and μ are the concrete density, flow velocity, pressure, and concrete viscosity, respectively. The negative and positive terms at the right side of Eq. (4.9) represent the normal and tangential shear stresses, respectively. It is worthy to mention that the no-slip boundary condition was assigned to the concrete-pipe wall interface in the employed SPM simulations of concrete pumping in literature [6]. In order to consider the effect of LL presence, the simulation domain is

divided in two zones, corresponding to the BC and LL and discretized in different mesh cells. The rheological and tribological properties of the BC and LL measured using the rheometer and tribometer set-ups, respectively, are then assigned to the mesh cells corresponding to each zone.

The most recent numerical investigations on concrete pumping employed a bi-viscous rheological model by combining the Newtonian and Bingham models and using ANSYS Fluent software [6,49-51]. A relatively high viscosity value (η_N = 100 Pa.s) was selected for the Newtonian part corresponding to very low shear rate values. This was assumed for computational purposes to avoid zero-dominator in calculating the apparent viscosity ($\mu_{app} = \frac{\tau}{\dot{\gamma}} = \mu_p + \frac{\tau_0}{\dot{\gamma}}$) in plug zone where shear rate equals zero. Beyond a critical shear rate value, a Bingham model corresponding to the yield stress and plastic viscosity values of the BC or LL is applied depending on the radial position of the mesh cells. According to the literature, various LL thicknesses of 0 to 10 mm are examined to evaluate the effect of LL on pressure loss of investigated mixtures in Sliper [50] as well as small- [51] and large-scale [6] pipelines. The numerical simulations showing the best fit with experimental measurements of the pressure loss values were reported as the most optimized model. It is worth mentioning that a LL thickness of 2 and 4 mm was reported for HWC (e.g., SCC) and CVC, respectively [6].

Secrieru et al. [6] simulated a 160-m pipeline using the Sliper simulation results in terms of LL thickness. Although good agreements were obtained between the numerical SPM results and experimental pressure loss values, analytical models showed better accuracy for different types of concrete mixtures comparing to the employed bi-viscous and SPM models [6]. This can be explained by the errors occurred in the assumptions taken for the thickness and rheological properties of LL, optimized by Sliper simulations. As explained earlier, concrete flow conditions are significantly different through the Sliper and pipelines, especially for highly flowable concrete mixtures. This can lead to different LL characteristics in sliper and concrete pipes. More precise simulation of concrete pipe flow is thus required to consider the realistic concrete flow conditions for more accurate evaluation of LL characteristics.

In this study, a new viscosity model, namely tri-viscous model, was proposed to consider the radial variation of rheological properties of concrete in different flow zones across the pipe section, including plug flow, sheared BC, and LL zones. The proposed tri-viscous model was employed to

numerically simulate the pipe flow of different highly flowable mixtures, including 18 SCC and 4 HWC mixtures through a large-scale pumping circuit. The numerical models were validated using the experimental measurements of pressure loss carried out at the Université de Sherbrooke in Canada [3] and reported by Feys et al. [4] for different flow rates and pipe diameters. The results of the numerical simulations determined using new two-fluids and variable viscosity single fluid (tri-viscous) approaches are presented in terms of rheological properties and thickness of formed LL and plug zone. The simulated LL characteristics are compared to those obtained using a coaxial tribometer. The coupled effect of rheological properties of plug flow, BC, and LL, as well as flow rate magnitude and pipe diameter on pumpability of highly flowable mixtures are then evaluated using the numerical results.

4.3 Numerical simulation of concrete pipe flow

4.3.1 Pumping circuit

Khatib [3] carried out a comprehensive full-scale pumping investigation at the Université de Sherbrooke (Canada). Various concrete mixtures were pumped using a 30-m long loop circuit. As shown in Fig. 4.2, the main components of the circuit included two 11-m long straight horizontal pipes with two different diameters of 100 and 125 mm, as well as a 180° bend. At the end of the 125-mm straight pipe section, the circuit was completed by some horizontal and vertical segments to allow the discharge of the pumped concrete back to the pump's reservoir, located at 1.5-m superior elevation. The circuit was equipped with a piston-pump with a maximum discharge rate and pressure limit of 90 m3/h and 6000 kPa, respectively This complementary segment was used for sampling, calibration, and flow rate measurement purposes.

The horizontal straight pipes were instrumented with strain gauges near their beginning and end (spanning distance of 10 m), as shown in Fig. 4.2, to measure the pressure loss under same flow rate magnitude in pipes with different diameters. The concrete mixtures were pumped at four to six 30-min intervals, namely pumping test cycles. In each test cycle, the pumping flow rate decreased from its highest to minimum possible value at different steps for a given mixture depending on flowability. A detailed description of the pumping circuit, instrumentation, and calibration procedures is available in Ref. [3,4].

4.3.2 Concrete properties

In total pumpability of 25 high strength concrete mixtures, including 3 CVC, 4 HWC, and 18 SCC was investigated [3,4]. In the present study, the pumpability of only the HWC and SCC mixtures are numerically investigated (i.e., 22 mixtures). The main mixture design parameters included the initial slump flow, binder combination, water-to-binder ratio (w/b), paste volume, and sand-to-total aggregate ratio. Accordingly, the investigated HWC and SCC mixtures were proportioned with binder content of 558 to 681 kg/m3, w/b ranged between 0.23 and 0.35, and sand-to-total aggregate ratio of 0.47 to 0.54. The workability, rheological, and tribological properties of the investigated samples, taken from each test cycle, were measured using the slump flow, coaxial rheometer, and tribometer set-ups, respectively.
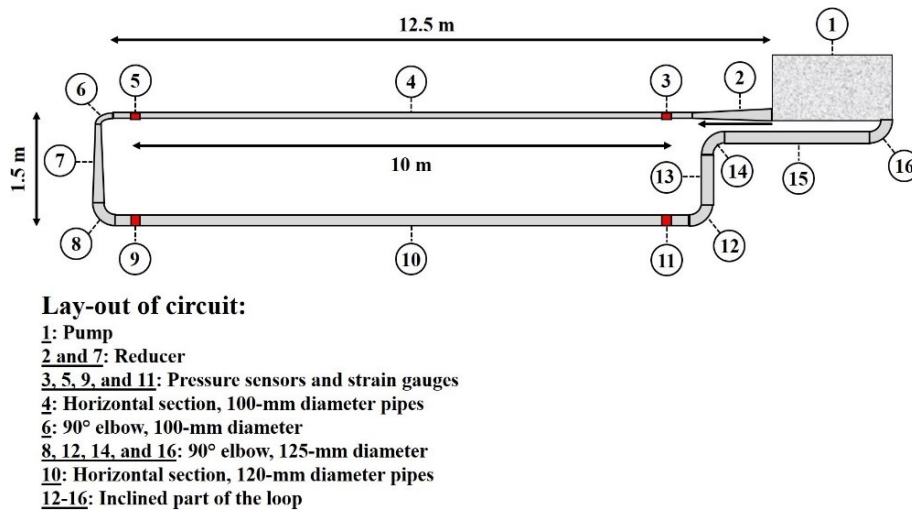
Fig. 4.2. Schematic of the used loop circuit for pumping tests, adapted from [3,4].

An ICAR coaxial rheometer was used for rheological measurements. The rotating inner cylinder consisted in a four-blade vane measuring 63.5-mm radius and 127-mm height. In order to avoid slippage, the outer cylinder was equipped with 15 ribs located at 143-mm distance to the container center. The shearing protocol consisted in 20-s pre-shearing at 0.6 rps speed followed by seven 5-s stepwise decrements from 0.6 to 0.03 rps. It is worthy to mention that the maximum rotational velocity of 0.6 rps corresponds to an approximately shear rate of 10 s-1 near the inner cylinder [4]. On the other hand, a coaxial interface rheometer, called tribometer, was employed to evaluate the viscous constant and yield stress of the lubrication layer of the investigated mixtures [3,4,33]. The tribometer consisted of a smooth rotating inner cylinder with 62.5-mm radius and 200 mm height

along with an inversed-cone shaped at the bottom, as well as an outer cylindrical container with 118.5 mm radius [33]. The shearing protocol of the tribological tests consisted of a 30-s pre-shearing of 0.9 rps rotational velocity of the inner cylinder, followed by ten 5-s stepwise decrements rotational velocity from 0.9 to 0.01 rps. In order to evaluate the tribological properties of the investigated mixtures after each test cycle, the corrections regarding the plug flow and sheared-concrete zones within the tribometer's gap was also considered [3,4]. This was carried out using the rheological values of the investigated mixtures. The yield stress ($\tau_{0\text{-LL}}$) and viscous constant (η_{LL}) of the lubrication layer, formed in the tribometer set-up, were obtained by the intercept and slope of the linear correlation of shear stress values at the inner cylinder of tribometer to their corresponding linear velocity gradient (LVGLL) over the unknown thickness of the LL (Eq. (4.10)). It is worth mentioning that the LVGLL values were calculated using the total rotational velocity over the entire gap of the tribometer minus the contribution of sheared-concrete zone.

$$\tau = \tau_{0\text{-LL}} + \eta_{LL} \times \text{LVG}_{LL} \tag{4.10}$$

It was reported by Khatib [3] and Feys et al. [4] that ICAR rheometer resulted in larger yield stress and significantly lower plastic viscosity values compared to those measured by ConTec 5 coaxial rheometer. It was revealed that application of rheological properties obtained by ICAR rheometer can sometimes lead to physically impossible rheological values. For instance, lower viscosity values obtained in ICAR led to an overestimation of the theoretical rotational velocity in the BC. This resulted then in a rotational velocity in the LL in the opposite direction of the inner cylinder. Accordingly, the rheological properties obtained from the ICAR rheometer were transformed to estimated values obtained using the ConTec 5 rheometer, using a supplementary experimental study that correlated the results of the ICAR and ConTec 5 set-ups [52,53]. The rheological and tribological properties of the investigated mixtures evaluated for the samples taken from each pumping test cycle are presented in Table 4.1.

Table 4.1. Fresh density, rheological, and tribological properties of the investigated mixtures [3,4].

Mix		Test 1	Test 2	Test 3	Test 4	Test 5	Test 6
HWC1	ρ (kg/m^3)	2373	2391	2367	2381	-	-
	$\tau_{0\text{-}C}$ (Pa)	188	146	330	518	-	-
	$\mu_{p\text{-}C}$ (Pa.s)	99	96	92	89	-	-
	$\tau_{0\text{-}LL}$ (Pa)	59	76	89	151	-	-
	η_{LL} (Pa.s.m^{-1})	2591	3549	2572	2563	-	-
HWC2	ρ (kg/m^3)	2347	2374	2370	2369	-	-
	$\tau_{0\text{-}C}$ (Pa)	99	119	128	239	-	-
	$\mu_{p\text{-}C}$ (Pa.s)	86	89	87	99	-	-
	$\tau_{0\text{-}LL}$ (Pa)	38	96	89	88	-	-
	η_{LL} (Pa.s.m^{-1})	2682	3377	3396	2979	-	-
HWC3	ρ (kg/m^3)	2360	2364	2373	2359	2363	-
	$\tau_{0\text{-}C}$ (Pa)	121	169	213	358	838	-
	$\mu_{p\text{-}C}$ (Pa.s)	56	55	65	59	56	-
	$\tau_{0\text{-}LL}$ (Pa)	4	73	83	67	129	-
	η_{LL} (Pa.s.m^{-1})	2117	1689	1464	2674	2680	-
HWC4	ρ (kg/m^3)	2340	2361	2362	2372	2359	-
	$\tau_{0\text{-}C}$ (Pa)	52	48	69	64	79	-
	$\mu_{p\text{-}C}$ (Pa.s)	62	62	60	57	57	-
	$\tau_{0\text{-}LL}$ (Pa)	44	77	65	54	62	-
	η_{LL} (Pa.s.m^{-1})	2607	1603	1576	2627	2007	-
SCC1	ρ (kg/m^3)	2424	2434	2435	2401	2380	-
	$\tau_{0\text{-}C}$ (Pa)	35	40	29	45	35	-
	$\mu_{p\text{-}C}$ (Pa.s)	52	47	47	50	58	-
	$\tau_{0\text{-}LL}$ (Pa)	29	20	29	13	72	-
	η_{LL} (Pa.s.m^{-1})	2223	1714	1778	2023	2577	-
SCC2	ρ (kg/m^3)	2404	2398	2423	2343	2306	-
	$\tau_{0\text{-}C}$ (Pa)	37	35	30	86	381	-
	$\mu_{p\text{-}C}$ (Pa.s)	40	39	40	44	50	-
	$\tau_{0\text{-}LL}$ (Pa)	0	46	51	76	105	-
	η_{LL} (Pa.s.m^{-1})	1860	1627	1632	1729	3001	-
SCC3	ρ (kg/m^3)	2377	2370	2340	2384	-	-
	$\tau_{0\text{-}C}$ (Pa)	23	48	92	138	-	-
	$\mu_{p\text{-}C}$ (Pa.s)	37	35	40	40	-	-
	$\tau_{0\text{-}LL}$ (Pa)	18	51	39	69	-	-
	η_{LL} (Pa.s.m^{-1})	1844	2058	1451	2399	-	-
SCC4	ρ (kg/m^3)	2397	2438	2412	2442	2430	-
	$\tau_{0\text{-}C}$ (Pa)	59	32	48	68	47	-
	$\mu_{p\text{-}C}$ (Pa.s)	52	43	39	37	36	-
	$\tau_{0\text{-}LL}$ (Pa)	39	38	24	31	16	-
	η_{LL} (Pa.s.m^{-1})	1754	1570	1611	1388	2167	-
SCC5	ρ (kg/m^3)	2359	2367	2348	2307	2372	-
	$\tau_{0\text{-}C}$ (Pa)	27	20	15	11	10	-
	$\mu_{p\text{-}C}$ (Pa.s)	33	30	27	27	26	-
	$\tau_{0\text{-}LL}$ (Pa)	0	4	4	11	0	-
	η_{LL} (Pa.s.m^{-1})	700	381	402	414	995	-
SCC7	ρ (kg/m^3)	2407	2444	2395	2465	-	-
	$\tau_{0\text{-}C}$ (Pa)	84	66	89	80	-	-
	$\mu_{p\text{-}C}$ (Pa.s)	76	63	62	69	-	-
	$\tau_{0\text{-}LL}$ (Pa)	19	49	35	49	-	-
	η_{LL} (Pa.s.m^{-1})	2330	2723	2567	1720	-	-
	$\tau_{0\text{-}LL}$ (Pa)	120	231	254	301	291	-
	η_{LL} (Pa.s.m^{-1})	5365	7893	6668	6983	6003	-

Chapter 4. Novel tri-viscous model to simulate pumping of flowable concrete through characterization of lubrication layer and plug zones

104

Table 4.1. Continued

	ρ (kg/m^3)	2451	2442	2371	2436	2424	-
	τ_{0-C} (Pa)	46	38	37	40	40	-
SCC8	μ_{p-C} (Pa.s)	55	63	61	59	57	-
	τ_{0-LL} (Pa)	0	9	17	24	52	-
	η_{LL} (Pa.s.m^{-1})	2463	2027	1847	1776	2525	-
	ρ (kg/m^3)	2355	2350	2374	2387	-	-
	τ_{0-C} (Pa)	38	28	19	19	-	-
SCC9	μ_{p-C} (Pa.s)	29	29	27	27	-	-
	τ_{0-LL} (Pa)	18	7	7	18	-	-
	η_{LL} (Pa.s.m^{-1})	490	240	252	326	-	-
	ρ (kg/m^3)	2255	2255	2265	2357	-	-
	τ_{0-C} (Pa)	41	49	41	54	-	-
SCC10	μ_{p-C} (Pa.s)	50	43	43	46	-	-
	τ_{0-LL} (Pa)	24	2	4	18	-	-
	η_{LL} (Pa.s.m^{-1})	1247	1372	1427	1334	-	-
	ρ (kg/m^3)	2335	2348	2335	2327	2325	-
	τ_{0-C} (Pa)	31	34	28	76	107	-
SCC11	μ_{p-C} (Pa.s)	33	30	31	35	46	-
	τ_{0-LL} (Pa)	6	9	13	27	54	-
	η_{LL} (Pa.s.m^{-1})	948	1279	1299	1024	3395	-
	ρ (kg/m^3)	2343	2338	2354	2315	-	-
	τ_{0-C} (Pa)	90	120	255	652	-	-
SCC12	μ_{p-C} (Pa.s)	83	97	102	104	-	-
	τ_{0-LL} (Pa)	70	121	93	171	-	-
	η_{LL} (Pa.s.m^{-1})	3714	4366	3279	2901	-	-
	ρ (kg/m^3)	2215	2256	2247	2258	2288	
	τ_{0-C} (Pa)	37	38	36	56	52	-
SCC13	μ_{p-C} (Pa.s)	46	40	41	39	41	-
	τ_{0-LL} (Pa)	17	37	37	24	26	-
	η_{LL} (Pa.s.m^{-1})	1424	1084	1083	729	1207	-
	ρ (kg/m^3)	2282	2279	2308	2315	-	-
	τ_{0-C} (Pa)	25	27	20	19	-	-
SCC14	μ_{p-C} (Pa.s)	38	28	29	32	-	-
	τ_{0-LL} (Pa)	37	19	21	10	-	-
	η_{LL} (Pa.s.m^{-1})	629	531	536	431	-	-
	ρ (kg/m^3)	2361	2345	2371	2357	2358	-
	τ_{0-C} (Pa)	64	53	59	46	73	-
SCC15	μ_{p-C} (Pa.s)	57	49	48	48	46	-
	τ_{0-LL} (Pa)	23	14	11	54	29	-
	η_{LL} (Pa.s.m^{-1})	1543	1720	1713	1767	1368	-
	ρ (kg/m^3)	2346	2369	2386	2383	2365	-
	τ_{0-C} (Pa)	51	47	53	67	99	-
SCC16	μ_{p-C} (Pa.s)	59	49	61	54	55	-
	τ_{0-LL} (Pa)	1	36	38	8	42	-
	η_{LL} (Pa.s.m^{-1})	2652	1913	1635	2118	1415	-
	ρ (kg/m^3)	2363	2366	2377	2373	2363	
	τ_{0-C} (Pa)	30	25	41	48	58	-
SCC17	μ_{p-C} (Pa.s)	48	41	43	50	42	-
	τ_{0-LL} (Pa)	12	49	34	24	8	-
	η_{LL} (Pa.s.m^{-1})	1360	1539	1424	1484	2051	-

Chapter 4. Novel tri-viscous model to simulate pumping of flowable concrete through characterization of lubrication layer and plug zones

105

Table 4.1. Continued

	ρ (kg/m^3)	2414	2411	2407	2389	2391	2391
	$\tau_{0\text{-C}}$ (Pa)	48	54	59	81	84	165
SCC18	$\mu_{p\text{-C}}$ (Pa.s)	65	65	67	73	69	88
	$\tau_{0\text{-LL}}$ (Pa)	11	39	35	17	11	37
	η_{LL} (Pa.s.m^{-1})	2493	2456	2386	1728	1940	2753
	ρ (kg/m^3)	2419	2420	2425	2398	2424	-
	$\tau_{0\text{-C}}$ (Pa)	84	91	138	138	476	-
SCC19	$\mu_{p\text{-C}}$ (Pa.s)	149	129	145	164	192	-
	$\tau_{0\text{-LL}}$ (Pa)	120	231	254	301	291	-
	η_{LL} (Pa.s.m^{-1})	5365	7893	6668	6983	6003	-

As explained earlier, each of the investigated mixtures underwent 4 to 6 pumping tests, each included descending flow rates from its maximum to minimum possible values. For each pumping test, the maximum and minimum pressure loss values per unit length (Δp: kPa/m) corresponding to the maximum and minimum flow rates (Q: l/s), respectively, measured at both 100- and 125-mm diameter pipes are summarized in Table 4.2.

Table 4.2. Maximum and minimum pressure loss (Δp: kPa/m) values and flow rates (Q: l/s) for each concrete in D_P = 100- and 125-mm diameter pipes and different pumping test cycles (1-6) [3,4].

Mix	D_P (mm)	Flow rate level	Test 1	Test 2	Test 3	Test 4	Test 5	Test 6
HWC1	100	Max (Δp-Q)	115-9.2	143-11.4	154-13.7	150-13.0	-	-
		Min (Δp-Q)	24.6-1.4	24.8-1.4	25.9-1.4	29.6-1.3	-	-
	125	Max (Δp-Q)	83.8-12.6	73.2-11.4	81.4-13.7	74.7-13.0	-	-
		Min (Δp-Q)	8.0-1.4	10.6-1.4	7.4-1.4	5.8-1.3	-	-
HWC2	100	Max (Δp-Q)	119-10.4	131-11.9	125-12.3	122-12.0	-	-
		Min (Δp-Q)	20.4-1.4	21.7-1.4	22.2-1.4	24.9-1.4	-	-
	125	Max (Δp-Q)	48.9-10.4	57.8-11.9	53.2-12.3	55.4-12.0	-	-
		Min (Δp-Q)	3.9-1.4	4.2-1.4	4.0-1.4	5.1-1.4	-	-
HWC3	100	Max (Δp-Q)	92.0-10.2	125-14.1	102-13.0	91.9-11.8	125-14.4	-
		Min (Δp-Q)	16.5-1.4	16.8-1.4	16.9-1.3	20.1-1.3	67.6-1.3	-
	125	Max (Δp-Q)	34.2-10.2	48.7-14.1	36.7-13.0	32.3-11.8	46.8-14.1	-
		Min (Δp-Q)	3.8-1.4	4.4-1.4	5.3-1.3	6.5-1.3	8.8-1.3	-
HWC4	100	Max (Δp-Q)	80.6-8.8	111-14.0	92.5-13.8	91.3-14.2	91.2-14.6	-
		Min (Δp-Q)	20.3-1.5	17.3-1.5	17.8-1.8	14.5-1.3	15.2-1.3	-
	125	Max (Δp-Q)	48.3-12.1	50.4-15.1	48.3-15.4	40.4-14.2	41.3-14.6	-
		Min (Δp-Q)	6.7-1.5	5.7-1.5	5.9-1.8	4.8-1.3	5.0-1.3	-
SCC1	100	Max (Δp-Q)	79.8-13.1	97.8-15.3	83.0-15.3	77.2-14.4	81.6-14.8	-
		Min (Δp-Q)	23.0-3.1	22.7-3.1	19.8-3.5	20.5-3.8	21.6-3.6	-
	125	Max (Δp-Q)	44.3-13.1	51.6-15.3	40.8-15.3	38.9-14.4	42.6-14.8	-
		Min (Δp-Q)	11.4-3.1	10.1-3.1	9.6-3.5	10.9-3.8	10.9-3.6	-
SCC2	100	Max (Δp-Q)	45.5-10.9	42.1-10.7	46.9-12.8	41.2-10.6	49.4-10.6	-
		Min (Δp-Q)	20.7-4.6	19.8-4.9	19.3-4.9	19.0-3.9	26.0-3.1	-
	125	Max (Δp-Q)	23.8-12.2	25.1-13.3	20.2-12.8	23.8-13.2	29.0-13.1	-
		Min (Δp-Q)	8.2-4.6	8.6-4.9	7.7-4.9	7.8-3.9	12.1-3.1	-
SCC3	100	Max (Δp-Q)	51.9-11.3	47.4-11.6	46.5-12.1	47.0-11.6	-	-
		Min (Δp-Q)	20.0-4.0	19.5-4.6	19.1-4.4	19.6-3.3	-	-
	125	Max (Δp-Q)	27.5-13.7	21.0-12.8	19.2-13.5	21.0-13.9	-	-
		Min (Δp-Q)	7.3-4.0	6.9-4.6	7.2-4.4	7.7-3.3	-	-

Chapter 4. Novel tri-viscous model to simulate pumping of flowable
concrete through characterization of lubrication layer and plug zones

106

Table 4.2. Continued

SCC4	100	Max (Δp-Q)	69.7-12.1	57.4-11.9	49.6-12.2	43.6-11.7	43.4-11.8	-
		Min (Δp-Q)	19.4-3.7	15.3-3.1	15.2-3.8	13.4-3.4	13.2-3.3	-
	125	Max (Δp-Q)	40.6-12.1	36.0-11.9	32.9-13.2	25.9-11.7	30.8-13.1	-
		Min (Δp-Q)	12.9-3.7	10.3-3.1	10.3-3.8	8.9-3.4	9.3-3.3	-
SCC5	100	Max (Δp-Q)	31.0-11.9	29.4-12.9	25.6-13.5	22.8-12.7	22.4-12.7	-
		Min (Δp-Q)	11.5-4.8	11.5-5.5	13.4-5.8	10.7-5.9	10.7-6.0	-
	125	Max (Δp-Q)	19.8-11.9	20.9-14.1	19.5-14.5	17.4-13.9	15.2-12.7	-
		Min (Δp-Q)	7.6-4.8	7.1-5.5	7.4-5.8	7.0-5.9	7.4-6.0	-
SCC7	100	Max (Δp-Q)	121-12.0	99.4-9.9	113-11.9	110-11.5	-	-
		Min (Δp-Q)	24.8-2.2	22.2-1.9	21.5-2.0	19.8-1.8	-	-
	125	Max (Δp-Q)	48.0-12.0	38.0-9.9	44.4-11.9	45.6-11.5	-	-
		Min (Δp-Q)	8.7-2.2	8.0-1.9	8.0-2.0	8.0-1.8	-	-
SCC8	100	Max (Δp-Q)	105-10.2	74.1-8.1	109-12.0	97.9-11.2	97.2-11.1	-
		Min (Δp-Q)	21.1-2.1	22.2-2.3	21.6-2.5	21.0-2.4	20.4-2.3	-
	125	Max (Δp-Q)	41.7-10.2	27.3-8.1	40.7-12.0	38.2-11.2	39.6-11.1	-
		Min (Δp-Q)	8.4-2.1	8.4-2.3	7.8-2.5	8.0-2.4	8.4-2.3	-
SCC9	100	Max (Δp-Q)	26.8-12.4	27.4-13.8	33.6-16.1	31.9-15.9	-	-
		Min (Δp-Q)	10.8-5.6	10.5-6.0	11.2-6.2	10.5-6.1	-	-
	125	Max (Δp-Q)	12.6-14.1	11.8-13.8	11.4-15.1	11.6-15.9	-	-
		Min (Δp-Q)	5.1-5.6	5.4-6.0	5.3-6.2	5.4-6.1	-	-
SCC10	100	Max (Δp-Q)	67.9-11.4	77.4-14.9	75.8-15.5	72.4-14.9	-	-
		Min (Δp-Q)	16.1-2.3	11.1-1.4	11.5-1.5	10.9-1.4	-	-
	125	Max (Δp-Q)	38.5-11.4	44.7-14.9	44.9-15.5	43.3-14.9	-	-
		Min (Δp-Q)	8.1-2.3	6.1-1.4	6.2-1.5	6.2-1.4	-	-
SCC11	100	Max (Δp-Q)	51.9-12.0	49.7-12.4	40.9-10.9	44.8-11.6	48.3-11.4	-
		Min (Δp-Q)	7.6-1.4	7.6-1.4	7.3-1.4	7.6-1.3	10.4-1.2	-
	125	Max (Δp-Q)	25.8-12.0	29.9-13.7	22.2-12.1	24.5-11.6	27.7-11.4	-
		Min (Δp-Q)	4.1-1.4	4.0-1.4	3.6-1.4	4.7-1.3	5.7-1.2	-
SCC12	100	Max (Δp-Q)	96.9-9.7	112-10.3	116-11.0	145-12.2	-	-
		Min (Δp-Q)	16.8-1.4	19.5-1.4	21.7-1.3	29.3-1.3	-	-
	125	Max (Δp-Q)	57.5-11.8	53.3-10.3	62.4-12.3	69.0-12.2	-	-
		Min (Δp-Q)	8.7-1.4	9.4-1.4	10.9-1.3	15.2-1.3	-	-
SCC13	100	Max (Δp-Q)	94.6-13.3	65.2-11.7	70.8-13.5	69.7-14.1	68.1-14.4	-
		Min (Δp-Q)	12.1-1.6	11.1-1.8	10.8-1.8	9.9-1.9	10.6-1.7	-
	125	Max (Δp-Q)	39.5-13.3	31.8-12.8	29.6-13.5	29.3-14.1	31.4-14.4	-
		Min (Δp-Q)	16.4-6.4	4.4-1.8	4.7-1.8	2.5-1.9	3.9-1.7	-
SCC14	100	Max (Δp-Q)	46.7-13.2	42.8-14.2	48.0-16.4	42.4-15.3	-	-
		Min (Δp-Q)	13.0-3.0	12.0-3.3	11.2-3.3	12.3-3.4	-	-
	125	Max (Δp-Q)	-	-	-	-	-	-
		Min (Δp-Q)	-	-	-	-	-	-
SCC15	100	Max (Δp-Q)	61.7-10.8	84.5-14.5	77.5-14.3	71.7-14.2	65.9-14.7	-
		Min (Δp-Q)	10.1-1.4	9.9-1.4	10.2-1.4	9.5-1.4	9.9-1.5	-
	125	Max (Δp-Q)	56.5-14.3	50.2-14.5	42.6-14.3	42.4-14.2	40.2-14.7	-
		Min (Δp-Q)	6.8-1.4	6.5-1.4	6.0-1.4	6.6-1.4	6.6-1.5	-
SCC16	100	Max (Δp-Q)	80.1-11.2	78.3-12.2	81.1-12.9	88.2-14.2	87.8-14.6	-
		Min (Δp-Q)	13.0-1.7	10.6-1.4	10.3-1.4	10.2-1.4	10.5-1.4	-
	125	Max (Δp-Q)	55.9-13.5	40.6-12.2	45.0-14.3	37.1-14.2	45.7-14.6	-
		Min (Δp-Q)	7.5-1.7	6.0-1.4	6.5-1.4	5.9-1.4	4.9-1.4	-

Chapter 4. Novel tri-viscous model to simulate pumping of flowable
concrete through characterization of lubrication layer and plug zones

107

Table 4.2. Continued

Mix	D_P (mm)	Flow rate level	Test 1	Test 2	Test 3	Test 4	Test 5	Test 6
SCC17	100	Max (Δp-Q)	60.9-10.7	64.1-11.8	71.9-13.6	59.8-12.1	76.2-14.6	-
		Min (Δp-Q)	9.4-1.6	9.5-1.5	9.8-1.5	10.1-1.5	10.9-1.5	-
	125	Max (Δp-Q)	30.4-10.7	38.1-14.0	35.4-14.9	31.3-13.4	32.3-14.6	-
		Min (Δp-Q)	4.7-1.6	5.0-1.5	5.1-1.5	5.3-1.5	5.5-1.5	-
SCC18	100	Max (Δp-Q)	88.3-9.4	80.0-10.5	99.9-13.7	92.3-13.0	93.6-13.0	96.7-13.1
		Min (Δp-Q)	16.4-1.5	13.7-1.4	14.0-1.5	14.0-1.4	15.3-1.4	17.5-1.4
	125	Max (Δp-Q)	44.6-11.2	32.4-10.5	36.4-13.7	35.4-13.0	35.5-13.0	36.4-13.1
		Min (Δp-Q)	5.2-1.5	5.0-1.4	5.4-1.5	6.0-1.4	5.9-1.4	7.0-1.4
SCC19	100	Max (Δp-Q)	220-9.5	209-9.7	193-9.9	202-9.7	223-9.6	-
		Min (Δp-Q)	33.8-1.4	34.3-1.4	33.8-1.3	37.4-1.3	47.6-1.3	-
	125	Max (Δp-Q)	96.2-9.5	94.8-9.7	93.6-9.9	96.1-9.7	106-9.6	-
		Min (Δp-Q)	10.9-1.4	12.9-1.4	14.7-1.3	17.0-1.3	23.0-1.3	-

4.4 New two-fluids and variable-viscosity single fluid (tri-viscous) approaches to simulate the pipe flow of the investigated mixtures

In this section, the computational fluid dynamic (CFD) method is applied to estimate the pressure loss values of the pumped investigated mixtures presented earlier. The inputs of the CFD models include the rheological characteristics of the LL and BC, experimentally measured at different pumping cycle times (Table 4.1). The concrete is simulated as homogeneous material (i.e., without taking into account the particles); however, the influence of LL was considered. This was applied as initial inputs in the simulation. As explained earlier, due to formation of LL, two non-Newtonian (Bingham) regions with different rheological properties appear in the pipe: one corresponding to the surrounding LL and another one is the bulk flow with higher viscosity and yield stress values. In the simulation set-up, two different methodologies are developed based on two-fluid and single-fluid approaches to model viscosity behavior of concrete, which is explained in detail in the following sections. By applying these proposed methodologies, not only three different regions, including plug flow, sheared concrete, and LL, can be distinguishable in the velocity profile of simulated model, but also the thickness and rheological properties of the LL and plug radius can be evaluated.

According to the rheological properties of the investigated mixtures, pipe diameter, and applied flow rates, the Reynolds number (Re = $\rho.V.D_P/\mu_{p-C}$) in the pumping circuit is less than 10. On the other hand, the hydrodynamic entry length ($L_{e-Laminar}$ = $0.05.Re.D_P$) is less than 0.04. Therefore,

the concrete pipe flow was considered as a laminar and fully developed flow type. The simulation of pressure loss, which is constant along the length of the pipeline, can be carried out in two dimensions using 1-m length pipe sections in order to reduce calculation time.

The numerical CFD simulations were carried out using OpenFOAM software [54]. OpenFOAM is an object-oriented and open source software developed using C++ language, which benefits from a set of precompiled libraries, provided as the source code. It allows users to conveniently customize their library and create their own model. Therefore, in addition to being computational-cost benefit, the time of the users for coding is saved. Powerful libraries and solvers of OpenFOAM are available to facilitate solve CFD problems [55]. The behavior of pumping concrete can be modelled by choosing proper solver and viscosity models in OpenFOAM. Since none of the existing viscosity models in OpenFOAM can correctly take into account the behavior of concrete in pipes, two new different viscosity models were developed and added to OpenFOAM's libraries. This includes two-fluids and single fluid flow models. By implementing the developed viscosity models, the effect of LL and plug flow zones on the concrete pumping pressure can be predicted.

4.4.1 *Two-fluids (Double-Bingham) approach*

In the first approach, two different phases were considered corresponding to the BC and the LL. The rheological behavior of each phase was described using the Bingham model. In order to develop the two-fluids model, the interFoam, as one of the standard solvers of OpenFOAM for two incompressible and isothermal immiscible fluids, was employed [56]. Two immiscible fluids were separated by introducing a parameter α, namely the volume fraction, which is further explained in the following sections.

4.4.1.1 *Governing equation of interFoam*

InterFoam solves the transport phase and Navier-Stokes equations using PISO (Pressure-Implicit with Splitting of Operators) algorithm for pressure-velocity coupling and applying volume of fluid (VOF) method to model the interface between two incompressible and isothermal immiscible fluids. InterFoam uses the FVM method to solve the problems [56-60]. Employing FVM, the geometry is discretized in the first step to finite volumes. This method transforms the partial differential equations into discrete algebraic equations over finite volumes. By integrating the

Chapter 4. Novel tri-viscous model to simulate pumping of flowable
concrete through characterization of lubrication layer and plug zones

109

extracted differential equations over the discretized elements, they are transformed into algebraic equations. The Governing equations for interFoam solver are considered, as follow [56-59].

Continuity equation: $\nabla. u = 0$ (4.11)

Transport phase equation (interface): $\frac{\partial \alpha}{\partial t} + \nabla.(u\alpha) = 0$ (4.12)

Momentum equation: $\frac{\partial(\rho u)}{\partial t} + \nabla.(\rho uu) = -\nabla p + \nabla.T + f_\sigma$ (4.13)

where u is velocity. Moreover, α represents the volume fraction which equals 1 in the region of first phase, 0 in the region of the second phase, and between 0 and 1 in the interface region (Table 4.3).

Table 4.3. Variation of volume fraction parameter (α) with different phases

Phase	Volumetric fraction parameter (α)
Fluid 1	$\alpha = 1$
Interface between two fluids	$0 < \alpha < 1$
Fluid 2	$\alpha = 1$

The stress tensor T has two components, including turbulent and viscous stresses. The surface tension force f_σ can be obtained using Eq. (4.14). The pressure can be decomposed into two terms, including hydrostatic and dynamic pressures, as presented in Eq. (4.15).

$f_\sigma = \sigma k_c \nabla\alpha$, where $k_c = -\nabla.(\frac{\nabla\alpha}{|\nabla\alpha|})$ (4.34)

$P_d = P - \rho gx$ (4.15)

where g and x are gravitational acceleration and position vectors, respectively. Density and viscosity are calculated according to the volume fraction of each phase, as shown in Eqs. (16) and (17):

$\rho = \alpha\rho_1 + (1 - \alpha)\rho_2$ (4.16)

$\mu = \alpha\mu_1 + (1 - \alpha)\mu_2$ (4.17)

where σ and k_c are surface tension constant and curvature, respectively. By substituting Eqs. (4.14-4.17) to Eq. (4.13), the following Eq. (4.18) can be obtained [59]:

*Chapter 4. Novel tri-viscous model to simulate pumping of flowable
concrete through characterization of lubrication layer and plug zones*

110

$$\frac{\partial(\rho u)}{\partial t} + \nabla.\left(\rho uu\right) = -\nabla p_d + \nabla.T - \rho g.x + \sigma k_c \nabla \alpha \tag{4.48}$$

Tracking of interfaces between phases are usually one of the critical challenges to solve multiphase problems. For this purpose, VOF method [60] is used in the interFoam solver [61]. To avoid numerical smearing of the interface, an interfacial compression flux term is added to the equation. The VOF method captures the interface, by which the surface cannot be tracked as by the techniques based on the interface tracking methods, the position of the surface is estimated by a phase fraction function. This method assumes that a continuous velocity field prevails along all the interfaces. This complies with the interface boundary conditions in the physics of fluids which means that the relative velocity between two phases is zero. In VOF method, additional transport equation Eq. (4.12) is added which is solved simultaneously with Navier-Stokes equation to obtain the volume fraction of one phase at each time step. This transport equation is only solved in the interface region where there is a gradient in the phase fraction, as presented in Table 4.3. The volume fraction α varies between 0 and 1 at the interface between two phases [61], while the volume fraction is either zero or one in the region of each phase.

Since pressure term does not exist in the continuity equation, a suitable approach should be implemented to solve the coupling between pressure and velocity. As mentioned earlier, applying the PISO algorithm, pressure-velocity coupling is solved in interFoam. This method is written based on the predictor and corrector steps. Accordingly, the pressure and flux at previous iteration are used to approximate velocity field in the momentum equation, which is called momentum predictor. Then, the pressure is calculated based on the predicted velocity. Next, the new flux value is obtained using the calculated pressure. At the corrector stage, the velocity field is corrected based on updated pressure and flux. Further discussions about PISO algorithm are available in Ref. [62].

At the first step, initial value and boundary conditions are set up for variables. Then the solver starts to investigate the variables at new time step using their values at the pervious time step. Subsequently, the predicted value of velocity is calculated based on the momentum predictor stage. The PISO loop continues until the tolerance for pressure-velocity system is satisfied for a given level of precision. At this point, the updated values for velocity and pressure, as well as

conservative fluxes at new time step are obtained. According to the updated values, all other equations in the system are solved [62].

4.4.1.2 Discretized geometry and initial and boundary conditions

The 2-D geometries of two-phase model of concrete flow in 100- and 125-m diameter and 1-m length pipes were made in OpenFOAM. The domain was discretized in two mesh blocks, corresponding to the BC and LL. As can be observed in Fig. 4.3a, the width of the mesh block corresponding to the LL was selected as an initial thickness assumption of LL. It is worthy to mention that applying transient solver (i.e., interFoam) makes changes in the thickness of LL by time. Therefore, the initial thickness should be less than 2 mm to reach about 2-mm thickness in the steady state. Simulating different cases, it was revealed that an initial thickness of around 0.5 mm enables us to achieve appropriate results. The initial values of α was then fixed to each mesh block to divide the region in two domains corresponding to the volume fraction of each phase in each domain.

The boundary conditions for velocity were selected as the fixed value at the inlet and zero-gradient at outlet for both BC and LL phases. On the other hand, the boundary conditions for pressure were zero gradient in inlet and fixed value in outlet for both phases [63]. The no-slip and symmetry boundary conditions were applied for walls and center axis of the pipe, respectively [64,65] (Fig. 4.3b). The boundary conditions for α are similar to the velocity boundary conditions (i.e., fixed value at the inlet and zero-gradient in outlet).

Chapter 4. Novel tri-viscous model to simulate pumping of flowable
concrete through characterization of lubrication layer and plug zones

112

(a)

(b)
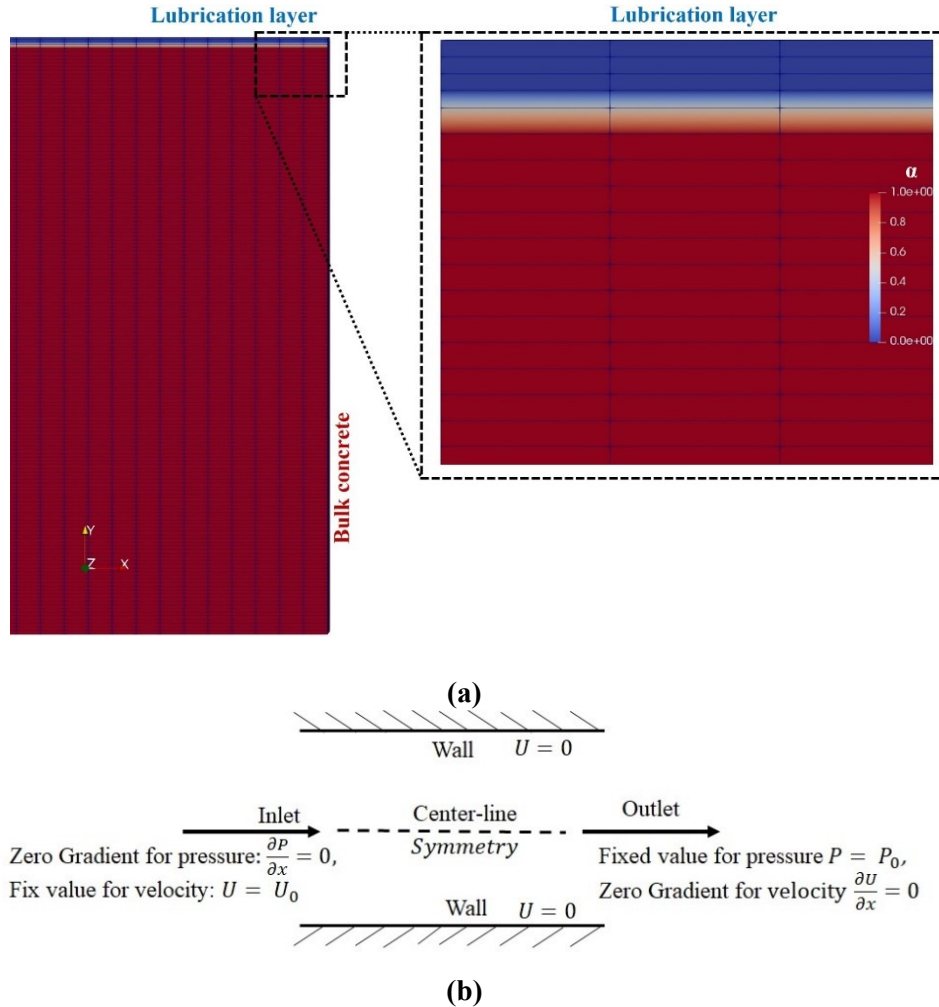
Fig. 4.3. (a) Pipe modelling and **(b)** boundary conditions for numerical simulations.

4.4.1.3 Discretized geometry and initial and boundary conditions

In total, five different viscosity models are available in OpenFOAM V6 to describe the rheological behavior of modelled fluids, including Bird-Carreau, Cross-Power Law, Hershel-Bulkley, Power-Law, and Newtonian models. The interFoam solver enables us to consider two different rheological models for both employed phases. In the two-phases approach, the Herschel-Bulkley (H-B) model was employed to describe the flow behavior of BC and LL. The H-B model consists in a power-law relationship between the shear stress τ and shear rate $\dot{\gamma}$, where τ_0 is yield stress, k is consistency factor, and n is pseudoplasticity index, as follows:

$$\tau = \tau_0 + k \times \dot{\gamma}^n \tag{4.59}$$

For sole of simplicity, by considering n = 1, Eq. (4.19) turns to the Bingham model (Eq. (4.20) and Fig. 4a), which is used in two-fluids approach to simulate the rheological behavior of the BC and LL phases in the interFoam solver.

$$\tau = \tau_0 + \mu_p \times \dot{\gamma} \tag{4.20}$$

where μ_p is the plastic viscosity of the investigated fluid. The apparent viscosity μ_{app} is calculated, as follows:

$$\mu_{app} = \frac{\tau}{\dot{\gamma}} = \frac{\tau_0}{\dot{\gamma}} + \mu_p \tag{4.21}$$

The Bingham fluid can show two different behaviors depending on the value of applied shear stress. When the magnitude of the applied shear stress is lower than the yield stress and deformation of fluid is zero, the apparent viscosity approaches infinity. This part of flow corresponds to the unsheared bulk flow. On the other hand, the material behaves linearly as a Bingham fluid with a plastic viscosity (μ_p) if the magnitude of the applied shear stress is higher than its yield stress. In the numerical modelling, the modeling of unsheared bulk flow causes disconvergencies of the solution because of its infinity apparent viscosity. This problem was solved using the bi-viscous model that consists in combining Newtonian and Bingham models [66].

In order to prevent the aforementioned disconvergency, a critical value of shear rate ($\dot{\gamma}_c$) was defined in the Viscosity-Model class of OpenFOAM. For shear rate values lower than the critical value (i.e., $\dot{\gamma} < \dot{\gamma}_c$), corresponding to the un-sheared zone, the fluid acts like a Newtonian fluid with a relatively high viscosity μ_0, namely the artificial viscosity. Moreover, for shear rate values higher than $\dot{\gamma}_c$ (i.e., $\dot{\gamma} \geq \dot{\gamma}_c$) the flow follows the Bingham model of the investigated fluid (Eq. (20)). Due to the use of two different values of viscosity (μ_0, μ_p) to describe the flow behavior of a Bingham fluid, this model is referred to as the bi-viscous model [66,67], which is schematically presented in Fig. 4.4b.
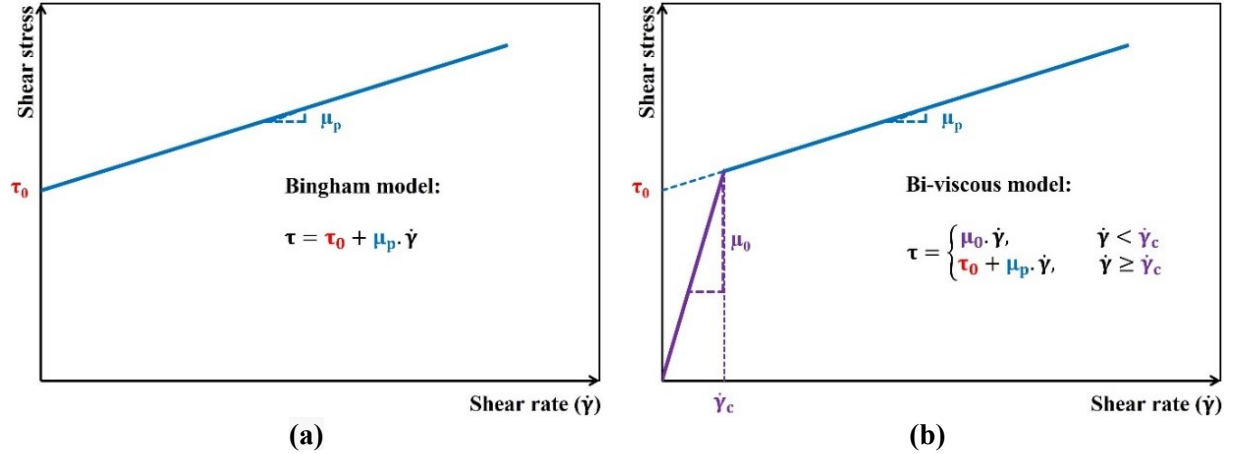
Fig. 4.4. Relationships between shear stress and shear rate values in **(a)** Bingham and **(b)** bi-viscous rheological models, considering the critical shear rate ($\dot{\gamma}_c$) and artificial viscosity (μ_0) values [66,67].

In OpenFOAM, the bi-viscous model is applied using a loop in the whole discretized domain. The loop enables to calculate the apparent viscosity for each cell based on the Eq. (21). The apparent viscosity of each cell is then updated according to the minimum value between the artificial and calculated apparent viscosities, as follows:

$$\mu_{app} = \min(\mu_0, \frac{\tau_0}{\dot{\gamma}} + \mu_p) \tag{4.22}$$

where μ_0 and μ_{app} represent the artificial and updated apparent viscosity values, respectively. Although μ_0 cannot be infinity, it should be large enough to capture the unsheared zone of Bingham fluid. For cells with shear rate lower than $\dot{\gamma}_c$, the magnitude of their calculated apparent viscosities becomes higher than artificial viscosity. Therefore, after the comparison step in the loop, the updated apparent viscosity equals the value of artificial viscosity (i.e., $\mu_{app}(\dot{\gamma} < \dot{\gamma}_c) = \mu_0$). For other values the apparent viscosity can be calculated as $\mu_{app}(\dot{\gamma} \geq \dot{\gamma}_c) = \frac{\tau_0}{\dot{\gamma}} + \mu_p$. Such approach can avoid infinity apparent viscosity values in points which have shear rate lower than the critical value. The value of apparent viscosity for each cell is then updated.

4.4.1.4 Inputs of transport properties

The value for surface tension between two phases σ and rheological properties, including τ_0, μ_0, and μ_p, of each phase should be defined as inputs of the transport file of interFoam solver. It is worthy to mention that the magnitudes and dimensions of parameters in OpenFOAM incompressible solvers, including interFoam, are scaled by the constant density of the investigated

Chapter 4. Novel tri-viscous model to simulate pumping of flowable
concrete through characterization of lubrication layer and plug zones
115

fluid. Therefore, the kinematic plastic and artificial viscosity values ($\upsilon = \mu/\rho$) of the investigated fluids were used in the numerical models. As mentioned earlier, the viscosity of the LL is not directly measured, but its viscous constant η_{LL} was experimentally measured by the tribometer. It means that the plastic viscosity of LL depends on the thickness of the layer which causes a challenge to model it. The plastic viscosity of LL can be estimated indirectly by multiplying its assumed thickness e_{LL} of 2 mm by the viscous constant $\eta_{LL.}$

As shown in the two-fluids model algorithm (Fig. 5), the problem is solved based on a trial-and-error procedure. Accordingly, the simulation error ε is defined, as follows:

$$\varepsilon = \frac{\Delta p_{sim} - \Delta p_{exp}}{\Delta p_{exp}} \times 100\% \qquad (4.23)$$

where Δp_{exp} and Δp_{sim} are the experimental and numerical pressure drops, respectively. As indicated in Fig. 4.5, once the difference between experimental and numerical pressure drops becomes lower than 5%, ($|\varepsilon| < 5\%$), the simulation stops. It is worthy to mention that achieving simulations with physically meaningful results and error less than 5% was not possible for all the cases. In this situation, varying the LL viscosity (υ_{p-LL}), artificial viscosity of LL (υ_{0-LL}) and BC (υ_{0-C}), size of mesh in y direction (N), and initial LL thickness (e_{LL}) was undertaken to obtain physically meaningful results and minimum prediction error ($|\varepsilon|$). Therefore, the final result was chosen based on the lubrication thickness that is able to correctly simulate the pipe flow case. It is important to note that this procedure was done for a total of 404 pipe flow experiments, including 22 investigated concrete mixtures with different rheological properties (Table 4.1), pipe diameters, and under low and high flow rates (Q_{min} and Q_{max}) carried out at 4 to 6 pumping tests (Table 4.2).

Since the interFoam is an unsteady solver, the thickness of LL is increased during the simulation period till the end of simulation to achieve its eventual value e_{LL}. Subsequently, the simulated η_{LL} values, are then calculated by dividing the plastic viscosity values of LL ($\mu_{p-LL} = \upsilon_{p-LL} \times \rho_{LL}$) by simulated thickness e_{LL} and compared to the experimental ones. It is worthy to mention that same density values were assumed for the BC and its corresponding LL, using the experimental data reported in Ref. [3,4].

Knowing the significant influence of the LL characteristics on concrete pumpability, one of the important challenges to model concrete pipe flow is to apply an appropriate viscosity model. The proper viscosity model should capture three different regions in the cross section of pipe, including the plug flow, sheared-bulk flow, and LL. In the two-fluids approach, the three regions can be modeled. Applying interFoam solver with two H-B model in OpenFOAM enabled defining three different regions across the pipe section. The effect of LL on the pressure drop of flow can then be investigated. Also, the result of tribometer was compared with the simulation results and provided useful insight in understanding the LL characteristics. However, implementing of two-phase solver needs more computational time comparing to a single-phase solver. Therefore, a new approach is proposed to simulate the concrete pipe flow using single-fluid approach by adding a new viscosity model in OpenFOAM called tri-viscous model, as discussed below.
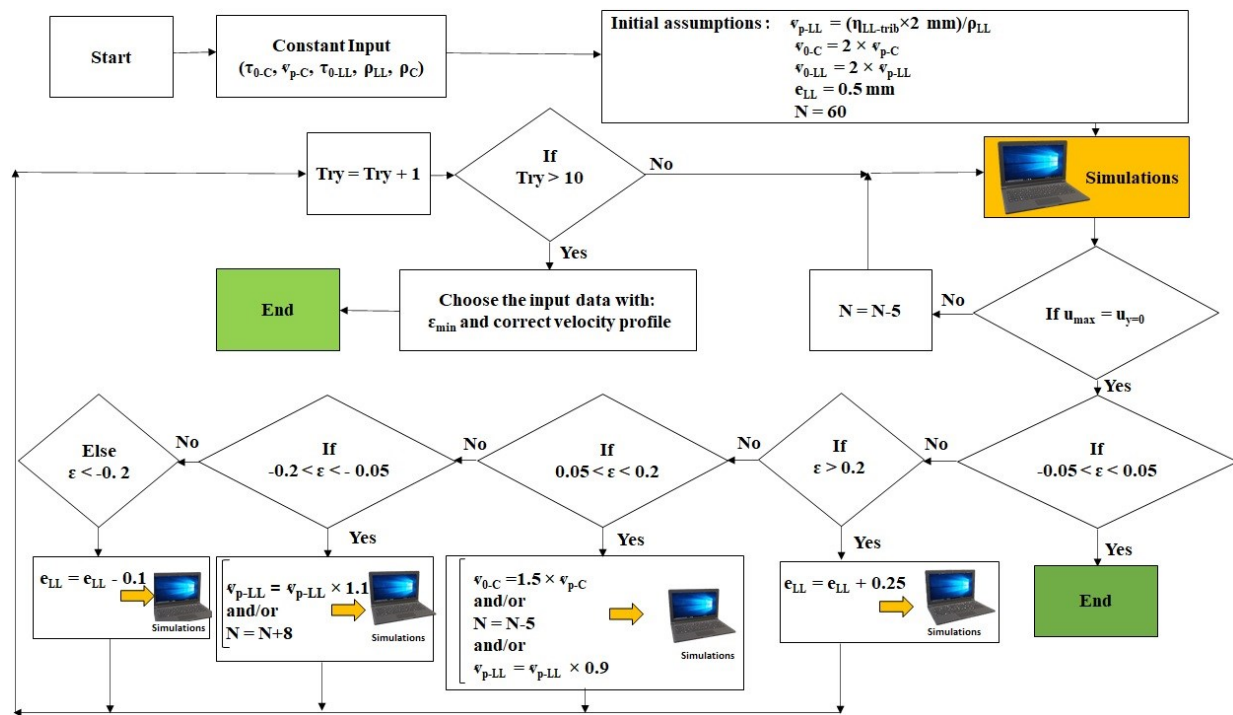
Fig. 4.5. Schematics of the algorithm applied for two-fluids approach (double-Bingham model). (N is the number of mesh rows in y direction).

4.4.2 Numerical simulation of concrete pipe flow using variable-viscosity single-fluid approach (Tri-viscous model)

In this approach, the BC and LL are considered as a single fluid which experiences a laminar and fully developed flow in the pumping circuit with different pipe diameters of 100 and 125 mm, different flow rates, and rheological properties, as summarized in Tables 4.1 and 4.2. In order to model the flow using the single-phase approach, simpleFoam, as a steady-state solver, was employed [63,68,69]. The model solves the Navier-Stokes equations for incompressible fluid, using SIMPLE (Semi-Implicit Method for Pressure Linked Equations) algorithm and the pressure-velocity coupling. In SIMPLE technique, the discretized momentum equations are solved using the initial values of pressure and velocity [68,69]. The variables are corrected using the pressure correction equation and applying the under-relaxation factor. The selection of such factor plays an important role to reach stability and convergency and is defined by the user [63,70].

4.4.2.1 Governing equations

In SimpleFoam, the continuity and momentum equations are solved for one-fluid at steady-state. Due to constant density of incompressible fluids, the continuity and momentum equations are considered, as follow [68]:

Continuity equation: $\nabla . u = 0$ (4.24)

Momentum equation: $\nabla . (uu) = -\frac{1}{\rho}\nabla p + \frac{1}{\rho}\nabla . T$ (4.25)

where u and T represent the velocity and the stress tensor, respectively. The stress tensor is combined of turbulent and viscous stresses. As simpleFoam is made for incompressible fluid, the variables in Navier-Stokes equations, such as viscosity and yield stress, should be divided by fresh density of the investigated mixtures.

4.4.2.2 Boundary conditions

The no-slip and symmetry conditions are considered for the wall and center axis of the pipe, respectively. The inlet boundary conditions for velocity and pressure are fixed values and zero

gradient, respectively [63-65]. On the other hand, for the outlet boundary conditions, a constant value for pressure and zero gradient for velocity were applied (Fig. 4.3).

4.4.2.3   Tri-viscous model

As explained earlier, due to shear-induced particle migration from higher to lower shear-rate zones, a very thin layer of fine mortar, namely LL, is formed in the region close to the higher shear rate zones (vicinity of pipe wall). This can lead to radial variations in the rheological properties of pumped concrete across the pipe's cross section [13,41]. The use of single-fluid approach to simulate this behavior can result in solving a single Navier-Stokes equation, rather than two in the case of two-fluids approach (double-Bingham model). Moreover, there is no need to solve Eq. (4.12) to consider the interaction between the multi-phases using the parameter α. Using single-fluid approach can lead to lower calculation time comparing to two-fluids modeling approach. However, according to the changes in flow properties close to pipe wall, which causes a discontinuity in velocity of fluid at pipe wall interface, the continuity assumption should be checked [71].

In order to consider the presence of LL on concrete pumpability using the single-fluid approach, the developed model should enable to simulate the radial variations of the rheological properties of concrete across a given pipe's cross section. These variations can be considered as functions of the radial distances of each cell (cell's center point) to the center axis (i.e., y coordinate). Taking into account that the 5 existing viscosity models in OpenFOAM are unable to capture the variations in their rheological parameters (i.e., fixed value during simulation), new viscosity model is required to be developed.

In order to develop a new model, a proper criterion should be selected to determine the transition point in the rheological parameters from those of the BC (i.e., τ_{0-C} and μ_{p-C}) to those corresponding to the LL (i.e., τ_{0-LL} and μ_{p-LL}) in a single viscosity model. In this study, a new approach is proposed to consider the variation of the rheological parameters of the modelled fluid as a function of the radial distance to the center axis. A critical distance to the center axis (i.e., $y_{critical}$ coordinate) is thus selected, beyond which the viscosity model follows the rheological properties of the LL (i.e., τ_{0-LL} and μ_{p-LL}). On the other hand, the rheological properties of the cells with $y < y_{critical}$ coordinates correspond to the BC (i.e., τ_{0-C} and μ_{p-C}).

This model is developed based on the H-B viscosity model of OpenFOAM and the criterion corresponded to the geometric position of LL and BC in the pipe. Assuming the LL as a very thin layer with a constant thickness formed near the pipe wall, if the cell center is located at a distance less than the thickness of LL from the wall, the rheological behavior of the fluid in the cell can be governed by the LL properties. On the other hand, the viscosity behavior should follow the BC properties. The concept of this model is schematically presented in Fig. 4.6.

This model predicts the variation of rheological properties of concrete by comparing the vertical distance of each cell's center point (i.e., "y" coordinate) from the centerline of the pipe and the critical distance (i.e., $y_{critical}$ coordinate) which is calculated, as follows:

$$y_{critical} = R - e_{LL} \qquad\qquad\qquad\qquad (4.26)$$

where R and e_{LL} represent the radius of the pipe and thickness of LL, respectively. For example, assuming the formation of 2-mm LL in the 100-mm diameter pipe, the $y_{critical}$ is set to 0.050 - 0.002 = 0.048 m. For each point, the y coordinate is checked, if it is smaller than 0.048 m, the rheological properties of the cell correspond to those of the BC (i.e., τ_{0-C} and μ_{p-C}), otherwise, to the rheological properties of the LL (i.e., τ_{0-LL} and μ_{p-LL}). The loop presented in Fig. 4.6 was thus added to the H-B viscosity class of OpenFOAM to apply the proposed tri-viscous model.
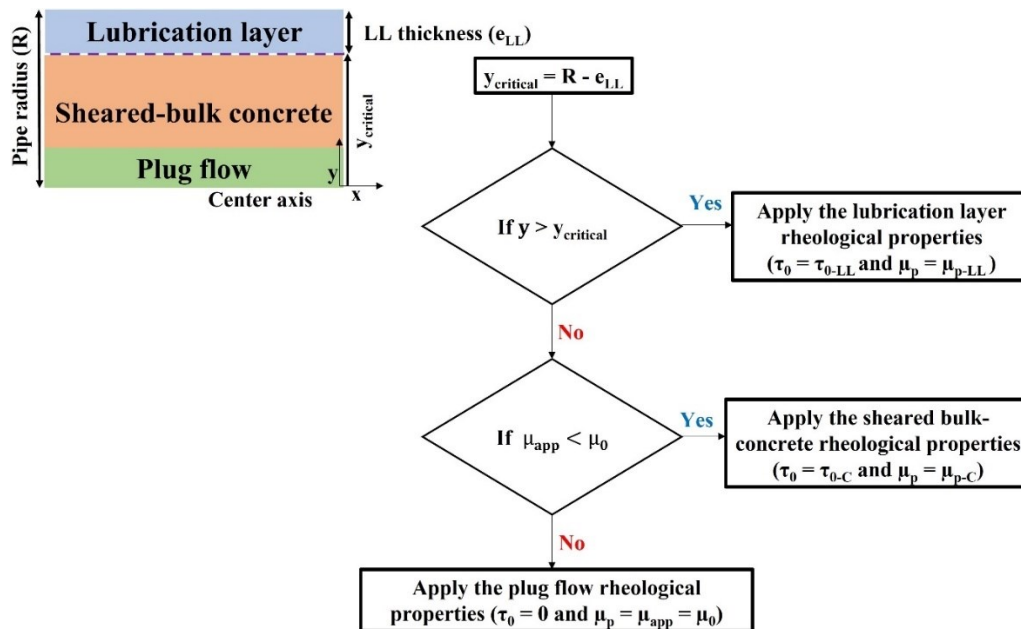
Fig. 4.6. New proposed tri-viscous model, considering the radial variation of the rheological properties of concrete across the pipe section.

Chapter 4. Novel tri-viscous model to simulate pumping of flowable
concrete through characterization of lubrication layer and plug zones

120

4.4.2.4 Inputs of the transport properties file

The transport properties file of this model needs eight input parameters, including n, $\tau_{0\text{-}C}$, $\upsilon_{p\text{-}C}$, $\upsilon_{0\text{-}C}$, $\tau_{0\text{-}LL}$, $\upsilon_{p\text{-}LL}$, $\upsilon_{0\text{-}LL}$, and $y_{critical}$. The term $\upsilon_{0\text{-}C}$ is the artificial viscosity of the unsheared zone, explained in two-fluids approach (double-Bingham model), introduced to solve disconvergence problem resulted from infinity viscosity of unsheared zone. By applying two plastic viscosities of the BC and LL in addition to the artificial viscosity results in this so-called tri-viscous model. The algorithm used to model concrete pipe flow is presented in Fig. 4.7. In this approach, an initial assumption of LL thickness (e_{LL}) is required to calculate the plastic viscosity of the LL based on the tribometer data as well as $y_{critical}$ that depends on e_{LL} and radius of the pipe.
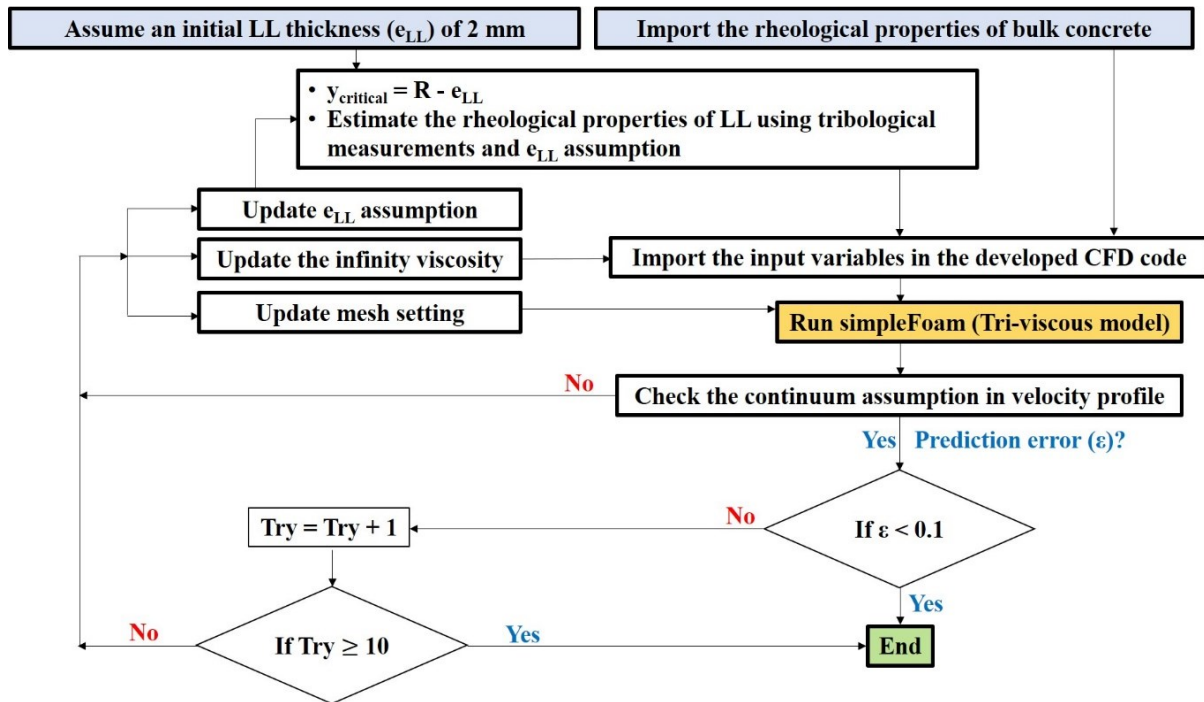
Fig. 4.7. Schematics of algorithm applied for variable-viscosity single-fluid approach (tri-viscous model).

It is worthy to mention that numerical simulations were carried out using an E5-1607 v2 CPU 3.00 GHz processor. The simulations of 1-m long pipelines required a total running time of 69 to 528 s for two-fluids modelling approach and from 3 to 26 s for the single-fluid tri-viscous one. This reveals the high proficiency of the proposed tri-viscous modelling approach to ensure efficient calculation time/cost (more than 20 times lower calculation time) compared to the two-fluids modelling approach. As elaborated earlier, this is due the possibility of solving a single Navier-

Stokes equation in the tri-viscous approach instead of two and the possibility of neglecting interface interaction between the BC and LL compared to the case of double-Bingham approach.

4.5 Results and discussion

The flow of the investigated HWC and SCC mixtures in pipes measuring 1-m length, 100- and 125-mm diameter, under different flow rate magnitudes (Qmin and Qmax in Table 4.2) and at different pumping test cycles were simulated using the two-fluids and tri-viscous models. The total pressure loss per length of the pipe (ΔP/L), velocity, shear rate, and apparent viscosity profiles across the pipe cross section were investigated. Moreover, the final thickness and rheological properties of the LLs, as well as the viscosity and radius of plug flow zones were evaluated for the investigated mixtures using the numerical results. As mentioned earlier, a total of 404 pipe flow experiments were simulated using each approach.

4.5.1 Prediction of pumping pressure-loss (ΔP/L) values

As shown in Fig. 4.8, the predicted pressure drop values using the numerical simulations are comparable to the experimental results reported in the Ref. [3,4]. Both the two-fluids and single-fluid tri-viscous approaches led to excellent prediction of pressure loss of the investigated mixtures that were pumped through different pipe diameters and under different flow rates. The two-fluids model led to slightly higher R2 and lower root-mean squared error (RMSE) values compared to the single-fluid approach. On the other hand, the tri-viscous approach resulted in closer estimation index to unity (i.e., 0.994) than the two-fluids model (estimation index of 0.976). Feys et al. [4] analytically evaluated the pressure loss values using the Kaplan et al. model (Eqs. (1) and (2)) and compared them with the experimental measurements. The analytical results showed an estimation index of 1.08 and R2 of 0.88. Comparing to the results presented in Fig. 4.8, the numerical simulations led to higher accuracy in estimating the pressure loss values than analytical models, reflecting closer estimation indices and R2 to unity, as well as lower RMSE values. This is due to better estimation of the LL characteristics (thickness and plastic viscosity) compared to those measured by a tribometer. Given the high precision of the single-fluid tri-viscous approach and the significant lower calculation time and cost required with this approach, the pumpability of the investigated mixtures are further analyzed using the tri-viscous approach.

Chapter 4. Novel tri-viscous model to simulate pumping of flowable
concrete through characterization of lubrication layer and plug zones

122

(a) Two-fluids model   **(b) Tri-viscous model**
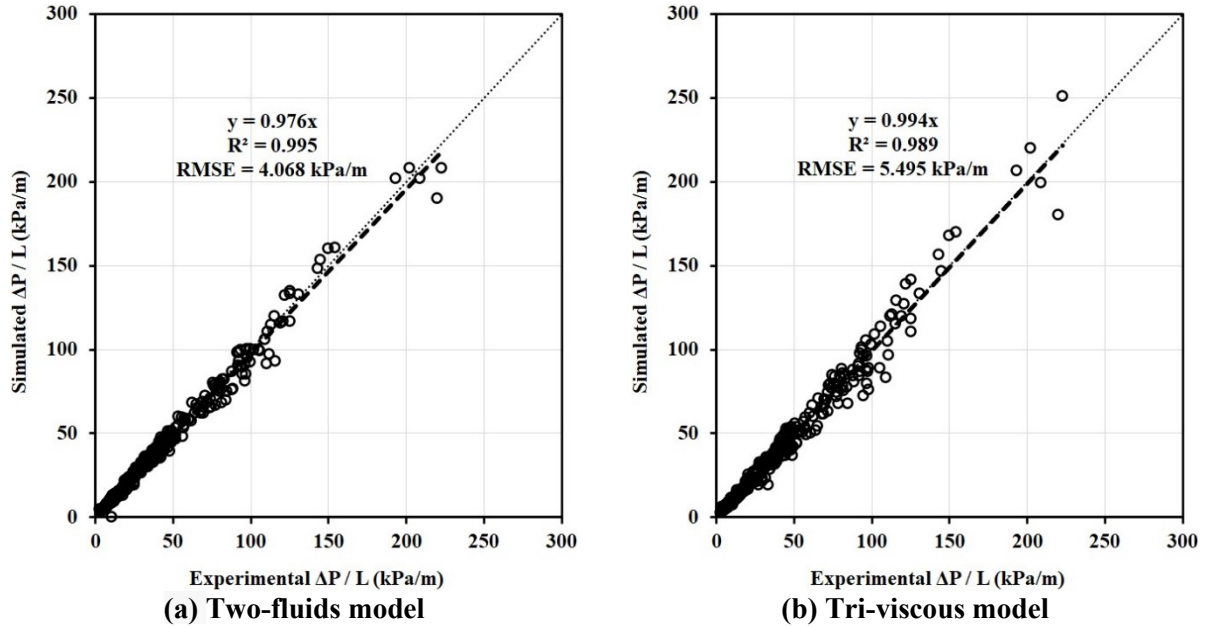
Fig. 4.8. Comparison between the experimental and simulated pressure loss values using (a) two-fluids and (b) single-fluid tri-viscous models.

The prediction of the pressure loss obtained using the tri-viscous approach are presented in Fig. 4.9 for different pipe diameters and flow rates. The results indicate that using the tri-viscous approach led to highly accurate prediction of pressure loss values. Higher R2 and lower RMSE values were obtained for the simulations of 125-mm diameter pipe flow compared to 100-mm ones (Figs. 4.9a and 4.9d). The lower RMSE values can be due to lower pressure values in the larger pipe under a given flow rate (lower velocity). Moreover, closer estimation indices to unity were obtained for maximum flow rates.
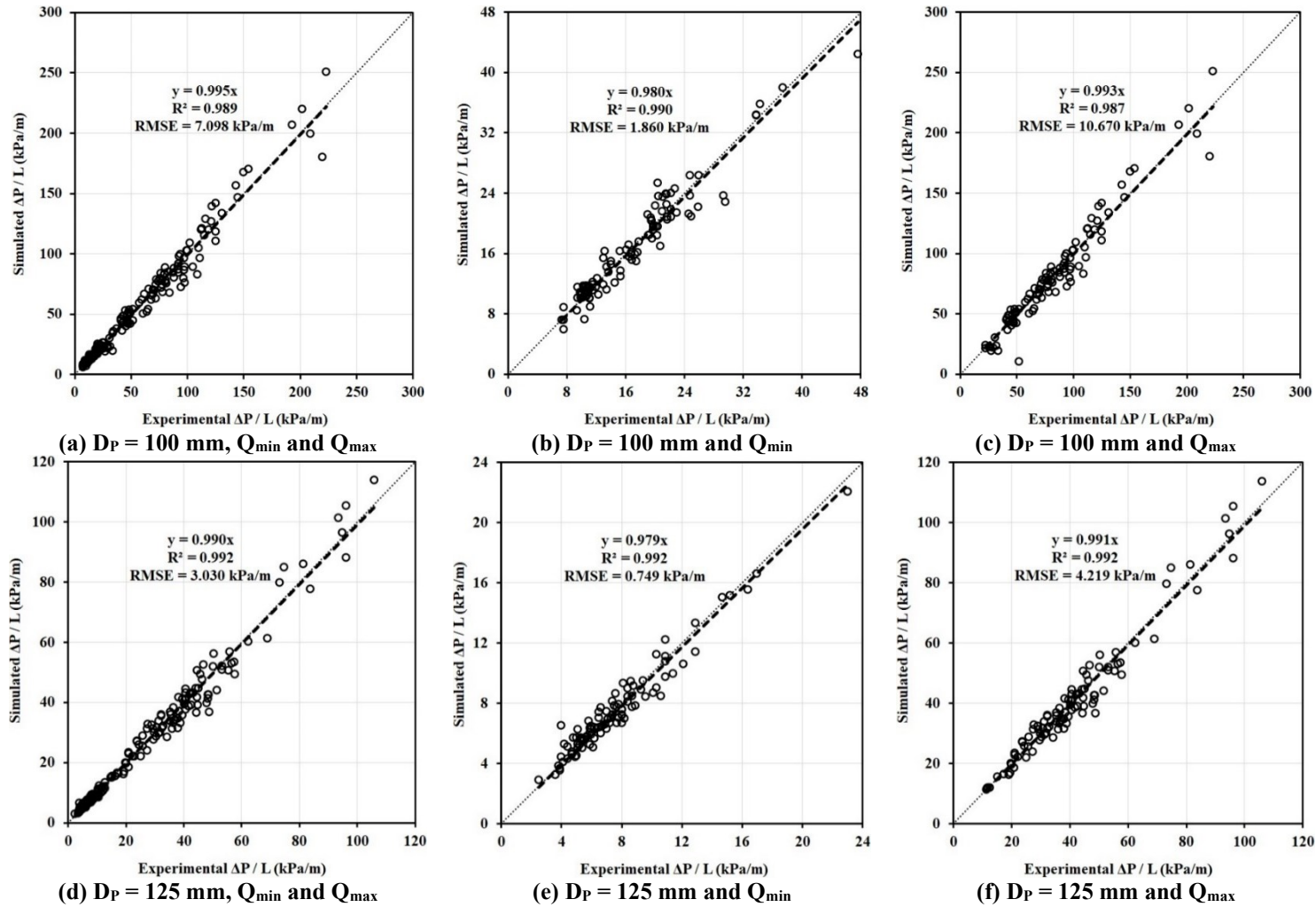
Fig. 4.9. Comparison between the experimental pressure loss values and those obtained using single-fluid tri-viscous model for all flow rate values: **(a)** 100-mm and **(d)** 125-mm diameter pipes, 100-mm diameter pipe: **(b)** minimum and **(c)** maximum flow rates, and 125-mm diameter pipe: **(e)** minimum and **(f)** maximum flow rates.

*Chapter 4. Novel tri-viscous model to simulate pumping of flowable
concrete through characterization of lubrication layer and plug zones*

124

4.5.2 *Characterization of lubrication layer*

The LL thickness was identified using the velocity profiles obtained from tri-viscous simulations (Fig. 10a) across the pipe cross-section. Regarding the lower plastic viscosity of the LL in vicinity of the pipe wall, the velocity profile shows different trends at the LL threshold. As shown in Fig. 10b, the LL radius corresponds to the zone that velocity profile shows significant changes in its derivation relative to the radial distance to the pipe center. Two different trend lines were correlated in the vicinity of the pipe wall to identify the exact radial position of the LL interface with the BC, and consequently LL thickness.
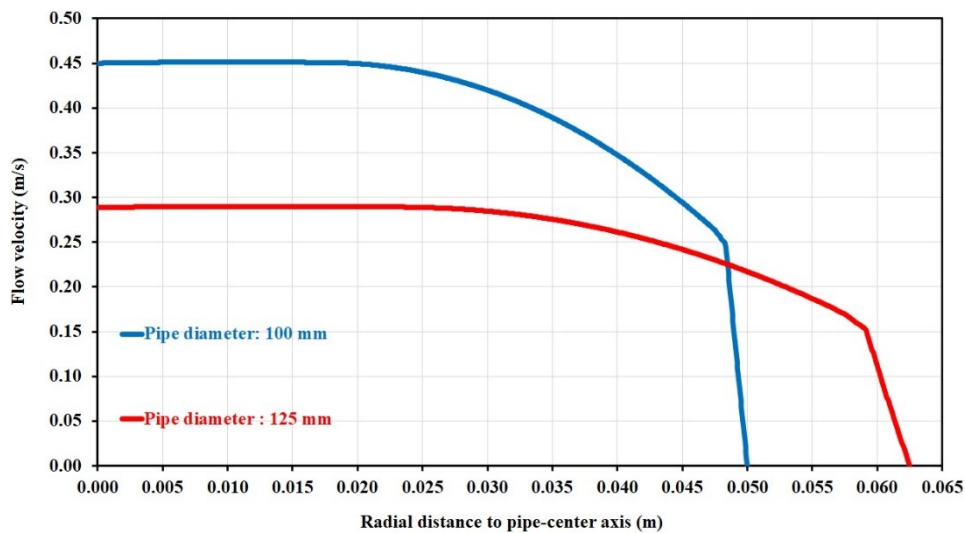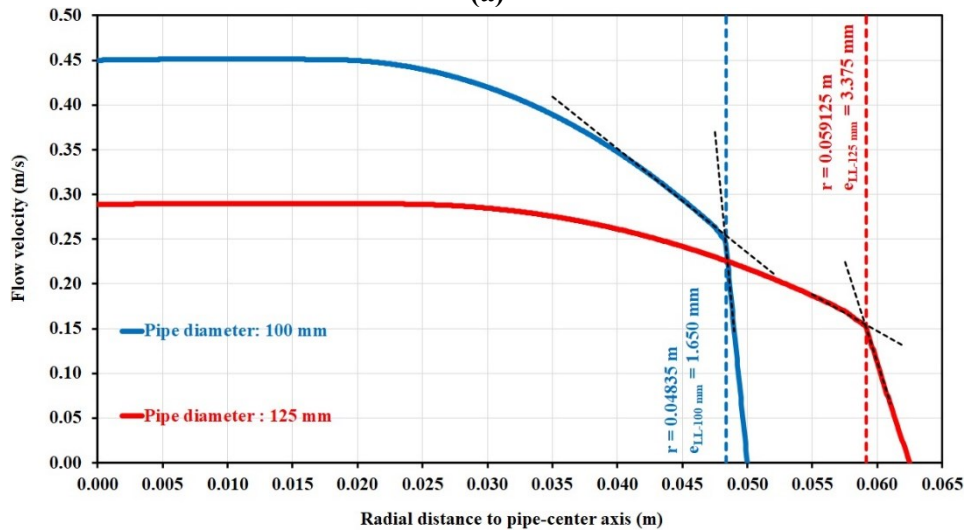
Fig. 4.10. Flow velocity profile across pipe sections with 100- and 125-mm diameters and **(b)** identification of thickness of LL using velocity profile (example for pipe flow of SCC1 at test 1 and minimum flow rate).

Estimating the LL thicknesses and using the viscosity found for the zone corresponding to the LL in the tri-viscous simulations, the simulated η_{LL} values were evaluated for each pumping test. As illustrated in Fig. 4.11, the LL viscous constants obtained using the numerical tri-viscous simulations were compared to the experimental ones measured using the tribometer. As can be observed, the tri-viscous approach led to viscous constants ranging between 0.296 to 2.000 times values compared to tribological results with a root-mean squared difference (RMSD) of 0.566 to 0.929 kPa.s/m. As shown earlier in Figs. 4.8 and 4.9, the use of such optimized η_{LL} led to better estimation of pumping pressure losses of the investigated mixtures compared to the analytical models where the tribometer results were applied.

Moreover, the maximum variation relative to the tribological viscous constants were obtained for 100-mm diameter pipes and maximum flow rate (estimation index up to 2.000). It is also worth mentioning that the minimum ranges of relative viscous constants compared to the tribometer results were obtained for the 125-mm pipes and minimum flow rate (0.296-1.185 times). This can correspond to lower and larger LL thicknesses created at 100- and 125-mm pipes, respectively, compared to those formed in the tribometer. This can be due to higher and lower flow velocity values in the 100- and 125-mm pipes, respectively. Accordingly, the LL thicknesses (e_{LL}) obtained for different pipe diameters and flow rates are compared in Fig. 4.12. As can be observed in Figs. 12a and 12b, under a given flow rate level, increasing the pipe diameter mostly led to form the LLs with larger thicknesses. On the other hand, as shown in Figs. 4.12c and 4.12d, for a given pipe diameter, pumping with a lower flow rate can mostly lead to a larger LL thickness.

Chapter 4. Novel tri-viscous model to simulate pumping of flowable concrete through characterization of lubrication layer and plug zones

126
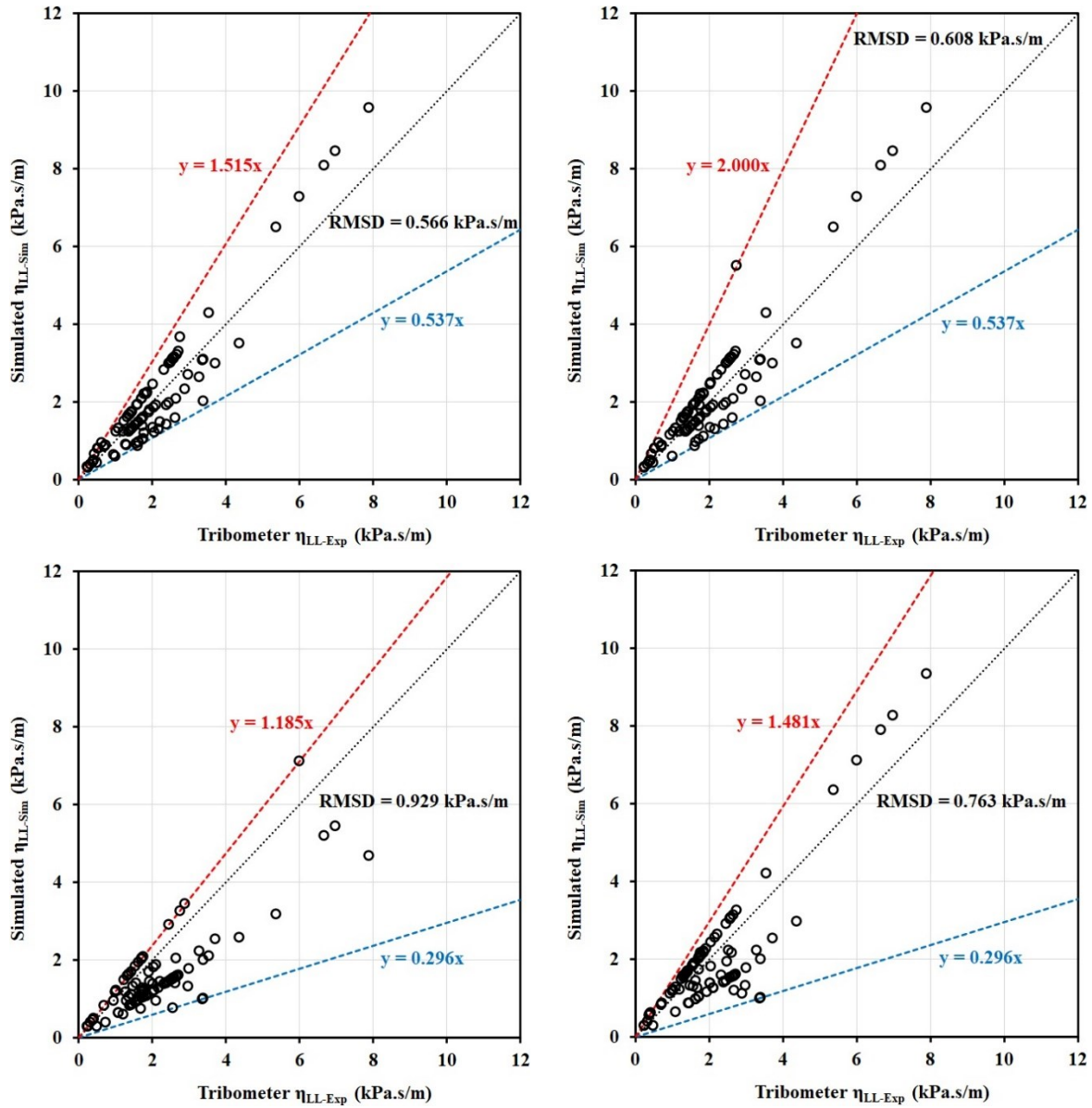
Fig. 4.11. Comparison between viscous constants obtained using the tri-viscous approach ($\eta_{LL\text{-}Sim}$) and experimental tribological measurements ($\eta_{LL\text{-}Exp}$) for 100-mm diameter pipe under **(a)** minimum and **(b)** maximum flow rates, and 125-mm diameter pipe under **(c)** minimum and **(d)** maximum flow rates.

Chapter 4. Novel tri-viscous model to simulate pumping of flowable
concrete through characterization of lubrication layer and plug zones

127
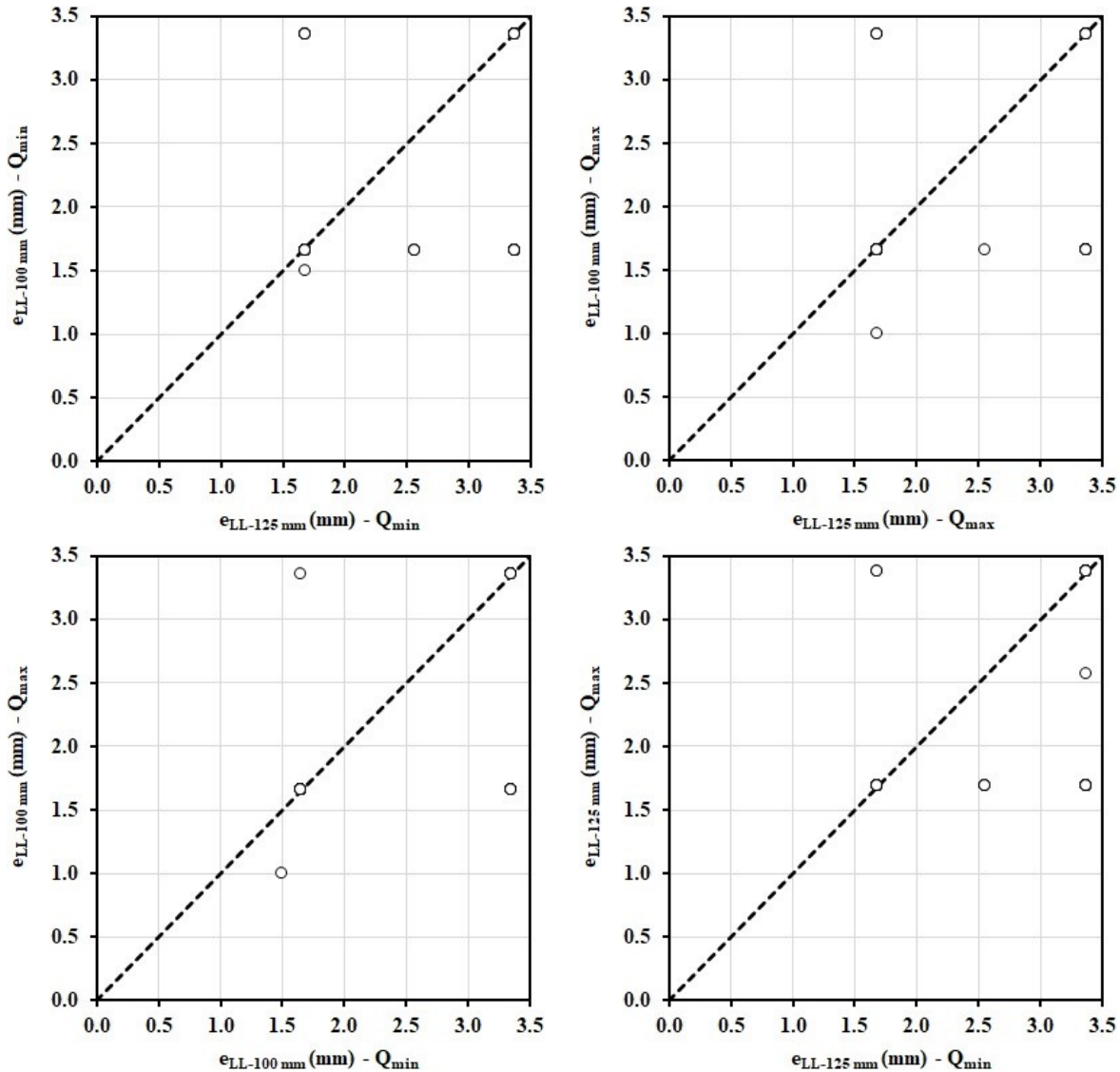
Fig. 4.12. Comparison between the LL thickness (eLL) obtained using the tri-viscous approach for 100- and 125-mm pipes under (a) minimum (Qmin) and (b) maximum (Qmax) flow rates, as well as maximum and minimum flow rates at (c) 100- and (d) 125-mm diameter pipes.

Frequency distribution of the obtained LL thicknesses for different pipe diameters and flow rate magnitudes are presented in Fig. 4.13. As can be observed in Fig. 4.13a, in the case of the minimum flow rates, the majority of the LL thicknesses for 100- and 125-mm diameter pipes ranges between 1.5 to 2 mm (80.2%) and 3 to 3.5 mm (63.3%), respectively. However, increasing the flow rate (maximum flow rates) led to form LL with thicknesses ranging from 1.5 to 2 mm with major frequencies for both 100-mm (85.4%) and 125-mm (63.3%) diameter pipes (Fig. 4.13b). Moreover, as shown in Fig. 4.13c, the LL thicknesses formed in 100-mm diameter pipes had the highest frequency for a thickness of 1.5 to 2 mm for both the minimum (80.2%) and maximum

Chapter 4. Novel tri-viscous model to simulate pumping of flowable
concrete through characterization of lubrication layer and plug zones

128

(85.4%) flow rates. On the other hand, the minimum and maximum flow rates resulted in higher frequencies (63.3%) of LL thicknesses of 3 to 3.5 mm and 1.5 to 2 mm, respectively, in 125-mm diameter pipe (Fig. 4.13d).
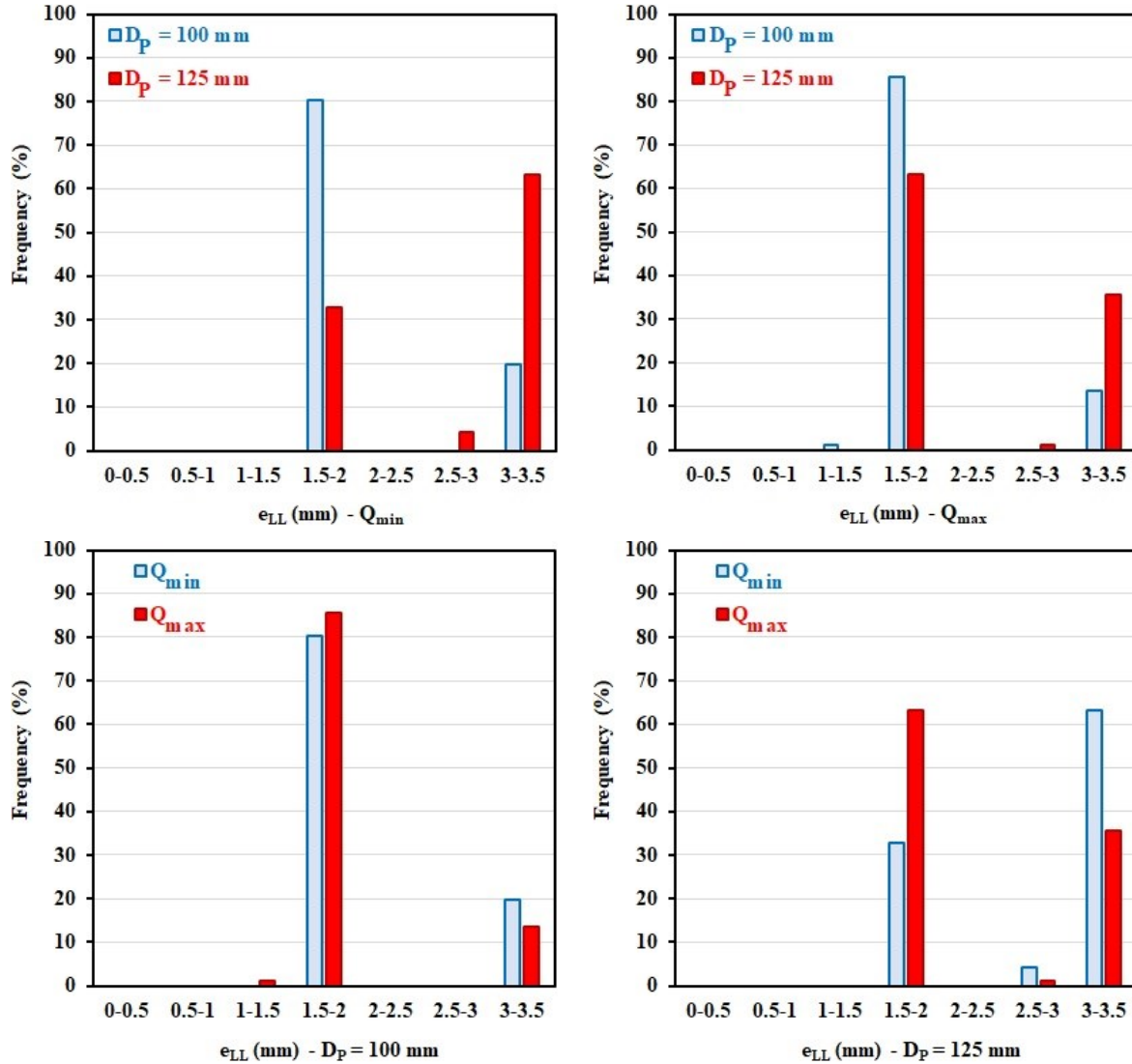
Fig. 4.13. Frequency of the LL thicknesses (e_{LL}) obtained using the tri-viscous approach for 100- and 125-mm diameter pipes under **(a)** minimum (Q_{min}) and **(b)** maximum (Q_{max}) flow rates, as well as maximum and minimum flow rates at **(c)** 100- and **(d)** 125-mm diameter pipes.

4.5.3 *Characterization of plug zone*

In addition to the LL, the plug zone shows different characteristics compared to the BC. As explained earlier, this was considered in the proposed tri-viscous model. Accordingly, the rheological behavior of plug zone is modelled as a Newtonian fluid with relatively higher viscosity

Chapter 4. Novel tri-viscous model to simulate pumping of flowable
concrete through characterization of lubrication layer and plug zones

129

(μ0-Plug) compared to LL and BC zones. Therefore, the apparent viscosity profile across the pipe section must show its maximum value (μ0-Plug) through the plug zone. Accordingly, the apparent viscosity μapp(r) in a radial distance r from the pipe center was calculated in OpenFOAM, as follows:

$$\mu_{app}(r) = \min\left[\mu_{0-Plug}, \mu_p(r) + \frac{\tau_0(r)}{\dot{\gamma}}\right] \tag{4.27}$$

Hence, for very low shear rate values (≈ 0), whereby defined as the plug zone, $\mu_{app}(r)$ equals μ_{0-Plug}. The radii of plug zones of the investigated pumped mixtures were identified using the apparent viscosity profiles across the pipe cross section. As shown in Fig. 4.14, the apparent viscosity radially varies across the pipe. The drop in the apparent viscosity from its maximum value corresponds to the plug flow radius r_{Plug}.

The effect of pipe diameter and flow rate magnitudes on the plug radius are evaluated, as shown in Fig. 4.15. For a given flow rate magnitude, increasing the pipe diameter resulted in larger plug radius. On the other hand, for a given pipe diameter, decreasing flow rate led in greater pipe radius. This can be explained by lower flow velocity, hence inducing lower shear rate in larger pipes. Accordingly, the smallest plug radii up to 24.150 mm were obtained in the case of 100-mm diameter pipe and the maximum flow rates. On the other hand, the largest plug radii up to 58.188 mm were obtained in 125-mm diameter pipe and the minimum flow rates.

Chapter 4. Novel tri-viscous model to simulate pumping of flowable concrete through characterization of lubrication layer and plug zones

130

(a) SCC1: Test 1, Q$_{min}$

(b) SCC1: Test 1, Q$_{max}$
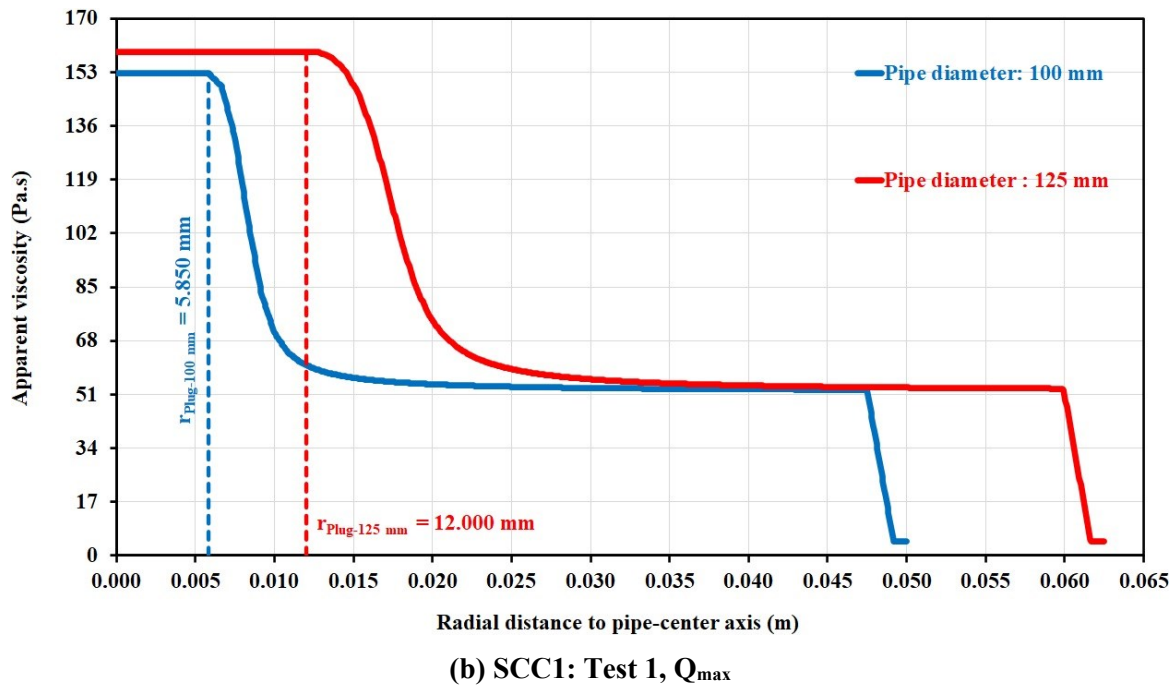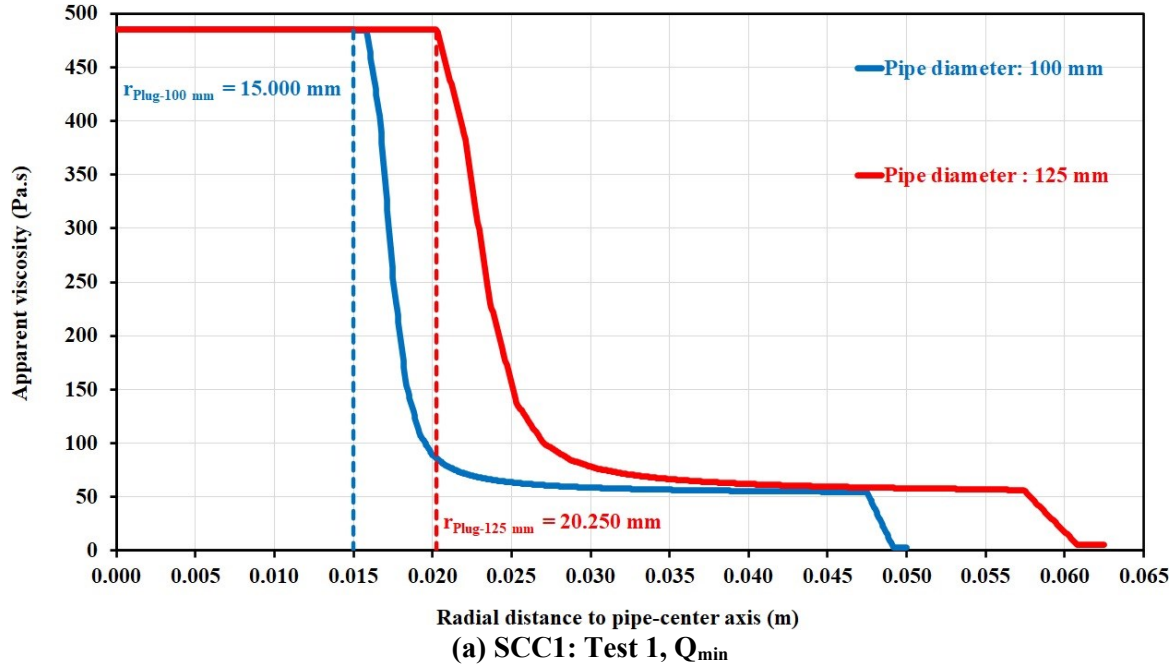
Fig. 4.14. Apparent viscosity profile across pipe sections with 100- and 125-mm diameters and identification of plug radius. An example for pipe flow SCC1 mixture at test 1 and under the **(a)** minimum and **(b)** maximum flow rates.

Chapter 4. Novel tri-viscous model to simulate pumping of flowable
concrete through characterization of lubrication layer and plug zones

131

(a) Q_{min}: $D_P = 100$ vs. 125 mm

(b) Q_{max}: $D_P = 100$ vs. 125 mm

(c) $D_P = 100$ mm: Q_{max} vs. Q_{min}

(d) $D_P = 125$ mm: Q_{max} vs. Q_{min}
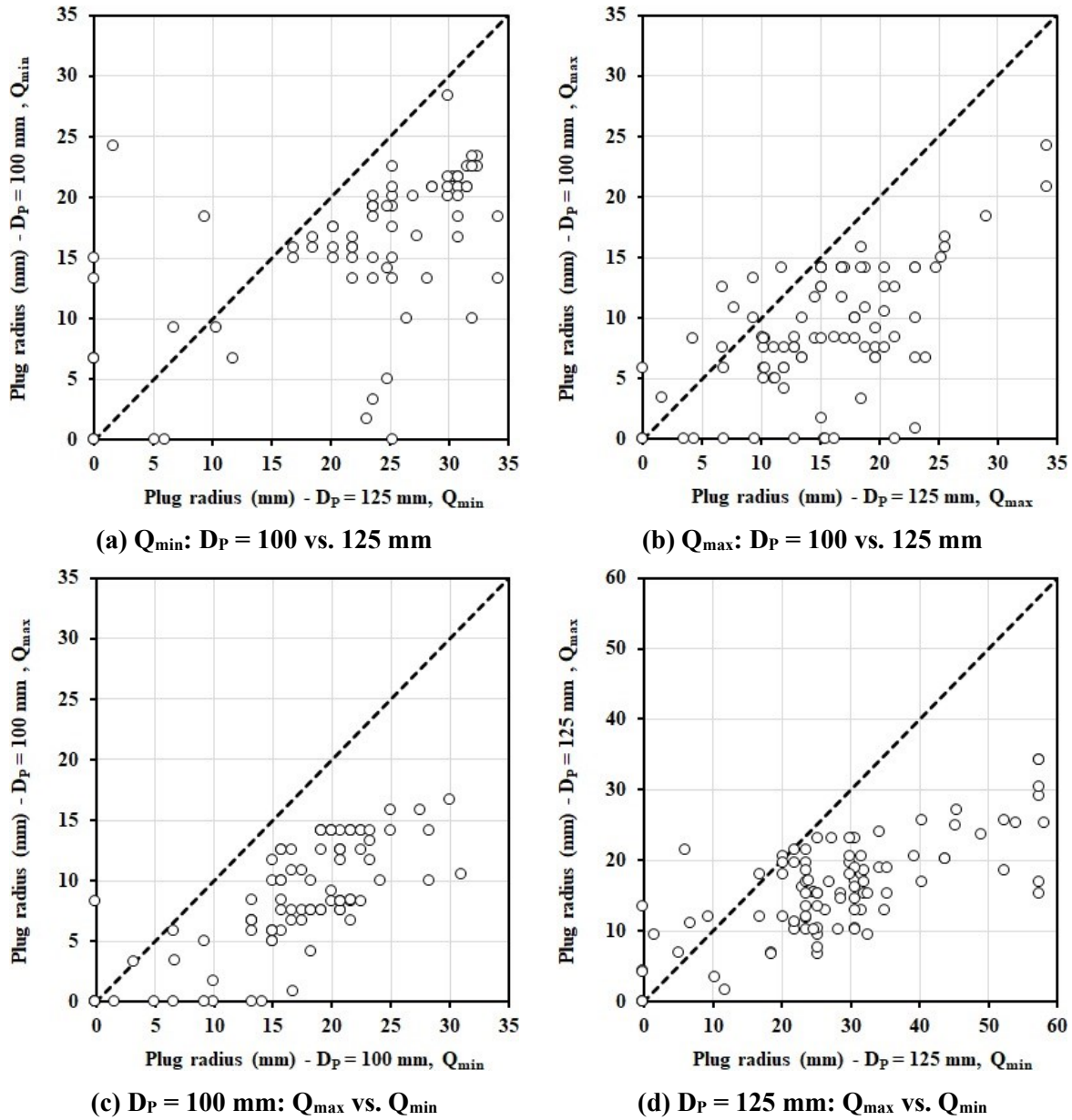
Fig. 4.15. Comparison between the plug radii obtained using the tri-viscous approach for 100- and 125-mm diameter pipes under **(a)** minimum (Q_{min}) and **(b)** maximum (Q_{max}) flow rates, as well as maximum and minimum flow rates in **(c)** 100- and **(d)** 125-mm diameter pipes.

The effect of pipe geometry and flow rate on plug radius can be also revealed by its frequency distribution. As shown in Figs. 4.16a and 16b for the minimum and maximum flow rates, increasing the pipe diameter from 100 to 125 mm increased the plug radius with the maximum frequency from 10-20 mm (45.8%) to 20-30 mm (41.8%) and from 0-10 mm (60.4%) to 10-20 mm (58.2%), respectively. On the other hand, as can be observed in Figs. 4.16c and 4.16d, decreasing the flow rate from its maximum to minimum values resulted in increasing the plug

Chapter 4. Novel tri-viscous model to simulate pumping of flowable
concrete through characterization of lubrication layer and plug zones

132

radius with the maximum frequency from 0-10 mm (60.4%) to 10-20 mm (45.8%) and from 10-20 mm (58.2%) to 20-30 mm (41.8%) created in 100- and 125-mm diameter pipes, respectively. Furthermore, the maximum frequency distributions of 60.4% and 58.2% were obtained for plug radii of 0-10 mm and 10-20 mm for the maximum flow rate values through the 100- and 125-mm diameter pipes, respectively.

(a) Q_{min}: D_P = 100 vs. 125 mm **(b) Q_{max}: D_P = 100 vs. 125 mm**

(c) D_P = 100 mm: Q_{max} vs. Q_{min} **(d) D_P = 125 mm: Q_{max} vs. Q_{min}**
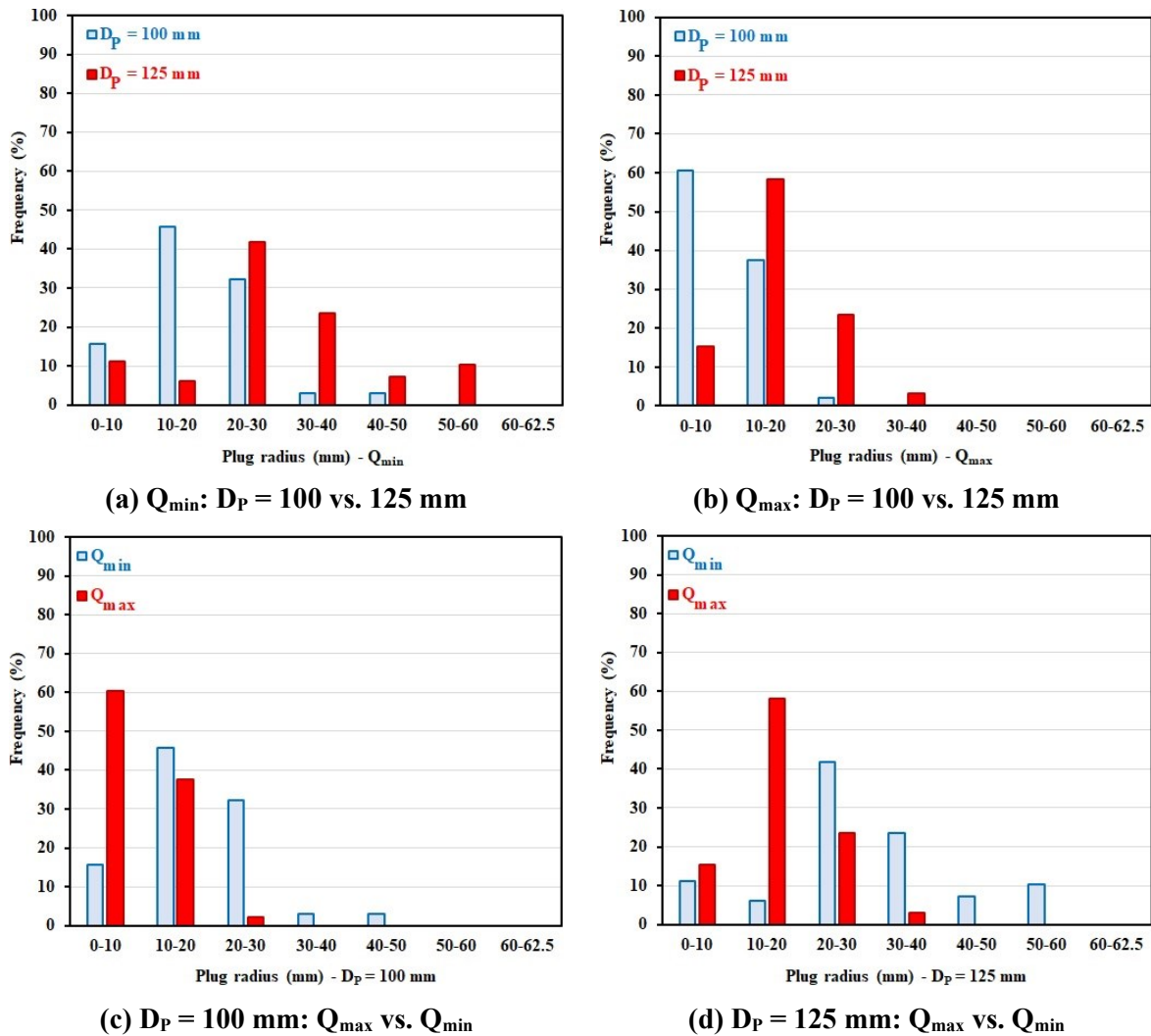
Fig. 4.16. Frequency of the plug radii (r_{Plug}) obtained using the tri-viscous approach for 100- and 125-mm diameter pipes under **(a)** minimum (Q_{min}) and **(b)** maximum (Q_{max}) flow rates, as well as maximum and minimum flow rates in **(c)** 100- and **(d)** 125-mm diameter pipes.

4.5.4 Coupled effect of characteristics of plug flow, bulk concrete, and lubrication layer zones, as well as pumping specifications on pressure loss of plug zone

The coupled effect of characteristics of different zones of pipe flow, including the plug flow, BC, and LL, as well as pumping specifications, including pipe diameter and flow rate, on pressure losses of the investigated mixtures were evaluated. The characteristics of different pipe flow zones include:

(i)   Plug flow zone: The viscosity $\mu_{0\text{-Plug}}$ (Pa.s) and radius r_{Plug} (mm) of plug zone, numerically obtained using the proposed tri-viscous model;

(ii)   Sheared-concrete zone: The rheological properties of BC, including yield stress $\tau_{0\text{-C}}$ (Pa) and plastic viscosity $\mu_{p\text{-C}}$ (Pa.s), experimentally obtained using the rheological measurements;

(iii)   LL: The yield stress $\tau_{0\text{-LL}}$ (Pa) and viscous constant η_{LL} (kPa.s/m) of the LL evaluated using the tribological measurements and tri-viscous simulations, respectively.

The experimental pumping pressure loss values of the investigated mixtures, $\Delta P/L$ (kPa/m), were then correlated to the above characteristics (i, ii, and iii), as well as pipe diameter D_P (mm) and flow rate magnitudes Q (l/s). The following pattern was firstly applied to evaluate the coupled effect of the investigated parameters as product of effect of characteristics of different zones of pipe flow, Q, and D_P:

$$\Delta P/_L = \text{Effect}_{(i,ii,iii)} \times Q^{A_1} \times D_P^{A_2} + A_3 \tag{4.28}$$

where A_1 and A_2 are the adjustment power indices for Q and D_P parameters, respectively, and A_3 is an adjustment constant. On the other hand, the effect of different pipe flow zones ($\text{Effect}_{(i,ii,iii)}$) was considered as a combination function of products of properties of different flow zones, as follows:

$$\text{Effect}_{(i,ii,iii)} = \left[A_4 \times \left(\frac{\mu_{0\text{-Plug}}}{A_5 \, r_{Plug}}\right)^{A_6}\right] + \left[A_7 \times \left(\tau_{0\text{-C}}^{A_8} \times \mu_{p\text{-C}}^{A_9}\right)\right] + \left[A_{10} \times A_{11}^{\tau_{0\text{-LL}}} \times \eta_{LL}^{A_{12}}\right] \tag{4.29}$$

where A_4 to A_{12} are the adjustment factors and power indices corresponding to characteristics of plug zone (A_4 to A_6), BC (A_7 to A_9) and LL (A_{10} to A_{12}). Using the rheological properties of the investigated mixtures (Table 4.1), as well as the characteristics of LL and plug zones, obtained using the tri-viscous simulations, a Microsoft Excel Solver was developed to identify the adjustment factors A_1 to A_{12} leading the closest pressure loss ($\Delta P/L$) values using Eqs. (28) and (29) to their corresponding experimental ones (Table 4.2). The developed solver then targeted to minimize the sum of squared-simulation errors ($\sum_{i=1}^{404}\left[\left(\Delta P/L\right)_{sim_i} - \left(\Delta P/L\right)_{exp_i}\right]^2$) for in total 404 pipe flow experiments by identifying the best adjustment factors A_1 to A_{12}. The result of the developed solver is then illustrated in Eq. (4.30).

The results of the established correlation Eq. (4.30) were compared to the experimental pressure loss values in Fig. 4.17. As can be observed, using the tri-viscous simulations results, the measured pressure loss values are in excellent agreement with the rheological characteristics of three different zones formed across the pipe section and pumping specifications (R^2 of 0.982, low RSME of 7.043 kPa/m, and estimation index of 0.982.). This can reflect higher accuracy of the established correlation (Eq. (4.28)) to predict pressure loss compared to those obtained using the analytical model proposed by Kaplan et al. (an estimation index of 1.08 and R^2 of 0.88), reported in Ref. [3,4] for the same experimental database.

According to the established correlation, higher rheological properties of plug, sheared concrete, and LL zones, as well as higher flow rate and smaller pipe diameter can result in higher pressure loss values. Regarding the obtained adjustment factors in Eq. (4.28), the rheological properties of the concrete and LL showed more dominant effect on pressure loss values compared to the plug flow characteristics (viscosity and radius). Moreover, among the rheological parameters, the plastic viscosity of BC and viscous constant of LL showed more significant effect on pumping pressure than yield stresses. On the other hand, the pipe diameter can significantly influence the pumping pressure than flow rate magnitudes. According to the obtained adjustment factors, the most influencing factors to control the pumping pressure loss in (descending) order of importance are pipe diameter, plastic viscosity of concrete, and flow rate.

$$\Delta P/L = \left[\underbrace{0.005\left(\frac{\mu_{0-Plug}}{4.429^{r_{Plug}}}\right)^{0.00001}}_{\text{(i) Plug-flow zone}} + \underbrace{109823.146\left(\tau_{0-C}{}^{0.0003} \times \mu_{p-C}{}^{1.112}\right)}_{\text{(ii) Sheared-concrete zone}} + \underbrace{2529896.055\left(0.9991^{\tau_{0-LL}} \times \eta_{LL}{}^{0.811}\right)}_{\text{(iii) Lubrication-layer zone}} \right] \times \underbrace{\left(\frac{Q^{0.783}}{D_P{}^{3.036}}\right)}_{\text{Pumping specifications}} - 3.160 \qquad (4.30)$$
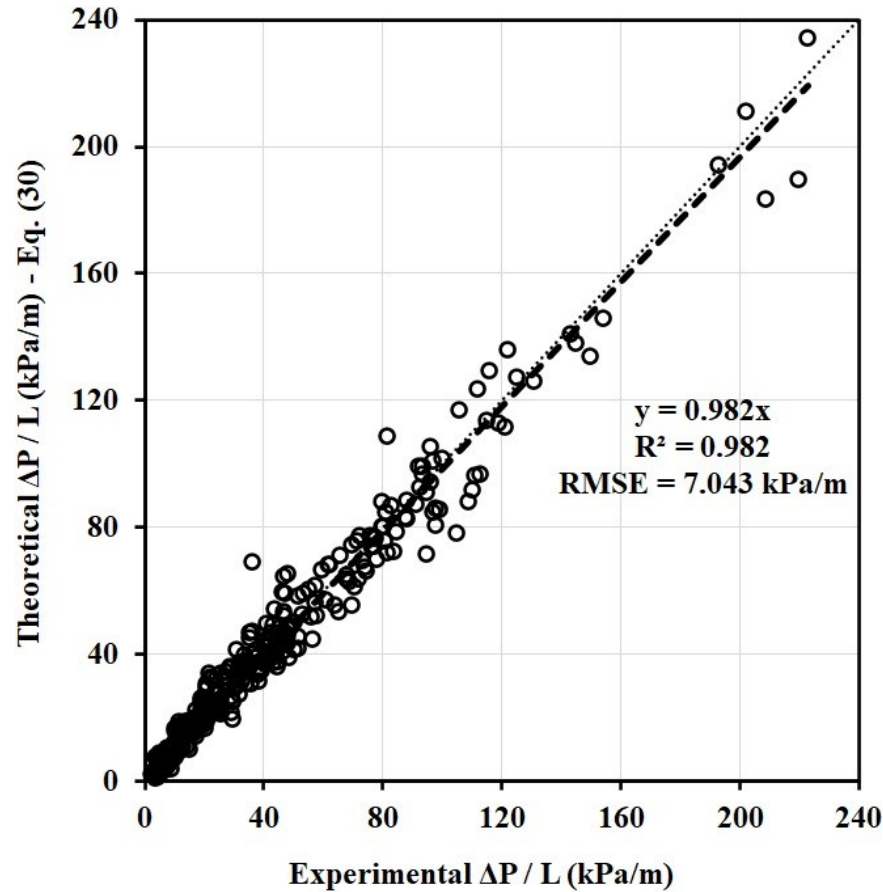
Fig. 4.17. Comparison between the experimental (Table 4.2) and theoretical pressure loss ΔP/L (kPa/m) values obtained using Eq. (4.30) and tri-viscous simulations' results.

Chapter 4. Novel tri-viscous model to simulate pumping of flowable
concrete through characterization of lubrication layer and plug zones

136

4.6 Conclusions

The pumping experiments reported in Ref. [3,4] were successfully simulated in this study. In total 18 SCC and 4 HWC mixtures were pumped through a 30-m pipeline circuit of diameters 100 and 125 mm, under low and high flow rates with 4 to 6 pumping cycles per concrete conducted at 30-min intervals (404 pipe flow experiments). The measured rheological and tribological properties of the investigated mixtures were considered. Two different numerical approaches were established and applied to simulate the 404 pipe flow cases using diverse SCC and HWC mixtures that were pumped at various flow rates [3,4] to achieve the lowest difference with experimental pressure loss measurements. Due to inability of the tribometers to perfectly represent the concrete pipe flow conditions, the optimized numerical models were exploited to characterize the LL and plug flow zones across the pipe sections, in terms of thickness and rheological properties. Such analysis is quite novel and has not been done before. According to the numerical results presented in this paper, the main concluding remarks can be summarized as follow:

- Two new modelling approaches, including two-fluids (double-Bingham) and variable-viscosity single-fluid (tri-viscous) models were proposed to simulate the concrete flow behavior across the pipes. New viscosity models were added to the OpenFOAM code library to consider the presence of different flow zones across the pipe section, including plug flow, sheared concrete, and LL with different radial positions to the pipe center and variable rheological properties. The proposed approaches led to significantly higher accuracy in predicting pressure losses compared to the analytical Kaplan et al. model.

- Using the two-fluids approach, the concrete flow in pipes were modeled as two different Bingham fluids, corresponding to the LL and BC (Double-Bingham model). The two-fluids approach resulted in highly precise prediction of pressure loss values. However, this approach requires relatively high calculation times (69 to 528 s using a 3.00 GHz CPU) due to consideration of LL and BC interface tracking and simulating multiphases flow.

- The tri-viscous approach was proposed to simulate radial variation of rheological properties across the pipe cross section as a single fluid. The use of single-fluid approach required to solve a single Navier-Stokes equation and neglect the interaction between different flow zones. This led to highly accurate predictions of pressure loss and more than 20 times shorter calculation time (3 to 26 s using a 3.00 GHz CPU) compared to the two-fluids approach.

- The tri-viscous approach was successfully employed to characterize different pipe flow zones, including thickness and viscous constant of LL, as well as the viscosity and radius of plug flow zone, which cannot be evaluated using the empirical and analytical tools.

- The simulated viscous constants, obtained using the tri-viscous approach, ranged between 30% to 200% values relative to those of the tribological measurements. The maximum and minimum variations relative to the tribological viscous constants were obtained for pumping tests with maximum and minimum flow rates in 100- and 125-mm diameter pipes, respectively. Increasing the pipe diameter and decreasing the flow rate magnitude led mostly to form LLs with larger thicknesses.

- Frequency distribution of the simulated LL thicknesses revealed that under low flow rate, the majority of the LL thicknesses for the 100- and 125-mm diameter pipes were between 1.5 to 2 mm (80.2%) and 3 to 3.5 mm (63.3%), respectively. On the other hand, increasing the flow rate resulted in LL thicknesses of 1.5 to 2 mm with greatest frequencies in both the 100-mm (85.4%) and 125-mm (63.3%) diameter pipes.

- The plug flow zone were successfully characterized in terms of viscosity and radius using the simulated apparent viscosity profiles across the pipe cross section. Increasing the pipe diameter and decreasing flow rate resulted in larger plug radius. Accordingly, increasing the pipe diameter from 100 to 125 mm increased the plug radius with the maximum frequency from 10-20 mm to 20-30 mm and from 0-10 mm to 10-20 mm under low and high flow rates, respectively. On the other hand, decreasing the flow rate (Q_{max} to Q_{min}) resulted in increasing the plug radius with the maximum frequency from 0-10 mm to 10-20 mm and from 10-20 mm to 20-30 mm created in the 100- and 125-mm diameter pipes, respectively.

- The coupled effect of the characteristics of plug flow, sheared concrete, and LLs zones obtained using the tri-viscous simulations, on pumping pressure loss was evaluated. The established correlation exhibited higher accuracy to predict the pumping pressure drop, compared to the Kaplan et al. model, reflected by higher R^2 (0.98 vs. 0.88) and closer estimation index (0.98 vs. 1.08) to unity. According to the established correlation, the increase in rheological properties of the plug, sheared concrete, and LL zones, as well as higher flow rate and smaller pipe diameter can increase the pumping pressure loss. The plastic viscosity of concrete and viscous constant of the LL showed the most dominant effect

Chapter 4. Novel tri-viscous model to simulate pumping of flowable concrete through characterization of lubrication layer and plug zones

138

on pressure loss compared to the viscosity and radius of the plug flow. Moreover, in the case of pumping specifications, the pressure loss is more controlled by pipe diameter rather than flow rate magnitudes.

4.7 Acknowledgment

REFERENCES

[1]   D. Kaplan, F. De Larrard, T. Sedran, Design of concrete pumping circuit, ACI Materials Journal, 102 (2) (2005) 110-117 https://doi.org/10.14359/14304.

[2]   A.N. Ede, The resistance of concrete pumped through pipelines, Magazine of Concrete Research, 9 (27) (1957) 129-140 https://doi.org/10.1680/macr.1957.9.27.129.

[3]   R. Khatib, Analysis and prediction of pumping characteristics of high-strength self-consolidating concrete, Ph.D. Thesis, Université de Sherbrooke (2013) http://hdl.handle.net/11143/6634.

[4]   D. Feys, K.H. Khayat, A. Perez-Schell, R. Khatib, Prediction of pumping pressure by means of new tribometer for highly-workable concrete, Cement and Concrete Composites, 57 (2015) 102-115 https://doi.org/10.1016/j.cemconcomp.2014.12.007.

[5]   D. Feys, K.H. Khayat, R. Khatib, How do concrete rheology, tribology, flow rate and pipe radius influence pumping pressure?, Cement and Concrete Composites, 66 (2016) 38-46 https://doi.org/10.1016/j.cemconcomp.2015.11.002.

[6]   E. Secrieru, W. Mohamed, S. Fataei, V. Mechtcherine, Assessment and prediction of concrete flow and pumping pressure in pipeline, Cement and Concrete Composites, 107 (2020) 103495 https://doi.org/10.1016/j.cemconcomp.2019.103495.

[7]   R.D. Browne, P.B. Bamforth, Tests to establish concrete pumpability, ACI Journal Proceedings, 74 (5) (1977) 193-203 DOI: 10.14359/11001.

[8]   V. Vand, Viscosity of solutions and suspensions. I. Theory, The Journal of Physical and Colloid Chemistry, 52 (2) (1948) 277-299 https://doi.org/10.1021/j150458a001.

Chapter 4. Novel tri-viscous model to simulate pumping of flowable
concrete through characterization of lubrication layer and plug zones

139

[9]   M. Hosseinpoor, B.I.O. Koura, A. Yahia, New methodology to evaluate the Reynolds dilatancy of self-consolidating concrete using 3D image analysis - Coupled effect of characteristics of fine mortar and granular skeleton, Cement and Concrete Composites, 108 (2020) 103547, https://doi.org/10.1016/j.cemconcomp.2020.103547.

[10]   M. Hosseinpoor, B.I.O. Koura, A. Yahia, Rheo-morphological investigation of Reynolds dilatancy and its effect on pumpability of self-consolidating concrete, Cement and Concrete Composites, 117 (2021) 103912, https://doi.org/10.1016/j.cemconcomp.2020.103912.

[11]   Y.C. Lam, X. Chen, K.W. Tan, J.C. Chai, S.C.M. Yu, Numerical investigation of particle migration in Poiseuille flow of composite system, Composites Science and Technology, 64 (7-8) (2004) 1001-1010 https://doi.org/10.1016/j.compscitech.2003.08.005.

[12]   S. Fataei, E. Secrieru, V. Mechtcherine, N. Roussel, A first-order physical model for the prediction of shear-induced particle migration and lubricating layer formation during concrete pumping, Cement and Concrete Research, 147 (2021) 106530, https://doi.org/10.1016/j.cemconres.2021.106530.

[13]   T. Tavangar, M. Hosseinpoor, A. Yahia, K.H. Khayat, Computational investigation of concrete pipe flow: Critical review, ACI Materials Journal, 118 (6) (2021) https://dx.doi.org/10.14359/51733124.

[14]   D. Feys, G. De Schutter, R. Verhoeven, Parameters influencing pressure during pumping of self-compacting concrete, Materials and Structures, 46 (2013) 533-555 https://doi.org/10.1617/s11527-012-9912-4.

[15]   M. Choi, C.F. Ferraris, N.S. Martys, D. Lootens, V.K. Bui, H.R.T. Hamilton, Metrology needs for predicting concrete pumpability, Advances in Materials Science and Engineering, (2015) 456238, http://dx.doi.org/10.1155/2015/456238.

[16]   S.H. Kwon, K.P. Jang, J.H. Kim, S.P. Shah, State of the art on prediction of concrete pumping, International Journal of Concrete Structures and Materials, 10 (3) (2016) 75-85 https://doi.org/10.1007/s40069-016-0150-y.

[17]   D. Kaplan, Pumping of Concrete. Ph.D. Thesis, LCPC, Paris, France (1999) (In French) https://tel.archives-ouvertes.fr/tel-01310219/.

[18]   D. Kaplan, T. Sedran, F. De Larrard, M. Vachon, G. Machese, Forecasting pumping parameters, In: Proc. of the 2nd Int RILEM symp. on self-compacting concrete, Tokyo, 2001, 556-564.

Chapter 4. Novel tri-viscous model to simulate pumping of flowable
concrete through characterization of lubrication layer and plug zones

140

[19]   E. Buckingham, On plastic flow through capillary tubes, ASTM Proceeding, 29 (21) (1921) 1154-1161.

[20]   G. De Schutter, D. Feys, Pumping of fresh concrete: Insights and challenges, RILEM Technical Letters, 1 (2016) 76-80 https://doi.org/10.21809/rilemtechlett.2016.15.

[21]   S.H. Kwon, S.D. Jo, C.K. Park, J.H. Jeong, S.D., Jo, S.H. Lee, Prediction of concrete pumping: Part II-analytical prediction and experimental verification, ACI Materials Journal, 110 (6) (2013) 657-668.

[22]   C.F. Ferraris, L.E. Brower, Comparison of concrete rheometers: international tests at MB (Cleveland OH, USA) in 2003. National Institute of Standards and Technology Interagency Report, NISTIR 71452.

[23]   L. Chen, G. Liu, W. Cheng, G. Pan, Pipe flow of pumping wet shotcrete based on lubrication layer, SpringerPlus 5, 945 (2016) https://doi.org/10.1186/s40064-016-2633-3.

[24]   M.S. Choi, Y.J. Kim, S.H. Kwon, Prediction on pipe flow of pumped concrete based on shear-induced particle migration, Cement and Concrete Research, 52 (2013) 216-224 https://doi.org/10.1016/j.cemconres.2013.07.004.

[25]   K.P. Jang, W.J. Kim, M.S. Choi, S.H. Kwon, A new method to estimate rheological properties of lubricating layer for prediction of concrete pumping, Advances in Concrete Construction, 6 (5) (2018) 465-483 http://dx.doi.org/10.12989/acc.2018.6.5.465.

[26]   S. Jacobsen, L. Haugan, T.A. Hammer, E. Kalogiannidis, Flow conditions of fresh mortar and concrete in different pipes, Cement and Concrete Research, 39 (11) (2009) 997-1006 https://doi.org/10.1016/j.cemconres.2009.07.005.

[27]   M.S. Choi, Y.J. Kim, S.H. Kwon, Prediction on pipe flow of pumped concrete based on shear-induced particle migration, Cement and Concrete Research, 52 (2013) 216-224 https://doi.org/10.1016/j.cemconres.2013.07.004.

[28]   H.D. Le, E.H. Kadri, S. Aggoun, J. Vierendeels, P. Troch, G. De Schutter, Effect of lubrication layer on velocity profile of concrete in a pumping pipe, Materials and Structures, 48 (2015) 3991-4003 https://doi.org/10.1617/s11527-014-0458-5.

[29]   E. Secrieru, S. Fataei, C. Schröfl, V. Mechtcherine, Study on concrete pumpability combining different laboratory tools and linkage to rheology, Construction and Building Materials, 144 (2017)

Chapter 4. Novel tri-viscous model to simulate pumping of flowable
concrete through characterization of lubrication layer and plug zones

141

451-461 https://doi.org/10.1016/j.conbuildmat.2017.03.199.

[30]   V. Mechtcherine, V.N. Nerella, K. Kasten, Testing pumpability of concrete using Sliding Pipe Rheometer, Construction and Building Materials, 53 (2014) 312-323 https://doi.org/10.1016/j.conbuildmat.2013.11.037.

[31]   T.T. Ngo, E.H. Kadri, R. Bennacer, F. Cussigh, Use of tribometer to estimate interface friction and concrete boundary layer composition during the fluid concrete pumping, Construction and Building Materials, 24 (7) (2010) 1253-1261, https://doi.org/10.1016/j.conbuildmat.2009.12.010.

[32]   F. Chapdelaine, Étude fondamentale et pratique sur le pompage du béton, Ph.D. Thesis, Université Laval (2007) http://hdl.handle.net/20.500.11794/18881.

[33]   D. Feys, K.H. Khayat, A. Perez-Schell, R. Khatib, Development of a tribometer to characterize lubrication layer properties of self-consolidating concrete, Cement & Concrete Composites, 54 (2014) 40-52 https://doi.org/10.1016/j.cemconcomp.2014.05.008.

[34]   M. Ouchi, J. Sakue, Self-compactability of fresh concrete in terms of dispersion and coagulation of particles of cement subject to pumping, In: Proceedings of the 3rd North-American conference on the design and use of self-consolidating concrete, Chicago (2008).

[35]   K. Takahasi, T. Bier, Mechanisms Mechanisms for the changes in fluidity and hydration kinetics of grouts after mixing. In: Proceedings of the 6th international RILEM conference on self-compacting concrete, Paris (2013).

[36]   T. Bier, T. Takahashi, Influence of pumping of fresh concrete properties for SCC, ACI Spring Convention, Kansas-City (2015).

[37]   D. Feys, G. De Schutter, K.H. Khayat, R. Verhoeven, Changes in rheology of self-consolidating concrete induced by pumping, Materials and Structures, 49 (2016) 4567-4677 https://doi.org/10.1617/s11527-016-0815-7.

[38]   National Ready Mixed Concrete Association (2005) CIP 21- Loss of air content in pumped concrete, https://www.nrmca.org/wp-content/uploads/2020/04/21pr.pdf.

[39]   American Concrete Pumping Association (2008) Concrete 101, A guide to understanding the qualities of concrete and how they affect pumping, http://www.concretepumpers.com/files/attachments/concrete_101.pdf.

Chapter 4. Novel tri-viscous model to simulate pumping of flowable
concrete through characterization of lubrication layer and plug zones

142

[40] R.J. Phillips, R.C. Armstrong, R.A. Brown, A.L. Graham, J.R. Abbott, A constitutive equation for concentrated suspensions that accounts for shear-induced particle migration, Physics of Fluids A: Fluid Dynamics 4, 30 (1992) 30-40 https://doi.org/10.1063/1.858498.

[41] S.D. Jo, C.K. Park, J.H. Jeong, S.H. Lee, S.H. Kwon, A computational approach to estimating a lubricating layer in concrete pumping, Computers Materials and Continua, 27 (3) (2012) 189-210 https://doi.org/10.3970/CMC.2011.027.189.

[42] M.S. Choi, Numerical prediction on the effects of the coarse aggregate size to the pipe flow of pumped concrete, Journal of Advanced Concrete Technology, 12 (2014) 239-249 https://doi.org/10.3151/jact.12.239.

[43] N. Roussel, A. Gram, M. Cremonesi, L. Ferrara, K. Krenzer, V. Mechtcherine, S. Shyshko, J. Skocec, J. Spangenberg, O. Svec, L.N. Thranse, K. Vasilic, Numerical simulations of concrete flow: A benchmark comparison, Cement and Concrete Research, 79 (2016) 265-271 https://doi.org/10.1016/j.cemconres.2015.09.022.

[44] Y. Zhan, J. Gong, Y. Huang, C. Shi, Z. Zuo, Y. Chen, Numerical study on concrete pumpability behavior via local flow simulation with discrete element method, Materials, 12 (9) (2019) 1415 https://doi.org/10.3390/ma12091415.

[45] G.R. Liu, M.B. Liu, Smoothed particle hydrodynamics: A Meshfree Particle Method, World Scientific Printers CO. Pte. Ltd., Singapore, ISBN 981-238-456-1.

[46] T. Tran-Duc, T. Ho, N. Thamwattana, A smoothed particle hydrodynamics study on effect of coarse aggregate on self-compacting concrete flows, International Journal of Mechanical Sciences, 190 (2021) 106046 https://doi.org/10.1016/j.ijmecsci.2020.106046.

[47] R. Schwarze, CFD-Modellierung: Grundlagen und Anwendungen bei Strömungsprozessen, Springer-Verlag, Berlin/Heidelberg, 2013 ISBN 978-3-642-24378-3, DOI: 10.1007/978-3-642-24378-3.

[48] M. Choi, N. Roussel, Y. Kim, J. Kim, Lubrication layer properties during concrete pumping, Cement and Concrete Research, 45 (2013) 69-78 https://doi.org/10.1016/j.cemconres.2012.11.001.

[49] E. Secrieru, Pumping behaviour of modern concretes – Characterisation and prediction, Ph.D. Dissertation, Technische Universität Dresden (2018) https://nbn-resolving.org/urn:nbn:de:bsz:14-qucosa-234912.

[50]   V.N. Nerella, V. Mechtcherine, Virtual Sliding Pipe Rheometer for estimating pumpability of concrete, Construction and Building Materials, 170 (2018) 366-377 https://doi.org/10.1016/j.conbuildmat.2018.03.003.

[51]   E. Secrieru, J. Khodor, C. Schröfl, V. Mechtcherine, Formation of lubrication layer and flow type during pumping of cement-based materials, Construction and Building Materials, 178 (2018) 507-517 https://doi.org/10.1016/j.conbuildmat.2018.05.118.

[52]   D. Feys, K.H. Khayat, Comparing rheological properties of SCC obtained with the ConTec and ICAR rheometers. In: Proceedings of the 5th North-American conference on self-consolidating concrete, Chicago (2013).

[53]   D. Feys, K.H. Khayat, Comparison and limitations of concrete rheometers. In: Proceedings of the 7th international RILEM symposium on self-compacting concrete, Paris (2013).

[54]   www.openfoam.org.

[55]   G. Chen, Q. Xiong, P.J. Morris, E.G. Paterson, A. Sergeev, Y.-C. Wang, OpenFOAM for Computational Fluid Dynamics, Notices of the AMS, 61 (4) (2014) 354-363 https://doi.org/10.1090/noti1095

[56]   S.S. Deshpande, L. Anumolu, M.F. Trujillo, Evaluating the performance of the two-phase flow solver interFoam, Computational Science & Discovery. 5 (2012) 014016 https://doi.org/10.1088/1749-4699/5/1/014016.

[57]   H. Jasak, Error analysis and estimation for finite volume method with applications to fluid flow, Ph.D. Thesis, University of London and Imperial College, 1996 http://hdl.handle.net/10044/1/8335.

[58]   P.T. Peeters, CFD of multiphase pipe flow: a comparison of solvers, Master Thesis, Delft University of Technology (2016) http://resolver.tudelft.nl/uuid:88a16dcd-f404-4d29-9bad-d3ffd0cc2023.

[59]   G.H. Kim, S. Park, Development of a numerical simulation tool for efficient and robust prediction of ship resistance, International Journal of Naval Architecture and Ocean Engineering, 9 (5) (2017) 537-551 https://doi.org/10.1016/j.ijnaoe.2017.01.003.

[60]   C.W. Hirt, B.D. Nichols, Volume of fluid (VOF) method for the dynamics of free boundaries, Journal of Computational Physics, 39 (1) (1981) 201-225 https://doi.org/10.1016/0021-9991(81)90145-5.

*Chapter 4. Novel tri-viscous model to simulate pumping of flowable
concrete through characterization of lubrication layer and plug zones*

144

[61]   G. Cerne, S. Petelin, I. Tiselj, Coupling of the interface tracking and the two-fluid models for the simulation of incompressible two-phase flow, Journal of Computational Physics, 171 (2) (2001) 776-804 https://doi.org/10.1006/jcph.2001.6810.

[62]   S.M. Damián, N.M. Nigro, An extended mixture model for the simultaneous treatment of small-scale and large-scale interfaces, International Journal for Numerical Methods in Fluids, 75 (8) (2014) 547-574 https://doi.org/10.1002/fld.3906.

[63]   C.J. Greenshields, OpenFOAM user guide version 6, OpenFOAM Found. Ltd. (2017) U-94. https://cfd.direct/openfoam/user-guide/.

[64]   R.E. Denton, Y. Hu, Symmetry boundary conditions, Journal of Computational Physics, 228 (13) (2009) 4823-4835 https://doi.org/10.1016/j.jcp.2009.03.033.

[65]   S. Richardson, On the no-slip boundary condition, Journal of Fluid Mechanics, 59 (4) (1973) 707-719 https://doi.org/10.1017/S0022112073001801.

[66]   J.D. Dent, T.E. Lang, A biviscous modified Bingham model of snow avalanche motion, Annals of Glaciology, 4 (1983) 42-46 https://doi.org/10.1017/S0260305500005218.

[67]   S.W. Jeong, Determining the viscosity and yield surface of marine sediments using modified Bingham models, Geoscience Journal, 17 (2013) 241-247 https://doi.org/10.1007/s12303-013-0038-7.

[68]   M. Winter, Benchmark and validation of Open Source CFD codes, with focus on compressible and rotating capabilities, for integration on the SimScale platform, Master Thesis, Chalmers University of Technology (2013) https://hdl.handle.net/20.500.12380/198965.

[69]   H. Khawaja, M. Moatamedi, Semi-implicit method for pressure-linked equations (SIMPLE) - solution in MATLAB®, The International Journal of Multiphysics, 12 (4) (2018) 313-326, https://doi.org/10.21152/1750-9548.12.4.313.

[70]   J.H. Ferziger, M. Perić, R.L. Street, Computational Methods for Fluid Dynamics Springer-Verlag Berlin Heidelberg (2002) DOI: 10.1007/978-3-642-56026-2.

[71]   P. Coussot, Rheometry of pastes, suspensions, and granular materials, John Wiley & Sons, Inc. (2005) Online ISBN:9780471720577, DOI: 10.1002/0471720577.

CHAPTER 5. Numerical simulation of flowable concrete pumping using a novel shear-rate dependent tri-viscous model

Authors and affiliations

Tooran Tavangar: Ph.D. candidate, Cement and Concrete Research Group, Department of Civil and Building Engineering, Université de Sherbrooke, Sherbrooke, Québec, Canada, J1K 2R1.

Masoud Hosseinpoor: Research Assitance, Cement and Concrete Research Group, Department of Civil and Building Engineering, Université de Sherbrooke, Sherbrooke, Québec, Canada, J1K 2R1.

Ammar Yahia: Professor, Cement and Concrete Research Group, Department of Civil and Building Engineering, Université de Sherbrooke, Sherbrooke, Québec, Canada, J1K 2R1.

Kamal H. Khayat, Professor, Department of Civil, Architectural and Environmental Engineering, Center for Infrastructure Engineering Studies, Missouri University of Science and Technology, Rolla, MO, USA.
.

Abstract

In this study, a novel shear-rate dependent tri-viscous model was proposed to simulate pipe flow of flowable concrete and characterize the lubrication layer (LL) and plug zones. The rheological properties of the various concrete materials across the simulated pipes are shown to vary depending on shear rate. The proposed model enabled successful prediction of pressure drop (ΔP) at 1-m pipe length measured for nearly 180 pumping experiments carried out using 22 flowable concrete mixtures pumped at flow rates of 8.1-16.4 l/s across 100- and 125-mm diameter pipes. The critical shear rates of 80-430 s^{-1}, maximum flow velocities of 0.8-2.4 m/s, and Reynolds numbers of 1.4-18.8 were successfully evaluated. The simulated LL-viscous constants ranged between 0.4-7.1 times those obtained using the tribometer. The simulated plug radii and LL thicknesses varied between 0-43.4 and 0.4-2.9 mm, respectively. The critical shear rate was revealed as the most dominant factor affecting the ΔP.

Keywords: Concrete pumping; Lubrication layer; Numerical simulation; Rheology; Shear rate.

5.1 Introduction

During concrete pumping process, a thin layer of fine mortar, namely lubrication layer (LL), is formed in vicinity of the pipe wall [1-4]. Because of its relatively higher volume of water and cement paste, the LL is more fluid than the bulk concrete (BC). This can thus facilitate displacement of concrete through the pipelines and accelerate the construction process [5,6]. Moreover, the formation of LL with lower viscosity and larger thickness can lead to lower pumping pressure (P). The significant effect of LL on concrete pumpability was reported in various analytical models describing the pumping flow rate (Q) - pressure drop (ΔP) relationship [5,7-9]. Kaplan et al. [5,7,8] developed analytical models for two general pipe-flow conditions, including plug flow and partially sheared BC. When the maximum shear stress at pipe walls (radius R and length L in Fig. 5.1), $\tau_w = \frac{\Delta P \times R}{2 \times L}$, is below the yield stress of concrete ($\tau_w < \tau_{0\text{-}C}$), BC remains totally unsheared and displaces with a uniform velocity across the pipe section. In this case, the pressure decay through a unit length of pipe ($\Delta p = \Delta P/L$) is proportional to the flow rate (Q), plastic viscosity ($\mu_{p\text{-}LL}$) and yield stress ($\tau_{0\text{-}LL}$) of LL, and inversely proportional to the pipe radius (R), filling coefficient of piston pumps' cylinders (k_r), and LL thickness (e_{LL}). On the other hand, when

BC is partially sheared along a radius greater than $\frac{2 \times L \times \tau_{0-C}}{\Delta P}$, increasing the plastic viscosity (μ_{p-C}) and yield stress (τ_{0-C}) of the BC can significantly increase Δp. More recently, Kwon et al. [10] proposed an analytical Δp-Q relationship that considers the radius of the plug-flow zone (RP) and LL thickness (e_{LL}). In order to ensure better precision of these analytical models, it is essential to accurately characterize the rheological and geometrical properties of all different flow zones, including LL, BC, and plug flow.
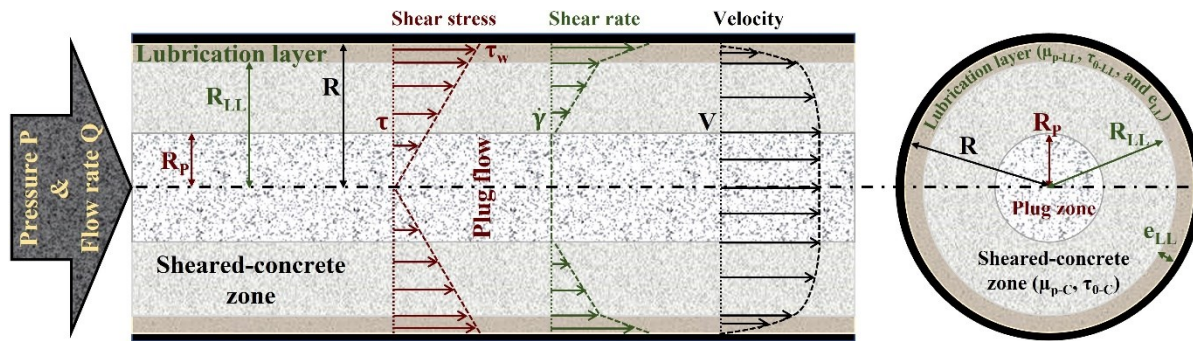
Fig. 5.1. Characteristics of pressure-driven flow field of concrete, including shear stress, shear rate, and velocity profiles in plug-flow, sheared-concrete, and LL zones [4,5,11,12].

As reported in literature [13], the shear stress and shear-rate (γ) gradient across the pipe are mainly responsible of radial variation of rheological properties of concrete and formation of the LL in pipe flow. Philips et al. [14] reported that the shear-rate gradient across the pipe section (Fig. 5.1) causes the migration of solid particles from the high-shear rate zone (vicinity of pipe walls) to the lower-shear rate zone closer to the pipe center, hence leading to dissimilar rheological properties across the pipe section [13]. Accordingly, the LL zone has a lower viscosity than the sheared BC and plug-flow zones (Fig. 5.1). This can alter the velocity and shear-rate profiles in different radial zones [15]. As illustrated in Fig. 5.1, the pipe radius where velocity and shear rate profiles change from uniform to non-constant and from zero to non-zero, respectively, corresponds to the plug radius (RP). Moreover, the radius where a rapid change is observed in shear-rate and velocity gradients corresponds to the pipe radius where the LL starts (RLL). The LL thickness can then be calculated as follows: $e_{LL} = R - R_{LL}$ [15]. In the case of highly-flowable concrete, a large fraction of concrete (LL and sheared BC) is exposed to high shear rates for long period during the pumping process. Shear rates can be on the order of several 10 s^{-1} for the BC and several 100 s^{-1} for the LL [15]. This can result in better dispersion of cement and fine particles and an increase in concrete temperature. Consequently, lower viscosity is expected during extended pumping distances [15-

19]. On the other hand, it was reported that depending on the availability of dispersing admixtures in the mixing water to cover the surface of fine particles, the yield stress can decrease, remain constant or increase during pumping [15,20]. Furthermore, high shear rate can lead to major changes in air-void system [21-26] which can subsequently alter the rheological properties of the pumped concrete. All these pumping-induced rheological changes are amplified in presence of higher shear-rate gradients. This can emphasize the significance of determination of shear-rate gradient across the pipes to allow better prediction of the concrete pumpability.

In order to evaluate the yield stress ($\tau_{0\text{-LL}}$) and viscous constant (η_{LL}) of the LL, interface rheometers, namely tribometers, are used. The shearing of concrete through pipes are simulated between the coaxial rotating-smooth inner cylinder and fixed cylindrical container of the tribometer [5,27-29]. It is worthy to mention that η_{LL} is an interdependent parameter defined as the ratio of plastic viscosity-to-thickness of LL ($\eta_{LL} = \frac{\mu_{p\text{-LL}}}{e_{LL}}$) where e_{LL} cannot be directly measured in tribometers. Tribometers cannot realistically simulate the concrete pipe flow fields due to the absence of pressure and relatively low applied shear rate. In fact, the LL is exposed to higher shear rates (up to several 100 s^{-1}) compared to the capacity of existing tribometers (< 10 s^{-1}). Therefore, the LL and plug-flow zones formed in tribometers are not representative for actual values during actual pumping [13,30]. Therefore, the use of tribological results as input parameters in analytical models can affect the degree of prediction of pressure loss [13,30]. Furthermore, analytical models do not consider pumping-induced changes in rheological properties of pumped concrete and their effect on the LL.

Numerical simulations can then be employed as alternative tools to characterize different pipe flow zones and accurately predict the concrete pumpability [13,31]. Contrary to analytical models, the physical interaction between coarse aggregate, suspending mortar, and pipe walls can be evaluated using numerical solutions. Depending on the scale of the given pipe flow in hand and intended properties to evaluate, various computational techniques were developed [13]. In order to simulate large-scale pumping experiments in a reasonable calculation time, the single-phase modeling approach is frequently used [13]. In this approach, the presence of particles is neglected, the flow domain is discretized in different mesh cells, and the rheological properties of the BC and LL are assigned to their corresponding cells as homogeneous and continuous fluids. The mass and momentum conversation equations are then solved for a steady and incompressible concrete pipe

flow, considering the no-slip boundary condition for the concrete-pipe wall interface [4]. The Navier-Stokes equations were then applied as the constitutive equations [4,32,33]. From a rheological point of view, the Bingham model is usually employed to describe the rheological behavior of different pipe-flow zones using a bi-viscous approach [4,34-38]. The bi-viscous model consists of the combination of both Newtonian and Bingham models, corresponding to shear rates lower and higher than a critical value, respectively. For computational purposes, a relatively high viscosity value ($\mu 0$) is assigned to the Newtonian part to avoid zero dominator to calculate the apparent viscosity ($\mu_{app} = \dfrac{\tau}{\dot{\gamma}} = \mu_p + \dfrac{\tau_0}{\dot{\gamma}}$) for the plug-flow zone. An initial assumption of LL thickness (generally between 0 to 10 mm) is required when a bi-viscous approach is employed. Accordingly, given the radial position of the cell, the yield stress and plastic viscosity of the BC or LL are employed [4,34-38]. Recently, contrary to the bi-viscous simulations, Tavangar et al. [30] modelled concrete as a single fluid with radially-variable rheological properties across the pipe's section, corresponding to the LL, sheared-BC, and plug-flow zones. Although the proposed model accurately predicted pressure drop values (Δp), the simulated e_{LL} values were found very limited to two short ranges of either 1-2 mm or 2.5-3.5 mm for an extensive number of 404 pipe flow cases of wide ranges of concrete workability, flow rate, and pipe diameter values [30]. This can be explained by the high dependency of the single-phase modelling approach on the initial e_{LL} assumptions and mesh settings, which were initially comparable for all the simulations (initial e_{LL} = 2 mm). Moreover, it is worth mentioning that single-phase pumping simulations in literature cannot evaluate the shear-rate gradients subjected to concrete during pumping process.

In this study, a new shear-rate dependent tri-viscous model is proposed to simulate the pipe flow of flowable concrete. In this model, the rheological properties of concrete across the pipe vary with shear-rate magnitudes calculated in each computational cell, hence avoiding grid sensitivity and coordination dependency of former single-phase simulations. Moreover, the proposed model can provide useful information about the shear rate magnitudes to study the shear-induced changes in concrete properties during pumping, which can be more significant for flowable concrete. Pumping experiments of 18 self-consolidating (SCC) and four highly workable concrete (HWC) mixtures through a 30-m long pumping circuit were simulated. The numerical simulations were validated using the experimental Δp measurements carried out at the Université de Sherbrooke (Canada) and reported by Feys et al. [2]. The simulated flow fields were measured in terms of

velocity, Reynolds number, shear rate, and apparent viscosity of concrete. Moreover, rheological properties and thickness of LL, sheared-BC, and plug-flow zones were characterized. The simulated LL characteristics were compared to those evaluated using a coaxial tribometer. Furthermore, the coupled effect of rheological properties of different pipe flow zones, shear rate, flow rate, and pipe diameter on pumping pressure loss was evaluated.

5.2 Pumping experiments

A large-scale pumping study was carried out at the Université de Sherbrooke (Canada) using a 30-m long loop circuit [1,2]. As shown in Fig. 5.2, the circuit consisted in two straight horizontal pipes measuring 100 and 125 mm in diameter with a number of bends and reducers. Pressure loss values were measured using strain gauges installed at 10-m intervals. A total of 18 SCC and four HWC mixtures were used in the pumping campaign. The mixtures were pumped at four to six 30-min intervals, namely pumping test cycles, under different flow rates depending on the flowability level of the concrete at that time. The rheological and tribological properties were evaluated in terms of yield stress ($\tau_{0\text{-}C}$ and $\tau_{0\text{-}LL}$), plastic viscosity ($\mu_{p\text{-}C}$), and viscous constant (η_{LL}) using a coaxial-cylinders rheometer and a specially designed tribometer, respectively [1,2]. The rheological and tribological characteristics and the corresponding pressure decay per unit length (Δp) measured in pipes with different diameters (D_P) and flow rates (Q) are presented in Table 5.1.

Lay-out of circuit:
R: Reducers
S: Pressure sensors and strain gauges
E: 90° elbows (100- and 125-mm diameter)
V: Vertical 125-mm diameter pipe
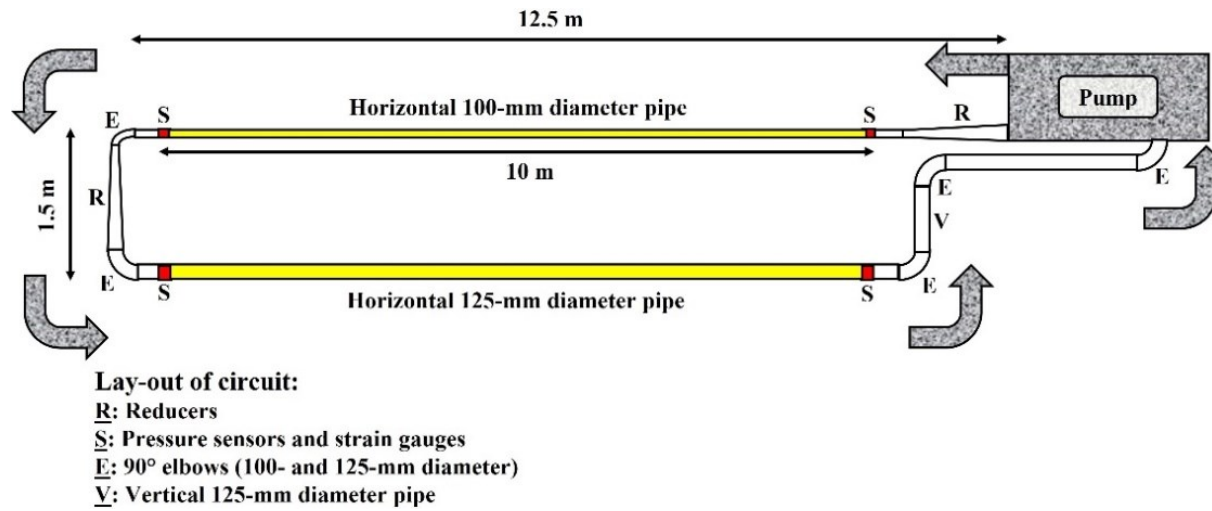
Fig. 5.2. Schematic of the used loop circuit for pumping tests, adapted from [3,4].

Table 5.1. Fresh density, rheological and tribological properties, pressure loss (Δp: kPa/m), and flow rates (Q: l/s) for 22 pumped concrete mixtures in $D_P = 100$- and 125-mm diameter pipes and different pumping test cycles (1-6) [2].

Mix	Properties		Test 1	Test 2	Test 3	Test 4	Test 5	Test 6
	Fresh density	ρ (kg/m³)	2340-2373	2361-2391	2362-2373	2359-2381	2359-2363	-
	Concrete rheology	$\tau_{0\text{-}C}$ (Pa)	52-188	48-169	69-330	64-518	79-838	-
		$\mu_{p\text{-}C}$ (Pa.s)	56-99	55-96	60-92	57-99	56-57	-
	LL properties	$\tau_{0\text{-}LL}$ (Pa)	4-59	73-96	65-89	54-151	62-129	
4 HWC mixtures: HWC1-4		η_{LL} (Pa.s/m)	2117-2682	1603-3549	1464-3396	2563-2979	2007-2680	-
	Q (l/s)	$D_P = 100$ mm	8.8-10.4	11.4-14.1	12.3-13.8	11.8-14.2	14.4-14.6	-
		$D_P = 125$ mm	10.2-12.6	11.4-15.1	12.3-15.4	11.8-14.2	14.1-14.6	-
	Δp (kPa/m)	$D_P = 100$ mm	80.6-119	111-143	92.5-154	91.3-150	91.2-125	-
		$D_P = 125$ mm	34.2-83.8	48.7-73.2	36.7-81.4	32.3-74.7	41.3-46.8	-
	Fresh density	ρ (kg/m³)	2215-2451	2255-2444	2247-2435	2258-2465	2288-2430	2391
	Concrete rheology	$\tau_{0\text{-}C}$ (Pa)	23-90	20-120	15-255	11-652	10-476	165
		$\mu_{p\text{-}C}$ (Pa.s)	29-149	28-129	27-145	27-164	26-192	88
	LL properties	$\tau_{0\text{-}LL}$ (Pa)	0-120	2-231	4-254	8-301	0-291	37
18 SCC mixtures: SCC1-5 and SCC7-19		η_{LL} (Pa.s/m)	490-5365	240-7893	252-6668	326-6983	995-6003	2753
	Q (l/s)	$D_P = 100$ mm	9.4-13.3	8.1-15.3	9.9-16.4	9.7-15.9	9.6-14.8	13.1
		$D_P = 125$ mm	9.5-14.3	27.4-209	25.6-193	9.7-15.9	9.6-14.8	13.1
	Δp (kPa/m)	$D_P = 100$ mm	26.8-220	8.1-15.3	9.9-15.5	22.8-202	22.4-223	96.7
		$D_P = 125$ mm	12.6-96.2	11.8-94.8	11.4-93.6	11.6-96.1	15.2-106	36.4

5.3 Numerical simulation using shear-rate dependent tri-viscous model

In this study, computational fluid dynamic (CFD) was employed to simulate the investigated pumping experiments using a single-phase modeling approach. Concrete was assumed as a single fluid with variable rheological properties across the pipe section, namely LL, sheared-BC, and plug-flow zones. The measured rheological and tribological properties of the investigated mixtures tested at different flow rates (Table 5.1) were used as the initial input of the numerical simulation. As reported by Tavangar et al. [30], according to the estimated Reynolds number ($Re = \rho.V.D_P/\mu_{P-C}$) and hydrodynamic entry length ($L_{e-Laminar} = 0.05.Re.D_P$) values, the entire pipe flow experiments can be considered as laminar and fully developed flow type. Therefore, a 2D simulation was carried out for 1-m pipe length to reduce the calculation time.

A numerical algorithm was then proposed to achieve the best fit with the experimental pressure loss values presented in Table 5.1. The OpenFOAM software [39] was used as an open-source code to introduce a new viscosity model, considering the radial variation of concrete across the pipe section, and carry out the proposed numerical algorithm. A steady-single fluid solver in OpenFOAM, namely simpleFoam [40-42], was employed to solve the Navier-Stokes equations for incompressible fluid using the SIMPLE (Semi-Implicit Method for Pressure Linked Equations) technique [41,42]. This technique can solve pressure-velocity coupling [41,42] using an iterative algorithm where the boundary conditions are set to allow the computation of velocity and pressure gradients. The discretized momentum equations are then solved to compute the intermediate velocity field. Subsequently, the (uncorrected) mass fluxes are computed. The pressure-correction equation is then solved to update the pressure field and boundary pressure corrections. Once the face mass fluxes are corrected, the velocity in each cell is corrected using the gradient of pressure corrections. The density is then updated due to pressure change [41,42].

5.3.1 Governing equations

Due to the incompressibility condition (i.e., constant density), the continuity and momentum equations in simpleFoam were considered, as follows [41]:

Continuity equation: $\nabla. u = 0$ 　　　　　　　　　　　　　　　　　　　　　　(5.1)

Momentum equation : $\nabla. \, (uu) = -\frac{1}{\rho}\nabla p + \frac{1}{\rho}\nabla.T$ (5.2)

where u and T represent the velocity and the stress tensor, respectively. It is worth mentioning that the variables in simpleFoam, including viscosity and yield stress, should be divided by the fresh density of the investigated mixtures to be implied in such incompressible fluid solver. It is worthy to mention that an equal density of the reference mixtures was assumed for different pipe-flow zones.

5.3.2 Boundary Conditions

The boundary conditions of the performed numerical simulations are illustrated in Fig. 5.3. A fixed value and zero gradient were applied for flow velocity as the inlet and outlet boundary conditions, respectively. In the case of pressure, the boundary conditions included the zero gradient at the inlet and constant value at the outlet. Moreover, no-slip and symmetry conditions were considered for the pipe wall and center axis, respectively [30].
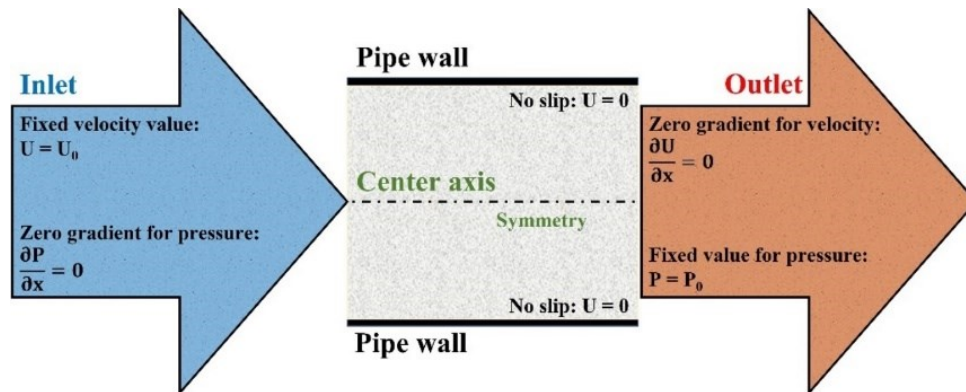
Fig. 5.3. Boundary conditions in performed numerical simulations.

5.3.3 Shear-rate dependent tri-viscous model

In this study, unlike the coordination-dependent bi-viscous pumping simulations in literature [4,34-38], the rheological properties of the concrete across the pipe are allowed to vary with shear-rate magnitude in each cell. Hence, different flow zones were identified based on their corresponding shear-rate values. Accordingly, a critical shear rate $\dot{\gamma}_{c\text{-LL}}$ is defined corresponding to the shear rate at the interface of the sheared-BC and LL (i.e., the minimum shear rate value in the LL or the maximum shear rate that the sheared-BC can experience). Therefore, shear rate

values of each cell at each time step are compared to this critical value. This method is referred to as the shear-rate dependent tri-viscous model with the tri-viscous term defined as follow:

(i) Bingham yield stress and plastic viscosity of LL (i.e., $\tau_{0\text{-LL}}$ and $\mu_{p\text{-LL}}$) are set to the cells with higher shear rates than $\dot{\gamma}_{c\text{-LL}}$;

(ii) the rheological parameters of the lower shear-rate cells (i.e., $\dot{\gamma} < \dot{\gamma}_{c\text{-LL}}$) correspond to those of the BC (i.e., $\tau_{0\text{-C}}$ and $\mu_{p\text{-C}}$);

(iii) the proposed tri-viscous model is developed based on the Herschel-Bulkley (H-B) viscosity model of OpenFOAM and the criterion corresponded to the shear rate of each computational cell. The loop presented in Fig. 4 was added to the H-B viscosity class of OpenFOAM to apply the proposed tri-viscous model. It is worthy to mention that any Bingham fluid in OpenFOAM, corresponding to different pipe flow zones, consists in an artificial viscosity (μ_0) in addition to its main parameters (i.e., yield stress τ_0 and plastic viscosity μ_p), as discussed earlier in introduction. The apparent viscosity for each cell is then calculated based on Eq. (5.3). The apparent viscosity (μ_{app}) of each cell is then updated according to the minimum value between the artificial and calculated apparent viscosities, as follows:

$$\mu_{app} = \min(\mu_0, \frac{\tau_0}{\dot{\gamma}} + \mu_p) \tag{5.3}$$

The artificial viscosity (μ_0) should be large enough to capture the unsheared zones ($\tau < \tau_0$) where the shear rate $\dot{\gamma}$ is lower than its critical value $\dot{\gamma}_c$. The magnitude of the calculated apparent viscosities ($\frac{\tau_0}{\dot{\gamma}} + \mu_p$) in the sheared and unsheared zones thus becomes smaller and larger than their μ_0, respectively. According to Eq. (5.3), the updated μ_{app} of the unsheared zones (i.e., plug-flow zone) equals μ_0. However, for other points, the μ_{app} is updated as was initially calculated (i.e., $\frac{\tau_0}{\dot{\gamma}} + \mu_p$).
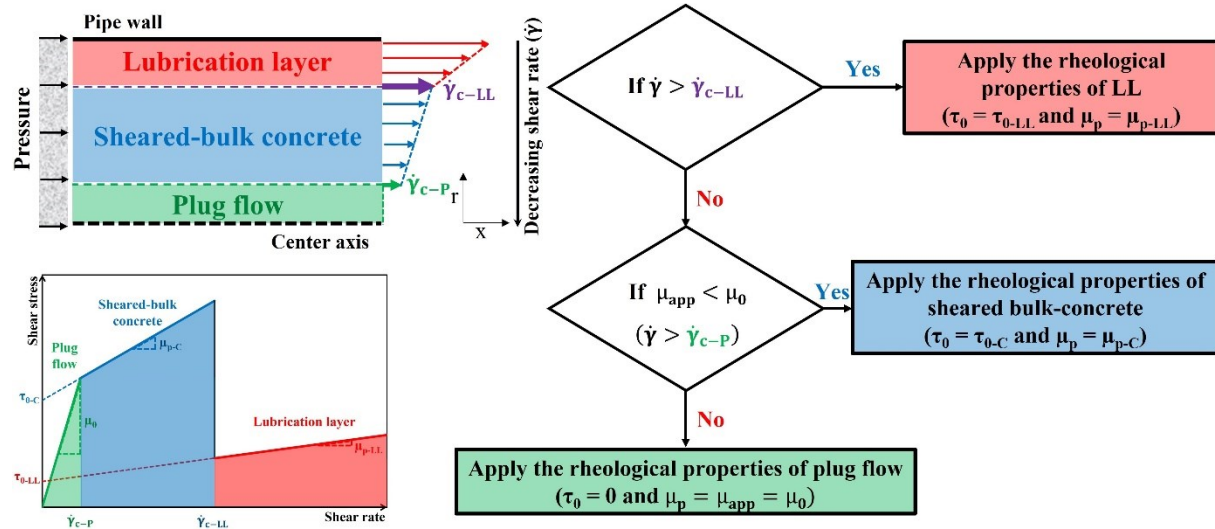
Fig. 5.4. Schematics of the proposed shear-rate dependent tri-viscous model considering radial variation of rheological properties of concrete across pipe section.

5.3.4 Numerical implementation of tri-viscous model layer

An algorithm was developed to implement the proposed shear-rate dependent tri-viscous model in the numerical simulations. As can be observed in Fig. 5.3, the inputs of the transport properties file of the numerical models included the rheological properties of BC ($\tau_{0\text{-C}}$ and $\mu_{\text{p-C}}$) and yield stress of LL ($\tau_{0\text{-LL}}$), presented in Table 5.1, as well as an initial assumption of the critical shear rate ($\dot{\gamma}_{\text{c-LL}}$) and artificial viscosity ($\mu_{0\text{-C}}$). The initial plastic viscosity of LL considered in the model was indirectly estimated by means of an initial e_{LL} assumption of 2 mm multiplied by the experimental η_{LL} values presented in Table 5.1. Due to abrupt radial changes in rheological parameters of concrete across the pipe, the continuum condition should be checked in each loop to confirm that the maximum velocity is obtained at the pipe center ($V_{\text{max}} = V_{r\,=\,0}$). According to the numerical algorithm presented in Fig. 5.3, different modelling assumptions were updated in maximum 10 trials, targeting a minimum prediction error ε of 5% relative to the experimental pressure drops, as defined in Eq. (5.4):

$$\varepsilon = \frac{\left|\Delta p_{\text{sim}} - \Delta p_{\text{exp}}\right|}{\Delta p_{\text{exp}}} \times 100\% \tag{5.4}$$

where Δp_{exp} and Δp_{sim} are the experimental and simulated pressure loss values, respectively. It is worth mentioning that the numerical simulations were carried out on an E5-1607 v2 CPU 3.00 GHz processor. The tri-viscous simulations required a total calculation time ranging from 14 to 300 s which is relatively shorter than the running times for two-fluid modelling simulations (69 to

528 s), carried out on the same processor [30]. As discussed earlier, this is due to solving a single Navier-Stokes equation in the proposed single-phase approach rather than two and neglecting the interaction between the two fluids (LL and BC) in double-fluid approach.
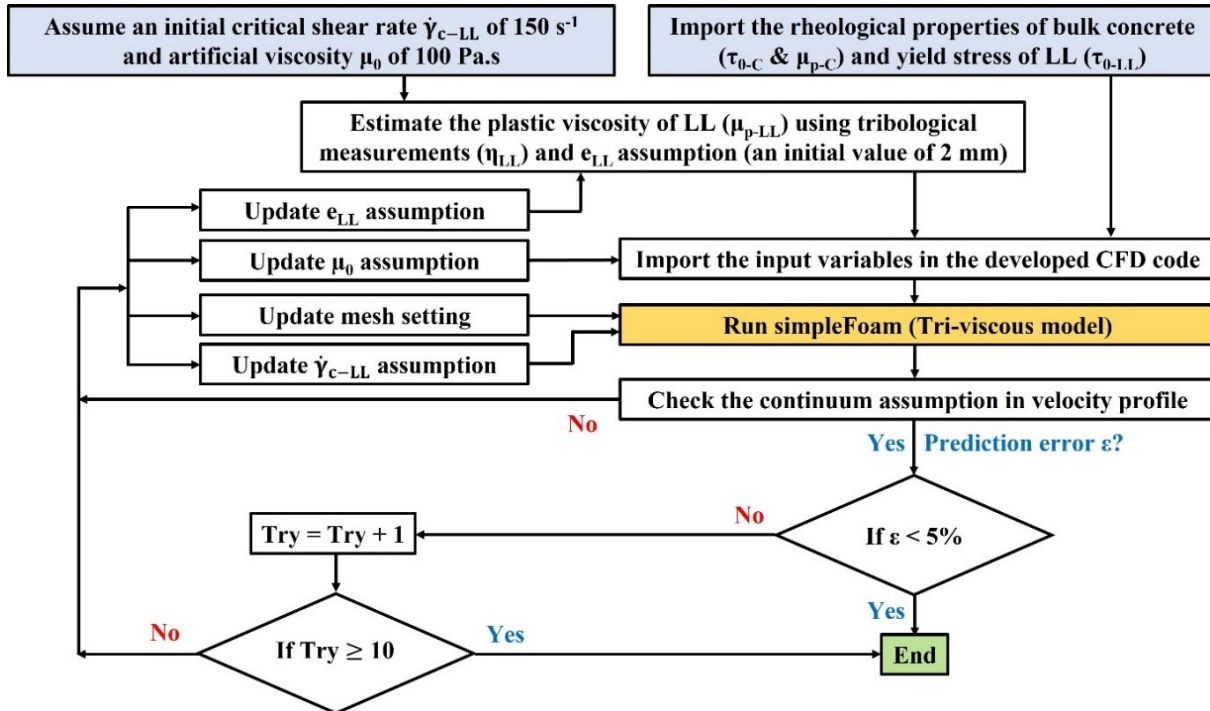
Fig. 5.5. The algorithm applied to implement the proposed shear-rate dependent tri-viscous model in the numerical simulations.

5.4 Results and discussions

The pumping experiments of the investigated flowable mixtures in reference [2], carried out in different pumping test cycles and under different flow rates (Table 5.1), were simulated through the 100- and 125-mm diameter pipes using the proposed tri-viscous approach. First, the numerical predictions were validated by the experimental values of pressure loss per unit length of pipe ($\Delta P/L$). The investigated pipe flow fields were then characterized in terms of flow velocity, Reynolds number, and shear rate. Moreover, using the obtained apparent viscosity and flow velocity profiles across the pipe section, different pipe flow zones, including LL and plug flow, were characterized in terms of rheological properties and thickness. The coupled effect of shear rate, rheological properties of different pipe flow zones, flow rate, and pipe diameter on pumping pressure loss was finally evaluated:

5.4.1 *Prediction of pumping pressure-loss*

As can be observed in Fig. 5.6a, the predicted pressure loss values using the proposed tri-viscous model are in very good agreement with the experimental measurements (Table 5.1), reflected by a R^2 of 0.997 and estimation index of 1.011, close to unity, as well as a low root-mean square-error (RMSE) of 4.377 kPa/m. Comparing to the analytical predictions made by Kaplan et al. models and reported by Feys et al. [2] (estimation index of 1.08 and R^2 of 0.88), the proposed tri-viscous simulations led to more precise predictions. It is worthy to mention that the analytical predictions were carried out using the LL viscous constants measured by tribological measurements. The higher accuracy of the numerical simulations can be explained by the more realistic estimation of the thickness and rheological properties of LL rather than those obtained by means of the tribometer. This is due to consideration of shear-rate dependency of rheological variation of pumped concrete across the pipe in the proposed tri-viscous model. As can be observed in Figs. 5.6b and 5.6c, the numerical simulations showed slightly higher accuracy for larger pipe. This was reflected by an estimation index of 0.993 closer to unity and lower RMSE of 3.615 kPa/m for 125-mm pipe rather than 1.015 and 4.998 kPa/m, respectively, for 100 mm one. The lower RMSE values can be explained by lower pressure loss values through the larger pipe under a given flow rate:

5.4.2 *Characterization of the investigated pipe flow fields*

5.4.2.1 *Flow velocity*

For a given pipe diameter, flow velocity decreases from the central axis towards pipe wall. Therefore, the maximum (Vmax) and zero velocity magnitudes are obtained at the central axis (r = 0) and vicinity of the pipe wall, respectively (Fig. 5.1). According to the numerical simulations, Vmax values ranged from 1.2 to 2.4 m/s (with maximum frequency of 29% for 1.7 ± 0.1 m/s) and 0.8 to 1.6 m/s (with maximum frequency of 36% for 1.3 ± 0.1 m/s) for the 100- and 125-mm diameter pipes, respectively. Moreover, as shown in Fig. 5.1, sudden changes were observed at velocity gradients across the pipe radius, which is due to the radial variation of rheological properties of concrete during pumping. Accordingly, low, medium, and significant changes in velocity gradient correspond to the plug-flow, sheared BC, and LL zones, respectively.

(a) All data   **(b) D_P = 100 mm**   **(c) D_P = 125 mm**
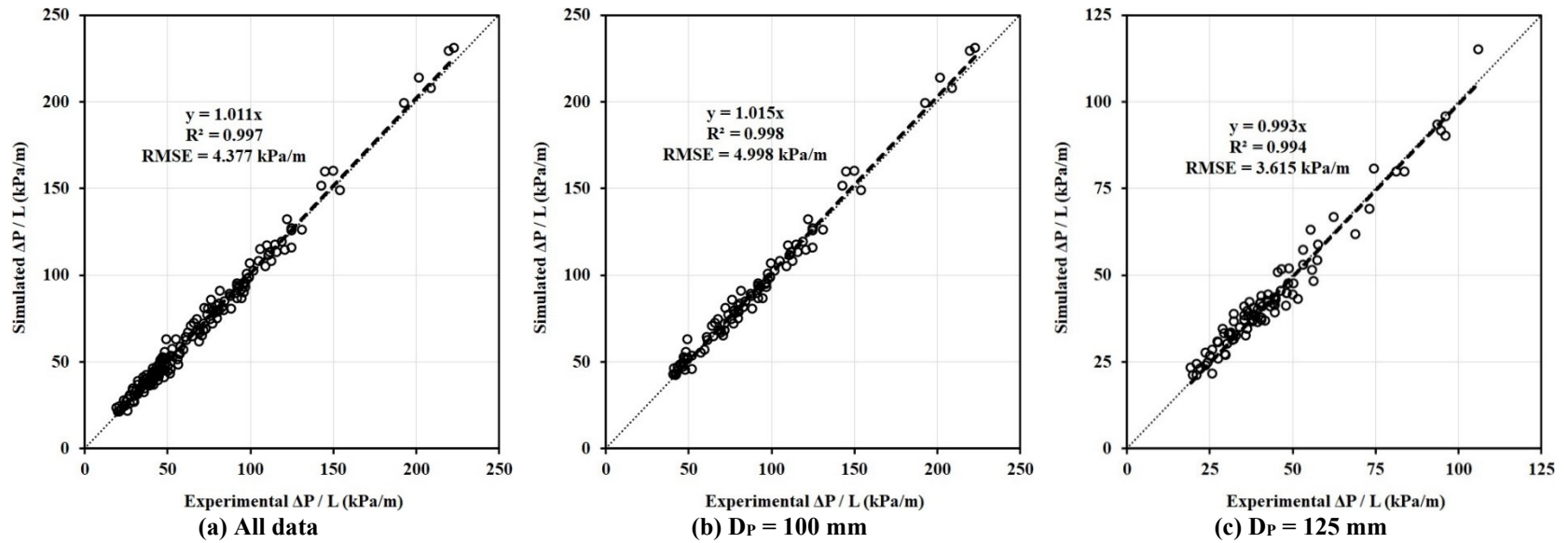
Fig. 5.6. Comparison between the simulated pressure loss values using the proposed shear-rate dependent tri-viscous model and experimentally measured values (Table 5.1), **(b)** 100-mm diameter pipes, and **(c)** 125-mm diameter pipes.

5.4.2.2 *Flow Reynolds number*

The Reynolds number (Re) is defined as the ratio of inertial-to-viscous forces within a fluid, which is subjected to relative internal movement due to different fluid velocities [43]. For pipe flow, the Re is generally defined by $Re = \frac{\rho \times V \times D_P}{\mu}$, as a function of density (ρ), velocity (V), and viscosity (μ) of the fluid and pipe diameter (D_P). When viscous forces are dominant, the flow tends to be laminar (Re < 2000) and is characterized by smooth and constant fluid motions [44]. In the case of concrete pipe flow, Re is low, and concrete pipe flow can be safely assumed laminar. However, due to low plastic viscosity of the of highly-flowable concrete mixtures, determining the possible range of Re for high-flow rate pumping processes, such as those investigated in this study, can reflect important information to predict the possible flow instabilities (e.g., particle migration, blockage, and wearing pipe walls). This can help other numerical modeling developers (e.g., DEM or CFD-DEM experts) to anticipate appropriate measures and settings to build up flow simulations more realistically for low-viscosity and high-flow rate simulations.

The Re of the investigated pumping experiments ranged from 1.8 to 18.8 (with the maximum frequency of 25% for 11 ± 1) and from 1.4 to 13.7 (with the maximum frequency of 22% for 7 ± 1) for the 100- and 125-mm diameter pipes, respectively. For a given pumping test cycle and concrete mixture, the Re corresponding to the pipe flows through the smaller pipe (D_P = 100 mm) are 13.7% higher than those obtained for the larger one (D_P = 125 mm). This is due to higher flow velocity in smaller pipes under a given flow rate.

5.4.2.3 *Critical shear rate*

Regarding the significant pumping-induced changes in concrete properties, it is of particular interest to determine the shear rate magnitudes that concrete may experience during pumping process but cannot be reproduced using the tribological experiments. Accordingly, the critical shear rates ($\dot{\gamma}_{c\text{-LL}}$) of the optimized simulations leading to the best fits with experimental pressure loss values were investigated. According to the numerical results, the investigated mixtures were subjected to critical shear rates ranged from 160 to 430 s^{-1} and 80 to 400 s^{-1} with maximum frequencies of 36% ± 1% for the $\dot{\gamma}_{c\text{-LL}}$ values of 275 ± 25 s^{-1} and 175 ± 25 s^{-1} at the interface of the sheared BC and LL in the 100- and 125-mm diameter pipes, respectively. The obtained $\dot{\gamma}_{c\text{-LL}}$ values are much higher than those obtained in through the coaxial-cylinders tribometer (< 10 s^{-1}). This can emphasis the significant dissimilarity between the flow conditions through tribological

measurements and real-scale pipe flows. The LLs formed in tribometer cannot represent those formed in vicinity of pipe walls. The critical shear rates obtained in 100-mm diameter pipe were found to be 30% higher than those occurred in 125-mm diameter pipe. This can be due to higher velocity in smaller pipes compared to the larger ones under a given flow rate, hence leading to higher radial-velocity gradient in the vicinity of smaller pipes' walls.

5.4.3 Characterization of lubrication layer

As elaborated earlier in section 4.2.1, due to the variation of rheological properties of concrete across the pipe, a sudden change is expected in radial velocity gradient at the LL-BC interface. Indeed, lower plastic viscosity of LL relative to the sheared-BC can lead to a sudden increase in velocity derivation relative to the radial distance from the pipe center. The LL thickness can thus be identified using the velocity profiles across the pipe (Fig. 5.7a). Accordingly, as shown in Fig. 5.7a, the exact radial position of the beginning of the LL zone corresponds to the point where a slight increase in the radial distance to the pipe center led to the highest difference in the slopes of tangent lines of the velocity profile.

The viscous constants of the simulated LLs (η_{LL}) were then evaluated by dividing the LL viscosity (μ_{p-LL}) to the LL thicknesses (e_{LL}), both obtained using the shear-rate dependent tri-viscous simulations. As can be observed in Figs. 5.7b and 5.7c, the ratios of the simulated η_{LL} values in 100- and 125-mm pipes-to-their corresponding tribological values ranged from 0.702 to 7.143 and 0.381 to 4.571, respectively. As shown earlier in Fig. 5.6, considering the shear-rate effect in the proposed tri-viscous model, the numerical simulations led to better predictions of pressure loss values rather than the analytical models where the experimental η_{LL} values were applied [2]. Hence, it can be concluded that the numerical simulations led to better characterization of the formed LL during the investigated pumping experiments compared to those experimentally evaluated in the coaxial-cylinders tribometer.
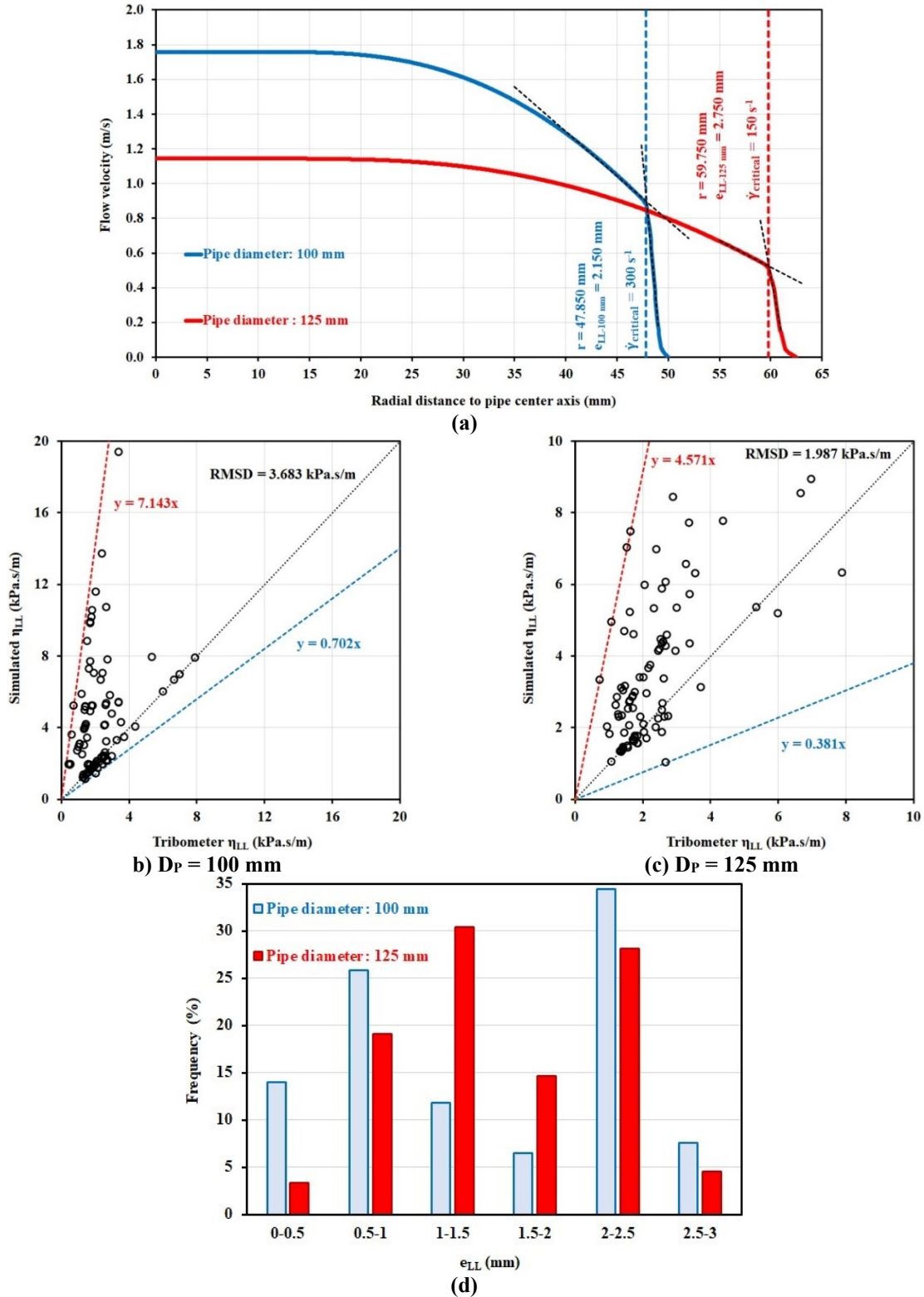
Fig. 5.7. (a) Identification of LL thickness using the velocity profile (example for pipe flow of SCC7 mixture at test 3), comparison between viscous constants (η_{LL}) obtained using numerical simulations and experimental tribological measurements for **(b)** 100- and **(c)** 125-mm diameter pipes, and **(d)** frequency distribution of LL thicknesses (e_{LL}) obtained using the proposed shear-rate dependent tri-viscous model for 100- and 125-mm diameter pipes.

Furthermore, as can be observed in Fig. 5.7d, the obtained LL thicknesses using the numerical simulations ranged from 0.4 to 2.9 mm which is in agreement with those reported in literature for highly flowable concrete mixtures (1-4 mm) [4,30,45]. On the other hand, the LL thicknesses obtained using the proposed shear-rate dependent tri-viscous model resulted in a wider distribution compared to those obtained using the radially variable tri-viscous approach [30]. In fact, considering the shear rate magnitudes as the determining criterion for rheological variation across the pipe, rather than the radial position in the tri-viscous model [30], led to less grid sensitivity and coordination dependency of simulated LL thicknesses. As can be seen in Fig. 5.7d, the majority of the LL thicknesses for 100- and 125-mm diameter pipes ranged from 2 to 2.5 mm (34%) and from 1 to 1.5 mm (30%), respectively.

5.4.4 Characterization of plug-flow zone

As discussed earlier, the plug-flow zone in the proposed tri-viscous model was simulated using a Newtonian model with relatively higher viscosity than the sheared-BC and LL ($\mu_{0\text{-Plug}} \gg \mu_{p\text{-C}}$ and $\mu_{p\text{-LL}}$). Therefore, the apparent viscosity profile across the pipe shows its maximum value ($\mu_{app\text{-max}}$) at the plug-flow zone, corresponding to very low shear rates ($\dot{\gamma} \approx 0$). Regarding the assumed Newtonian behavior of the plug flow in the proposed model, the $\mu_{app\text{-max}}$ values are expected to be constant across the plug-flow zone and equal to $\mu_{0\text{-Plug}}$. Accordingly, as shown in Fig. 5.8a, by increasing the radial distance to the pipe center, the point where the apparent viscosity profile suddenly drops from its maximum value can correspond to the plug radius (r_{Plug}).

According to the numerical results, the r_{Plug} values obtained for 100- and 125-mm diameter pipes ranged from 0 to 24.7 and 43.4 mm, respectively. Larger plug-flow zones obtained across the larger pipes can be due to lower flow velocity in larger pipes under a given flow rate magnitude. Indeed, under lower flow velocities, smaller portion of concrete is potentially subjected to shear, hence leading to larger plug radius. As can be observed in Fig. 5.8b, the majority of the plug radii in both pipe sizes ranged from 10 to 20 mm (50.5% for $D_P = 100$ mm and 55.1% for $D_P = 125$ mm).
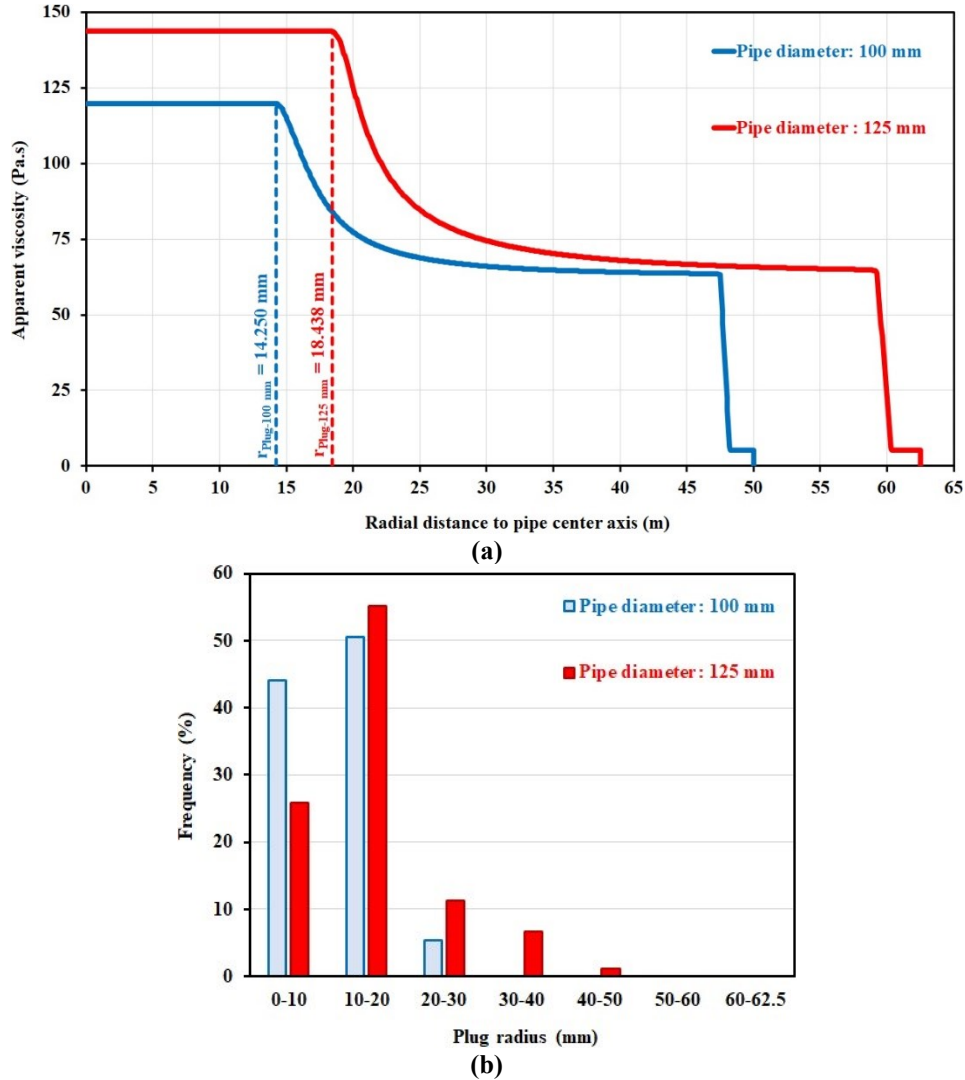
Fig. 5.8. (a) Apparent viscosity profile across pipe's sections and identification of plug radius r_{Plug} (an example for pipe flow SCC7 mixture at test 3) and **(b)** frequency distribution of r_{Plug} values in different pipe diameters obtained using the proposed shear-rate dependent tri-viscous model.

5.4.5 *Coupled effect of shear rate, rheology of different pipe-flow zones, and pipeline specifications on pressure loss*

Different pipe flow zones were characterized in terms of rheological properties and radial positions. Accordingly, the viscosity μ_{0-Plug} (Pa.s) and radius r_{Plug} (mm) of plug-flow zones were numerically evaluated using the proposed tri-viscous model. The yield stress τ_{0-C} (Pa) and plastic viscosity μ_{P-C} (Pa.s) of sheared-BC were experimentally measured using the concrete rheometer (Table 5.1). The LLs of the investigated pumping experiments were characterized in terms of the yield stress τ_{0-LL} (Pa), measured using the coaxial-cylinder tribometer (Table 5.1). On the other hand, the critical shear rate $\dot{\gamma}_{c-LL}$ and viscous constant η_{LL} (kPa.s/m) were evaluated using the proposed tri-

viscous model. Also, the pipeline specifications include the flow rate Q (l/s) and pipe diameter D_P (mm) (Table 5.1). The coupled effect of characteristics of different flow zones, including $Effect_{LL}$, $Effect_{Sheared-BC}$, and $Effect_{Plug-flow\ zone}$, and pumping specifications (Q and D_P) on pumping pressure loss are evaluated in this section. The experimental $\Delta P/L$ (kPa/m) values were then correlated to the effect of different pipe-flow zones, Q (l/s), and D_P (mm), as follows:

$$\Delta P/_L = \left(Effect_{Plug-flow\ zone} + Effect_{Sheared-BC} + Effect_{LL}\right) \times Q^{A_1} \times D_P^{A_2} + A_3 \tag{5.5}$$

where A1, A2, and A3 are the adjustment power indices for Q and DP parameters and an adjustment constant, respectively. Moreover, the effect of characteristics of different pipe flow zones were considered, as follow:

$$Effect_{Plug-flow\ zone} = A_4 \times \left(\frac{\mu_{0-Plug}}{A_5^{r_{Plug}}}\right)^{A_6} \tag{5.6}$$

$$Effect_{Sheared-BC} = A_7 \times \left(\tau_{0-C}^{A_8} \times \mu_{p-C}^{A_9}\right) \tag{5.7}$$

$$Effect_{LL} = A_{10} \times A_{11}^{\tau_{0-LL}} \times \eta_{LL}^{A_{12}} \times \dot{\gamma}_{c-LL}^{A_{13}} \tag{5.8}$$

where A_4 to A_{13} are the adjustment factors and power indices corresponding to the characteristics of plug-flow zone (A_4 to A_6), sheared-BC (A_7 to A_9), and LL (A_{10} to A_{13}). A Microsoft Excel Solver was developed based on Eqs. (5) to (8) to identify the adjustment factors A_1 to A_{13} allowing the best fit with experimental pressure loss ($\Delta P/L$) values (Table 5.1). The results of the developed solver are then presented in Eq. (5.9).

$$\Delta P/_L = \left[\underbrace{39863.4\left(\frac{\mu_{0-Plug}}{0.9726^{r_{Plug}}}\right)^{0.7484}}_{\text{Plug-flow zone}} + \underbrace{74220.2\left(0.9996^{\tau_{0-C}} \times \mu_{p-C}^{0.9993}\right)}_{\text{Sheared-bulk concrete zone}} \right.$$
$$\left. + \underbrace{17.1\left(1.0053^{\tau_{0-LL}} \times \eta_{LL}^{0.2253} \times \dot{\gamma}_{c-LL}^{1.8973}\right)}_{\text{Lubrication-layer zone}}\right] \times \underbrace{\left(\frac{Q^{0.3454}}{D_P^{2.6345}}\right)}_{\text{Pumping specifications}} - 8.464 \tag{5.9}$$

As can be observed in Fig. 5.9, the experimental pressure drop values are well correlated to the characteristics of the three different flow zones formed across the pipe section and critical shear rate obtained using the proposed model, flow rate, and pipe diameter. The high precision of the derived correlation had an R^2 and estimation index of 0.988 and low RMSE of 8.489 kPa/m. The

correlation led to more precise pressure-drop prediction compared to the analytical prediction proposed by Kaplan et al. [5,7,8], where the tribological measurements were applied (estimation index of 1.08 and R^2 of 0.88) [2]. This is due to consideration of shear-rate effect and plug-flow zone in the proposed tri-viscous model, hence leading to better optimization of the characteristics of different pipe flow zones compared to the experimental characterization of LL using the coaxial-cylinders tribometer.
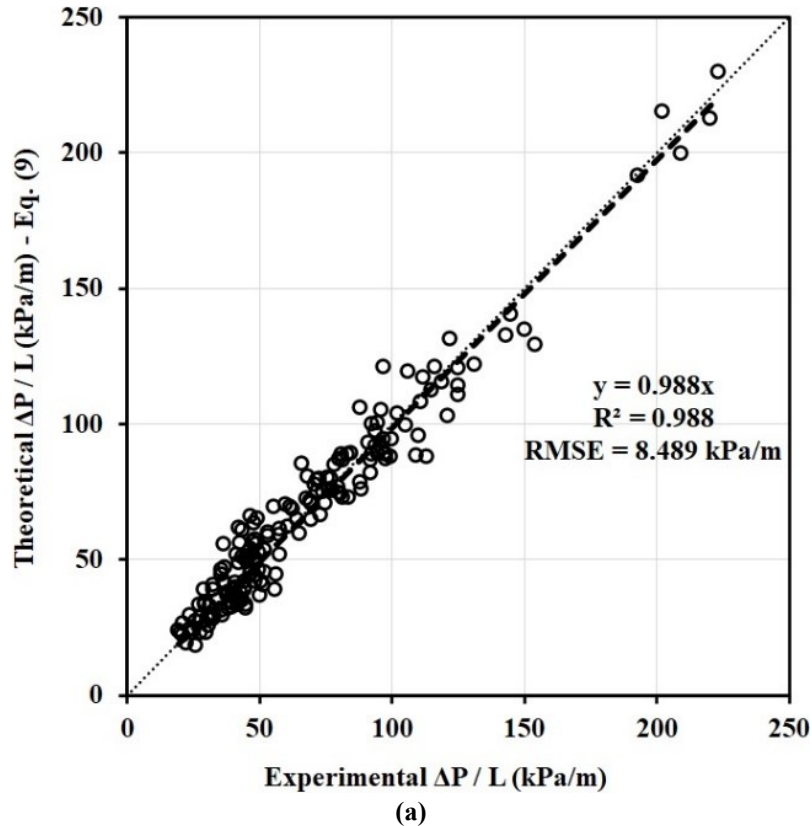
Fig. 5.9. Comparison between experimental (Table 1) and theoretical pressure loss ΔP/L (kPa/m) values obtained using Eq. (5-9).

According to the established Eq. (5.9), pressure drop increased with the rheological properties of the plug-flow, sheared-BC, and LL zones, as well as the higher flow rate and critical shear rate, and smaller pipe diameter. Regarding the obtained power indices, for a given flow rate and pipe diameter, the critical shear-rate in LL showed the most dominant effect on pressure loss rather than the rheological properties of different pipe flow zones. Moreover, the viscosity values of the sheared-BC and plug-flow zones are found to be the most effective rheological properties on pumping pressure loss, rather than the η_{LL}. However, the viscous constant of LL was found more

effective on pressure decay rather than its yield stress. On the other hand, Eq. (5.9) revealed that the pumping pressure is more controlled by the pipe diameter rather than the pumping flow rate.

5.5 Conclusions

In this study, a novel shear-rate dependent tri-viscous model was proposed to simulate the shear-induced radial variations of rheological properties of pumped concrete. The proposed model was employed to simulate 182 pumping experiments carried out using 22 highly flowable concrete mixtures, reported in references [1,2]. The numerical simulations were successfully carried out using OpenFOAM software to predict the pressure loss values for 1-m pipe length to reduce the calculation time. According to the simulation results presented in this study, the following conclusions are warranted:

- The proposed shear-rate dependent tri-viscous model led to considerably lower calculation time (14 to 300 s) compared to the two-fluid approach (69 to 528 s).

- The proposed tri-viscous model successfully characterized different pipe flow zones (LL, sheared-BC, and plug flow zones) in terms of rheological properties and thicknesses, which could not be achieved using the empirical measurements and analytical models. By considering the shear-rate effect, the numerical simulations led to higher precision of pressure-drop prediction compared to the analytical model proposed by Kaplan et al [5].

- Under 8.1-16.4 l/s flow rates, the simulated maximum flow velocity (V_{max}), Reynolds number (Re), and critical shear rate ($\dot{\gamma}_{c-LL}$) values of the investigated mixtures ranged between 0.8-2.4 m/s, 1.4-18.8, and 80-430 s^{-1}, respectively. The investigated mixtures exhibited 44% higher V_{max}, 14% higher Re, and 30% higher $\dot{\gamma}_{c-LL}$ values for flow through a 100-mm diameter pipe compared to 125-mm diameter pipe.

- Compared to tribological measurements, the simulated viscous constant (η_{LL}) values obtained for the 100- and 125-mm diameter pipes had 0.7 to 7.1 and 0.4 to 4.6 higher values, respectively. The simulated LL thicknesses using the proposed tri-viscous model varied between 0.4 and 2.9 mm for both pipe diameters. Plug radii up to 25 and 43 mm were obtained for the 100- and 125-mm diameter pipes, respectively. The majority of the plug radii in both pipe sizes ranged from 10 to 20 mm.

- The coupled effect of critical shear rate, rheological properties and thickness of different pipe-flow zones, flow rate, and pipe diameter on pumping pressure loss was successfully evaluated using a power-law correlation. This resulted in higher precision of pressure-drop prediction compared to the analytical Kaplan et al. model [5]. The $\dot{\gamma}_{\text{c-LL}}$ showed the most dominant effect on pressure drop rather than the rheological characteristics and thickness of different pipe flow zones. Among the various rheological properties, pressure loss is shown to be more influenced by viscosities of the sheared-BC and plug-flow zones rather than that of the viscous constant of the LL.

5.6 Declaration of competing interest

The authors declare that they have no known competing financial interests or personal relationships that could have appeared to influence the work reported in this paper.

5.7 Acknowledgement

REFERENCES

[1]   R. Khatib, Analysis and prediction of pumping characteristics of high-strength self-consolidating concrete, Ph.D. Thesis, Université de Sherbrooke (2013). http://hdl.handle.net/11143/6634.

[2]   D. Feys, K.H. Khayat, A. Perez-Schell, R. Khatib, Prediction of pumping pressure by means of new tribometer for highly-workable concrete, Cement and Concrete Composites, 57 (2015) 102-115. https://doi.org/10.1016/j.cemconcomp.2014.12.007.

[3]   D. Feys, K.H. Khayat, R. Khatib, How do concrete rheology, tribology, flow rate and pipe radius influence pumping pressure?, Cement and Concrete Composites, 66 (2016) 38-46. https://doi.org/10.1016/j.cemconcomp.2015.11.002.

[4]   E. Secrieru, W. Mohamed, S. Fataei, V. Mechtcherine, Assessment and prediction of concrete flow and pumping pressure in pipeline, Cement and Concrete Composites, 107 (2020) 103495.

https://doi.org/10.1016/j.cemconcomp.2019.103495.

[5]   D. Kaplan, F. de Larrard, T. Sedran, Design of concrete pumping circuit, ACI Materials Journal, 102 (2) (2005) 110-117. https://doi.org/10.14359/14304.

[6]   A.N. Ede, The resistance of concrete pumped through pipelines, Magazine of Concrete Research, 9 (27) (1957) 129-140. https://doi.org/10.1680/macr.1957.9.27.129.

[7]   D. Kaplan, Pumping of Concrete. Ph.D. Thesis, LCPC, Paris, France (1999) (In French). https://tel.archives-ouvertes.fr/tel-01310219/.

[8]   D. Kaplan, T. Sedran, F. De Larrard, M. Vachon, G. Machese, Forecasting pumping parameters, In: Proc. of the 2nd Int RILEM symp. on self-compacting concrete, Tokyo, 2001, 556-564.

[9]   S.H. Kwon, K.P. Jang, J.H. Kim, S.P. Shah, State of the art on prediction of concrete pumping, International Journal of Concrete Structures and Materials, 10 (3) (2016) 75-85. https://doi.org/10.1007/s40069-016-0150-y.

[10]   S.H. Kwon, S.D. Jo, C.K. Park, J.H. Jeong, S.D., Jo, S.H. Lee, Prediction of concrete pumping: Part II-analytical prediction and experimental verification, ACI Materials Journal, 110 (6) (2013) 657-668. https://dx.doi.org/10.14359/51686333.

[11]   S. Fataei, E. Secrieru, V. Mechtcherine, N. Roussel, A first-order physical model for the prediction of shear-induced particle migration and lubricating layer formation during concrete pumping, Cement and Concrete Research, 147 (2021) 106530. https://doi.org/10.1016/j.cemconres.2021.106530.

[12]   G. De Schutter, D. Feys, Pumping of fresh concrete: Insights and challenges, RILEM Technical Letters, 1 (2016) 76-80. https://doi.org/10.21809/rilemtechlett.2016.15.

[13]   T. Tavangar, M. Hosseinpoor, A. Yahia, K.H. Khayat, Computational investigation of concrete pipe flow: Critical review, ACI Materials Journal, 118 (6) (2021) 203-215. https://dx.doi.org/10.14359/51733124.

[14]   R.J. Phillips, R.C. Armstrong, R.A. Brown, A.L. Graham, J.R. Abbott, A constitutive equation for concentrated suspensions that accounts for shear-induced particle migration, Physics of Fluids A: Fluid Dynamics, 4 (30) (1992) 30-40. https://doi.org/10.1063/1.858498.

[15]   D. Feys, G. De Schutter, S. Fataei, N.S. Martys, V. Mechtcherine, Pumping of concrete: Understanding a common placement method with lots of challenges, Cement and Concrete Research,

154 (2022) 106720. https://doi.org/10.1016/j.cemconres.2022.106720.

[16]   F. Li, W. Shen, Q. Yuan, X. Hu, Z. Li, C. Shi, An overview on the effect of pumping on concrete properties, Cement and Concrete Composites, 129 (2022) 104501. https://doi.org/10.1016/j.cemconcomp.2022.104501.

[17]   M. Ouchi, J. Sakue, Self-compactability of fresh concrete in terms of dispersion and coagulation of particles of cement subject to pumping, In: Proceedings of the 3rd North-American conference on the design and use of self-consolidating concrete, Chicago (2008).

[18]   K. Takahasi, T. Bier, Mechanisms for the changes in fluidity and hydration kinetics of grouts after mixing. In: Proceedings of the 6th international RILEM conference on self-compacting concrete, Paris (2013).

[19]   T. Bier, T. Takahashi, Influence of pumping of fresh concrete properties for SCC, ACI Spring Convention, Kansas-City (2015).

[20]   D. Feys, G. De Schutter, K.H. Khayat, R. Verhoeven, Changes in rheology of self-consolidating concrete induced by pumping, Materials and Structures, 49 (2016) 4567-4677. https://doi.org/10.1617/s11527-016-0815-7.

[21]   R. Dyer, An investigation of concrete pumping pressure and the effects of pressure on the air void system of concrete, University of Washington, Ph.D. Dissertation, 1991. https://hdl.handle.net/11244/320968.

[22]   J. Yingling, G. Mullings, R. Gaynor, Loss of air content in pumped concrete, Concrete International, 14 (10) (1992) 57-61.

[23]   R. Pleau, M. Pigeon, A. Lamontagne, M. Lessard, Influence of pumping on characteristics of air-void system of high-performance concrete, Transportation Research Record (1995) 30-36. http://onlinepubs.trb.org/Onlinepubs/trr/1995/1478/1478-004.pdf.

[24]   J. Vosahlik, K. Riding, D. Feys, W. Lindquist, K. Keller, S. Van Zetten, B. Schulz, Concrete pumping and its effect on the air void system, Materials and Structures, 51 (4) (2018) 94. https://doi.org/10.1617/s11527-018-1204-1.

[25]   T. Fantous, A. Yahia, Effect of viscosity and shear regime on stability of the air-void system in self-consolidating concrete using Taguchi method, Cement and Concrete Composites, 112 (2020) 103653. https://doi.org/10.1016/j.cemconcomp.2020.103653.

[26] D. Gálvez-Moreno, D. Feys, K. Riding, Characterization of air dissolution and reappearance under pressure in cement pastes by means of rheology, Frontiers in Materials, 6 (2019) 73. https://doi.org/10.3389/fmats.2019.00073.

[27] T.T. Ngo, E.H. Kadri, R. Bennacer, F. Cussigh, Use of tribometer to estimate interface friction and concrete boundary layer composition during the fluid concrete pumping, Construction and Building Materials, 24 (7) (2010) 1253-1261. https://doi.org/10.1016/j.conbuildmat.2009.12.010.

[28] F. Chapdelaine, Étude fondamentale et pratique sur le pompage du béton, Ph.D. Thesis, Université Laval (2007). http://hdl.handle.net/20.500.11794/18881.

[29] D. Feys, K.H. Khayat, A. Perez-Schell, R. Khatib, Development of a tribometer to characterize lubrication layer properties of self-consolidating concrete, Cement & Concrete Composites, 54 (2014) 40-52. https://doi.org/10.1016/j.cemconcomp.2014.05.008.

[30] T. Tavangar, M. Hosseinpoor, A. Yahia, K.H. Khayat, Novel tri-viscous model to simulate pumping of flowable concrete through characterization of lubrication layer and plug zones, Cement and Concrete Composites, 126 (2022) 104370. https://doi.org/10.1016/j.cemconcomp.2021.104370.

[31] M. Choi, C.F. Ferraris, N.S. Martys, D. Lootens, V.K. Bui, H.R.T. Hamilton, Metrology needs for predicting concrete pumpability, Advances in Materials Science and Engineering, (2015) 456238 http://dx.doi.org/10.1155/2015/456238.

[32] R. Schwarze, CFD-Modellierung: Grundlagen und Anwendungen bei Strömungsprozessen, Springer-Verlag, Berlin/Heidelberg, 2013 ISBN 978-3-642-24378-3. https://doi.org/10.1007/978-3-642-24378-3.

[33] M. Choi, N. Roussel, Y. Kim, J. Kim, Lubrication layer properties during concrete pumping, Cement and Concrete Research, 45 (2013) 69-78. https://doi.org/10.1016/j.cemconres.2012.11.001.

[34] J.D. Dent, T.E. Lang, A biviscous modified Bingham model of snow avalanche motion, Annals of Glaciology, 4 (1983) 42-46. https://doi.org/10.1017/S0260305500005218.

[35] S.W. Jeong, Determining the viscosity and yield surface of marine sediments using modified Bingham models, Geoscience Journal, 17 (2013) 241-247. https://doi.org/10.1007/s12303-013-0038-7.

[36] E. Secrieru, Pumping behaviour of modern concretes – Characterisation and prediction, Ph.D. Dissertation, Technische Universität Dresden (2018). https://nbn-resolving.org/urn:nbn:de:bsz:14-qucosa-234912.

[37] V.N. Nerella, V. Mechtcherine, Virtual Sliding Pipe Rheometer for estimating pumpability of concrete, Construction and Building Materials, 170 (2018) 366-377. https://doi.org/10.1016/j.conbuildmat.2018.03.003.

[38] E. Secrieru, J. Khodor, C. Schröfl, V. Mechtcherine, Formation of lubrication layer and flow type during pumping of cement-based materials, Construction and Building Materials, 178 (2018) 507-517. https://doi.org/10.1016/j.conbuildmat.2018.05.118.

[39] www.openfoam.org.

[40] C.J. Greenshields, OpenFOAM user guide version 6, OpenFOAM Found. Ltd. (2017) U-94. https://cfd.direct/openfoam/user-guide/.

[41] M. Winter, Benchmark and validation of Open Source CFD codes, with focus on compressible and rotating capabilities, for integration on the SimScale platform, Master Thesis, Chalmers University of Technology (2013). https://hdl.handle.net/20.500.12380/198965.

[42] H. Khawaja, M. Moatamedi, Semi-implicit method for pressure-linked equations (SIMPLE) - solution in MATLAB®, The International Journal of Multiphysics, 12 (4) (2018) 313-326. https://doi.org/10.21152/1750-9548.12.4.313.

[43] N. Rott, Note on the history of the Reynolds number, Annual Review of Fluid Mechanics, 22 (1990) 1-12. https://doi.org/10.1146/annurev.fl.22.010190.000245.

[44] R.B. Bird, W.E. Stewart, E.N. Lightfoot, Transport Phenomena, John Wiley & Sons, ISBN: 978-0-470-11539-8, 2006.

[45] R. Khatib, K.H. Khayat, Pumping of flowable concrete: Analytical prediction and experimental validation, ACI Materials Journal, 118 (5) (2021) 3-16. https://dx.doi.org/10.14359/51732928.

Chapter 6. Discrete-element modeling of shear-induced particle migration during zones concrete pipe flow: Effect of size distribution and concentration of aggregate on formation of lubrication layer

173

CHAPTER 6. Discrete-element modeling of shear-induced particle migration during zones concrete pipe flow: Effect of size distribution and concentration of aggregate on formation of lubrication layer

Authors and affiliations

Tooran Tavangar: Ph.D. candidate, Cement and Concrete Research Group, Department of Civil and Building Engineering, Université de Sherbrooke, Sherbrooke, Québec, Canada, J1K 2R1.

Masoud Hosseinpoor: Research Assistance, Cement and Concrete Research Group, Department of Civil and Building Engineering, Université de Sherbrooke, Sherbrooke, Québec, Canada, J1K 2R1.

Jeffery S. Marshall: Professor, Department of Mechanical Engineering, Université de Sherbrooke, Burlington, VT, USA.

Ammar Yahia: Professor, Cement and Concrete Research Group, Department of Civil and Building Engineering, Université de Sherbrooke, Sherbrooke, Québec, Canada, J1K 2R1

Kamal H. Khayat, Professor, Department of Civil, Architectural and Environmental Engineering, Center for Infrastructure Engineering Studies, Missouri University of Science and Technology, Rolla, MO, USA.

Chapter 6. Discrete-element modeling of shear-induced particle migration during zones concrete pipe flow: Effect of size distribution and concentration of aggregate on formation of lubrication layer

174

Abstract

The paper seeks to better understand the particulate mechanics giving rise to the lubrication layer (LL) in flows with wide particle-size distributions (PSD) typical of concrete pumping applications. The study uses a soft-sphere discrete element method (DEM) to simulate the shear-induced particle migration (SIPM) mechanism of formation of the LL. To provide realistic understanding of SIPM and rheological heterogeneity of concrete, three wide PSDs (fine, medium, and coarse) and three different concentrations (10%-40%) of five spherical-particle subclasses (1-17 mm diameter) were investigated. The radial evolution of concentration and particle distribution was simulated over time and the LL formation was successfully simulated. The predicted LL thicknesses compared well with experimental values. The coupled effect of PSD, concentration, and mean diameter of particles on wall effect, SIPM, and rheological heterogeneities across the pipe was evaluated. Higher rheological heterogeneity across the pipe was obtained for higher concentration and coarser particle size distributions.

Keywords: Concrete pumping; Discrete element method; Lubrication layer; Particle-size distribution; Shear-induced particle migration.

6.1 Introduction

Concrete pumping is a widespread technique to continuously transport large amounts of material long distances [1,2]. However, pumped concrete is reported to experience major changes in its rheological properties and homogeneity under applied pressure and shear [3-7]. One such change is the formation of a thin layer of highly flowable mortar in the vicinity of the pipe wall, called the lubrication layer (LL). Simultaneous with the LL formation, a higher concentration of aggregate in the pipe center can result in higher yield stress values, which increases the risk of plug flow. Such rheological heterogeneity across the pipe mainly governs the concrete pumpability. The mechanisms behind such multiphasic behavior of concrete pipe flow need to be investigated to avoid pumping damage, optimize the characteristics of different phases, and ensure successful pumpability [8]. However, the opaque nature of fresh concrete, wide particle-size distribution (PSD) of aggregate (from several μm to several mm), and non-Newtonian behavior of suspending cement paste/mortar matrix bring numerous complexities to both experimental and theoretical investigations of the pressure-driven concrete flow behavior.

When the concrete pipe flow is fully developed, the relative concentration of aggregate gradually increases from the vicinity of the pipe wall towards the pipe center. This gradient in particle size is caused by the mechanism of shear-induced particle migration (SIPM) [8]. SIPM is an irreversible phenomenon occurring under a non-uniform shear-rate profile which leads the particles to migrate in the perpendicular direction to the shear plane. The variation of the particle concentration and size profiles caused by SIPM impacts the flow field, leading to radial viscosity variation of the flowing suspension. This phenomenon was firstly recognized by Karnis et al. [9], who reported that the flow velocity profile of suspensions becomes blunter by increasing the size or concentration of solid particles. It was observed that the blunted velocity profile forms due to the migration of particles from higher to lower shear-rate zones [10-12]. Various rheological and phenomenological models were proposed to describe the SIPM mechanism [13-17], using the mass conservation and particle momentum equations [14] to derive approximate diffusion equations for particle motion [15-17]. The shear-induced diffusion model (SIDM) explains the particle diffusion in terms of collision and viscosity fluxes. It was revealed that SIPM is significantly controlled by the size and concentration of particles and flow shear rate [11,15-17]. The simulated shear-induced variations in local concentrations across the pipe using SIDM confirmed the radial variation of rheological properties of concrete, hence leading to formation of the LL and plug zones [18-21]. It was confirmed that the characteristics of LL can significantly affect the pumpability of concrete [1,8,22-24]. Therefore, to better control the concrete pumpability under a given flow rate (shearing condition), the effect of concentration and PSD of aggregate on formation of LL should be investigated.

For concrete pumping applications, typical values of the LL thickness of 1-10 mm have been reported [19,25-28]. The LL has been observed to consist of low concentrations of aggregate finer than 2 mm and high concentration of cement paste [29-31]. In order to better predict the pumpability of concrete, it is of particular importance to accurately characterize the LL in terms of its thickness, composition (e.g., content and size distribution of solid content), and rheological properties through the experimental procedures and theoretical simulations of its multiphasic mechanism of formation. The LL has been characterized using various experimental techniques [8,24]. These include digital image processing (DIP) of hardened concrete in pipe cross sections

Chapter 6. Discrete-element modeling of shear-induced particle migration during zones concrete pipe flow: Effect of size distribution and concentration of aggregate on formation of lubrication layer

176

[32] and ultrasonic pulse velocimetry (UPV) [19,25] to estimate the LL thickness. Frictional rheometers, including sliding rheometers [33] and rotational tribometers [1,29,34,35], have been employed to evaluate the rheological properties of the LL. However, measurements with these approaches suffer from loss of precision due to the technical complexities of DIP and UPV methods, as well as the absence of pressure and significantly lower shear rate values (< 10 s-1) encountered in frictional rheometers compared to those of real concrete pipe flows (several 100 s-1) [8]. Recently, numerical modeling has been increasingly employed as an alternative to directly simulate the mechanism of formation of the LL, to characterize the LL, and to predict concrete pumpability [8].

Both continuum and discrete numerical approaches have been used in the literature to simulate fresh concrete flow [8,36,37]. In the continuum approach, neglecting the presence of aggregate, concrete is mostly modelled as one or two homogeneous fluids (single-phase approach) corresponding to the bulk concrete (BC) and the LL with different rheological properties [30,38-41]. This approach requires significantly lower calculation time for modeling the large-scale pipelines than does the discrete approach [8]. However, the single-phase approach cannot directly simulate the particle-particle, particle-pipe wall, and fluid-particle interactions governing the SIPM mechanism leading to formation of the LL [8]. For these purposes, discrete computational methods that simulate motion of individual particles, such as discrete-element method (DEM) [42-46], are required [8].

DEM is a Lagrangian approach that is widely used in granular-flow modeling [47] to understand the fundamental phenomena occurring at the particle level, including segregation and blocking [48]. Regarding the wide range of concentration and size of aggregate in concrete matrix, DEM can be a suitable approach to consider the interactions between the particles and simulate the SIPM during concrete pipe flow [8,42-46]. Cao et al. [43] simulated the concrete pumping pressure in 90° bends using a soft-sphere DEM approach. The coarse aggregate (10-40 mm) and mortar (10-20 mm) were modeled using spherical particles. The viscous behavior of concrete and interparticle contacts were modeled using a viscous damping model and a linear model was used to approximate normal elastic rebound. The DEM simulations revealed that increasing the coarse aggregate content (10% to 70%) led to higher pumping pressure. Haustein et al. [44] used a soft-sphere DEM

approach to simulate the effect of spherical-particle contacts on SIPM of a dry, bidisperse granular mixture under pulsating pumping without taking into account any suspending fluid and hydrodynamics. The numerical simulations revealed that the particles located close to the central axis exhibited high packing density. On the other hand, the packing density of the particles exposed to shear was loosened in vicinity of the pipe wall. Although an initial framework was established to understand the mechanism of formation of the LL, the investigated particle sizes (0.5 and 1 mm) and neglected effect of the suspending fluid on the particles, such as the particle drag force, limited the extent that the results are representative of typical concrete mixtures. More recently, Zhan et al. [45] and Hoe et al. [46] employed a soft-sphere DEM to predict the pumping pressure loss of various self-consolidating concrete mixtures. Zhan et al. [45] simulated the coarse aggregate of 5-60 mm having a Gaussian PSD using a clumping approach to represent the small spheres. Hoe et al. [46] considered a size range of 6-16 mm for coarse aggregate while the mortar matrix was modelled using uniform 4-mm particles. The presence of the mortar phase was taken into account by optimizing the interparticle and particle-boundary contact-model parameters. According to the numerical simulations, the pressure loss significantly increased for mixtures containing larger size and higher content of coarse aggregate [45,46]. However, the mechanism of formation of the LL was not studied. The use of Gaussian PSD for coarse aggregate [45] and uniform 4-mm particles for mortar matrix [46] is also not representative of the typical aggregate PSDs used to proportion concrete mixtures [49].

While the SIPM mechanism has been well studied for uniform size particles [11-14], the mechanics of this phenomenon are not well understood for particles with a distribution of different sizes. The objective of this study is to further understanding of the LL formation mechanism for particle distributions typical of concrete pipe flow, attempting to a provide more realistic understanding of the pumping-induced migration of particles and rheological heterogeneity across the pipe. The current paper used simulations performed with a multiple time-scale soft-sphere DEM approach [50] in a fully-developed concrete pipe flow within a section of cylindrical pipe, taking into account particle collisions with each other and with the pipe wall as well as forces and torques on the particles from the suspending fluid. Particle size distributions and concentration values were selected to be representative of fine and coarse aggregate and realistically characterize

Chapter 6. Discrete-element modeling of shear-induced particle migration during zones concrete pipe flow: Effect of size distribution and concentration of aggregate on formation of lubrication layer

178

the radial heterogeneity of particles leading to formation of LL during concrete pumping processes. The computational model has been widely used in the literature to simulate flows with modest particle size variation [51-55], but it has not been previously used for flows with very large particle size differences. The concrete particulate distribution in the current paper consisted of a wide range of fine and coarse aggregate of 1-, 3.5-, 7.5-, 12-, and 17-mm diameter particles, corresponding to aggregate retained between different ASTM standard sieves. Distribution of particles across the pipe cross section was investigated at different radial zones during the pipe-flow period. Different measures were proposed to evaluate the rheological heterogeneities across the pipe. Finally, the coupled effect of PSD and concentration of particles on the pipe-wall effect and pumping-induced heterogeneities of the investigated mixtures was evaluated. The fluid drag force on the particle motion was accounted for including particle crowding and inertia effects [56]. However, it is worth mentioning that the simplification was made to fix the suspending fluid rheology, so that the effect of particle heterogeneity on the suspending fluid flow, the time dependency of rheological properties and thixotropic behavior of the suspending fluid, and the pumping-induced changes in air-void system were not taken into account.

6.2 Numerical Methodology

6.2.1 Governing equations

The translational and rotational motions of particles were governed by conservation of linear and angular momentum, given.

$$m \frac{d\mathbf{v}}{dt} = \mathbf{F}_F + \mathbf{F}_C \tag{6.1}$$

$$I \frac{d\mathbf{\Omega}}{dt} = \mathbf{M}_F + \mathbf{M}_C \tag{6.2}$$

where m, $\mathbf{v}$, I, and $\mathbf{\Omega}$ are the mass, velocity, inertia, and angular velocity of a particle, respectively. Here, $\mathbf{F}_F$ and $\mathbf{M}_F$ denote the force and torque on a particle from the surrounded fluid, respectively. The collision-induced forces and torques on a particle are denoted by $\mathbf{F}_C$ and $\mathbf{M}_C$, respectively.

Chapter 6. Discrete-element modeling of shear-induced particle migration during zones concrete pipe flow: Effect of size distribution and concentration of aggregate on formation of lubrication layer

179

6.2.1.1 *Fluid forces and torques*

The dominant fluid force acting on particles is the drag force, which is given for isolated particles at low particle Reynolds number by Stokes' law. In the presence of surrounding particles, a correction factor is typically applied, which is known as the particle crowding effect [56]. The correction factor fDF was calculated using the Di Felice [57] correlation, giving the drag force as

$$\mathbf{F}_F = -3\pi\, d\, \mu\, (\mathbf{v} - \mathbf{u}_f)\, f_{DF} \tag{6.3}$$

$$f_{DF} = (1 - c)^{-\beta} \tag{6.4}$$

where μ is the fluid viscosity and d is the particle diameter. The velocity of the fluid at the particle centroid location, $\mathbf{u}_f$, is obtained by tri-linear interpolation from the grid covering the fluid flow. The correction factor f_{DF} depends on the β index and local concentration $c(x,t)$. The β index was defined as a function of the particle Reynolds number (Re_p) [57], as follows

$$\beta = 2.7 - \frac{0.65}{\mathrm{Exp}\left[\frac{[1.5 - \ln(Re_p)]^2}{2}\right]} \tag{6.5}$$

$$Re_p = \frac{|\mathbf{v} - \mathbf{u}_f|\, d}{v} \tag{6.6}$$

where v is the kinematic viscosity of the suspending fluid. The local concentration was computed using a concentration-blob method to provide a smooth concentration field [58]. In this approach, the particle volume was distributed onto the flow field using a 3D Gaussian function with a specific radius R_n and amplitude A_n. The concentration at a given point was estimated by summing over the contributions of the nearby concentration blobs, as

$$c(\mathbf{x},t) = \sum_{n=1}^{N} A_n f(\mathbf{x} - \mathbf{x}_n, R_n) \tag{6.7}$$

where $f(\mathbf{x} - \mathbf{x}_n, R_n)$ was chosen to have the Gaussian form

$$f(\mathbf{x} - \mathbf{x}_n, R_n) = \frac{2}{3\pi\, R_n^3\, \mathrm{Exp}\left(\frac{|\mathbf{x} - \mathbf{x}_n|^2}{R_n^2}\right)} \tag{6.8}$$

The other important effect of the fluid on the particles is the viscous torque $\mathbf{M}_F$, given

Chapter 6. Discrete-element modeling of shear-induced particle migration during zones concrete pipe flow: Effect of size distribution and concentration of aggregate on formation of lubrication layer

180

$$\mathbf{M}_F = \pi\mu d^3 \left(\frac{1}{2}\boldsymbol{\omega}\text{-}\boldsymbol{\Omega}\right) \tag{6.9}$$

where $\boldsymbol{\omega}$ is the fluid vorticity evaluated at the particle centroid position. This torque is particularly important in flows with frequent particle collisions. Collisions of particles often result in substantial particle rotation due to frictional effects, which are damped by the viscous torque imposed by the fluid.

6.2.1.2 Collision forces and torques

The interactions between particles during the contact period can be categorized into four different types, including normal collision, sliding, twisting, and rolling contacts, which are schematically shown in Fig. 6.1.

| **(a)** | **(b)** | **(c)** | **(d)** |
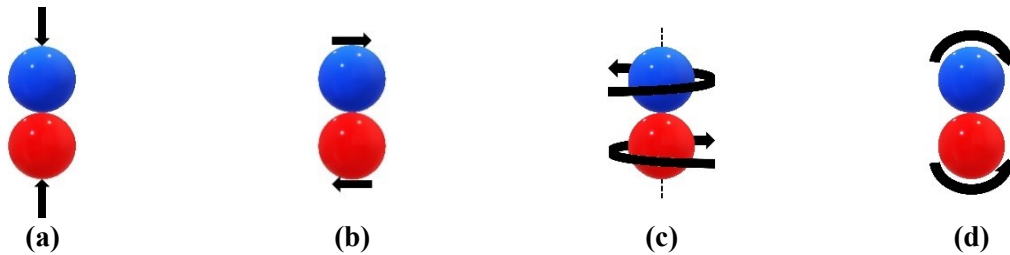
Fig. 6.1. Schematics of different contact types between particles, including **(a)** normal, **(b)** sliding, **(c)** twisting, and **(d)** rolling contacts [50].

As shown in Fig. 6.2, the contact forces between two collided particles "i" and "j" of radii ri and rj centroid positions at xi and xj , respectively, were decomposed in normal and tangential directions, as follows:

$$\mathbf{F}_{c,ij} = \mathbf{F}^{\mathbf{n}}_{c,ij} + \mathbf{F}^{\mathbf{s}}_{c,ij} \tag{6.30}$$

where $\mathbf{F}^{\mathbf{n}}_{c,ij}$ and $\mathbf{F}^{\mathbf{s}}_{c,ij}$ are contact forces between particles "*i*" and "*j*" in normal and tangential directions, respectively, and the normal direction "**n**" was given by

$$\mathbf{n} = (\mathbf{x}_j - \mathbf{x}_i) / |\mathbf{x}_j - \mathbf{x}_i| \tag{6.14}$$

Chapter 6. Discrete-element modeling of shear-induced particle migration during zones concrete pipe flow: Effect of size distribution and concentration of aggregate on formation of lubrication layer

181
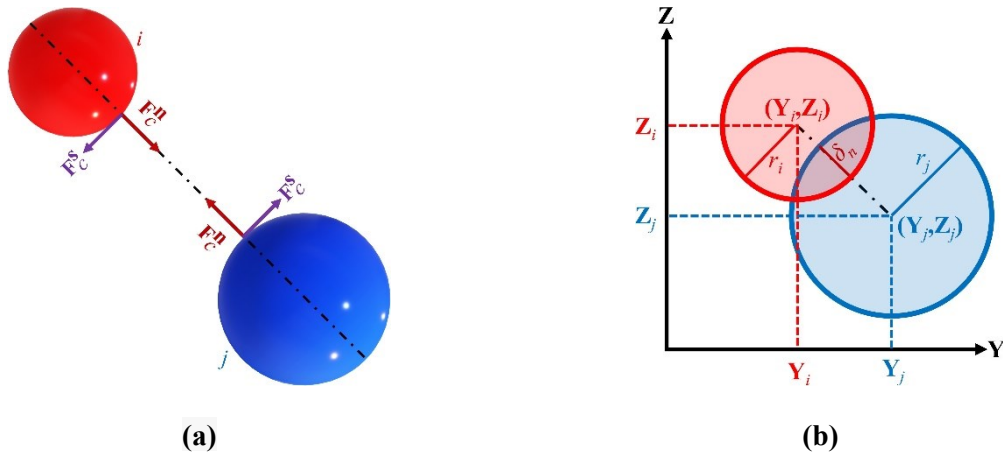
Fig. 6.2. Schematic illustration of **(a)** normal ($\mathbf{F}_c^{\mathbf{n}}$) and tangential ($\mathbf{F}_c^{\mathbf{s}}$) interparticle-contact forces and **(b)** two particles during the collision period.

The interparticle-contact forces are associated with the elastic deformation of particles and energy losses during collision. Various contact models are available to simulate the resistance of particles against the relative motion during collision [56]. In this study, the collision between particles was modeled using a spring-dashpot-slider system proposed by Cundall and Strack [47], schematically shown in Fig. 6.3.
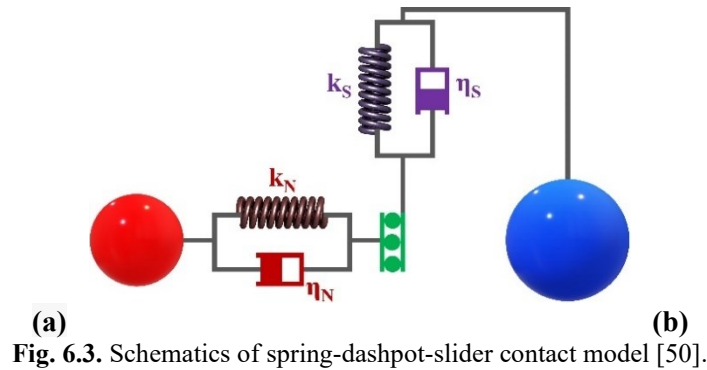
Fig. 6.3. Schematics of spring-dashpot-slider contact model [50].

The normal elastic force between contacted particles was modeled computed using the Hertz model [59], as follows:

$$\mathbf{F}_{c,ij}^{\mathbf{n}e} = k_N \delta_N = -K \delta_N^{3/2} \tag{6.12}$$

Chapter 6. Discrete-element modeling of shear-induced particle migration during zones concrete pipe flow: Effect of size distribution and concentration of aggregate on formation of lubrication layer

182

where $\mathbf{F}^{ne}_{c,ij}$ is normal elastic-contact force between particles "*i*" and "*j*". The elastic (k_N) and stiffness coefficients (K) were calculated as

$$k_N = \frac{4}{3} E \, a(t) \tag{6.13}$$

$$K = \frac{4}{3} E \sqrt{r_e} \tag{6.14}$$

where "δ_N" and "a" are normal overlap and contact region radius, respectively, calculated by

$$\delta_N = r_i + r_j - |\mathbf{x}_i - \mathbf{x}_j| \tag{6.15}$$

$$a^2 = r_e \, \delta_N \tag{6.16}$$

Here, r_e and E are the effective particle radius and elastic modulus, respectively. Assuming elastic moduli, E_i and E_j, and Poisson's ratios, σ_i and σ_j, for the two colliding particles "*i*" and "*j*", the effective particle radius (r_e), elastic modulus (E), and shear modulus (G) were defined by

$$\frac{1}{r_e} = \frac{1}{r_i} + \frac{1}{r_j} \tag{6.57}$$

$$\frac{1}{E} = \frac{1 - \sigma_i^2}{E_i} + \frac{1 - \sigma_j^2}{E_j} \text{ for } r_{\text{Plug}} \leq r \leq R_{\text{LL}} \tag{6.68}$$

$$\frac{1}{G} = \frac{2 - \sigma_i}{G_i} + \frac{2 - \sigma_j}{G_j} \tag{6.79}$$

The damping contact force in the normal direction between two colliding particles "i" and "j" was modeled as

$$\mathbf{F}^{nd}_{c,ij} = -\eta_N \mathbf{v}_R . \mathbf{n} \tag{6.20}$$

where η_N is the damping coefficient. The relative velocity $\mathbf{v}_R$ of the two particles at the contact surface can be written as

$$\mathbf{v}_R = \mathbf{v}_{ci} - \mathbf{v}_{cj} \tag{6.21}$$

where $\mathbf{v}_{ci}$ and $\mathbf{v}_{cj}$ are the particle velocities at the contact surface, which can be obtained using the centroid velocities ($\mathbf{v}_i$ and $\mathbf{v}_j$), vectors from the particle centroids to the contact point ($\mathbf{r}_i = r_i\mathbf{n}$ and $\mathbf{r}_j = -r_j\mathbf{n}$), and rotation rates ($\mathbf{\Omega}_i$ and $\mathbf{\Omega}_j$) as

$$\mathbf{v}_{ci} = \mathbf{v}_i + \mathbf{\Omega}_i \times \mathbf{r}_i \tag{6.22}$$

$$\mathbf{v}_{cj} = \mathbf{v}_j + \mathbf{\Omega}_j \times \mathbf{r}_j \tag{6.23}$$

There are a number of different models available for computation of the normal damping coefficient, which were summarized in [56]. For the current work, we used the simple model proposed by Tsuji et al. [60] which gives a constant restitution coefficient. In this model, Tsuji et al. [60] expresses the normal damping coefficient as a function of the normal stiffness k_N and restitution coefficient e as

$$\eta_N = \alpha\sqrt{m\,k_N} \tag{6.24}$$

where α is a 6th-degree polynomial function of the restitution coefficient given by [50]

$$\alpha = 1.2728 - 4.2783e + 11.087e^2 - 22.348e^3 + 27.467e^4 - 18.022e^5 + 4.821e^6 \tag{6.25}$$

The contact sliding force in the tangential direction $\mathbf{F}_c^s$, caused by the virtual spring and dashpot, were considered as the first and second terms on the right side of the following equation

$$\mathbf{F}_c^s = -k_T\left(\int_{t_0}^{t} \mathbf{v}_S(\xi)\mathrm{d}\xi\right).\mathbf{t}_S - \eta_T\mathbf{v}_S.\mathbf{t}_S \tag{6.26}$$

where k_T and η_T are tangential stiffness and dissipation coefficients, respectively. The dissipation coefficients for both normal and tangential directions are typically assumed to be identical, such that, $\eta_T = \eta_N$. Using the expression presented by Mindlin [61], the tangential spring coefficient was calculated as

Chapter 6. Discrete-element modeling of shear-induced particle migration during zones concrete pipe flow: Effect of size distribution and concentration of aggregate on formation of lubrication layer

184

$$k_T = 8G\, a(t) \tag{6.27}$$

The relative velocity of particles at the contact surface in the tangential direction is given by

$$\mathbf{v}_S = \mathbf{v}_R - (\mathbf{v}_R.\mathbf{n})\mathbf{n} \tag{6.28}$$

The unit vector in the slip direction tS can then be defined as

$$\mathbf{t}_S = \mathbf{v}_S\, /\, |\mathbf{v}_S| \tag{6.29}$$

It was assumed that slipping motion between two particles starts when the magnitude of $\mathbf{F}_c^{\mathbf{s}}$ exceeds a critical value. If the evaluated force from Eq. (6.26) is greater than the critical value, then $\mathbf{F}_c^{\mathbf{s}}$ is set equal to the critical force; otherwise, it will be equal to the force obtained using Eq. (6.26). According to Amonton's law, this critical value (F_{crit}) depends on the normal force magnitude F_n and the friction coefficient μ_f as

$$F_{crit} = \mu_f |F_n| \tag{6.30}$$

where the friction coefficient is set equal to 0.3 in this study. Twisting torque is also exerted on the particles (Fig. 6.1c) due to the existence of a relative rotational rate between two colliding particles. The relative rotational rate is given by:

$$\Omega_T = (\mathbf{\Omega}_i - \mathbf{\Omega}_j).\mathbf{n} \tag{6.31}$$

Using an approach similar to that employed for sliding friction, the twisting torque (M_t) was calculated in [50] as

$$M_t = \frac{2}{a^2} \int_0^a F_s(r) r^2 \mathrm{d}r = -\frac{k_T a^2}{2} \int_{t_0}^t \Omega_T(\tau)\mathrm{d}\tau - \frac{\eta_T a^2}{2} \Omega_T \tag{6.32}$$

The particles start spinning if the calculated torque (M_t) is higher than the critical value ($M_{t\text{-}crit}$), derived as

Chapter 6. Discrete-element modeling of shear-induced particle migration during zones concrete pipe flow: Effect of size distribution and concentration of aggregate on formation of lubrication layer

185

$$M_{t\text{-}crit} = \frac{2}{3} a\, F_{crit} \tag{6.33}$$

For any M_t greater than $M_{t\text{-}crit}$, the exerting twisting torque on the particles equals

$$M_t = -M_{t\text{-}crit}\, \Omega_T/|\Omega_T| \tag{6.34}$$

As shown in Fig. 6.1d, in addition to twisting and sliding, there is a rolling motion exerted on the contacted particles. The rolling resistance is a function of the rolling velocity ($\mathbf{v}_L$), which was defined by Bagi and Kuhn [62] as

$$\mathbf{v}_L = -r_e(\boldsymbol{\Omega}_i - \boldsymbol{\Omega}_j) \times \mathbf{n} - \frac{1}{2}\left(\frac{r_j - r_i}{r_j + r_i}\right)\mathbf{v}_S \tag{6.35}$$

The rolling torque (M_r), exerted on the particles in the direction of $\mathbf{t}_R = \frac{\mathbf{v}_L}{|\mathbf{v}_L|}$, is then given by

$$M_r = -k_R\left(\int_{t_0}^{t} \mathbf{v}_L(\tau)\mathrm{d}\tau\right).\mathbf{t}_R - \eta_R \mathbf{v}_L.\mathbf{t}_R \tag{6.36}$$

where k_R is the rolling spring coefficient and η_R is the rolling damping coefficient, defined by

$$\eta_R = \mu_R\, |F_{ne}| \tag{6.37}$$

where μ_R is the rolling coefficient. An expression for rolling coefficient is derived by Brilliantov and Pöschel [63] based on the viscoelastic particle response to deformation as

$$\mu_R = \frac{1 - e}{2.283 w_0^{1.5}(K/m)^{2/5}} \tag{6.38}$$

where w_0 is the relative velocity between two particles before the collision and e is the normal restitution coefficient. Combining the various effects discussed above, the total torque exerted on the particle "i" with radius r_i consists of the sliding, rolling (M_r), and twisting (M_t) torques, which can be combined to write

$$M_C = r_i\, F_S(\mathbf{n} \times \mathbf{t}_S) + M_r(\mathbf{t}_R \times \mathbf{n}) + \mathbf{M}_t.\mathbf{n} \tag{6.39}$$

It is worth mentioning that normal force does not apply any torque on the particles due to its direction along with the center line of the particles.

6.2.2 Numerical solution method

The numerical computations were performed using the multiple time-step soft-sphere DEM approach described by Marshall [50]. The computations were performed on a Cartesian grid, and a level-set approach was used to detect the interparticle and particle-wall collisions using an interpolation scheme [56]. The DEM algorithm consists of an efficient multi-timescale approach including fluid, particle, and collision timescales with corresponding time steps on each scale, as illustrated in the block diagram in Fig. 6.4. The fluid timescale occurs at the largest time step (ΔT_f), which is used to describe the fluid motion and update lists of local particles. Particles were advected using the particle time step (ΔT_p), during which particles that experience collisions were detected. Particles were advected using a second-order implicit algorithm described in [50]. The motion of the colliding particles was resolved using a smaller time step, called collision time step (ΔT_c). Variables were non-dimensionalized using the pipe radius R as a length scale and mean fluid velocity U as a velocity scale. Time scales were non-dimensionalized by the convection time R/U. The simulations were carried out for a cylindrical pipe of 100 mm diameter (D_{Pipe}) and 500 mm length (L_{Pipe}). The values of various non-dimensional parameters used in the simulations are summarized in Table 6.1. Particles were initialized in the pipe using a random number generator function. Particle locations were examined to avoid interparticle and particle-wall overlap in the initial positions. The generator subroutine was iterated until the desired concentration and PSD were achieved. Details on PSD used in the simulations are given in Section 3.1. The maximum total number of particles was set to $n_{max} = 5 \times 10^5$ due to the memory limitations of the employed code. This is worth mentioning that this study concerned the simulation of a fully-developed flow in the pipe, not at its entrance. Therefore, it has been assumed that the simulated segment of the pipe is sufficiently far enough from the entrance where flow is fully developed and can be simulated in a laminar flow regime.

The discrete element method on which this study is based has become widely used in the fluid dynamics literature. The original paper (Ref. [50]) has multiple references in Google Scholar,

Chapter 6. Discrete-element modeling of shear-induced particle migration during zones concrete pipe flow: Effect of size distribution and concentration of aggregate on formation of lubrication layer

187

many of which are from papers by a wide variety of authors who used the method for various applications. This discrete element method was also the basis of a monograph, available in Ref. [56], on discrete element method, which provides more detailed discussions and extensions of the model.

Table 6.1. Applied dimensionless-DEM and -CFD parameters in numerical simulations.

Simulation parameters	Assumption
Coefficient of restitution (e)	0.10
Fluid time step (ΔT_f)	0.01
Fluid time step/Particle time step ($\Delta T_f / \Delta T_p$)	20
Particle time step/collision time step ($\Delta T_p / \Delta T_c$)	40
Suspending-fluid flow Reynolds number (Re)	500
Suspending-fluid velocity ($\mathbf{u}_f$)	A parabolic-laminar flow velocity profile $\mathbf{u}_f = 1 - (y^2 + z^2)$
Pipe length (L_{Pipe})	10

Chapter 6. Discrete-element modeling of shear-induced particle migration during zones   188
concrete pipe flow: Effect of size distribution and concentration of aggregate on
formation of lubrication layer
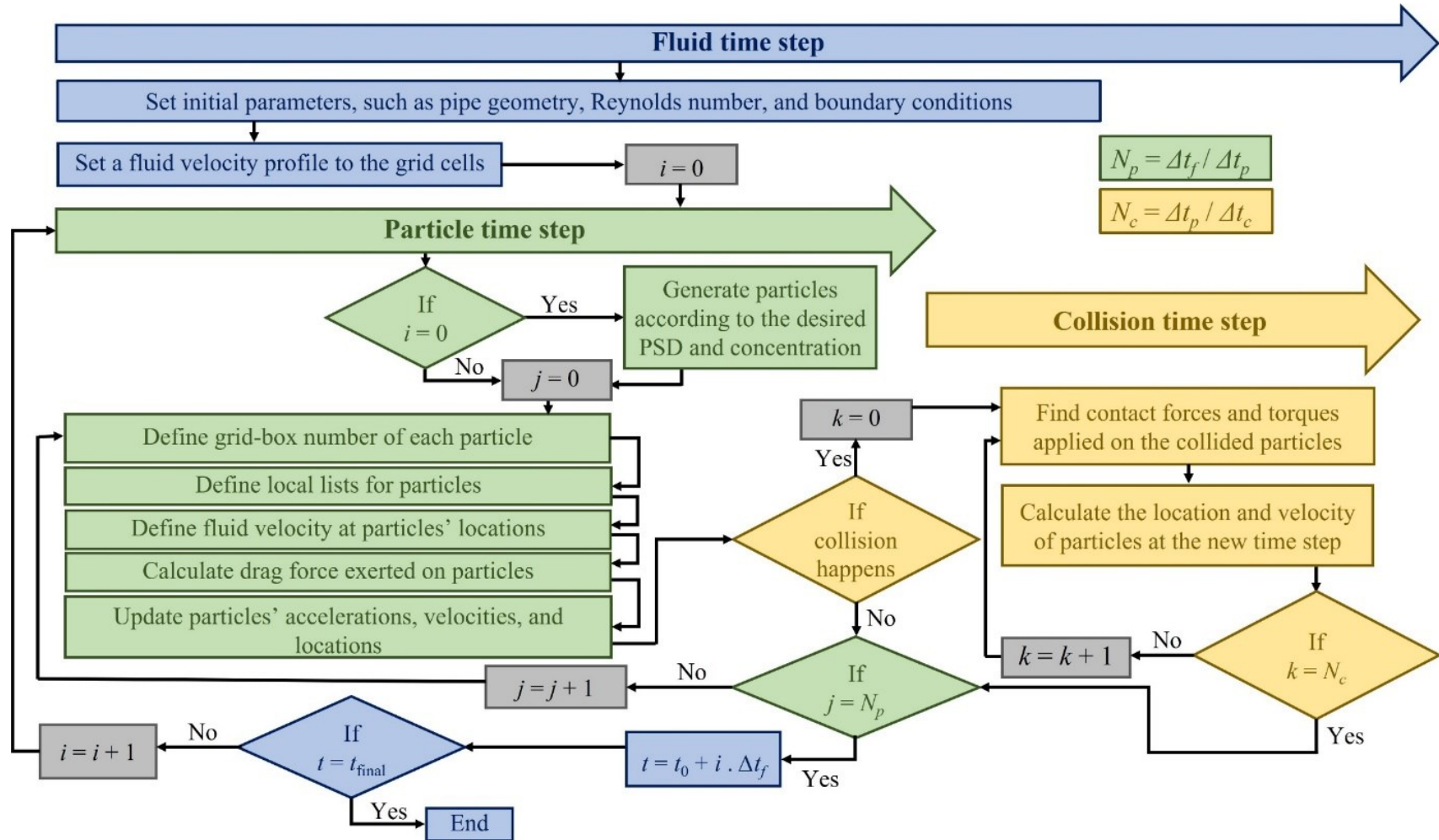
Fig. 6.4. The schematic illustration of the multiscale algorithm applied in this study.

6.3 Specifications of the concrete pipe-flow models

6.3.1 Proportioning of the modeled suspensions

In this study, the model concrete mixtures consisted of sand (0-5 mm) and three different classes of coarse aggregate CA1 (2.5-10 mm), CA2 (5-14 mm), and CA3 (5-20 mm). The Canadian Standards Association (CSA)'s standard for concrete materials (CSA A23.1:19/CSA A23.2:19) recommended specific limits for the particle-size distribution (PSD) of each class of aggregate to use in concrete (Table 6.2) [64].

Table 6.2. Grading limits for different classes of fine (sand) and coarse aggregate (CA1-3), recommended by CSA A23.1:19/CSA A23.2:19 standard [64] in terms of the minimum (*min*) and maximum (*max*) allowed cumulative passing percentages (%) from each standard sieve.

Standard sieve size (mm)	Sand (0-5 mm)		CA1 (2.5-10 mm)		CA2 (5-14 mm)		CA3 (5-20 mm)	
	min	*max*	*min*	*max*	*min*	*max*	*min*	*max*
28					-	-	100	100
20	-	-	-	-	100	100	85	100
14			100	100	90	100	50	90
10	100	100	85	100	45	75	25	60
5	95	100	10	30	0	15	0	10
2.5	80	100	0	10	0	5	0	5
1.25	50	90	0	5				
0.630	25	65						
0.315	10	35	-	-	-	-	-	-
0.160	2	10						
0.080	0	3						

As shown in Table 6.3, in order to conform to the recommended CSA limits, the cumulative passing percentages (*CPP* in vol.%) of the investigated classes of aggregate models were selected as the average of the minimum (*min*) and maximum (*max*) allowed limits for each standard-sieve size (*CPP* = (*min* + *max*)/2). Accordingly, the remaining volumetric fractions (*RVF* in vol.%) of each class of sand and coarse aggregate on each sieve were calculated and presented in Table 6.3. As shown in Table 6.4, the modelled fine and coarse aggregate consisted of dispersions of five different subclasses of spherical particles P1 (1 mm), P2 (3.5 mm), P3 (7.5 mm), P4 (12 mm), and P5 (17 mm), representing the sieve-size ranges of 0-2.5, 2.5-5, 5-10, 10-14, and 14-20 mm, respectively. Subsequently, As presented in Table 6.5, three different PSDs of aggregate, namely fine, medium, and coarse PSDs, were considered as three dispersions of different volumetric fractions of four aggregate classes of sand and CA-3, as well as their corresponding five particle subclasses of P1-5 (Table 6.4).

Chapter 6. Discrete-element modeling of shear-induced particle migration during zones concrete pipe flow: Effect of size distribution and concentration of aggregate on formation of lubrication layer

190

Table 6.3. PSDs of the modelled sand and coarse aggregate (CA1-3), in terms of *CPP* (vol.%) and *RVF* (vol.%) on each standard sieve, conforming to the CSA A23.1:19/CSA A23.2:19 standard [64].

Standard sieve size (mm)	Sand (0-5 mm) CPP (%)	RVF (%)	CA1 (2.5-10 mm) CPP (%)	RVF (%)	CA2 (5-14 mm) CPP (%)	RVF (%)	CA3 (5-20 mm) CPP (%)	RVF (%)
20					-		100	-
14	-		-	-	100	-	70	30
10		-	100		60	40	42.5	27.5
5	100		20	80	7.5	52.5	5	37.5
2.5	90	10	5	15	2.5	5	2.5	2.5
1.25	70	20	2.5	2.5				
0.630	45	25						
0.315	22.5	22.5				2.5		2.5
0.160	6	16.5	-	2.5 (< 1.25 mm)	-	(< 2.5 mm)	-	(< 2.5 mm)
0.080	1.5	4.5						
Base	-	1.5						

Table 6.4. Proportioning of the modelled sand and coarse aggregate (CA1-3), in terms of volumetric fractions (vol.%) of P1-5 subclasses.

	P1: 1 mm	P2: 3.5 mm	P3: 7.5 mm	P4: 12 mm	P5: 17 mm
Particle subclasses					
Sand	90.0%	10.0%	-	-	-
CA1	5.0%	15.0%	80.0%	-	-
CA2	2.5%	5.0%	52.5%	40.0%	-
CA3	2.5%	2.5%	37.5%	27.5%	30.0%

Table 6.5. Proportioning of the investigated PSDs of aggregate, in terms of volumetric fractions (vol.%) of 4 aggregate classes (sand and CA1-3) and their corresponding 5 particle subclasses (P1-5) in unit volume of aggregate

PSD #	Aggregate classes (vol.%) Sand	CA1	CA2	CA3	Particle subclasses (vol.%) P1: 1 mm	P2: 3.5 mm	P3: 7.5 mm	P4: 12 mm	P5: 17 mm
Fine	40	30	20	10	38	10	38	11	3
Medium	25	25	25	25	25	8	43	17	8
Coarse	10	20	30	40	12	7	47	23	12

In this study, the pipe flow of in total nine different suspensions, consisted of three total particle concentrations (φ) of 10% (low), 25% (medium), and 40% (high), and three different PSDs (Table 5) were investigated. The proportioning of the investigated suspensions are presented in Table 6.6, in terms of total particle concentration (φ), number of each particle classes of P1-5, and total number of particles (n), as well as the average diameter (D_{avg}), packing density (φ_{max}), and relative-solid packing fraction (φ/φ_{max}) of particles in each suspension. The simulations were carried out for a cylindrical pipe of 100-mm diameter (D_{Pipe}) or 50-mm radius (R) and 500-mm length (L_{Pipe}).

Chapter 6. Discrete-element modeling of shear-induced particle migration during zones concrete pipe flow: Effect of size distribution and concentration of aggregate on formation of lubrication layer

191

The investigated suspensions were entitled by FPSD, MPSD, CPSD, LC, MC, and HC labels in Table 6.6 which correspond to the fine-, medium-, and coarse-PSDs, as well as low (10%), medium (25%), and high (40%) concentrations of aggregate, respectively.

Table 6.6. Proportioning of the investigated suspensions, including total particle concentration (φ), number of each particle subclasses of P1-5, and total number of particles (n), as well as the D_{avg} and φ_{max} of particles ($n_{max} = 5 \times 10^5$).

| Model # | PSD | Concentration level | Number of particles | | | | | | D_{avg} (mm) | φ_{max} | $\frac{L_{Pipe}}{R}$ |
			P1	P2	P3	P4	P5	n			
1-FPSD-LC	Fine	Low ($\varphi = 10\%$)	286875	1706	680	47	5	289313	5.429	0.847	10.000
2-MPSD-LC	Medium		187500	1421	756	73	11	189761	6.990	0.858	10.000
3-CPSD-LC	Coarse		88125	1137	831	100	18	90211	8.635	0.868	10.000
4-FPSD-MC	Fine	Medium ($\varphi = 25\%$)	495720	2947	1175	81	8	499931	5.398	0.847	6.912
5-MPSD-MC	Medium		468750	3553	1889	183	29	474404	7.030	0.857	10.000
6-CPSD-MC	Coarse		220313	2843	2078	250	46	225530	8.657	0.868	10.000
7-FPSD-HC	Fine	High ($\varphi = 40\%$)	495720	2947	1175	81	8	499931	5.398	0.847	4.320
8-MPSD-HC	Medium		494025	3745	1991	193	30	499984	7.016	0.857	6.587
9-CPSD-HC	Coarse		352500	4548	3324	399	73	360844	8.646	0.868	10.000

Moreover, the virtual packing density (φ_{max}) of a polydisperse mixture of five particle subclasses were calculated using the linear-packing model proposed by Stovall et al. [65] and de Larrard [66], as follow:

$$\varphi_{max} = \min_{i=1}^{5} \left[\frac{\alpha_i}{1 - (1 - \alpha_i) \sum_{j=1}^{i-1} a_{ij}\, \varphi_j - \sum_{j=i+1}^{5} b_{ij}\, \varphi_j} \right] \tag{6.40}$$

where, $\alpha_i = \frac{\pi}{3\sqrt{2}}$, φ_j, a_{ij}, and b_{ij} are the highest packing density amongst all possible lattice packings of spherical particles of all subclasses 'i' = 1 to 5, volumetric content of subclass 'j', loosening (Eq. (6.41)), and wall effects (Eq. (6.42)) for particles of subclass 'i' (diameter d_i) due to the influence of particles of subclass 'j' (diameter d_j), respectively.

$$a_{ij} = \begin{cases} \sqrt{1 - \left(1 - \frac{d_j}{d_i}\right)^{1.02}}, & d_i > d_j \\ 0, & d_i \le d_j \end{cases} \tag{6.41}$$

$$b_{ij} = \begin{cases} 1 - \left(1 - \frac{d_i}{d_j}\right)^{1.50}, & d_j > d_i \\ 0, & d_j \le d_i \end{cases} \tag{6.42}$$

Chapter 6. Discrete-element modeling of shear-induced particle migration during zones concrete pipe flow: Effect of size distribution and concentration of aggregate on formation of lubrication layer

192

Furthermore, the mean diameter of particles (D_{avg-i}) in a given suspension "i" ($i = 1$ to 9) was calculated using the volumetric-weighted arithmetic average of diameter of their corresponding particles of subclasses "j" ($j = 1$ to 5), as

$$D_{avg-i} = \frac{\sum_{j=1}^{5}\left(\varphi_{ji}\, d_j\right)}{\sum_{j=1}^{5}\varphi_{ji}} \tag{6.43}$$

where φ_{ji} is the volumetric concentration of particle subclass "j" in a given suspension "i

6.3.2 Evaluation of the radial particle migrations

In order to evaluate the pumping-induced particle migration of the investigated suspensions across the pipe (pipe radius $R = D_{Pipe}/2 = 50$ mm), four different radial zones of Z1, Z2, Z3, and Z4, corresponding to the radial ranges of 0-0.5R, 0.5R-0.75R, 0.75R-0.875R, and 0.875R-R, respectively, were defined (Fig. 6.5). The bulk concrete (BC) and lubrication layer (LL) zones were taken to correspond to the radial ranges 0-0.875R (i.e., Z1-3) and 0.875R-R (i.e., Z4), respectively. Accordingly, the concentration of each of the particle subclasses P1-5 and the total particle concentrations were calculated in each zone (Z1-4, BC, and LL) for the whole computational time period ($t = 0$ - 20). Using the calculated volume of each of particle subclass P1-5 and also the total volume of particles in each zone, the packing density (φ_{max-i}) and mean diameter of particles (D_{avg-i}) in each zone ($i = 1$ to 4) were calculated using Eqs. (40) to (43), respectively, at a given time ($t = 0$ - 20). The measures described in the following subsections are then proposed to evaluate the radial SIPM of the investigated suspensions across the pipe.

Chapter 6. Discrete-element modeling of shear-induced particle migration during zones concrete pipe flow: Effect of size distribution and concentration of aggregate on formation of lubrication layer

193
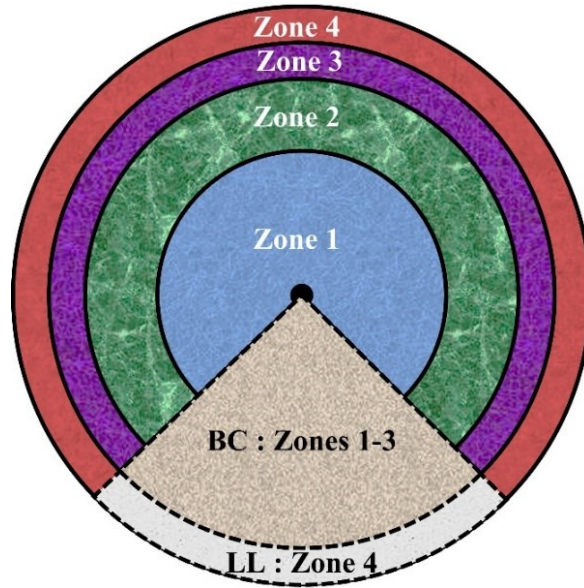
Fig. 6.5. Radial zones Z1, Z2, Z3, and Z4, corresponding to the radial ranges of 0-$0.5R$, $0.5R$-$0.75R$, $0.75R$-$0.875R$, and $0.875R$-R, respectively, as well as the bulk concrete BC (Z1-3: 0-$0.875R$) and lubrication layer LL (Z4: $0.875R$-R).

6.3.2.1   *Radial heterogeneity of the investigated pipe flows*

The radial heterogeneity of the investigated pipe flows was evaluated using the coefficient of variation of particle concentrations (φ) in different radial zones Z1-4 ($COV(\varphi)_{Z1-4}$), as follows:

$$COV(\varphi)_{Z1-4} = \frac{\sigma(\varphi)_{Z1-4}}{Avg(\varphi)_{Z1-4}} \times 100\% \tag{6.44}$$

where $\sigma(\varphi)_{Z1-4}$ and $Avg(\varphi)_{Z1-4}$ are the standard deviation and average of the total particle concentrations in zones Z1-4, respectively

6.3.2.2   *Shear-induced particle migration (SIPM)*

The calculated heterogeneity at a given pipe flow time step (t) is caused by the wall effect (WE) induced by the pipe walls and SIPM. The individual effect of SIPM was thus evaluated using the variation of COV values calculated at time t (using Eq. (6.44)), relative to their initial values (at t = 0), as follows:

$$\Delta COV\,(t)_{Z1-4} = COV\,(t)_{Z1-4} - COV\,(t=0)_{Z1-4} \tag{6.45}$$

Chapter 6. Discrete-element modeling of shear-induced particle migration during zones concrete pipe flow: Effect of size distribution and concentration of aggregate on formation of lubrication layer

194

6.3.2.3 *Wall effect (WE)*

During pipe flow, the radial displacements of the aggregate are limited due to presence of the pipe walls. The coarser fraction of aggregate cannot fit very close to the pipe walls, thus leaving room for formation of a thin layer of finer particles near the walls. This can lead to an initial heterogeneity in radial distribution of particles, as measured by the particle concentration profile, PSD, and packing density, across the pipe and, consequently, partial formation of the LL even prior being subjected to any shear and SIPM (at $t = 0$). This is namely called the pipe wall effect (WE) [8]. In this study, the wall-effect index (*WEI*) was evaluated by the ratio of the difference between the initial relative solid-packing fraction of particles in BC ($\left(\frac{\varphi(t=0)}{\varphi_{max}(t=0)}\right)_{\text{BC: Z1-3}}$) and LL ($\left(\frac{\varphi(t=0)}{\varphi_{max}(t=0)}\right)_{\text{LL: Z4}}$) zones (at $t = 0$) to that of the reference mixture ($\left(\frac{\varphi}{\varphi_{max}}\right)_{\text{Ref}}$), as follows.

$$WEI \, (\%) = \frac{\left(\frac{\varphi(t=0)}{\varphi_{max}(t=0)}\right)_{\text{BC}} - \left(\frac{\varphi(t=0)}{\varphi_{max}(t=0)}\right)_{\text{LL}}}{\left(\frac{\varphi}{\varphi_{max}}\right)_{\text{Ref}}} \times 100\% \tag{6.46}$$

The φ and φ_{max} values of the reference mixtures were calculated as the total concentration and packing density of the particles in the whole pipe domain (0-R), respectively, as shown in Table 6.6.

6.3.2.4 *Rheological heterogeneity of the investigated pipe flows*

The yield stress $\tau_0(\varphi)$ and plastic viscosity $\mu_p(\varphi)$ of the suspensions of the investigated mixtures in the different radial zones, relative to those of the suspending fluid (i.e., $\tau_0(0)$ and $\mu_p(0)$), were calculated as functions of concentrations (φ_i) and packing density ($\varphi_{max\text{-}i}$) of the spherical particles in the reference mixtures (whole pipe domain) and given radial zone i using the models proposed by Chateau et al. [67] (Eq. (6.47)) and Krieger and Dougherty [68] (Eq. (6.48)), respectively, as follows:

$$\tau_{0\text{-}r\text{-}i} = \frac{\tau_0(\varphi_i)}{\tau_0(0)} = \sqrt{(1 - \varphi_i)\left(1 - \frac{\varphi_i}{\varphi_{max\text{-}i}}\right)^{-2.5\varphi_{max\text{-}i}}} \tag{6.47}$$

Chapter 6. Discrete-element modeling of shear-induced particle migration during zones concrete pipe flow: Effect of size distribution and concentration of aggregate on formation of lubrication layer

195

$$\mu_{p\text{-}r\text{-}i} = \frac{\mu_p(\varphi_i)}{\mu_p(0)} = \left(1 - \frac{\varphi_i}{\varphi_{max\text{-}i}}\right)^{-2.5\varphi_{max\text{-}i}} \tag{6.48}$$

The radial heterogeneity of the rheological properties of the suspensions across the pipe was then evaluated using the ratio of the difference between the final relative rheological properties, including yield stress ($\tau_{0\text{-}r}$) and plastic viscosity ($\mu_{p\text{-}r}$), in BC and LL zones at the end of flow period ($t = 20$), to those of the reference mixture, as follows:

$$\text{Yield stress-heterogeneity index YSHI (\%)} = \frac{\tau_{0\text{-}r\text{-}BC} - \tau_{0\text{-}r\text{-}LL}}{\tau_{0\text{-}r\text{-}Ref}} \times 100\% \tag{6.49}$$

$$\text{Yield stress-heterogeneity index YSHI (\%)} = \frac{\tau_{0\text{-}r\text{-}BC} - \tau_{0\text{-}r\text{-}LL}}{\tau_{0\text{-}r\text{-}Ref}} \times 100\% \tag{6.50}$$

6.4 Results and discussion

The simulation results are discussed in terms of the evolution of concentration of each of particle subclasses, as well as the total concentration and mean diameter of particles in different radial zones as a function of time. The radial heterogeneity of the investigated pipe flows was then evaluated in terms of evolution of the $COV(\varphi)_{Z1\text{-}4}$ values, reflecting the WE and SIPM effects. The rheological properties of the BC and LL zones of the investigated suspensions across the pipe were evaluated at the end of the pipe flow computations ($t = 20$). The coupled effects of the PSD, volumetric content, and packing density of the aggregate on the wall effect and rheological heterogeneity of the investigated suspensions were finally evaluated.

6.4.1 Evolution of particle concentration across the pipe

Three examples of the evolution of the volumetric concentration of different particle subclasses P1-5 in different radial zones Z1-4 are presented in Fig. 6.6 for suspensions #1-FPSD-LC, #5-MPSD-MC, and #9-CPSD-HC. Results for the all the suspensions examined are available in Figs. A1-A3 in the Appendix. The different runs and locations within the flow domain are indicated in the figure by a label denoted as ZiPj, where *i* and *j* are numbers that denote the zone (Z1-Z4) and particle size (P1-P4) subclass, respectively. As expected, results for the larger particles exhibit more noise than those for smaller particles due to the lower number of larger particles, where even

Chapter 6. Discrete-element modeling of shear-induced particle migration during zones concrete pipe flow: Effect of size distribution and concentration of aggregate on formation of lubrication layer

196

a slight displacement of large particles between different zones can significantly change their local concentrations.

In the case of Z4 (0.875R-R), corresponding to the LL, only the concentration of the finest particle P1 (1 mm) increased over time while concentration decreased for the larger particles (P2-5). This observation is consistent with migration of finer particles towards the pipe walls and formation of the LL, whereas larger particles migrate to adjacent zones in the inner sections of the pipe flow. Moreover, the concentration of the finest particle P1 always decreased in Z3, which is the closest to the LL. The concentration of P1 in Z2 significantly decreased in the case of suspensions proportioned with low concentration 10% (Fig. 6.6-top and Fig. 6.A1 in appendix) while no major changes were observed for Z2P1 values for medium- (Fig. 6.6-middle and Fig. 6.A2 in appendix) and high-concentration (Fig. 6.6-bottom and Fig. 6.A3 in appendix) suspensions. This can confirm that the finest particles (P1: 1 mm) in Z3 mostly migrated to Z4 (LL) in the vicinity of the pipe wall. Indeed, due to higher number of interparticle collisions in central zones, caused by higher velocity and particle concentrations, P1 particles in Z3 could not easily move to Z2 and were mostly pushed into zone Z4 (LL).

The concentrations of all particle subclasses, regardless of their sizes, increased in the central zone Z1 (0-0.5R), which straddles the pipe center. This concentration increase is consistent with the gradual increase in particle packing density in the central zones over time due to migration of particles towards the central axis. However, more significant increases in particle concentration in Z1 were observed for the larger particle sizes P2-P5 than for the finest particle size (P1). This led to development of a coarser PSD in the pipe center at the end of the computation relative to the reference suspension and the other zones Z2-4.

As can be observed, the concentration of both P2 (3.5 mm) and P3 (7.5 mm) particles in Z2 (0.5R-0.75R) mostly increased over time. On the other hand, contrary to the medium- (MC = 25% in Fig. 6-middle and Fig. 6.A2 in appendix) and high- (HC = 40% in Fig. 6-bottom and Fig. 6.A3 in appendix) concentration suspensions, the concentrations of P2 and P3 increased and decreased in Z3 for low-concentration suspensions (LC = 10% Fig. 6.6-top and Fig. 6.A1 in appendix), respectively. Moreover, the concentration of P4 (12 mm) increased in the central zone Z1 while decreased in Z3 nearby the LL (Z4). However, no specific trend was observed for P4

concentrations in Z2. Furthermore, higher concentrations of the coarsest particle P5 (17 mm) were mostly obtained in the central zones Z1 and Z2 rather than Z3 and Z4 for almost all of the investigated suspensions, excluding the #7-FPSD-HC suspension (Fig. 6.A3 in appendix). This confirms the increase in the compacity of relatively large particles P4 and P5 in the central zone Z1 rather than other radial zones Z3 and Z4.

Chapter 6. Discrete-element modeling of shear-induced particle migration during zones concrete pipe flow: Effect of size distribution and concentration of aggregate on formation of lubrication layer

198
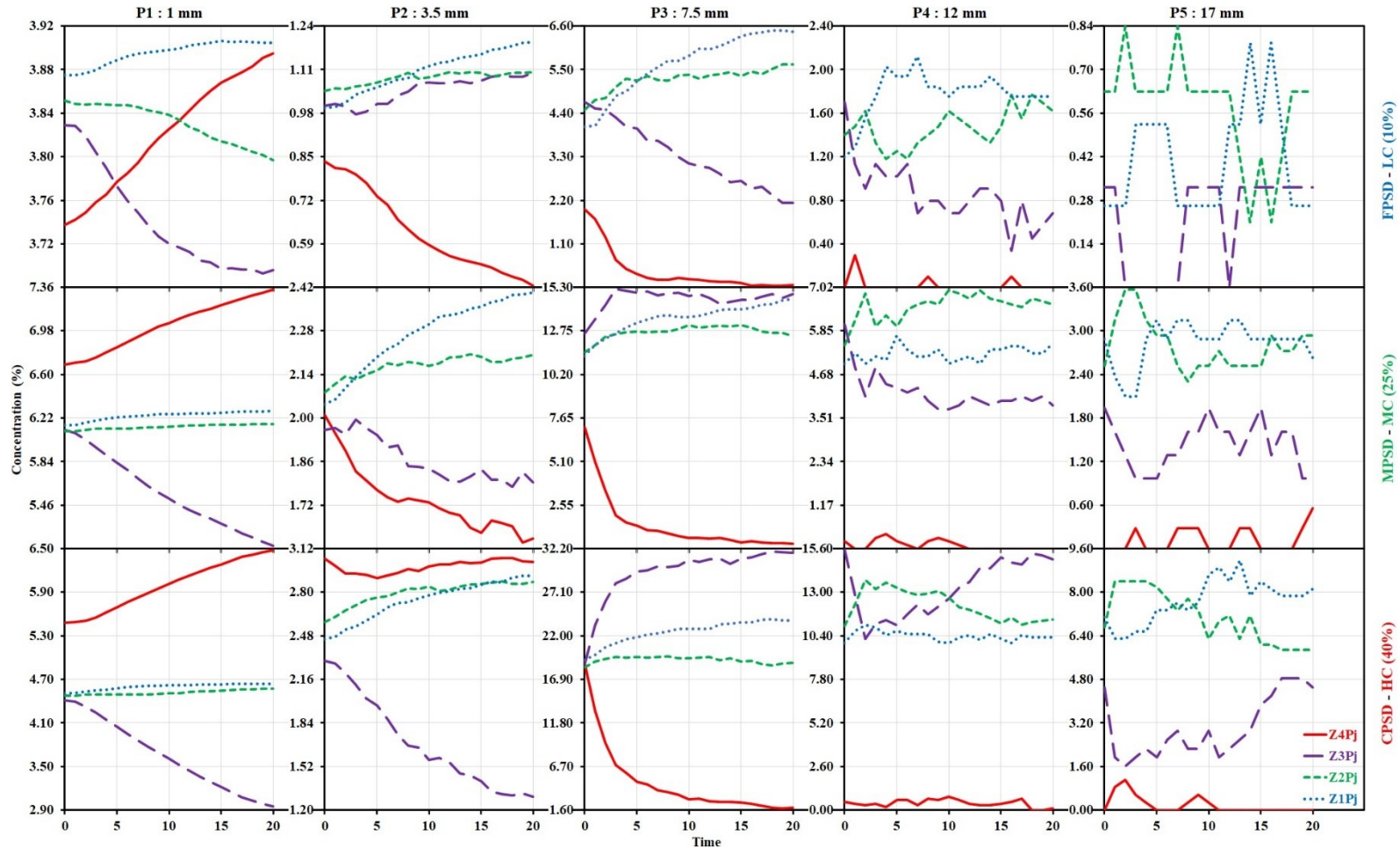
Fig. 6.6. Concentrations (ZiPj) of particles Pj (j = 1-5) in four different radial zones Zi (i = 1-4) for the mixtures containing low concentration (10%) of fine PSD (#1-FPSD-LC), medium concentration (25%) of medium PSD (#5-MPSD-MC), and high concentration (40%) of coarse PSD (#9-CPSD-HC) of particles over time

Chapter 6. Discrete-element modeling of shear-induced particle migration during zones   199
concrete pipe flow: Effect of size distribution and concentration of aggregate on
formation of lubrication layer

6.4.2 *Radial variation of the total concentration and PSD of particles*

The radial variation of the total concentration of particles over time across the radial zones Z1-4 is presented in Fig. 6.7 for different suspensions. As can be observed for all the suspensions, comparable initial particle concentrations (at t = 0) were observed across the BC (Z1-3: 0-0.875R). However, despite the random generation of particles across the pipe in the beginning of the pipe flow (t = 0), the lowest initial particle concentration was obtained at the LL (Z4), rather the BC (Z1-3) and reference mixtures. This can be attributed to the effect of pipe wall on distribution of nearby particles. Moreover, the lowest total concentration was obtained in the zone Z4 over time (t > 0), hence confirming the formation of the LL in vicinity of the pipe wall presented.

In the case of the LC (10%) suspensions, the total concentration of particles gradually decreased from the central zone (Z1) towards the LL zone (Z4). The total concentration of particles in Z1 of the LC suspensions more significantly increased over time than those in Z2. However, the particle concentrations of outer zones Z3-4 decreased over time. These observations confirm the scenario in which there is an overall migration of particles from the high shear-rate zones (Z3-4) towards the low shear-rate central zones (Z1-2). Furthermore, the ascending and descending rates of particle concentrations in Z1 and Z3-4, respectively, increased for coarser PSD. Accordingly, among the three LC suspensions, the highest and lowest particle concentrations at the end of the computation were respectively obtained in zones Z1 (17.2%) and Z4 (2.0%) of the #3-CPSD-LC suspension, proportioned with the coarse PSD.

In the case of MC (25%) suspensions, #4-FPSD-MC mixture with fine PSD exhibited comparable concentrations in zones Z1-3, with slightly higher value in the central zone Z1 at the end of pipe-flow period. For coarser PSDs, the particle concentration at LL (Z4) decreased and variations in the final concentrations across the BC (Z1-2 vs. Z3) increased over time. Accordingly, the highest variations across the BC (Z1-3) and the lowest concentration in LL of the MC suspensions was obtained for #6-CPSD-MC (φ_{Z1} = 36.1%, φ_{Z2} = 29.1%, φ_{Z3} = 26.7%, and $\varphi_{Z4\text{-}LL}$ = 6.4% at t = 20). These observations are consistent with the conclusion that for a given particle concentration, coarser PSD can lead to higher SIPM.

Chapter 6. Discrete-element modeling of shear-induced particle migration during zones concrete pipe flow: Effect of size distribution and concentration of aggregate on formation of lubrication layer

200
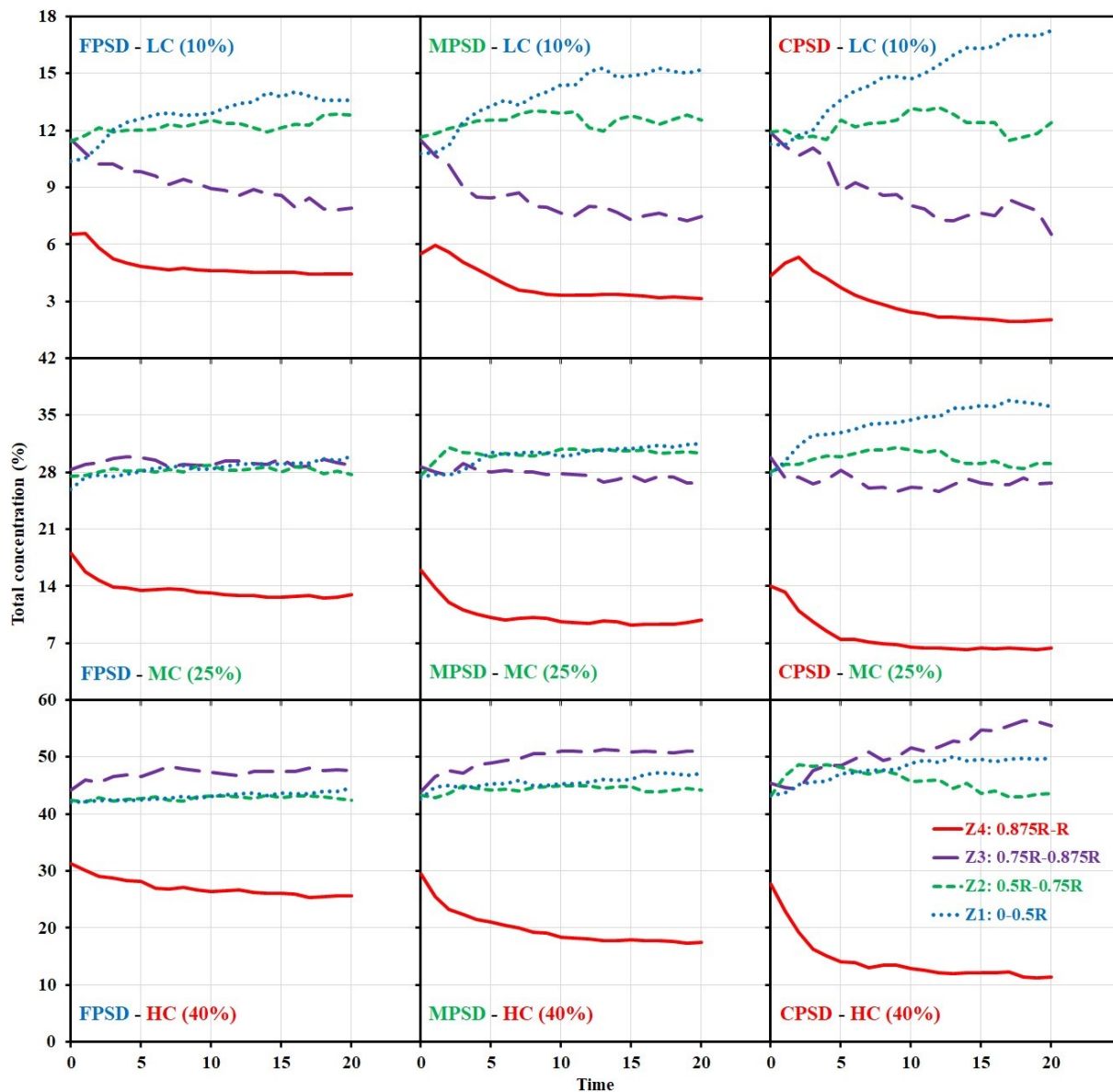
Fig. 6.7. Total concentrations of particles in four different radial zones Z1 to Z4 over time.

For HC (40%) suspensions, unlike the LC and MC cases, the highest concentration was obtained in Z3 ($0.75R$-$0.875R$), but not in the central zones Z1-2. This can be attributed to the employed one-way fluid-particle coupling simplification which neglected the effect of particles on the suspending fluid dynamics. A fully fluid-particle coupling approach (4-way CFD-DEM coupling) is then recommended for high concentration of particles ($\varphi \geq 40\%$) to achieve more precise SIPM simulations. However, higher concentrations were still obtained in the central zone Z1 rather than Z2. On the other hand, the particle concentration of the Z3 and Z4 (LL) zones of the HC suspensions significantly increased and decreased, respectively, for coarser PSD of particles.

Chapter 6. Discrete-element modeling of shear-induced particle migration during zones
concrete pipe flow: Effect of size distribution and concentration of aggregate on formation of
lubrication layer

201

The radial variations of the mean diameter of particles ($D_{avg\text{-}i}$, i = 1 to 4) in zones Z1-4 of the investigated suspensions over time are presented in Fig. 6.8. The $D_{avg\text{-}i}$ in a given radial zone i was calculated using the volumetric-weighted arithmetic average of diameter of its corresponding dj-diameter particles of subclass j (j = 1 to 5 in Table 6.4), as follows:

$$D_{avg\text{-}i} = \frac{\sum_{j=1}^{5}\left(\varphi_{ji}\, d_j\right)}{\varphi_i} \tag{6.51}$$

where φ_{ji} and $\varphi_i = \sum_{j=1}^{5} \varphi_{ji}$ are the volumetric concentration of particle subclass j (Figs. A1-A3 in appendix) and total particle concentration (Fig. 6.7) in the radial zone i. As can be observed in Fig. 6.8, for a given particle concentration, greater D_{avg} values were obtained in different radial zones Z1-4 of the suspensions of coarser PSD, as could be expected.

As shown in Fig. 6.8, despite the random generation of particles across the pipe, smaller initial Davg values in the beginning of the pipe flow computation were obtained in the LL zone (Z4) rather than the BC (Z1-3). This can be explained due to the wall effect, as similarly indicated earlier for low initial concentration of particles in the LL zone (Fig. 6.7). In addition, for the whole pipe-flow period, the smallest mean diameter of particles was obtained in the LL zone compared to BC, following by a consistent decrease over time. This observation confirms the migration of larger particles from the high shear-rate zone (Z4: LL) towards the lower shear-rate central zones (Z1-3: BC), which are then replaced in the high shear-rate zone by the finer particles. Hence, the LL is formed in the vicinity of the pipe walls, consisting of relatively finer particles compared to the BC. The final Davg values of 1.4-2.2, 1.7-2.7, and 2.4-2.8 mm were obtained in the LL zones of the LC, MC, and HC suspensions, respectively, at the end of the computation. These values are in good agreement with literature, where a maximum size of aggregate of up to 2.5 mm was generally reported for the fine particles in the LL extracted from the pumping experiments [8,25].

Chapter 6. Discrete-element modeling of shear-induced particle migration during zones concrete pipe flow: Effect of size distribution and concentration of aggregate on formation of lubrication layer

202
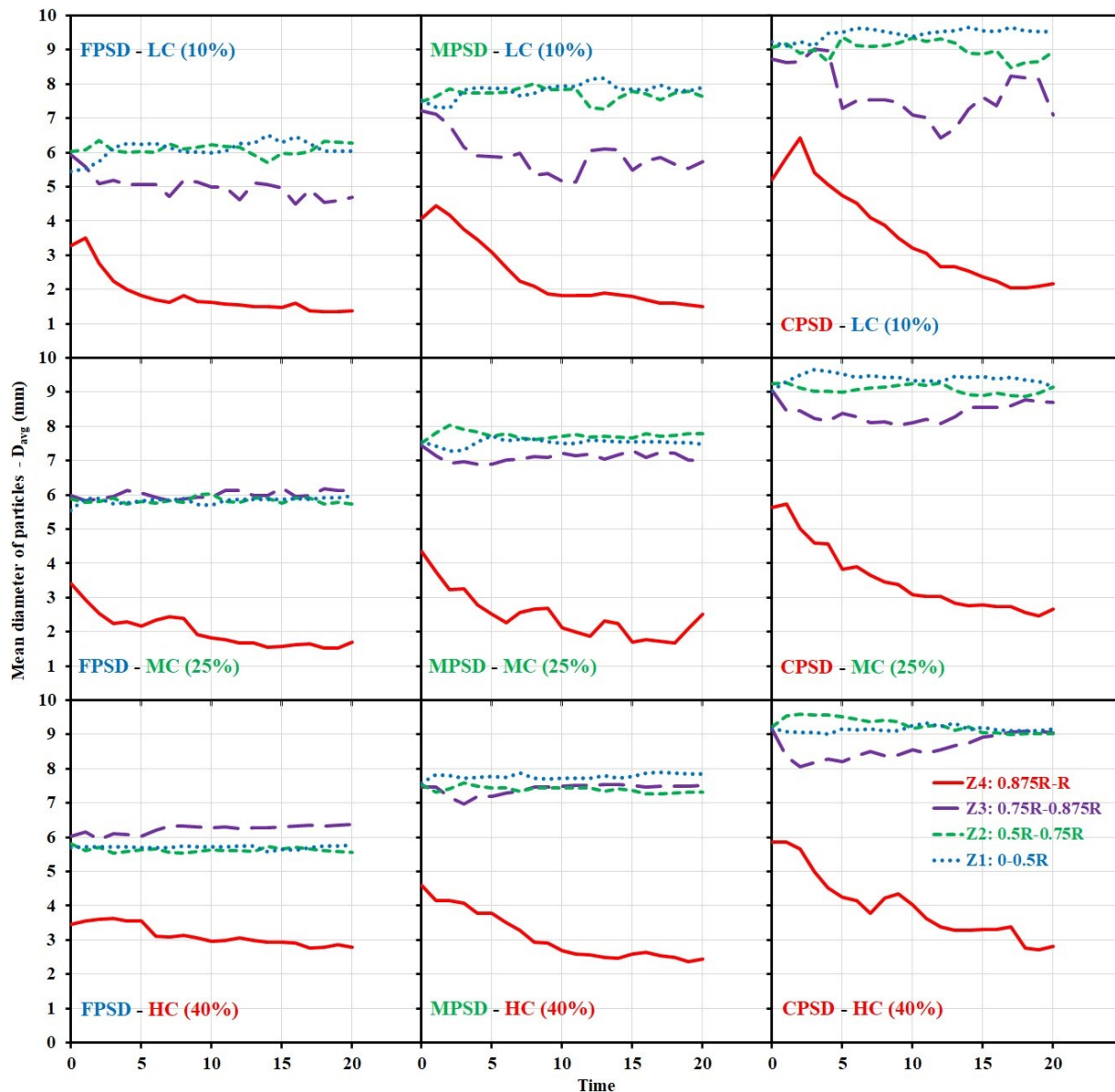
Fig. 6.8. Variation of mean diameter (D_{avg}) of particles in four different radial zones Z1 to Z4 over time.

As can be observed in Fig. 6.8, in the case of all the LC suspensions (#1-3), as well as the MC and HC suspensions of medium and coarse PSDs (#5-6 and #8-9), greater D_{avg} values were obtained in the lower-shear rate central zones Z1-2 rather than the relatively higher shear rate zone Z3. Despite the slight increase in the D_{avg} values of zones Z1-2, the mean diameter of particles in the zone Z3 of the LC suspensions experienced a consistent decrease over time. However, lower differences were observed between the D_{avg} of the Z3 and central zones Z1-2 by increasing the particle concentration in the MC and HC suspensions of MPSD and CPSD (#5-6 and #8-9).

Chapter 6. Discrete-element modeling of shear-induced particle migration during zones concrete pipe flow: Effect of size distribution and concentration of aggregate on formation of lubrication layer

203

Furthermore, in the case of suspension model #4, proportioned with medium concentration (25%) of fine PSD of particles, comparable D_{avg} values were obtained across the BC zone (i.e., Z1-3) over time. However, Z3 exhibited higher D_{avg} values compared to the central zones Z1-2 for suspension #7, proportioned with high concentration (40%) of fine PSD of particles (Fig. 8). This can be due to limitations of the one-way fluid-particle coupling approach for high concentration cases.

6.4.3 Radial heterogeneity of the investigated pipe flows

As described in Eq. (6.44), the radial heterogeneity of the investigated pipe flows was evaluated using the coefficient of variation of particle concentration (φ) in different radial zones Z1-4 (COV(φ)Z1-4), which is presented in Fig. 6.9. As mentioned earlier, the overall radial heterogeneities are the consequences of the coupled effect of the presence of the pipe walls (WE) and shear-induced particle migration (SIPM). As can be observed in Fig. 6.9, the radial heterogeneity of the investigated suspensions increased over time. For a given concentration, the suspensions proportioned with coarser PSD of particles exhibited higher radial heterogeneities over time, corresponding to higher WE and SIPM contribution. Moreover, increasing the concentration of particles resulted in lower radial heterogeneities across the pipe. Accordingly, by increasing the particle concentration from 10% (LC) to 40% (HC), the COV(φ)Z1-4 values deceased from 44.4% to 24.6%, 55.8% to 38.1%, and 69.8% to 49.1% for fine, medium, and coarse PSDs of particles, respectively.

The observed heterogeneities of the investigated pipe flows are well conformed with the spatially varying particles' interaction frequency described by Phillips et al. [17], as follows

$$N_{collision} = -K_c a_p{}^2(\varphi^2 \nabla \dot{\gamma} + \varphi \dot{\gamma} \nabla \varphi) \tag{6.52}$$

where $N_{collision}$ is collision flux, a_p and φ are radius and concentration of particles, $\dot{\gamma}$ represents the shear rate, and K_c is a shape-dependent factor [17]. Indeed, in a heterogeneous suspension subjected to shear, the particles irreversibly move from their original streamline due to the interparticle collisions.

Chapter 6. Discrete-element modeling of shear-induced particle migration during zones concrete pipe flow: Effect of size distribution and concentration of aggregate on formation of lubrication layer

204

(a) Low concentration (10%)   **(b) Medium concentration (25%)**   **(c) High concentration (40%)**
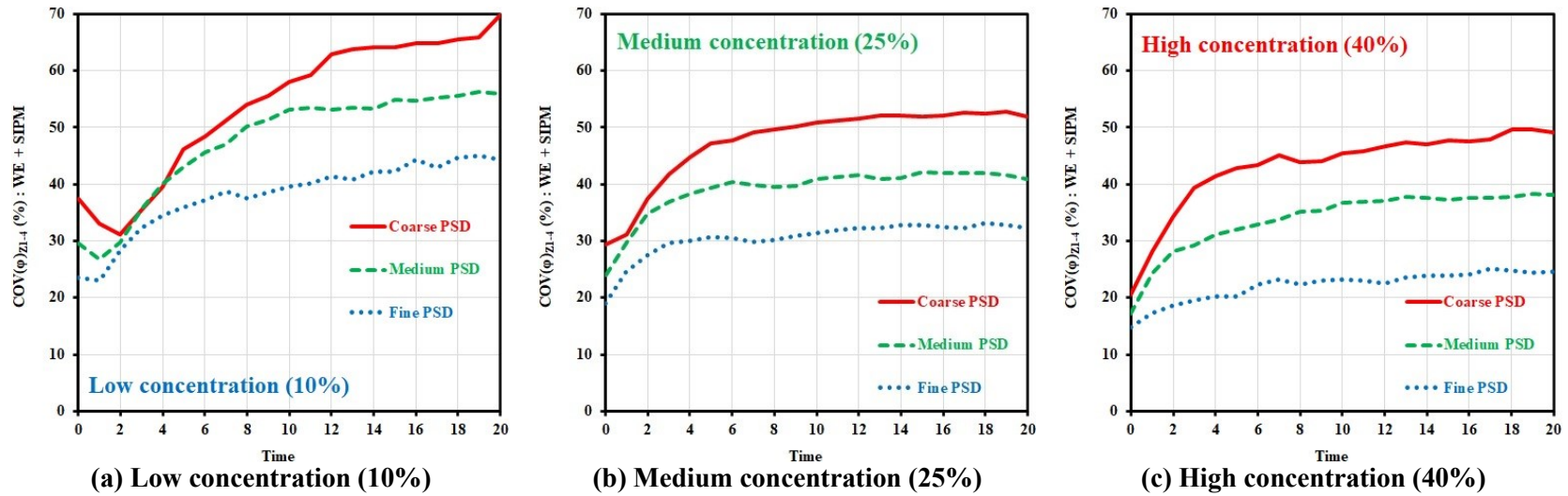
Fig. 6.9. Combined wall effect (WE) and shear-induced particle migration (SIPM): Coefficient of variation of particles' concentrations in four different radial zones Z1 to Z4 ($COV(\varphi)_{Z1-4}$) for the mixtures containing different PSD and **(a)** low (10%), **(b)** medium (25%), and **(c)** high (40%) concentrations of particles over time

Chapter 6. Discrete-element modeling of shear-induced particle migration during zones concrete pipe flow: Effect of size distribution and concentration of aggregate on formation of lubrication layer

205

According to Phillips et al. [17], the particles located in more concentrated zone experience a higher frequency of collisions and can migrate towards the lower collision frequency (i.e., lower concentration and shear rate) and normal to their shear plane. As shown in Eq. (6.52), the flux $N_{collision}$, caused by the spatially varying interaction frequency of particles, is dependent on the mean radius and concentration of solid particles, and shear rate. According to Eq. (6.52), for a given particle concentration (φ) and shear-rate gradient ($\nabla\dot{\gamma}$), the induced heterogeneity is dependent on the particle size (a_p). Accordingly, higher radial heterogeneity is expected for the coarser PSD of particles (i.e., higher "a_p"). Moreover, as shown in Eq. (6.52), the term "$\varphi^2\nabla\dot{\gamma}$" emphasizes that the shear-rate gradient ($\nabla\dot{\gamma}$) results in particle migration from the higher (close to pipe walls) to lower shear-rate zones (pipe axis). Indeed, the higher shear-rate values lead to higher number of collisions. On the other hand, as reflected by the term "$\varphi\dot{\gamma}\nabla\varphi$", any gradient in the particle concentrations (i.e., heterogeneous distribution: $\nabla\varphi \neq 0$) results in spatial variation in the frequency of interactions. As can be observed in Fig. 6.9 for different particle concentrations, the coarse-PSD suspensions exhibited higher initial heterogeneities in the beginning of the flow period, reflected by higher $COV(\varphi)_{Z1-4}$ values at $t = 0$. This can explain the higher radial heterogeneities obtained for coarser-PSD suspensions due to their higher initial gradients in particle concentrations ($\nabla\varphi$) across the pipe.

6.4.3.1   *Shear-induced particle migration (SIPM)*

As described in Eq. (6.45), by distinguishing from the wall effect (WE), the effect of SIPM on radial heterogeneity of the investigated suspensions was evaluated using the $\Delta COV(t)Z1-4$ values and presented in Fig. 6.10. As can be observed, for a given particle concentration, suspensions with coarser PSDs experienced higher SIPM, reflected by higher $\Delta COVZ1-4$ values at the end of the pipe-flow period ($t = 20$). In the case of suspensions proportioned with fine PSD of particles, increasing the total particles' concentrations from 10% to 25% and 40% decreased the final $\Delta COVZ1-4$ values (at $t = 20$) from 20.9% to 13.3% and 9.9%, respectively. However, the minimum and maximum SIPMs of both the medium- and coarse-PSD suspensions, reflected by the lowest and highest $\Delta COVZ1-4$ ($t = 20$) values, were obtained for the medium (MC = 25%) and low (LC = 10%) concentrations of particles, respectively.

Chapter 6. Discrete-element modeling of shear-induced particle migration during zones concrete pipe flow: Effect of size distribution and concentration of aggregate on formation of lubrication layer

206

(a) Low concentration (10%)   **(b) Medium concentration (25%)**   **(c) High concentration (40%)**
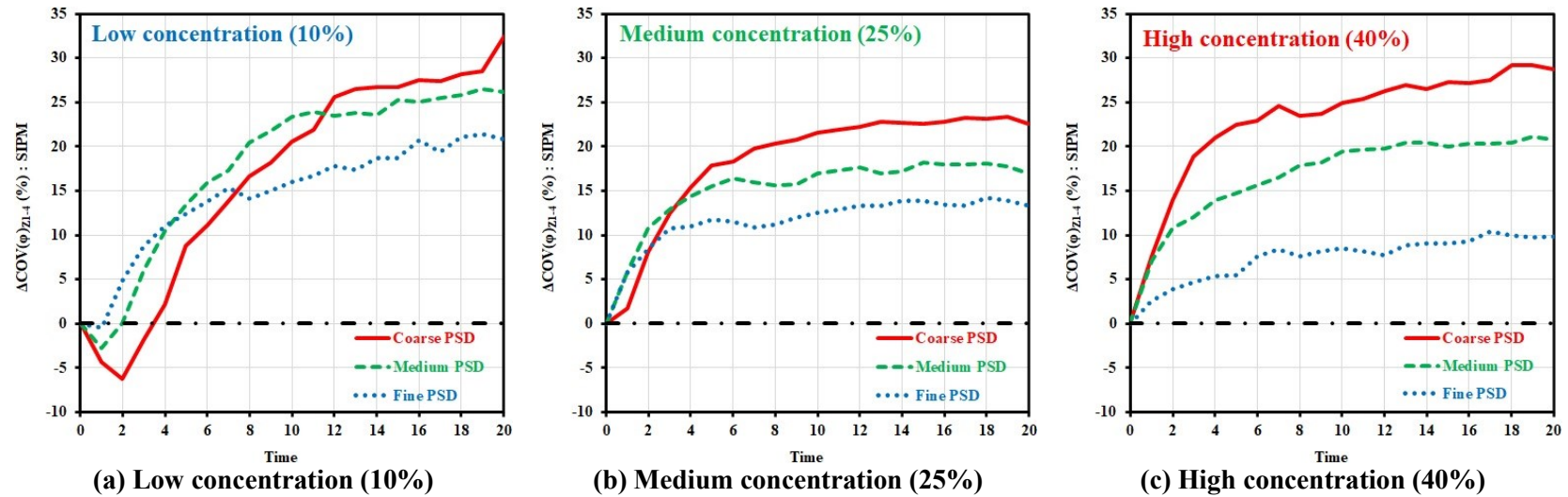
Fig. 6.10. Shear-induced particle migration (SIPM): Variation of *COV* of particles' concentrations in four different radial zones Z1 to Z4 relative to its initial value at *t* = 0 ($\Delta COV(\varphi)_{Z1-4}$) for the mixtures containing different PSD and **(a)** low (10%), **(b)** medium (25%), and **(c)** high (40%) concentrations of particles over time

Furthermore, the LC (10%) suspensions experienced a decrease in their ΔCOV_{Z1-4} values at their initial 5%-10% periods of the pipe flow ($t = 0$ to 1 or 2), referred to an initial shear-induced re-homogenization of particles in the beginning of the pipe flow. Lower variations in ΔCOV_{Z1-4} values can refer to achieve an equilibrium state in SIPM at longer flow times.

6.4.3.2   *Rheological heterogeneity of the investigated pipe flows*

The yield stress and plastic viscosity of the investigated suspensions relative to those of the suspending fluid were calculated as functions of their corresponding concentration ($\varphi = 10\%$, 25%, and 40%) and packing density (φ_{max}) values of the particles (Table 6.6) using Eqs. (47) and (48) and are shown in Figs. 11a and 12a, respectively. As can be observed, the relative yield stress and plastic viscosity values of the modeled concrete mixtures were mostly governed by their corresponding particle concentration (φ). However, for a given φ, coarser PSD of particles led to slightly lower rheological properties, due to their higher φ_{max} values (i.e., lower φ/φ_{max} values). Accordingly, the minimum and maximum yield stress and plastic viscosity values were obtained for the #3-CPSD-LC and #7-FPSD-HC suspensions proportioned with low (10%) and high (40%) concentrations of coarse and fine PSDs of particles, respectively. The yield stress and plastic viscosity of the investigated concrete models ranged from 1.08 to 1.52 and 1.30 to 3.88 relative to the suspending fluid, respectively.

Considering the concentration of each particle subclass (P1-5) and total particle concentrations (Figs. 6-7 and A1-A3 in appendix), packing density of particles located in each of the BC (Z1-3) and LL (Z4) zones at the end of the computation was calculated using Eqs. (40) - (42). The yield stress and plastic viscosity values of the BC and LL zones of the investigated suspensions, relative to those of the suspending fluid were then evaluated using Eqs. (47) and (48) and presented in Figs. 11b-c and 12b-c, respectively. As can be observed, higher yield stress and plastic viscosity were obtained for both the BC and LL zones of the suspensions proportioned with higher particle concentrations.

On the other hand, the PSD of particles showed opposite effects on the rheological properties of the BC and LL zones. As can be observed in Figs. 11b and 12b, higher yield stress and plastic viscosity values were obtained for the BC zones of the suspensions proportioned with coarser PSD. However, as shown in Figs. 11c and 12c, the LL for coarser-PSD suspensions exhibited lower

Chapter 6. Discrete-element modeling of shear-induced particle migration during zones concrete pipe flow: Effect of size distribution and concentration of aggregate on formation of lubrication layer

208

plastic viscosity and yield stress values. Accordingly, among all the investigated suspensions, the pipe flow of the suspension model #9-CPSD-HC resulted in the most-stiff BC (i.e., the highest $\tau_{0\text{-}BC}$ and $\mu_{p\text{-}BC}$ values) but, on the other hand, the most-flowable LL (the lowest $\tau_{0\text{-}LL}$ and $\mu_{p\text{-}LL}$ values) zones. According to Eq. (6.52), this can be attributed to the highest pumping-induced particle migration from the high-shear rate zones (pipe walls) towards the low-shear rate zones (pipe center), obtained for higher concentration (more interparticle collisions) and larger sizes of particles. The yield stress and plastic viscosity of the BC zones ranged from 1.10 to 1.75 and 1.37 to 5.95, respectively, relative to those of the suspending fluid. On the other hand, the yield stress and plastic viscosity of the LLs of the investigated suspensions' pipe flows ranged from 1.02 to 1.27 and 1.05 to 2.16, respectively, relative to those of the suspending fluid.

As shown in Figs. 11d-e and 14d-e, the pumping process led to a radial rheological heterogeneity across the pipe where higher and lower rheological properties were obtained in the BC and LL zones compared to the reference mixture, respectively. As shown in section 3.2.4 and Eqs. (6-49) and (50), this was evaluated using the ratio of the difference between the final rheological properties of the BC and LL zones (at $t = 20$)-to-those of the reference mixture. These include the yield stress- (*YSHI*) and viscosity-heterogeneity indices (*VHI*). As can be observed in Figs. 13a and 13b, increasing both the concentration and size of particles resulted in higher radial heterogeneity in both yield stress and viscosity values. Accordingly, the minimum and maximum rheological heterogeneities across the pipe were obtained for the suspension models #1-FPSD-LC and #9-CPSD-HC, proportioned with low (LC = 10%) and high (HC = 40%) concentrations of fine (FPSD) and coarse (CPSD) PSDs of particles, respectively.

As can be observed in Fig. 6.13c, the investigated pipe flows led to almost 2.85 times higher radial heterogeneity in the viscosity values compared to those obtained for the yield stresses. According to the obtained results, the *YSHI* and *VHI* indices ranged from 6.0% to 42.9% and 19.2% to 120.3%, respectively.

(a) Reference concrete mixture **(b) Bulk concrete (BC: Z1-3)** **(c) Lubrication layer (LL: Z4)**

(d) BC versus reference concrete **(e) LL versus reference concrete**
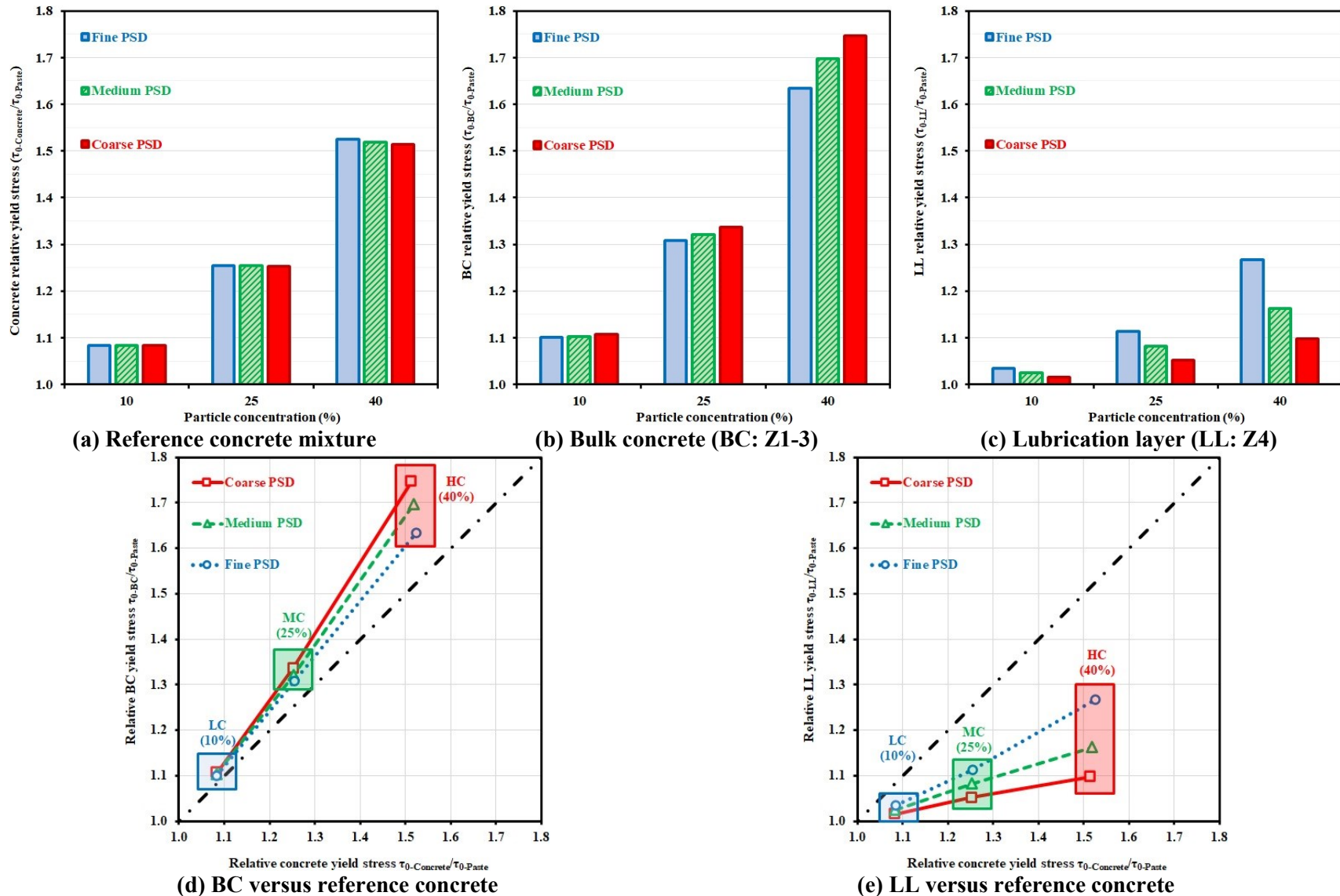
Fig. 6.11. Yield stress of the **(a)** reference concrete mixtures and their corresponding **(b)** BC and **(c)** LL, as well as yield stress of **(d)** BC and **(e)** LL versus those of the reference concrete mixtures containing different PSD and concentrations of particles, relative to that of the suspending fluid

Chapter 6. Discrete-element modeling of shear-induced particle migration during zones concrete pipe flow: Effect of size distribution and concentration of aggregate on formation of lubrication layer

210

(a) Reference concrete mixture   **(b) Bulk concrete (BC: Z1-3)**   **(c) Lubrication layer (LL: Z4)**

(d) BC versus reference concrete   **(e) LL versus reference concrete**
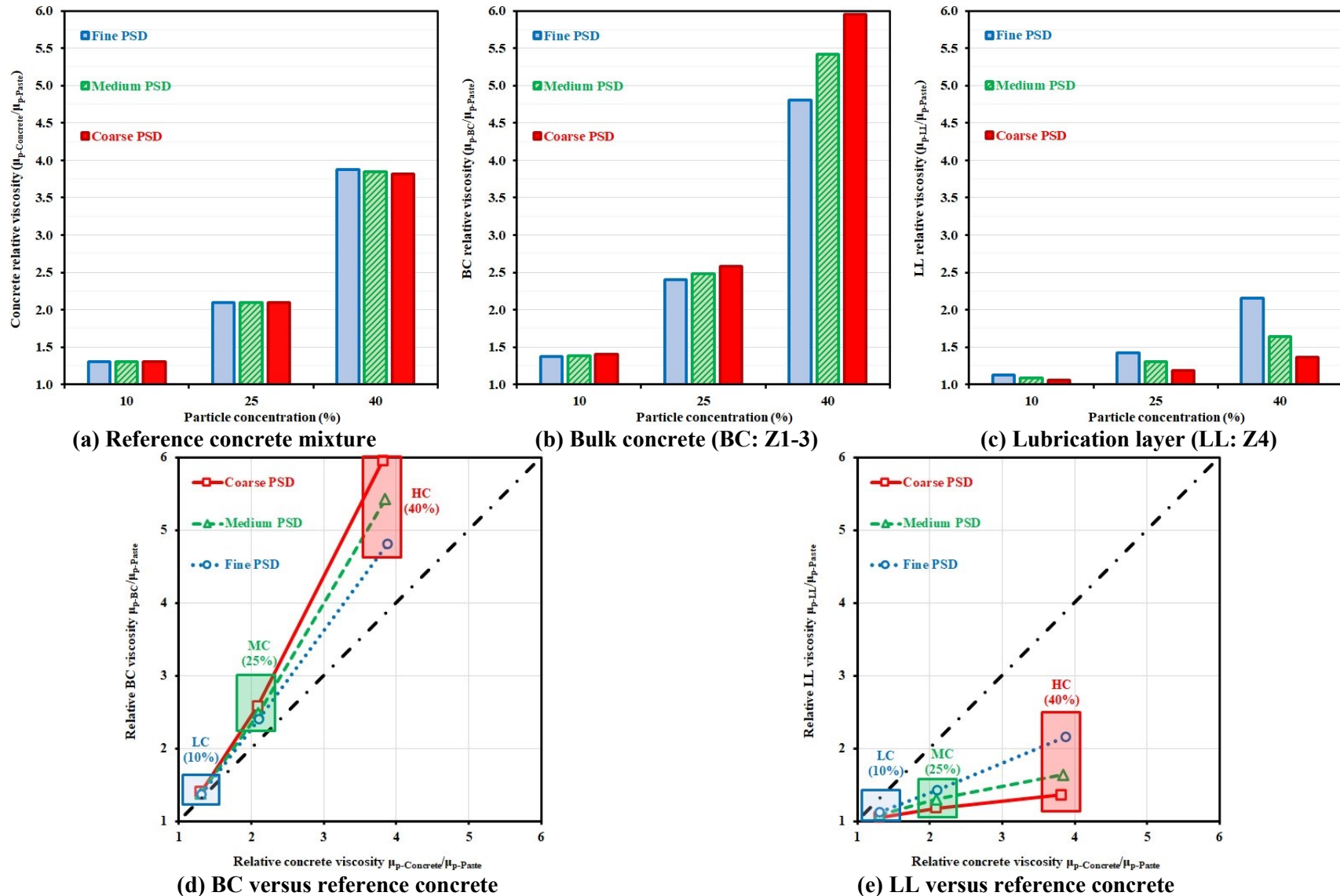
Fig. 6.12. Viscosity of the **(a)** reference concrete mixtures and their corresponding **(b)** BC and **(c)** LL, as well as viscosity of **(d)** BC and **(e)** LL versus those of the reference concrete mixtures containing different PSD and concentrations of particles, relative to that of the suspending fluid

(a) Reference concrete mixture   **(b) Bulk concrete (BC: Z1-3)**   **(c) Lubrication layer (LL: Z4)**
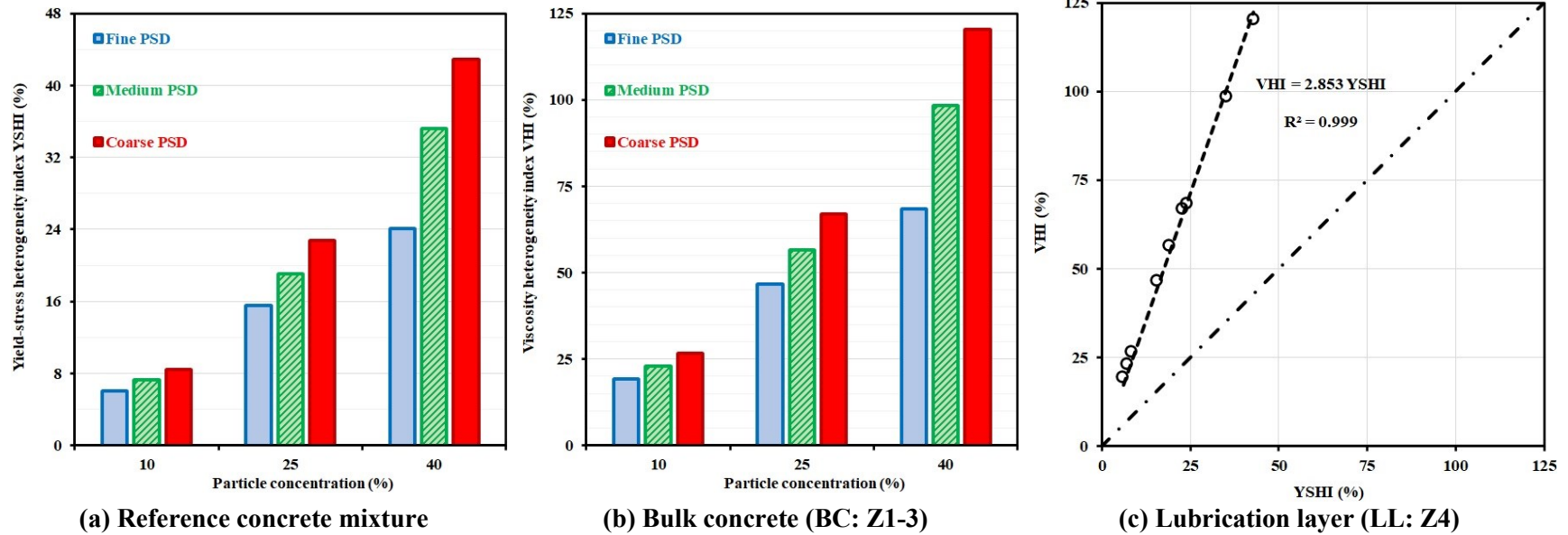
Fig. 6.13. (a) Yield-stress- (*YSHI*) and **(b)** viscosity- (*VHI*) heterogeneity indices as well as **(c)** comparison between the *VHI* and *YSHI* of the investigated suspensions' pipe flows

Chapter 6. Discrete-element modeling of shear-induced particle migration during zones concrete pipe flow: Effect of size distribution and concentration of aggregate on formation of lubrication layer

212

6.4.4 Coupled effect of particles' characteristics on the pumping-induced heterogeneities

As shown in the previous sections, the pumping process caused radial heterogeneities in concentration, PSD, and packing density of particles across the pipe. These were induced due to the effect of the pipe wall (WE) on initial distribution of particles and shear-induced migration of particles (SIPM) over time. As described in Eqs. (6.46) to (6.50), several measures were proposed to evaluate the radial heterogeneities induced by the WE and SIPM. As can be observed in Fig. 6.14, the coupled effect of particles' characteristics, including the concentration (φ), packing density (φ_{max}), and PSD (D_{avg}), on the radial heterogeneity indices was evaluated. The investigated heterogeneity indices include the initial heterogeneity of particles due to the pipe wall effect, reflected by *WEI* values (Eq. (6.46)), as well as the radial yield stress- (*YSHI* in Eq. (6.49)) and viscosity-heterogeneity indices (*VHI* in Eq. (6.50)), shown in Figs. 14a, 14b, and 14c, respectively.

As can be observed in Fig. 6.14, all the proposed heterogeneity measures are in excellent agreement with mean diameter (D_{avg}) and relative-solid packing fraction (φ/φ_{max}) of particles of the investigated suspensions (R^2 of 0.999 and low root-mean square-error, RMSE). As presented in Fig. 6.14a, the pipe walls showed more influence (*WEI*) on the initial heterogeneity of the suspensions proportioned with lower concentration (φ) and higher packing density (i.e., lower φ/φ_{max}) and coarser PSD (i.e., higher D_{avg}) of particles in the beginning of the computation. According to the established correlation in Fig. 6.14a, the D_{avg} and φ/φ_{max} of particles are more effective on the *WEI* values in presence of lower concentration of particles with higher packing density (i.e., lower φ/φ_{max}) and coarser PSD (i.e., higher D_{avg}) of particles, respectively.

Moreover, as shown in Figs. 14b and 14c, higher concentration and lower packing density (i.e., higher φ/φ_{max}) and coarser PSD (i.e., higher D_{avg}) of particles resulted in higher radial heterogeneity indices across the pipe. According to the established correlations, the D_{avg} and φ/φ_{max} of particles showed more influences on the radial rheological heterogeneities of the suspensions proportioned with higher concentration of particles with lower packing density (i.e., higher φ/φ_{max}) and coarser PSD (i.e., higher D_{avg}) of particles, respectively.

Chapter 6. Discrete-element modeling of shear-induced particle migration during zones concrete pipe flow: Effect of size distribution and concentration of aggregate on formation of lubrication layer

213

$$WEI\,(\%) = \cfrac{1}{0.034 + \cfrac{0.098}{D_{avg}^{0.567}} + 0.067 \times \left(\cfrac{\varphi}{\varphi_{max}}\right)^{0.501} \times \ln\left(\cfrac{\varphi}{\varphi_{max}}\right)} - 3.679$$

$R^2 = 0.999$

RMSE = 0.440%

(a) WEI

$$YSHI\,(\%) = \cfrac{1}{\cfrac{0.705}{D_{avg}^{2.069}} + 0.074 \times \left(\cfrac{\varphi}{\varphi_{max}}\right)^{0.309} - 0.082} - 5.921$$

$R^2 = 0.999$

RMSE = 0.321%

$$VHI\,(\%) = \cfrac{1}{0.00072 + \cfrac{0.369}{D_{avg}^{2.181}} + 0.0066 \times \left[\ln\left(\cfrac{\varphi}{\varphi_{max}}\right)\right]^2} - 4.35$$

$R^2 = 0.999$

RMSE = 1.169%
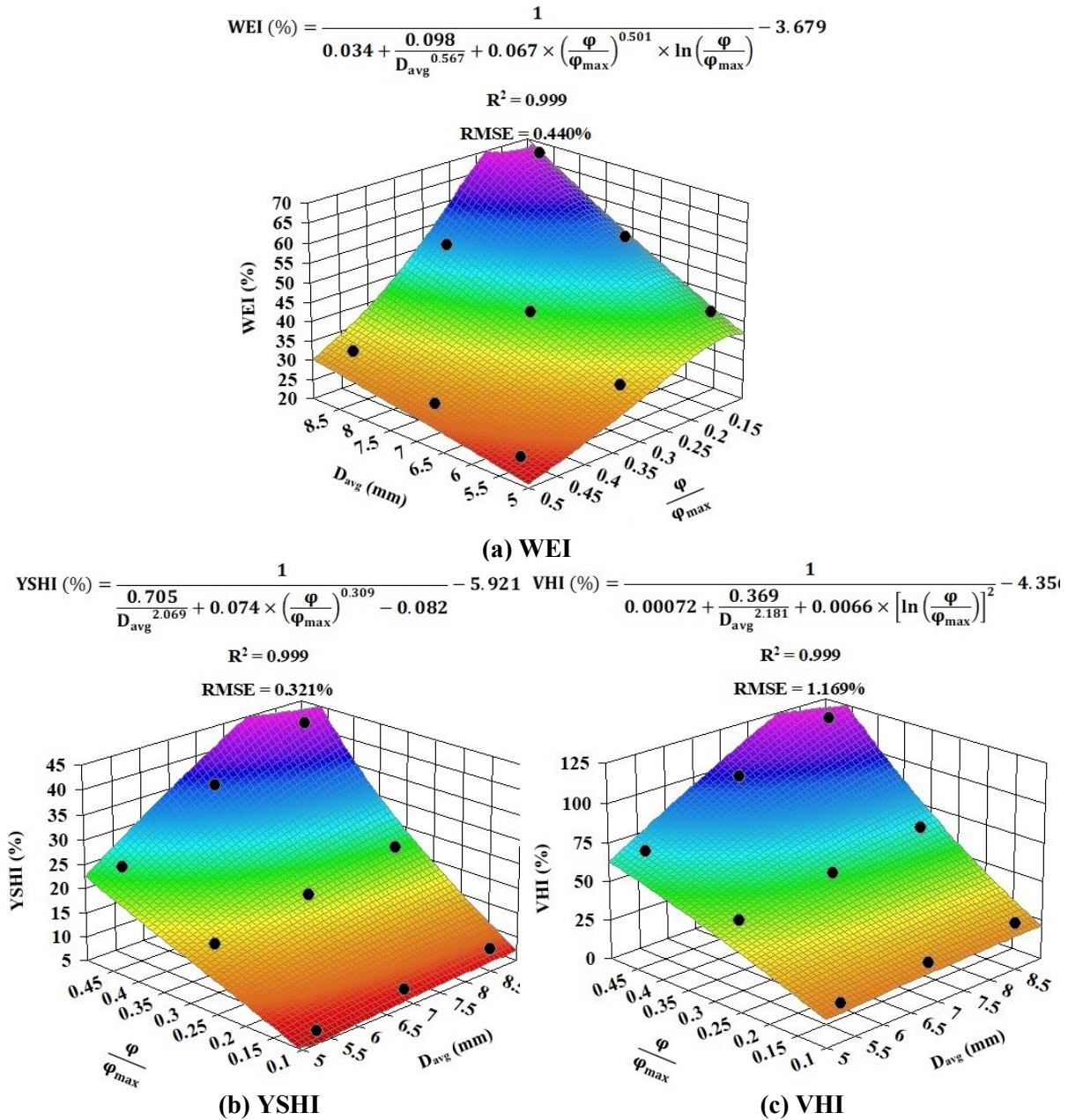
(b) YSHI

(c) VHI

Fig. 6.14. Coupled effect of mean diameter of particles (D_{avg}) and relative-solid packing fraction $\left(\dfrac{\varphi}{\varphi_{max}}\right)$ of particles on **(a)** *WEI*, **(b)** *YSHI*, and **(c)** *VHI* indices.

6.5 Validation of the LL thickness estimations

The LL generally refers to a thin layer of a highly flowable micro-mortar enriched with higher content of cement paste and fine sand and containing no fraction of coarse particles. The determination of LL thickness depends on how the LL is practically defined. For instance, the LL is sometimes defined using a maximum particle-size threshold that the LL can contain, which is typically finer than 2 mm according to the literature [8,25]. Accordingly, the thickness of any fraction of concrete in the vicinity of the pipe wall that only contains particles of a size

Chapter 6. Discrete-element modeling of shear-induced particle migration during zones concrete pipe flow: Effect of size distribution and concentration of aggregate on formation of lubrication layer

214

finer than the selected threshold can be referred to the LL thickness. This definition is practically applied to measure the LL thickness by digital image processing (DIP) of the cut sections of hardened concrete in pipes [32]. Using DIP techniques, the LL thickness corresponds to the zone where no particle coarser than the selected threshold can be detected in vicinity of the pipe walls. On the other hand, the LL thickness can be also defined as the zone in the vicinity of the pipe wall which contains lower volumetric content of aggregate than a certain threshold. This concept is practically used for ultrasonic pulse velocimetry (UPV) techniques applied on pipelines [19,25] where the LL thickness is deduced by detecting an abrupt drop in velocity profile next to the wall, corresponding to a sudden drop in particle concentration in the LL zone. In order to validate the results of the carried-out simulations, the real LL thicknesses of the simulated pipe flow was evaluated at the final time step ($t = 20$) according to both abovementioned concepts, as follows:

(i)   Image analysis technique: A snapshot of the pipe cross section was captured at the middle of the pipe length for all the investigated mixtures using the post-processing results. A quarter of the captured snapshots were investigated using image analysis to evaluate the LL thickness, corresponding to the maximum thickness in vicinity of the pipe wall where no particles larger than P1 (1 mm) can be observed. As shown in Fig. 6.15, the finest particles P1 (1 mm) and larger particles P2-5 were colored in black and white, respectively, for easier differentiation. As can be observed in Fig. 6.15, the evaluated LL thicknesses of the investigated pipe flows ranged from 1.2 to 3.3 mm, which is in general accordance with experimentally observed values using the DIP technique (1-3 mm).

(ii)   Concentration profile: The simulated concentration profiles of the investigated pipe flows were extracted for the zone 0.5*R*-*R* (25-50 mm) at each 1-mm distance. As shown in Fig. 6.16, the LL thickness has then been referred to the thickness of the zone in vicinity of the pipe wall where an abrupt drop is observed in the concentration-profile trend. As can be observed in Fig. 6.16, the estimated LL thicknesses of the investigated pipe flows using the concentration profiles ranged from 4 to 10 mm which is in good accordance with the typical values reported in literature (1-10 mm). Compared to the image analysis approach results, the concentration profiles led to larger estimation of the LL thicknesses.

Chapter 6. Discrete-element modeling of shear-induced particle migration during zones concrete pipe flow: Effect of size distribution and concentration of aggregate on formation of lubrication layer

215
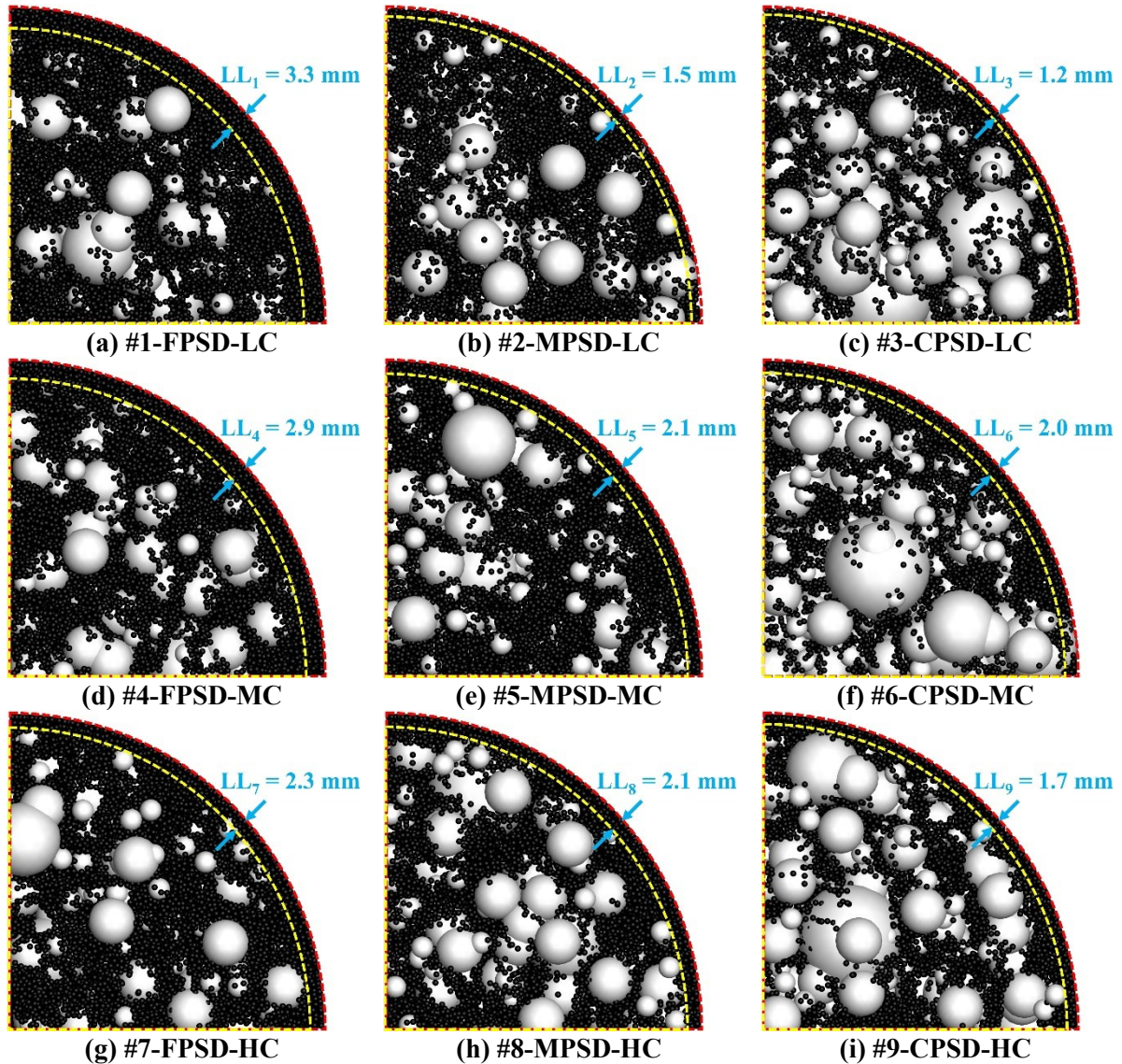
Fig. 6.15. Estimation of LL thicknesses of **(a)** #1-FPSD-LC, **(b)** #2-MPSD-LC, **(c)** #3-CPSD-LC, **(d)** #4-FPSD-MC, **(e)** #5-MPSD-MC, **(f)** #6-CPSD-MC, **(g)** #7-FPSD-HC, **(h)** #8-MPSD-HC, and **(i)** #9-CPSD-HC mixtures using image-analysis technique.

Chapter 6. Discrete-element modeling of shear-induced particle migration during zones concrete pipe flow: Effect of size distribution and concentration of aggregate on formation of lubrication layer

216
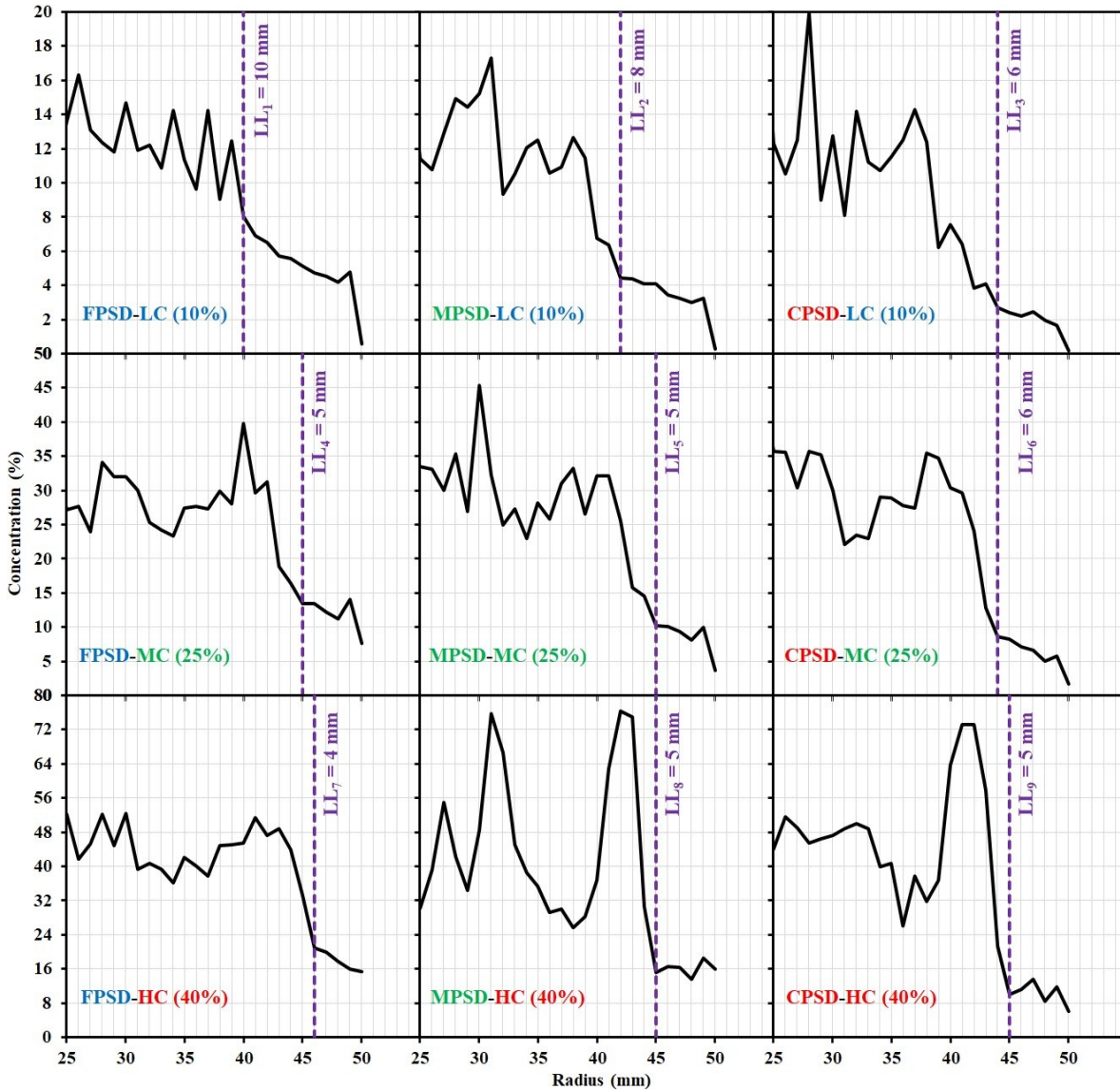
Fig. 6.16. Estimation of LL thicknesses of the investigated mixtures using concentration profiles across the pipe.

Therefore, it can be concluded that depending on the definition used, the numerical simulations were well validated in terms of the LL thickness estimations compared to the typical values reported in literature for actual concrete pumping experiments.

6.6 Limitations and perspectives

The employed DEM approach showed a great potential to simulate the SIPM mechanism and WE leading to formation of LL during concrete pipe flow, covering wide ranges of concentrations and PSDs of aggregate. However, the numerical solution approach used was not without its limitations. Below we list some of these limitations, with a view toward further development and applications of the approach for concrete pipe flow simulation: The employed

DEM approach showed a great potential to simulate the SIPM mechanism and WE leading to formation of LL during concrete pipe flow, covering wide ranges of concentrations and PSDs of aggregate. However, the numerical solution approach used was not without its limitations. Below we list some of these limitations, with a view toward further development and applications of the approach for concrete pipe flow simulation.

- Although the employed soft-sphere approach was able to successfully resolve the particle collisions, the numerical stiffness imposed by the soft-sphere approach limited the number of particles that could be used and the simulation time step. These restrictions can be used with use of a hard-sphere DEM approach, in which the particle collisions are not resolved by the computations. However, since the hard-sphere approach restricts the flow to binary particle collisions, its utility is limited for higher values of the particle concentration. This is particularly true for broad PSDs, for which simultaneous collisions of multiple particles are common.

- The simplification was made by considering a spherical form for all the particles. This assumption significantly facilitated the configuration of the interparticle contacts and particle momentum. The use of realistic morphology of the irregularly shaped particles can lead to provide more realistic simulations; however, it would also significantly slow down the computation time.

- This initial study assumed one-way couple fluid-particle interaction, which becomes increasingly inappropriate as the particle concentration increases. This approach was able to successfully predict a constant decrease in the particle concentration from the central zone Z1 (0-$0.5R$) to the LL (Z4: $0.875R$-R) for the LC (10%) and MC (25%) suspensions. However, neglecting the effect of particles on the suspending fluid flow also led to a non-physical effect on the simulated distribution of particles for HC (40%) suspensions where the highest concentration of particles was unexpectedly obtained in Z3 ($0.75R$-0-$0.875R$). A fully fluid-particle coupling approach (4-way CFD-DEM) is recommended for pumping simulation of high-concentration concrete suspensions.

- It was reported in the literature that pumped concrete mixtures experience multiple time- and shear-dependent variations of rheological properties [3,6,7]. These include a reduction in concrete viscosity after pumping due to pumping-induced increases in temperature and additional dispersion of cement particles and superplasticizer action [6]. Moreover, high shear rates and pressure exerted on pumped concrete mixtures can lead

to major changes in air-void system [3,4,6,7,69] which can subsequently alter their rheological properties. These pumping-induced variations in rheological properties of the suspending paste/mortar matrix were neglected in the current simulations to specifically concentrate on simulation of the SIPM phenomenon during concrete pipe flow as a diphasic suspension. While taking into account the presence of the third material's phase, i.e., air bubbles, as well as time-, temperature-, and shear-dependency of the suspending-fluid rheology can lead to achieve more realistic simulation of the concrete pipe flow, this can add significant complexities to the numerical model and significantly extend computational time and memory requirements.

6.7 Conclusions

In this study, the pipe-wall effect (WE), shear-induced particle migration (SIPM), and the mechanism of formation of the lubrication layer (LL) during concrete pumping were simulated using a multiple time-step soft-sphere DEM approach. In total, nine diphasic concrete suspensions, containing a wide range of spherical particle subclasses of 1 to 17 mm, were investigated. The effect of concentration (10% to 40%) and PSD (fine, medium, and coarse) of aggregate on radial heterogeneities across the pipe was evaluated. The concentration of particles of different particle subclasses was assessed at four different radial zones over the pipe-flow period. The bulk concrete (BC) and LL zones were characterized at the end of the pipe-flow period. According to the numerical results, the following conclusions can be drawn.

- The numerical simulations successfully simulated the migration of finer particles (1 mm) towards the pipe walls and formation of the LL. The lowest concentration and smallest mean diameter (D_{avg}) of particles were obtained in the outer radial zone Z4, hence confirming the formation of the LL in the vicinity of the pipe wall. The mean diameter of particles in the simulated LLs ranged between 1.4 to 2.8 mm.

- The volumetric concentrations of all particle subclasses gradually increased in the central zone (Z1) over time, leading to higher packing of particles in the pipe center. This was observed more for the larger particles (3.5-17 mm) than for the finest particle size (1 mm), leading to relatively coarser PSD in the pipe center compared to the outer radial zones and the reference mixture.

- For a given particle concentration, coarser PSD of particles led to higher rates of particle migration across the pipe. Moreover, in the case of the low- (LC = 10%) and medium-

Chapter 6. Discrete-element modeling of shear-induced particle migration during zones concrete pipe flow: Effect of size distribution and concentration of aggregate on formation of lubrication layer

219

(MC = 25%) concentration suspensions, the total concentration of particles continuously decreased from the pipe center towards the LL zone. The high-concentration (HC = 40%) suspensions showed the highest particle concentration in Z3 (0.75R-0.875R), followed by the central zones Z1 and Z2 (0-0.75R). Therefore, a fully fluid-particle coupling approach (4-way CFD-DEM) is recommended for more accurate simulation of the highly concentrated suspension pipe flows.

- For a given particle concentration, a larger mean diameter of particles (Davg) was obtained across the pipe for the coarser-PSD suspensions. Moreover, for all the investigated suspensions, comparable Davg values were obtained in the central three-quarters of the pipe (0-0.75R). Comparison between the Davg values confirmed the migration of larger particles from the higher-shear rate zones (0.75R-R) towards the central lower-shear rate zones (0-0.75R).

- The suspensions proportioned with lower concentration and coarser PSD of particles exhibited higher COV of particle concentrations in different radial zones over time. For a given concentration, suspensions with coarser PSDs experienced higher SIPM. In the case of fine-PSD suspensions, higher particle concentrations led to lower SIPM.

- The yield stress of the BC and LL zones at the end of flow period ranged from 1.10 to 1.75 and 1.02 to 1.27, relative to the suspending fluid, respectively. The relative plastic viscosity of the BC and LL zones to the suspending fluid ranged between 1.37-5.95 and 1.05-2.16, respectively. The highest rheological heterogeneity across the pipe was obtained for the highest concentration and coarsest PSD of particles.

- Different measures were proposed to evaluate the pumping-induced heterogeneity of the investigated suspensions across the pipes in terms of the wall effect (*WEI*), yield stress- (*YSHI*) and viscosity-heterogeneity indices (*VHI*). The proposed *WEI*, *YSHI*, and *VHI* indices were found to be in very good agreement with mean diameter (D_{avg}) and relative-solid packing fraction (φ/φ_{max}) of particle.

- Higher wall effect was obtained for the suspensions proportioned with lower concentration and higher packing density (i.e., lower φ/φ_{max}) and coarser PSD of particles. On the other hand, higher concentration and lower packing density (i.e., higher φ/φ_{max}), and coarser PSD of particles resulted in higher rheological heterogeneity across the pipe.

- The estimated LL thicknesses of the investigated pipe flows, using the image analysis of post-processing of the pipe cross sections (1.2-3.3 mm) and concentration profiles (4-10 mm), were well validated compared to values typically reported in the literature for actual concrete pumping experiments.

6.8 Acknowledgement

Chapter 6. Discrete-element modeling of shear-induced particle migration during zones concrete pipe flow: Effect of size distribution and concentration of aggregate on formation of lubrication layer

221

APPENDIX A

The evolution of the volumetric concentration of different particle subclasses P1-5 in different radial

zones Z1-4 are presented in Figs. A1-A3 for LC (10%), MC (25%), and HC (40%) suspensions.

APPENDIX A
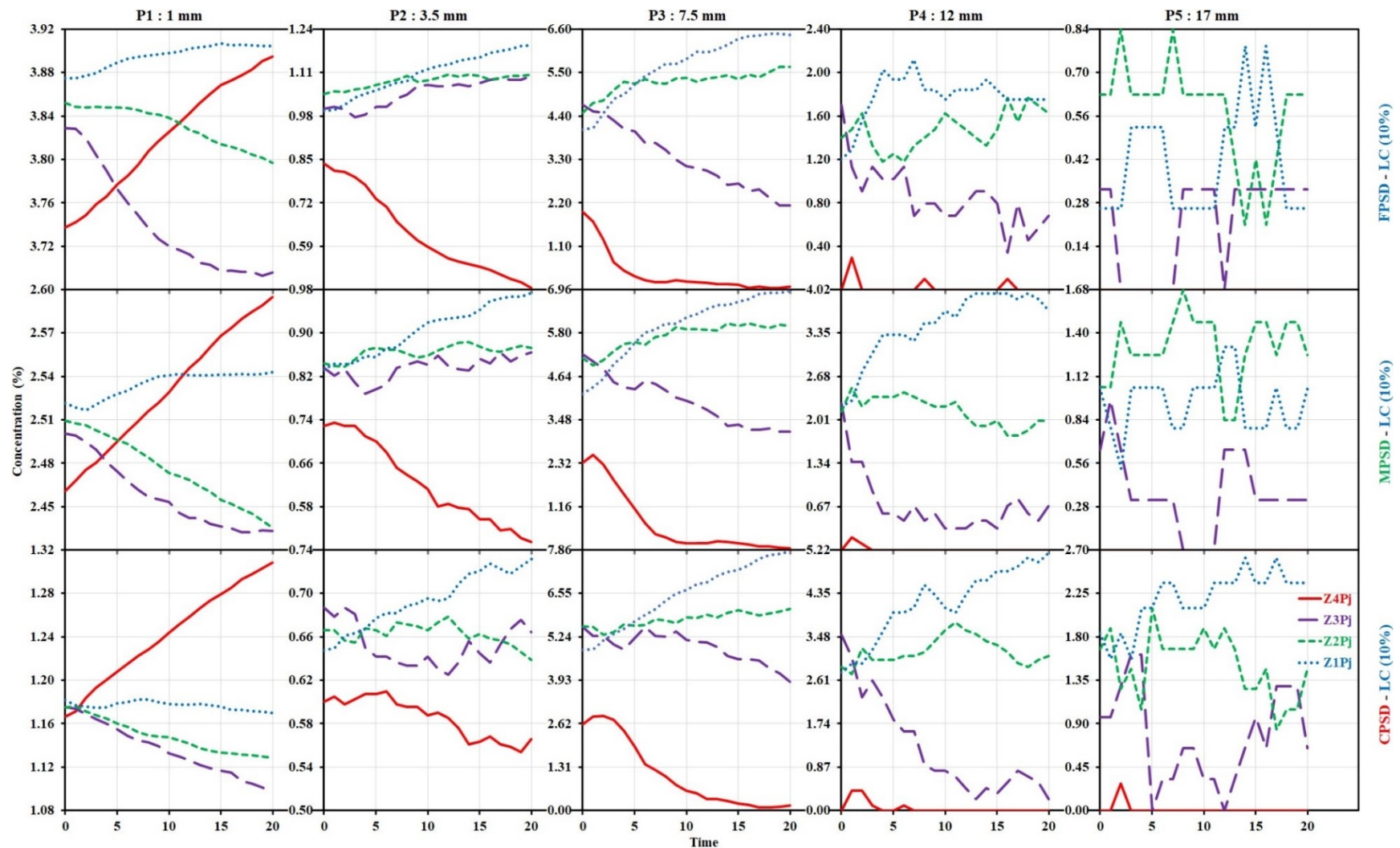
Fig. 6.61. Concentrations (ZiPj) of particles Pj (j = 1-5) in four different radial zones Zi (i = 1-4) for the mixtures containing low (10%) concentration of fine (FPSD), medium (MPSD) and coarse (CPSD) PSD of particles over time.

Chapter 6. Discrete-element modeling of shear-induced particle migration during zones concrete pipe flow: Effect of size distribution and concentration of aggregate on formation of lubrication layer

223
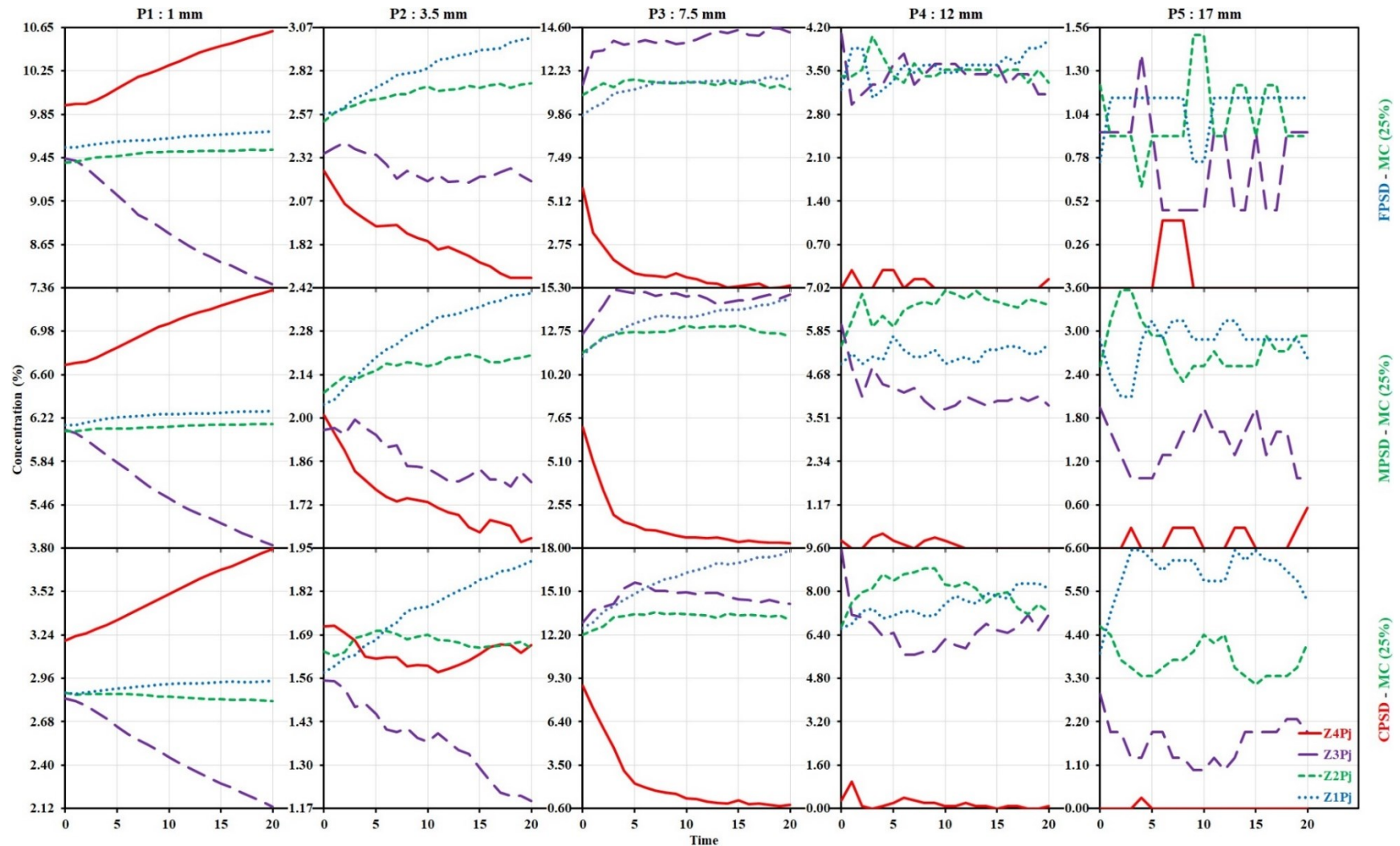
Fig. 62. Concentrations (ZiPj) of particles Pj (j = 1-5) in four different radial zones Zi (i = 1-4) for the mixtures containing medium (25%) concentration of fine (FPSD), medium (MPSD) and coarse (CPSD) PSD of particles over time.

Chapter 6. Discrete-element modeling of shear-induced particle migration during zones concrete pipe flow: Effect of size distribution and concentration of aggregate on formation of lubrication layer

224
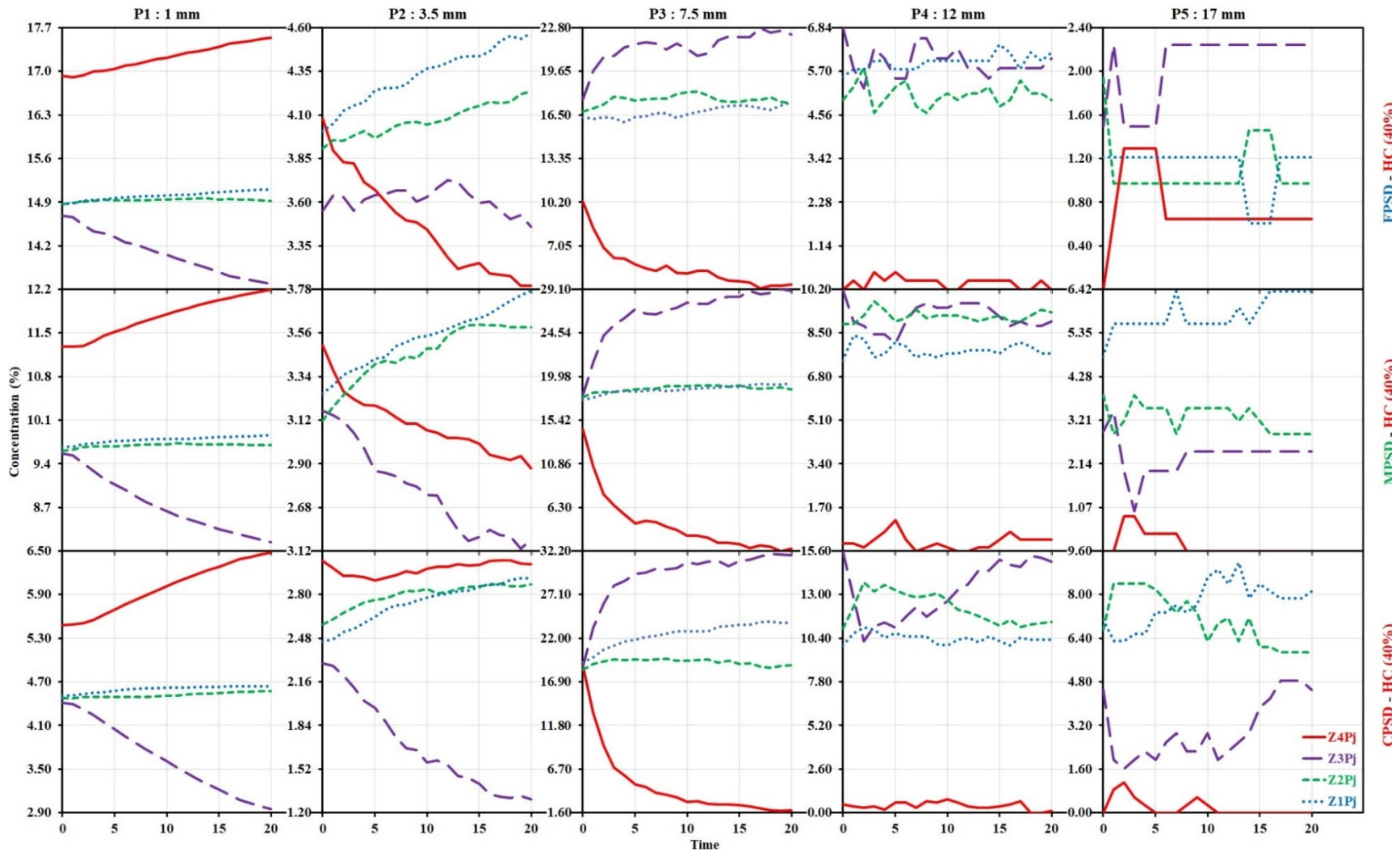
Fig. 6.63. Concentrations (ZiPj) of particles Pj (j = 1-5) in four different radial zones Zi (i = 1-4) for the mixtures containing high (40%) concentration of fine (FPSD), medium (MPSD) and coarse (CPSD) PSD of particles over time.

Chapter 6. Discrete-element modeling of shear-induced particle migration during zones concrete pipe flow: Effect of size distribution and concentration of aggregate on formation of lubrication layer

225

APPENDIX B

Repeatability of the carried-out simulation

In this study, for each of the investigated mixtures, given the concentration and PSD of particles (Table 6.6), the particles were produced using a random number generator function in a descending order of size (i.e., larger particles were generated earlier). Given a definite environment, the used random function generates a defined sequence of random numbers. The subroutine keeps an internal state, which is the source of random numbers. Once the random function is called, it changes the internal state and generates a new random number. It means, starting from a particular state, the same sequence of random numbers are generated, i.e., given the number of particles to be generated, the random generator produces exactly the same values (i.e., coordinates in our case). This reproducibility is useful to reproduce the same results in simulation, when another variable is investigated, such as suspending fluid rheology or flow rate magnitude, etc.

The repeatability of the model due to the initial distribution of particles was evaluated using an additional seed to the particle numbers added to the present random generator. Therefore, the generated coordinates are different by the original values used in the carried-out model while keeping the same PSD and concentration, depending on the new seed which is computer time/date in this case. The modified random generator was applied for two additional cases for #3-CPSD-LC mixture, as the suspension showing the highest SIPM among all the investigated mixtures, reflected by the highest $COV(\varphi)_{Z1-4}$ value over time (Fig. 6.9a). The results of the total particles' concentrations in different radial zones Z1-4 are presented in Fig. 6.B1.a. As can be observed, all the particle generation trials showed comparable trends and values. Moreover, as shown in Fig. 6.B1.b, negligible differences were found between the $COV(\varphi)_{Z1-4}$ values obtained for the original generation of particles (Trial #1) and two additional random generations #2 and #3, reflected by low root-mean squared-errors (RMSE) of 2.2% and 3.5%, respectively.

Chapter 6. Discrete-element modeling of shear-induced particle migration during zones concrete pipe flow: Effect of size distribution and concentration of aggregate on formation of lubrication layer

226
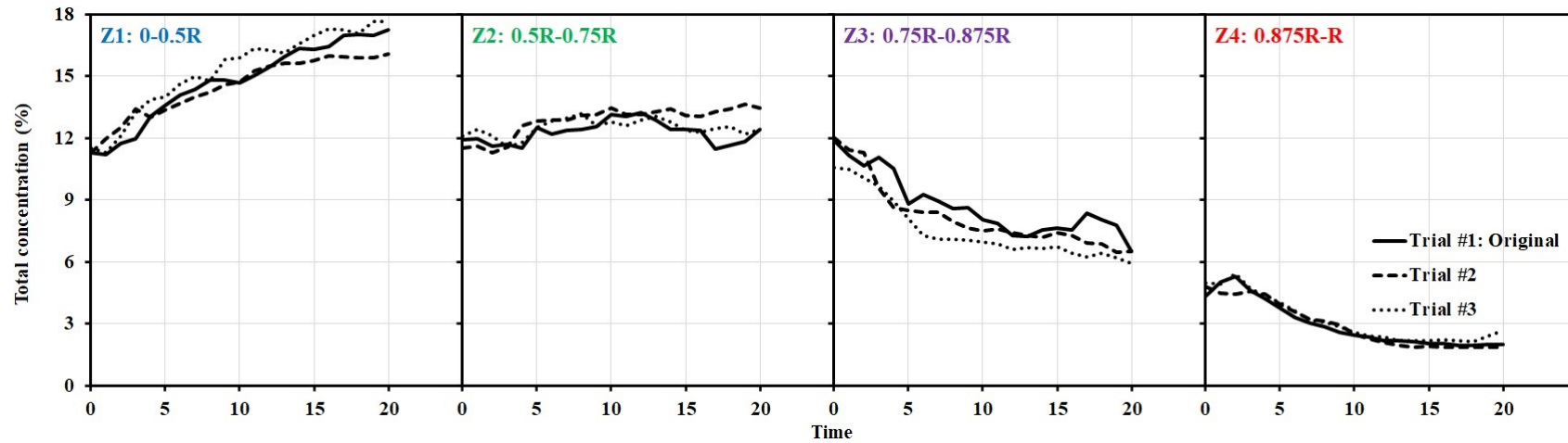
(a)
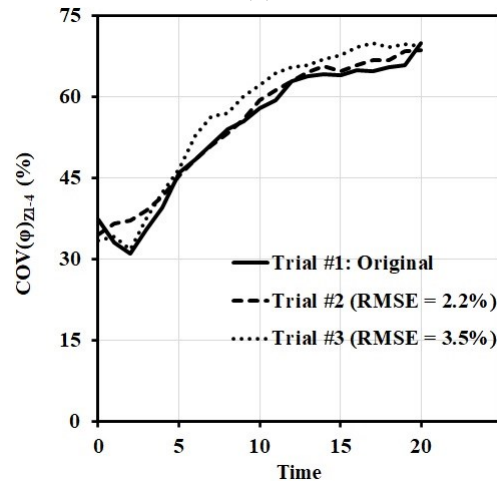
(b)

Fig. 61. (a) Total concentrations of particles and **(b)** coefficient of variation (COV) of particles' concentrations in four different radial zones Z1 to Z4 over time for three trials of random generation of particles (#3-CPSD-LC (10%)).

Chapter 6. Discrete-element modeling of shear-induced particle migration during zones 227
concrete pipe flow: Effect of size distribution and concentration of aggregate on formation of
lubrication layer

Moreover, the repeatability of the employed approach due to variation of the selected fluid time step (ΔT_f) was assessed for the same mixture #3-CPSD-LC. Two additional ΔT_f of 0.008 and 0.012 were applied in addition to that of the original carried-out model (ΔT_f of 0.01). As can be observed in Fig. 6.B2.a, very similar concentration values and trends were obtained at different radial zones Z1-4 over time for all three different applied ΔT_f values. Accordingly, as shown in Fig. 6.B2.b, low RMSEs of 1.6% and 2.1% were obtained for the $COV(\varphi)_{Z1-4}$ values corresponding to ΔT_f of 0.008 and 0.012 compared to those of the original model (ΔT_f of 0.01).

Chapter 6. Discrete-element modeling of shear-induced particle migration during zones concrete pipe flow: Effect of size distribution and concentration of aggregate on formation of lubrication layer

228
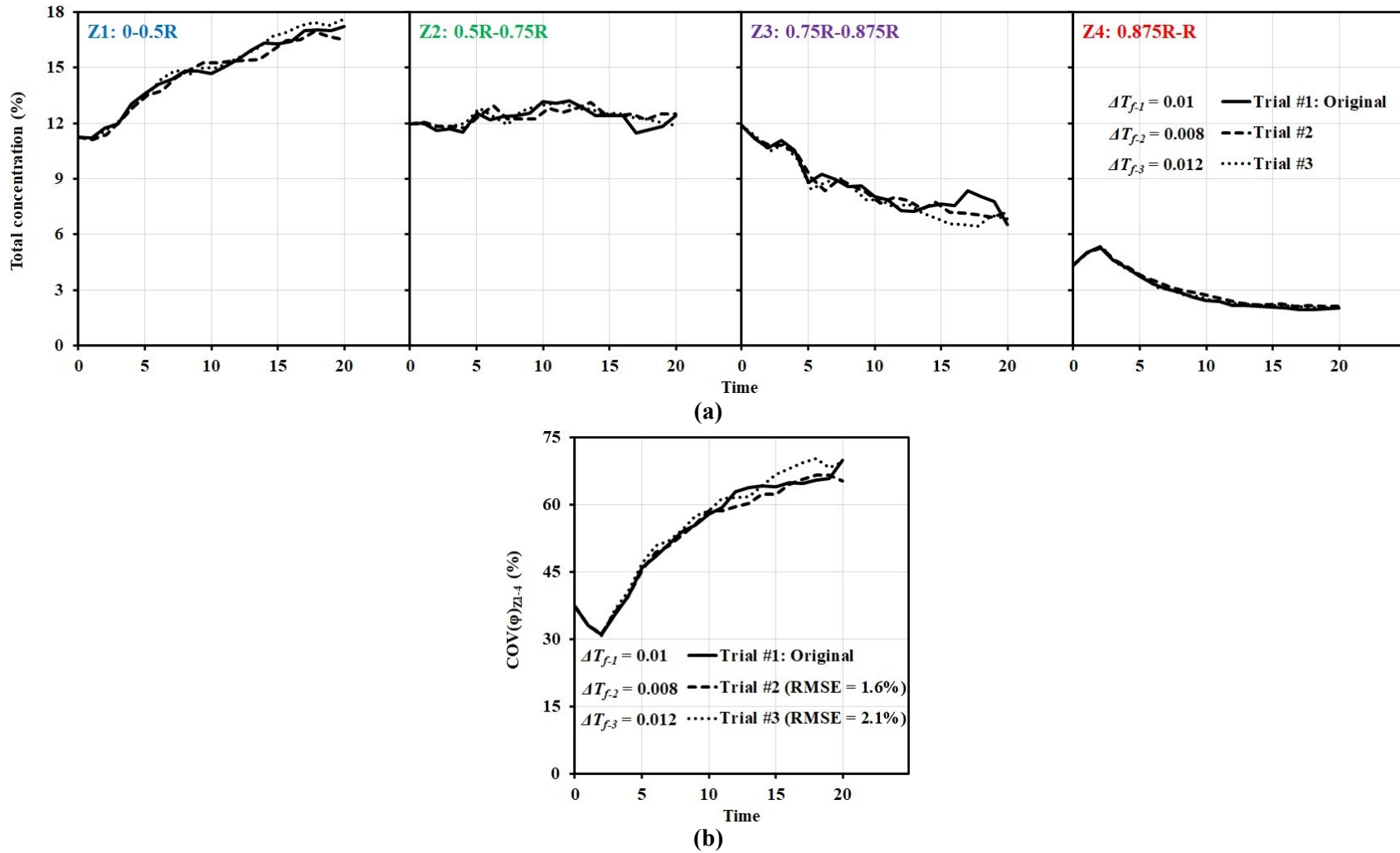
Fig. 62. (a) Total concentrations of particles and **(b)** coefficient of variation (COV) of particles' concentrations in four different radial zones Z1 to Z4 over time for three trials of fluid time step (#3-CPSD-LC (10%)).

Chapter 6. Discrete-element modeling of shear-induced particle migration during zones   229
concrete pipe flow: Effect of size distribution and concentration of aggregate on formation of
lubrication layer

REFERENCES

[1]   D. Kaplan, F. De Larrard, T. Sedran, Design of concrete pumping circuit, ACI Materials Journal, 102 (2) (2005) 110-117. https://doi.org/10.14359/14304.

[2]   J. Aldred, Burj Khalifa - a new high for high-performance concrete, Proceedings of the Institution of Civil Engineers - Civil Engineering, 163 (2) (2010) 66-73. https://doi.org/10.1680/cien.2010.163.2.66.

[3]   D. Feys, G. De Schutter, S. Fataei, N.S. Martys, V. Mechtcherine, Pumping of concrete: Understanding a common placement method with lots of challenges, Cement and Concrete Research, 154 (2022) 106720. https://doi.org/10.1016/j.cemconres.2022.106720.

[4]   National Ready Mixed Concrete Association (2005) CIP 21- Loss of air content in pumped concrete. https://www.nrmca.org/wp-content/uploads/2020/04/21pr.pdf.

[5]   American Concrete Pumping Association (2008) Concrete 101, A guide to understanding the qualities of concrete and how they affect pumping. http://www.concretepumpers.com/files/attachments/concrete_101.pdf.

[6]   D. Feys, G. De Schutter, K.H. Khayat, R. Verhoeven, Changes in rheology of self-consolidating concrete induced by pumping, Materials and Structures, 49 (2016) 4567-4677. https://doi.org/10.1617/s11527-016-0815-7.

[7]   F. Li, W. Shen, Q. Yuan, X. Hu, Z. Li, C. Shi, An overview on the effect of pumping on concrete properties, Cement and Concrete Composites, 129 (2022) 104501. https://doi.org/10.1016/j.cemconcomp.2022.104501.

[8]   T. Tavangar, M. Hosseinpoor, A. Yahia, K.H. Khayat, Computational investigation of concrete pipe flow: Critical review, ACI Materials Journal, 118 (6) (2021) 203-215. https://dx.doi.org/10.14359/51733124.

[9]   A. Karnis, H.L. Goldsmith, S.G. Mason, The kinetics of flowing dispersions: I. Concentrated suspensions of rigid particles, Journal of Colloid and Interface Science, 22 (6) (1966) 531-553. https://doi.org/10.1016/0021-9797(66)90048-8.

[10]   F. Gadala-Maria, A. Acrivos, Shear-induced structure in a concentrated suspension of solid spheres, Journal of Rheology, 24 (6) (1980) 799-814. https://doi.org/10.1122/1.549584.

Chapter 6. Discrete-element modeling of shear-induced particle migration during zones concrete pipe flow: Effect of size distribution and concentration of aggregate on formation of lubrication layer

230

[11]   D. Leighton, A. Acrivos, The shear-induced migration of particles in concentrated suspensions, Journal of Fluid Mechanics, 181 (1987) 415-439. https://doi.org/10.1017/S0022112087002155.

[12]   J.R. Abbott, N. Tetlow, A.L. Graham, S.A. Altobelli, E. Fukushima, L.A. Mondy, T.S. Stephens, Experimental observations of particle migration in concentrated suspensions: Couette flow, Journal of Rheology, 35 (5) (1991) 773-795. https://doi.org/10.1122/1.550157.

[13]   D. Talib, E. Lemaire, L. Lobry, F. Moukalled, Shear-induced particle migration: Predictions from (1994) 157-1experimental evaluation of the particle stress tensor, Journal of Non-Newtonian Fluid Mechanics, 198 (2013) 78-95. https://doi.org/10.1016/j.jnnfm.2013.03.006.

[14]   P.R. Nott, J.F. Brady, Pressure-driven flow of suspensions: Simulation and theory, Journal of Fluid Mechanics, 275 99. https://doi.org/10.1017/S0022112094002326.

[15]   J.F. Morris, F. Boulay, Curvilinear flows of noncolloidal suspensions: The role of normal stresses, Journal of Rheology, 43 (5) (1999) 1213-1237. https://doi.org/10.1122/1.551021.

[16]   Y. Li, J. Fu, Z. Geng, H. Dong, CFD simulations of shear induced migration in pressure-driven flow with non-Brownian suspensions, International Journal of Multiphase Flow, 147 (2022) 103918. https://doi.org/10.1016/j.ijmultiphaseflow.2021.103918.

[17]   R.J. Phillips, R.C. Armstrong, R.A. Brown, A.L. Graham, J.R. Abbott, A constitutive equation for concentrated suspensions that accounts for shear-induced particle migration, Physics of Fluids A: Fluid Dynamics, 4 (1) (1992) 30-40. https://doi.org/10.1063/1.858498.

[18]   S.D. Jo, C.K. Park, J.H. Jeong, S.H. Lee, S.H. Kwon, A computational approach to estimating a lubricating layer in concrete pumping, Computers, Materials & Continua, 27 (3) (2012) 189-210. https://doi.org/10.3970/cmc.2011.027.189

[19]   M.S. Choi, Y.J. Kim, S.H. Kwon, Prediction on pipe flow of pumped concrete based on shear-induced particle migration, Cement and Concrete Research, 52 (2013) 216-224. https://doi.org/10.1016/j.cemconres.2013.07.004.

[20]   M.S. Choi, Numerical prediction on the effects of the coarse aggregate size to the pipe flow of pumped concrete, Journal of Advanced Concrete Technology, 12 (8) (2014) 239-249. https://doi.org/10.3151/jact.12.239.

[21]   X. Xie, L. Zhang, C. Shi, X. Liu, Prediction of lubrication layer properties of pumped concrete based

Chapter 6. Discrete-element modeling of shear-induced particle migration during zones concrete pipe flow: Effect of size distribution and concentration of aggregate on formation of lubrication layer

231

on flow induced particle migration, Construction and Building Materials, 322 (7) (2022) 126115. https://doi.org/10.1016/j.conbuildmat.2021.126115.

[22]   D. Kaplan, Pumping of Concrete. Ph.D. Thesis, LCPC, Paris, France (1999) (In French). https://tel.archives-ouvertes.fr/tel-01310219/.

[23]   D. Kaplan, T. Sedran, F. De Larrard, M. Vachon, G. Machese, Forecasting pumping parameters, In: Proc. of the 2nd Int RILEM symposium on self-compacting concrete, Tokyo, 2001, 556-564.

[24]   S.H. Kwon, K.P. Jang, J.H. Kim, S.P. Shah, State of the art on prediction of concrete pumping, International Journal of Concrete Structures and Materials, 10 (3) (2016) 75-85. https://doi.org/10.1007/s40069-016-0150-y.

[25]   K.P. Jang, W.J. Kim, M.S. Choi, S.H. Kwon, A new method to estimate rheological properties of lubricating layer for prediction of concrete pumping, Advances in Concrete Construction, 6 (5) (2018) 465-483. http://dx.doi.org/10.12989/acc.2018.6.5.465.

[26]   S. Jacobsen, L. Haugan, T.A. Hammer, E. Kalogiannidis, Flow conditions of fresh mortar and concrete in different pipes, Cement and Concrete Research, 39 (11) (2009) 997-1006. https://doi.org/10.1016/j.cemconres.2009.07.005.

[27]   H.D. Le, E.H. Kadri, S. Aggoun, J. Vierendeels, P. Troch, G. De Schutter, Effect of lubrication layer on velocity profile of concrete in a pumping pipe, Materials and Structures, 48 (2015) 3991-4003. https://doi.org/10.1617/s11527-014-0458-5.

[28]   E. Secrieru, S. Fataei, C. Schröfl, V. Mechtcherine, Study on concrete pumpability combining different laboratory tools and linkage to rheology, Construction and Building Materials, 144 (2017) 451-461. https://doi.org/10.1016/j.conbuildmat.2017.03.199.

[29]   T.T. Ngo, E.H. Kadri, R. Bennacer, F. Cussigh, Use of tribometer to estimate interface friction and concrete boundary layer composition during the fluid concrete pumping, Construction and Building Materials, 24 (7) (2010) 1253-1261. https://doi.org/10.1016/j.conbuildmat.2009.12.010.

[30]   E. Secrieru, Pumping behaviour of modern concretes - Characterisation and prediction, Ph.D. Dissertation, Technische Universität Dresden (2018). https://nbn-resolving.org/urn:nbn:de:bsz:14-qucosa-234912.

[31]   A. Salinas, D. Feys, Estimation of lubrication layer thickness and composition through reverse

Chapter 6. Discrete-element modeling of shear-induced particle migration during zones concrete pipe flow: Effect of size distribution and concentration of aggregate on formation of lubrication layer

232

engineering of interface rheometry tests, Materials, 13 (8) (2020) 1799. https://doi.org/10.3390/ma13081799.

[32]   L. Chen, G. Liu, W. Cheng, G. Pan, Pipe flow of pumping wet shotcrete based on lubrication layer, SpringerPlus 5, 945 (2016) https://doi.org/10.1186/s40064-016-2633-3.

[33]   V. Mechtcherine, V.N. Nerella, K. Kasten, Testing pumpability of concrete using Sliding Pipe Rheometer, Construction and Building Materials, 53 (2014) 312-323. https://doi.org/10.1016/j.conbuildmat.2013.11.037.

[34]   F. Chapdelaine, Étude fondamentale et pratique sur le pompage du béton, Ph.D. Thesis, Université Laval (2007). http://hdl.handle.net/20.500.11794/18881.

[35]   D. Feys, K.H. Khayat, A. Perez-Schell, R. Khatib, Development of a tribometer to characterize lubrication layer properties of self-consolidating concrete, Cement & Concrete Composites, 54 (2014) 40-52. https://doi.org/10.1016/j.cemconcomp.2014.05.008.

[36]   N. Roussel, A. Gram, M. Cremonesi, L. Ferrara, K. Krenzer, V. Mechtcherine, S. Shyshko, J. Skocec, J. Spangenberg, O. Svec, L.N. Thranse, K. Vasilic, Numerical simulations of concrete flow: A benchmark comparison, Cement and Concrete Research, 79 (2016) 265-271. https://doi.org/10.1016/j.cemconres.2015.09.022.

[37]   M.A. Haustein, M.E. Pirharati, S. Fataei, D. Ivanov, D.J. Heredia, N. Kijanski, D. Lowke, V. Mechtcherine, D. Rostan, T. Schäfer, C. Schilde, Benchmark simulations of dense suspensions flow using computational fluid dynamics, Frontiers in Materials, 9 (2022) 874144. https://doi.org/10.3389/fmats.2022.874144.

[38]   V.N. Nerella, V. Mechtcherine, Virtual Sliding Pipe Rheometer for estimating pumpability of concrete, Construction and Building Materials, 170 (2018) 366-377. https://doi.org/10.1016/j.conbuildmat.2018.03.003.

[39]   E. Secrieru, J. Khodor, C. Schröfl, V. Mechtcherine, Formation of lubrication layer and flow type during pumping of cement-based materials, Construction and Building Materials, 178 (2018) 507-517. https://doi.org/10.1016/j.conbuildmat.2018.05.118.

[40]   E. Secrieru, W. Mohamed, S. Fataei, V. Mechtcherine, Assessment and prediction of concrete flow and pumping pressure in pipeline, Cement and Concrete Composites, 107 (2020) 103495. https://doi.org/10.1016/j.cemconcomp.2019.103495.

Chapter 6. Discrete-element modeling of shear-induced particle migration during zones concrete pipe flow: Effect of size distribution and concentration of aggregate on formation of lubrication layer

233

[41]   T. Tavangar, M. Hosseinpoor, A. Yahia, K.H. Khayat, Novel tri-viscous model to simulate pumping of flowable concrete through characterization of lubrication layer and plug zones, Cement and Concrete Composites, 126 (2022) 104370. https://doi.org/10.1016/j.cemconcomp.2021.104370.

[42]   A.A. Mahmood, M. Elektorowicz, A review of discrete element method research on particulate systems, Soft Soil Engineering International Conference 2015 (SEIC2015), IOP Conference Series: Materials Science and Engineering, 136 (2016) 012034. https://www.dx.doi.org/10.1088/1757-899X/136/1/012034.

[43]   G. Cao, H. Zhang, Y. Tan, J. Wang, R. Deng, X. Xiao, B. Wu, Study on the effect of coarse aggregate volume fraction on the flow behavior of fresh concrete via DEM, Procedia engineering, 102 (2015) 1820-1826. https://doi.org/10.1016/j.proeng.2015.01.319.

[44]   M.A. Haustein, G. Zhang, R. Schwarze, Segregation of granular materials in a pulsating pumping regime, Granular Matter, 21 (2019) 111. https://doi.org/10.1007/s10035-019-0967-6.

[45]   Y. Zhan, J. Gong, Y. Huang, C. Shi, Z. Zuo, Y. Chen, Numerical study on concrete pumping behavior via local flow simulation with discrete element method, Materials, 12 (9) (2019) 1415. https://doi.org/10.3390/ma12091415.

[46]   J. Hao, C. Jin, Y. Li, Z. Wang, J. Liu, H. Li, Simulation of motion behavior of concrete in pump pipe by DEM, Advances in Civil Engineering, (2021) 3750589. https://doi.org/10.1155/2021/3750589.

[47]   P.A. Cundall, O.D.L. Strack, A discrete numerical model for granular assembles, Géotechnique, 29 (1) (1979) 47-65. https://doi.org/10.1680/geot.1979.29.1.47.

[48]   H.R. Norouzi, R. Zarghami, R. Sotudeh-Gharebagh, N. Mostoufi, Coupled CFD-DEM Modeling: Formulation, Implementation and Application to Multiphase Flows, Wiley (2016) ISBN 978-1-119-00529-2.

[49]   Z.S. Ali, M. Hosseinpoor, A. Yahia, New aggregate grading models for low-binder self-consolidating and semi-self-consolidating concrete (Eco-SCC and Eco-semi-SCC), Construction and Building Materials, 265 (2020) 120314. https://doi.org/10.1016/j.conbuildmat.2020.120314.

[50]   J.S. Marshall, Discrete-element modeling of particulate aerosol flows, Journal of Computational Physics, 228 (5) (2009) 1541-1561. https://doi.org/10.1016/j.jcp.2008.10.035.

Chapter 6. Discrete-element modeling of shear-induced particle migration during zones concrete pipe flow: Effect of size distribution and concentration of aggregate on formation of lubrication layer

234

[51]   G.F. Hewitt, J.S. Marshall, Particle focusing in a suspension flow through a corrugated tube, Journal of Fluid Mechanics, 660 (2010) 258-281. https://doi.org/10.1017/S0022112010002697.

[52]   K. Sala, J.S. Marshall, Stochastic vortex structure method for modeling particle clustering and collisions in homogeneous turbulence, Physics of Fluids, 25 (10) (2013) 103301. https://doi.org/10.1063/1.4824278.

[53]   M, Faletra, J.S. Marshall, M. Yang, S. Li, Particle segregation in falling polydisperse suspension droplets, Journal of Fluid Mechanics, 769 (2015) 79-102. https://doi.org/10.1017/jfm.2015.111.

[54]   F.F. Dizaji, J.S. Marshall, J.R. Grant, A stochastic vortex structure method for interacting particles in turbulent shear flows, Physics of Fluids, 30 (1) (2018) 013301. https://doi.org/10.1063/1.5007743.

[55]   F.F. Dizaji, J.S. Marshall, J.R. Grant, Collision and breakup of fractal particle agglomerates in a shear flow, Journal of Fluid Mechanics, 862 (2019) 592-623. https://doi.org/10.1017/jfm.2018.959.

[56]   J.S Marshall, S. Li, (2014), Adhesive Particle Flow: A Discrete-Element Approach, Cambridge: Cambridge University Press, (2014) ISBN 9781139424547.

[57]   R. Di Felice, The voidage function for fluid-particle interaction systems, International Journal of Multiphase Flow, 20 (1) (1994) 153-159. https://doi.org/10.1016/0301-9322(94)90011-6.

[58]   J.S. Marshall, Comparison of methods for computing the concentration field of a particulate flow, International Journal of Multiphase Flow, 56 (2013) 4-14. https://doi.org/10.1016/j.ijmultiphaseflow.2013.05.009.

[59]   H. Hertz, Ueber die Berührung fester elastischer Körper, Journal für die reine und angewandte Mathematik 92, (1882) 156-171. https://doi.org/10.1515/9783112342404-004.

[60]   Y. Tsuji, T. Tanaka, T. Ishida, Lagrangian numerical simulation of plug flow of cohesionless particles in a horizontal pipe, Powder Technology, 71 (3) (1992) 239-250. https://doi.org/10.1016/0032-5910(92)88030-L.

[61]   R.D. Mindlin, Compliance of elastic bodies in contact, Journal of Applied Mechanics, 16 (3) (1949) 259-268. https://doi.org/10.1115/1.4009973.

[62]   K. Bagi, M.R. Kuhn, A definition of particle rolling in a granular assembly in terms of particle translations and rotations, Journal of Applied Mechanics, 71 (4) (2004) 493-501.

Chapter 6. Discrete-element modeling of shear-induced particle migration during zones concrete pipe flow: Effect of size distribution and concentration of aggregate on formation of lubrication layer

235

https://doi.org/10.1115/1.1755693.

[63] N.V. Brilliantov, T. Pöschel, Rolling as a "continuing collision", The European Physical Journal B - Condensed Matter and Complex Systems, 12 (1999) 299-301. https://doi.org/10.1007/s100510051007.

[64] Canadian Standards Association CSA A23.1:19/CSA A23.2:19 standard, Concrete materials and methods of concrete construction/Test methods and standard practices for concrete, CSA Group (2019) SKU: 2425145.

[65] T. Stovall, F. de Larrard, M. Buil, Linear packing density model of grain mixtures, Powder Technology, 48 (1) (1986) 1-12. https://doi.org/10.1016/0032-5910(86)80058-4.

[66] F. de Larrard, Concrete mixture proportioning — a scientific approach, in: S. Mindess, A. Bentur (Eds.), Modern Concrete Technology Series No. 7, E&FN SPON, London (1999) ISBN 9780419235002.

[67] X. Chateau, G. Ovarlez, K.L. Trung, Homogenization approach to the behavior of suspensions of noncolloidal particles in yield stress fluids, Journal of Rheology, 52 (2) (2008) 489-506. https://doi.org/10.1122/1.2838254.

[68] M I.M. Krieger, T.J. Dougherty, A mechanism for non-Newtonian flow in suspensions of rigid spheres, Transaction of the Society of Rheology, 3 (1959) 137-152. https://doi.org/10.1122/1.548848.

[69] J. Vosahlik, K. Riding, D. Feys, W. Lindquist, K. Keller, S. Van Zetten, B. Schulz, Concrete pumping and its effect on the air void system, Materials and Structures, 51 (4) (2018) 94. https://doi.org/10.1617/s11527-018-1204-1.

CHAPTER 7.   Four-way CFD-DEM coupling to simulate concrete pipe flow Mechanism of formation of lubrication layer

Authors and affiliations

Tooran Tavangar: Ph.D. candidate, Cement and Concrete Research Group, Department of Civil and Building Engineering, Université de Sherbrooke, Sherbrooke, Québec, Canada, J1K 2R1.

Masoud Hosseinpoor: Research Assitance, Cement and Concrete Research Group, Department of Civil and Building Engineering, Université de Sherbrooke, Sherbrooke, Québec, Canada, J1K 2R1.

Jeffery S. Marshall: Professor, Department of Mechanical Engineering, Université de Sherbrooke, Burlington, VT, USA.

Ammar Yahia: Professor, Cement and Concrete Research Group, Department of Civil and Building Engineering, Université de Sherbrooke, Sherbrooke, Québec, Canada, J1K 2R1.

Kamal H. Khayat, Professor, Department of Civil, Architectural and Environmental Engineering, Center for Infrastructure Engineering Studies, Missouri University of Science and Technology, Rolla, MO, USA.

Titre française: Couplage CFD-DEM à quatre voies pour simuler l'écoulement du béton dans les tuyaux: Mécanisme de formation de la couche de lubrification.

Abstract

This study introduced a four-way CFD-DEM coupling approach to simulate the shear-induced particle migration (SIPM) mechanism leading to formation of the lubrication layer (LL) during concrete pumping. The CFD-DEM simulations considered the coupled effect of concentration (10%-40%) and wide size distribution (1-17 mm) of aggregate and rheology of the mortar for forces between the suspending matrix and the particles (and vice versa), as well as force transmission directly between particles (and the pipe wall). The formation of the LL was successfully simulated through a more realistic understanding the SIPM mechanism and rheological evaluation across the pipe with comparable calculation times compared to the one-way coupled DEM approach, especially for high concentrations. The simulated LL thicknesses of 0.8-2.7 mm compared well with experimental values. The flow rate and rheological heterogeneity of pumped concrete, and rheology of the LL, were found mostly controlled by the granular-skeleton characteristics rather than the suspending-matrix rheology.

Keywords: Coupled CFD-DEM; Concrete pumping; Lubrication layer, Particle-size distribution; Rheology; Shear-induced particle migration.

7.1 Introduction

Pumped concrete is subjected to a set of complex flow behaviors as it passes through pipelines, originated from its multiphasic nature. These flow behaviors include the effect of the pipe wall to reduce the aggregate concentration near its interface with concrete (called the wall effect (WE)) and shear-induced particle migration (SIPM) of aggregate towards the pipe center [1,2]. Due to the WE, the particles' radial displacements are limited, hence lowering the packing of aggregate close to the pipe wall [3]. The SIPM, occurring under a non-uniform shear-rate profile, refers to the irreversible migration of aggregate in the perpendicular direction to the shear plane from higher shear-rate zones near the concrete-pipe wall interface to lower shear-rate zones near the pipe center [1,2,4-7]. Accordingly, the WE and SIPM phenomena lead to formation of a thin layer of highly flowable mortar in the vicinity of the pipe wall, which is termed the lubrication layer (LL). The LL consists of a micro-mortar with relatively high volume of cement paste and fine particles (< 2 mm) compared to the bulk concrete (BC) [1,8-13]. On the other hand, the coarser aggregates

migrate to the central axis of the pipe, tending to achieve their highest packing arrangement, and consequently increase the local yield stress and risk of plug flow [14-16]. Such shear-induced rheological heterogeneity across the pipe can significantly influence the pumpability of concrete [1,2,10,11]. Various analytical models revealed that the relationship between the pumping pressure loss and flow rate is governed not only by the rheology of the bulk concrete, but also significantly by the plug radius and rheological properties and thickness of the LL [17-19]. Therefore, to better predict the concrete pumpability, it is essential to understand the multiphasic mechanisms governing the flow behavior of concrete in pipes. This can lead to evaluate the shear-induced rheological heterogeneities during concrete pumping process more precisely [1,2].

Due to its confined condition, characterization of the heterogeneities occurring during concrete pipe flow is problematic [1]. The LL characteristics can be empirically evaluated using indirect measurements, such as visual identification of the LL thickness using digital image processing (DIP) of hardened concrete in pipe cross-sections at the end of the pumping process [20], or use of frictional rheometers (tribometers) to evaluate the rheological properties of the LL for a given concrete mixture [9,21,22]. However, due to wide diversity of particle sizes and the opaque nature of the concrete matrix, the identification of a threshold to accurately measure the LL thickness using DIP is not reliable [1]. On the other hand, the use of interface tribometers does not account for pressure applied during the measurements and involves lower shear rate values compared to those exerted on concrete through actual pumping operations [1,23]. Therefore, tribometers cannot allow a full characterization of the flow conditions during the pumping procedure. Numerical modeling has gained special attention for the evaluation and prediction of concrete pumpability over the last decade [1,23,24]. Although the single-phase modeling approach showed high potential to predict the pressure loss for large-scale pipelines [1,12,24-26], it relies on a wide range of assumptions for simulating the development of heterogeneous behavior of concrete flow in pipes. Discrete simulation approaches, utilizing fundamental models of particle interactions with the flow and with each other, can be employed as an alternative to simulate the SIPM during pumping processes [1,24].

The discrete element method (DEM) is a well-known particle-based discrete modeling approach, which has seen widespread use for simulating a wide range of particulate flows [1,27,28]. Momentum conservation of both translational and angular particle motions is applied including

effects of both interparticle and particle-wall collisions as well as particle-fluid interactions. The elastic, viscous, and frictional components of particle interactions are represented in DEM by means of virtual spring, dashpot, and slider elements, respectively [1]. DEM can help to understand the heterogeneous phenomena during concrete flow including blockage and segregation by means of tracking of aggregate displacement [1,28]. DEM is thus used increasingly to simulate concrete pipe flow, accounting for the presence of solid particles, as a contrast to the single-phase modeling approach [1,29-32]. DEM has been mostly used to predict the concrete pumping pressure [28,30,31]. Due to computational limitations, realistic assumptions were generally not made for particle-size distribution (PSD) and concentration of aggregate in previous DEM simulations; nevertheless, the simulated pressure loss values in horizontal pipe [30-31] and bend [28] segments were found to be in reasonable agreement with experimental results.

A few previous studies have attempted to simulate the SIPM during pipe flow using DEM. Haustein et al. [29] simulated the pumping-induced particle migration of a dry granular mixture using soft-sphere DEM. The shear-induced rheological heterogeneity across the pipe was successfully simulated, identifying three different radial regions across the pipe by descending particle concentration towards the pipe wall. However, the simulated mixtures were far from conditions typically experienced in concrete pumping applications due to the very fine particle size used (0.5- and 1-mm diameter particles) and the neglect of the effect of the suspending matrix on the particles. Most recently, Tavangar et al. [32] successfully simulated the LL formation mechanism using a soft-sphere DEM model by accounting the particle-particle-pipe wall interactions and taking into account the suspending fluid drag force on particles, but with one-way interaction between the particles and suspending fluid. The investigated particles consisted of wide PSDs and concentrations (10%-40%) of five particle subclasses of 1-17 mm to be representative for typical concrete mixtures. The authors [32] reported the predicted LL thickness ranged from 1.2 to 3.3 mm which is in general agreement to those reported in literature for typical concrete pumping experiments (1 to 3 mm) [1,11-13,26]. Furthermore, a constant decrease in the particle concentration from the pipe center to the LL zone was successfully obtained for the low- (10%) and medium- (25%) concentration suspensions. However, in the case of high-concentration (40%) mixtures, the highest concentration of particles was not obtained in the central zone, which contradicts the expected SIPM behavior in concrete pipe flow. This anomalous result was

explained by the neglect of the effect of particle forcing on the fluid flow, which at sufficiently high concentrations can have a significant impact on the fluid velocity distribution.

A fully fluid-particle coupled approach is thus recommended for concrete pumping simulation at high concentrations. In order to evaluate the effect of particles on the suspending fluid flow, the Navier-Stokes equations can be solved simultaneously with the DEM equations for the particle motion using an appropriate computational fluid dynamics (CFD) model that accounts for the effective body force exerted by the particles on the fluid. The particle displacement in the DEM code is updated using the calculated hydrodynamic force in the CFD model in addition to the interparticle contact forces calculated at the collision period, yielding the fully-coupled, or four-way coupled, CFD-DEM approach [1,33-37]. Tan et al. [33] employed a CFD-DEM coupling approach to simulate concrete flow through different 90° elbow segments. The model concrete suspensions contained 25% cement paste (suspending fluid), 49% fine aggregate, and 26% coarse aggregate. The fine and coarse aggregate were modeled using single-size spherical particles of 2- and 15-mm diameter, respectively. Good agreement was obtained between the numerical simulations and location of the maximum erosive wear damages in the elbows, although the single-size assumptions for fine and coarse aggregate are not representative of the typical continuous PSDs used in concrete mixtures [38]. Zhou et al. [34] successfully employed the coupled CFD-DEM approach to simulate the SIPM in vertical pipe flow of diphasic suspension of 2.7%-10% concentrations of ceramic particles measuring 2.32 to 3.82 mm in diameter in water. However, the investigated size range and low concentration of particles, as well as rheology of the suspending fluid (water) cannot be representative of concrete mixtures. Most recently, Jiang et al. [36,37] optimized the spatial attitude of pump truck boom conveying pipes, including various straight horizontal and vertical pipes and bending segments, to minimize the pressure loss using a CFD-DEM coupling approach. Continuous PSDs of coarse aggregate of 5-20 [36] and 5-10 mm [37] were modeled as clumps of spherical particles, which does not yield accurate simulations of particle collisions. The numerical simulations led to reduction of pumping pressure loss values by 5.5% [36] and 2.6% [37]. However, the formation of the LL was not investigated, while its presence in the CFD code was taken into account as a secondary fluid phase [37] from the beginning of the flow, in addition to the mortar matrix [36]. The LL characteristics remained unchanged in terms of rheological properties, particle concentration, and thickness.

SIPM in heterogeneous suspensions has been described due to spatial variations in particle collision frequency and effective viscosity of the suspension. According to Phillips et al. [39], the particle fluxes leading to SIPM mainly depend on the particle-size distribution (PSD) and concentration of suspended particles, flow shear rate, and local viscosity heterogeneity of a given suspension across the pipe. The flow velocity profile of suspensions becomes blunter due to the migration of particles from higher to lower shear-rate zones depending on the size and concentration of solid particles [4,6,39]. The particle displacements in a flowing suspension are controlled by various forces, including inertia, interparticle collisions forces, and contact friction, as well as the drag forces exerted from the surrounding fluid. On the other hand, the suspending fluid flow field is influenced by the shear force, pumping pressure, and body forces exerted by the suspended particles, depending on the rheological properties of the suspending fluid, as well as the PSD and concentration of particles. Thus, it is important to take into account the coupled effect of the abovementioned factors while simulating the multiphasic flow behavior of concrete pipe flow by means of a given particle-based modeling approach. A four-way CFD-DEM approach can be used to account for such coupled effective factors for forces between the suspending fluid and the particles (and vice versa) as well as force transmission directly between particles (and pipe wall) via particle collisions [40].

The objective of this study is to simulate the effect of four-way particle-fluid interaction on the shear-induced mechanism of formation of the LL during concrete pipe flow and its characterization in terms of rheological properties and thickness. The SIPM mechanism was simulated for a fully-developed concrete pipe flow within a cylindrical pipe considering wide particle distributions typical of concrete pipe flow. A multiple time-scale four-way CFD-DEM coupling approach was developed to evaluate the coupled effect of the PSD and concentration of aggregate and rheology of the suspending mortar on shear-induced heterogeneities during concrete pipe flow. The particle motion was resolved through a soft-sphere DEM model [32,41] taking into account the particle-particle-wall collisions, as well as the forces and torques on the particles exerted by the surrounding fluid. The Stokes drag expression, considering the crowding and inertia effects of neighboring particles [42], as well as the effect of the suspending fluid viscoelastic behavior on particle drag force was taken into account [43]. A splitting algorithm following by a Fourier-spectral filter [44] was applied on the results of the DEM model in terms of the body forces and concentration field

of the particles [45]. The smoothed data were then translated to a CFD model to simulate the suspending fluid flow field using the Navier-Stokes equations. The evolution of five different spherical particles with diameters ranging from 1 to 17 mm were calculated across four radial zones of a 100-mm cylindrical pipe. Suspensions of 10%-40% concentration and with fine, medium, and coarse PSDs of particles, and flow Reynolds numbers of 100 and 500 were simulated. The SIPM and pumping-induced rheological heterogeneities as well as the rheological properties and thickness of the LL were evaluated at the end of the computational period. The simulation results were compared to those of a one-way coupled DEM approach [32,41] to highlight the significance of the full fluid-particle coupling as a function of PSD and particle concentration.

7.2 Computational methodology

In this study, a four-way coupled CFD-DEM method was applied to simulate the SIPM during concrete pipe flow using a multiple time-step soft-sphere DEM approach coupled to a Navier-Stokes CFD code for fully-developed, axisymmetric pipe flow [32,41]. The governing equations of the mathematical model are described in Section 2.1, and the numerical method used to solve these equations is discussed in Section 2.2.

7.2.1 *Governing equations of mathematical model*

7.2.1.1 *Governing equations for the particles*

The particle transport and their interaction with the surrounding fluid, neighboring particles, and pipe wall were computed using a soft-sphere DEM model [41]. The particles were modeled as elastic spheres with different mass (m), translational (v) and angular velocity (Ω), and inertia (I). Particle transport was evolved via the linear and angular momentum conservation equations, as follows.

$$m\frac{d\mathbf{v}}{dt} = \mathbf{F}_F + \mathbf{F}_C \tag{7.1}$$

$$I\frac{d\mathbf{\Omega}}{dt} = \mathbf{M}_F + \mathbf{M}_C \tag{7.2}$$

where $\mathbf{F}_F$ and $\mathbf{M}_F$ denote the force and torque applied on particles from the suspending fluid and $\mathbf{F}_C$ and $\mathbf{M}_C$ denote force and torque from particle collisions with the wall or with other particles. The suspending fluid mostly influences particle advection by the drag force and viscous torque.

Other forces, such as the Magnus, virtual mass, and Basset forces, were neglected in this study due to low particle relaxation times caused by typically high viscosity of suspending matrix (mortar) in concrete suspensions [46]. The drag force was computed using a modified form of the Stokes expression, given by

$$\mathbf{F}_F = -3\pi \, d \, \mu \, (\mathbf{v} - \mathbf{u}_f) \, f_C \, f_I \, f_{VE} \tag{7.3}$$

where d, μ, and c are the particle diameter, fluid viscosity, and local particle concentration, respectively. Expression (3) contains three correction factors to account for deviation from Stokes law due to particle crowding (f_C), particle inertia (f_I), and fluid viscoelastic response (f_{VE}). The crowding correction factor is given by Di Felice [42] as:

$$f_C = (1 - c)^{-\beta} \tag{7.4}$$

where β is a function of the particle Reynolds number Re_p, defined as:

$$\beta = 2.7 - \frac{0.65}{\mathrm{Exp}\left[\frac{[1.5 - \ln(Re_p)]^2}{2}\right]} \tag{7.5}$$

$$Re_p = \frac{|\mathbf{v} - \mathbf{u}_f| d}{v} \tag{7.6}$$

and v is the kinematic viscosity of the suspending fluid. The inertia correction factor is given by Schiller and Naumann [47] as:

$$f_I = 1 + 0.15 Re_p^{0.687} \tag{7.7}$$

which is valid for particle Reynolds numbers up to about 800. The viscoelastic correction factor account the effect of suspending fluid elasticity for a flow with small Stokes number. As discussed by Chhabra et al. [43], the drag correction due to fluid viscoelasticity is a function of the Weissenberg number We, defined by:

$$We = \frac{|\mathbf{v} - \mathbf{u}_f|}{r} \lambda \tag{7.8}$$

where λ and r are the relaxation time and particle radius, respectively. In this study, the λ values ranged from 0.3 to 100 ms were chosen from the experimental results reported by Fourmentin et

al. [48] for cementitious materials. Chhabra et al. [43] showed that for flows with We higher than 1, it is necessary to consider a correction for drag coefficient. The correction factor fVE was obtained using a fitted function presented in Fig. 7.1 to the We data reported by Chhabra et al. [43], as follows:

$$f_{VE} = 0.87 - 0.13 \tanh[2.48 \log(We)] \tag{7.9}$$
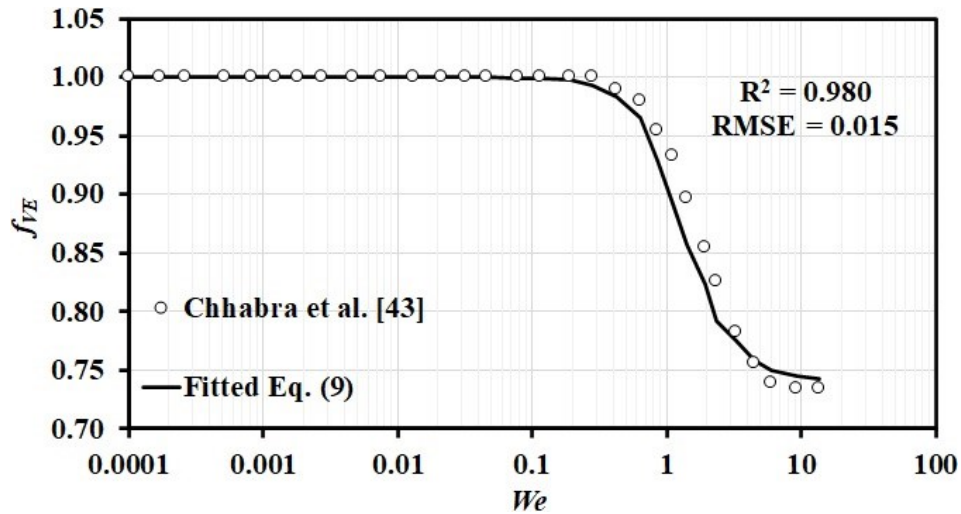
Fig. 7.1. Correction factor f_{VE} versus *We* number, fitting Eq. (7.9) to the reported data by Chhabra et al. [43].

The viscous torque $\mathbf{M}_F$ exerted on particles from the suspending fluid is given by [32,41]:

$$\mathbf{M}_F = \pi\mu d^3 \left(\frac{1}{2}\boldsymbol{\omega} - \boldsymbol{\Omega}\right) \tag{7.20}$$

where $\boldsymbol{\omega}$ is the vorticity of the surrounding fluid at the particle location. The contact force and torques exerted on particles due to interaction between neighbouring particles were modeled using the classical Hertz [49] collision theory for normal collisions and the spring-dashpot-slider model proposed by Cundall and Strack [50] for sliding resistance, with analogous expressions for twisting and rolling resistance [51]. The parameters and formulations used to model the contact forces and torques between two particles *i* and *j* are summarized in Tables 7.1 and 7.2.

Table 7.1. Parameters of the contact model used in the employed DEM model.

Parameters	Symbol	Formulation
Particle radius	r	r_i and r_j
Vector from the particle centroid to the contact point	$\mathbf{r}$	$\mathbf{r}_i = r_i\mathbf{n}$ and $\mathbf{r}_j = -r_j\mathbf{n}$
Particle mass	m	m_i and m_j
Poisson's ratio of particle	σ	σ_i and σ_j
Shear modulus of particle	G	G_i and G_j
Centroid position of particle	$\mathbf{X}$	$\mathbf{X}_i$ and $\mathbf{X}_j$
Restitution coefficient	e	0.1
Effective radius	r_e	$\dfrac{1}{r_e} = \dfrac{1}{r_i} + \dfrac{1}{r_j}$
Effective elastic modulus	E	$\dfrac{1}{E} = \dfrac{1 - \sigma_i^2}{E_i} + \dfrac{1 - \sigma_j^2}{E_j}$
Effective shear modulus	G	$\dfrac{1}{G} = \dfrac{2 - \sigma_i}{G_i} + \dfrac{2 - \sigma_j}{G_j}$
Particle velocity at the contact surface	$\mathbf{v}_c$	$\mathbf{v}_c = \mathbf{v} + \mathbf{\Omega} \times \mathbf{r}$
Normal overlap	δ_N	$\delta_N = r_i + r_j - \lvert \mathbf{x}_i - \mathbf{x}_j \rvert$
Contact region radius	a	$a^2 = r_e\, \delta_N$

Table 7.2. Formulation of the contact forces and torques used in the DEM model.

Interaction	Symbol	Formulation	Direction	Variables
Normal force	$\mathbf{F}^{\mathbf{n}}_{c,ij}$	$k_N \delta_N - \eta_N \mathbf{v}_R.\mathbf{n}$	$\mathbf{n} = (\mathbf{x}_j - \mathbf{x}_i) / \|\mathbf{x}_j - \mathbf{x}_i\|$	$k_N = \frac{4}{3} E\, a(t)$ $\eta_N = \alpha\sqrt{m\, k_N}$ $\alpha = 1.2728 - 4.2783e + 11.087e^2 - 22.348e^3 + 27.467e^4 - 18.022e^5 + 4.821e^6$ $\mathbf{v}_R = \mathbf{v}_{ci} - \mathbf{v}_{cj}$
Sliding force	$\mathbf{F}^{\mathbf{s}}_{c}$	$-k_T \left(\int_{t_0}^{t} \mathbf{v}_S(\xi)\mathrm{d}\xi \right).\mathbf{t}_S - \eta_T \mathbf{v}_S.\mathbf{t}_S$	$\mathbf{t}_S = \mathbf{v}_S / \|\mathbf{v}_S\|$	$k_T = 8G\, a(t)$ $\mathbf{v}_S = \mathbf{v}_R - (\mathbf{v}_R.\mathbf{n})\mathbf{n}$ $\eta_T = \eta_N$ If $\|\mathbf{F}^{\mathbf{s}}_c\| > F_{crit}$; reset to $\mathbf{F}^{\mathbf{s}}_c$
	F_{crit}	$\mu_f \|F_n\|$		$\mu_f = 0.3$
Twisting torque	M_t	$-\frac{k_T a^2}{2} \int_{t_0}^{t} \Omega_T(\tau)\mathrm{d}\tau - \frac{\eta_T a^2}{2} \Omega_T$	$\Omega_T/\|\Omega_T\|$	$\Omega_T = (\mathbf{\Omega}_i - \mathbf{\Omega}_j).\mathbf{n}$
	$M_{t\text{-}crit}$	$\frac{2}{3} a\, F_{crit}$		If $M_t > M_{t\text{-}crit}$; reset to M_t
Rolling torque	M_r	$-k_R \left(\int_{t_0}^{t} \mathbf{v}_L(\tau)\mathrm{d}\tau \right).\mathbf{t}_R - \eta_R \mathbf{v}_L.\mathbf{t}_R$	$\mathbf{t}_R = \dfrac{\mathbf{v}_L}{\|\mathbf{v}_L\|}$	$\mathbf{v}_L = -r_e(\mathbf{\Omega}_i - \mathbf{\Omega}_j) \times \mathbf{n} - \frac{1}{2}\left(\frac{r_j - r_i}{r_j + r_i}\right)\mathbf{v}_S$ $\eta_R = \mu_R\|F_{ne}\|$ $\mu_R = \dfrac{1 - e}{2.283 w_0^{1.5}(K/m)^{2/5}}$ w_0: The relative velocity between two particles before the collision $K = \frac{4}{3} E \sqrt{r_e}$
Total torque exerted on particle i	M_C	$r_i F_S(\mathbf{n}\times\mathbf{t}_S) + M_r(\mathbf{t}_R\times\mathbf{n}) + \mathbf{M}_t.\mathbf{n}$	-	-

7.2.1.2 Governing equations for the suspending fluid flow

The suspending fluid's flow was modelled using the Navier-Stokes equations [41], given by:

$$\frac{\partial}{\partial t}\left(c_v \rho_f\right) + \nabla \cdot \left(c_v \rho_f \mathbf{u}_f\right) = 0 \tag{7.13}$$

$$\frac{\partial}{\partial t}\left(c_v \rho_f \mathbf{u}_i\right) + \frac{\partial}{\partial \mathbf{x}_j}\left(c_v \rho_f \mathbf{u}_i \mathbf{u}_j\right) = \frac{\partial}{\partial \mathbf{x}_j}\left[c_v \mu \left(\frac{\partial \mathbf{u}_i}{\partial \mathbf{x}_j} + \frac{\partial \mathbf{u}_j}{\partial \mathbf{x}_i}\right)\right] - c_v \frac{\partial \mathbf{p}}{\partial \mathbf{x}_i} - \mathbf{b}_i \tag{7.42}$$

where $\mathbf{u}_f$, $\mathbf{p}$, and ρ_f imply velocity, pressure, and density of the suspending fluid, respectively. $\mathbf{b}$ denotes the body force, including the drag force exerted on the suspending fluid by particles. c_v is the volumetric fraction of the suspending fluid. For the current problem, the pressure term was assumed to be in the axial direction and was constant across the pipe, as is typical for fully-developed laminar flow. The flow was assumed to be axisymmetric, such that the fluid velocity field is a function only of radius and time. The mass and momentum equations were transformed to non-dimensional form using the pipe radius (R_{pipe}) and mean fluid velocity (u_f) as the length and velocity scales, respectively, giving the mass and momentum conservation equations as:

$$\frac{\partial}{\partial t}(c_v) + \frac{\partial}{\partial \mathbf{r}}(c_v \mathbf{u}_f) = 0 \tag{7.53}$$

$$\frac{\partial}{\partial t}(c_v \mathbf{u}_f) = \frac{1}{Re}\frac{1}{\mathbf{r}}\frac{\partial}{\partial \mathbf{r}}(\mathbf{r}\, c_v \frac{\partial \mathbf{u}_f}{\partial \mathbf{r}}) - c_v \frac{4}{Re} - \mathbf{b} \tag{7.64}$$

where the suspending fluid Reynolds number Re is given by

$$Re = \frac{\rho_f u_f D_{pipe}}{\mu} \tag{7.75}$$

7.2.2 Numerical method

Particles were randomly initiated in the pipe geometry, placed in descending order of particle size (i.e., larger particles were generated earlier). When each particle was placed, it was checked to make sure that no other particles overlapped the given particle position. The governing equations of the suspending fluid flow were integrated using a multiple-time-step algorithm [41], with fluid time step ΔT_f, non-colliding particle advection time step ΔT_p, and colliding particle time step ΔT_c. The pipe geometry was a cylinder of 100 mm diameter and 500 mm length.

A conservative particle blob method, introduced by Marshall [52], was employed to calculate the local concentration field for use in the particle crowding correction term in Eq. (7.4). A 3D-Gaussian function (f) with a specific radius R_n and amplitude A_n was defined to distribute the particle volume onto the flow field. The concentration at each point was then obtained using the effect of neighboring blobs, given by:

$$(\mathbf{x},t) = \sum_{n=1}^{N} A_n f(\mathbf{x} - \mathbf{x}_n, R_n) \tag{7.86}$$

$$(f(\mathbf{x} - \mathbf{x}_n, R_n) = \frac{2}{3\pi R_n^3 \, \mathrm{Exp}\left(\frac{|\mathbf{x} - \mathbf{x}_n|^2}{R_n^2}\right)} \tag{7.97}$$

The overall coupled CFD-DEM algorithm is schematically illustrated in Fig. 7.2. The particle transport and the coupling term between the particles and the suspending fluid phases were first computed in Cartesian coordinates using the DEM algorithm. A level set method was used to identify the pipe boundary on the Cartesian grid. A homogenization procedure (described below) was employed to compute the particle concentration and effective fluid body force terms for the fluid momentum equation. The fluid flow evolution was solved in polar coordinates using a finite-difference method, with central differencing in space and implicit second-order differencing in time. The computations used 20 mesh points in the radial direction and dimensionless time steps of $\Delta T_f = 0.01$, $\Delta T_p = \Delta T_f/20$, and $\Delta T_C = \Delta T_p/40$. Repeatability of the DEM method under different random initial positions of the particles and selected time steps was previously confirmed for concrete pipe flow in [32].
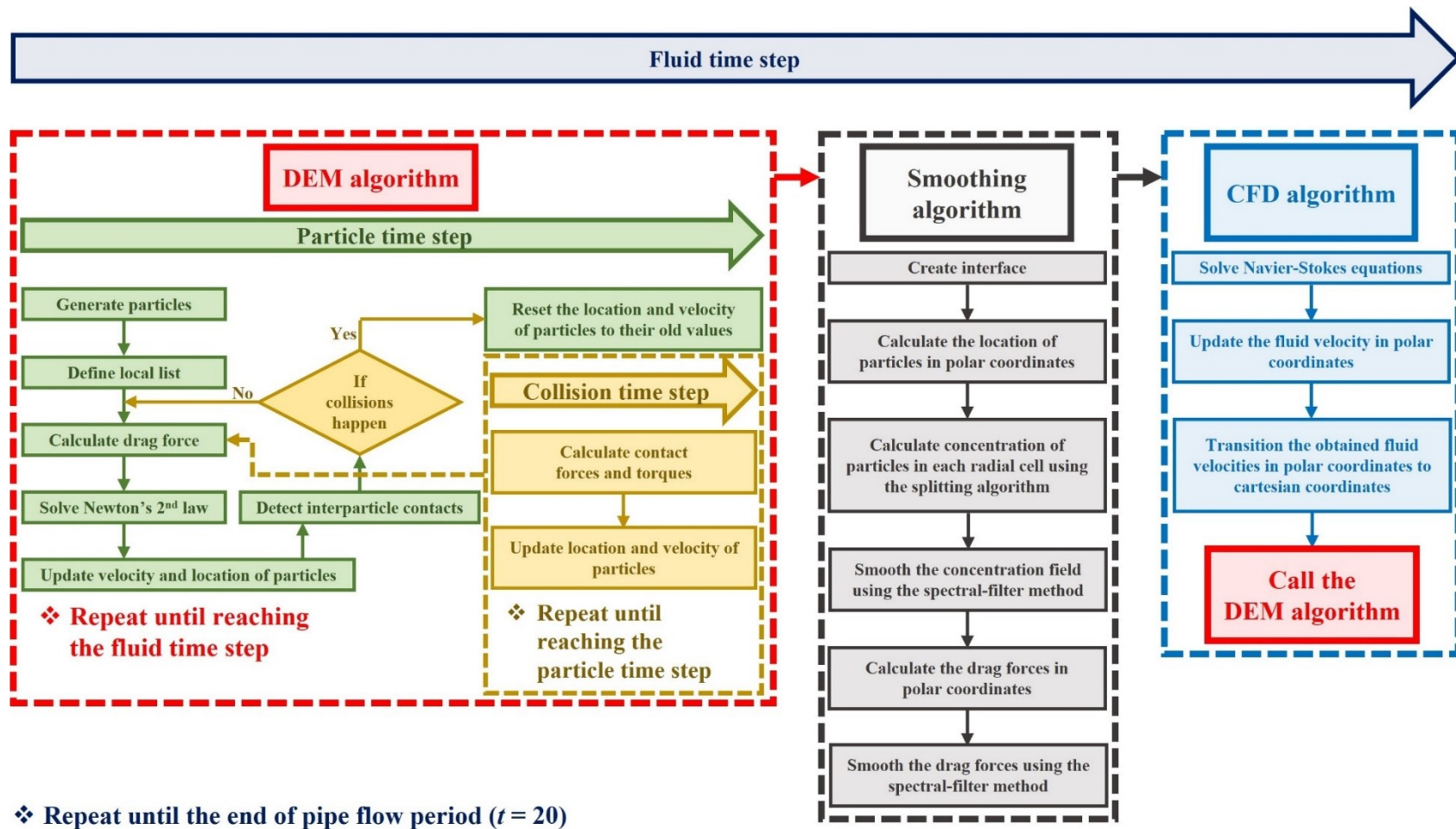
Fig. 7.2. The schematic illustration of the multiscale coupled CFD-DEM algorithm applied in this study.

7.2.2.1 suspending fluid flow

A homogenization procedure was introduced to calculate the effective body force acting on the fluid from the particles and the particle concentration field. As part of this procedure, it was first required to calculate the volume of particles located in each fluid cell. Due to the wide range of the particle sizes, the particle diameter-to-fluid mesh cell-size ratio may exceed unity. In order to reduce numerical noise, especially for fine fluid mesh cells [46], it is important to calculate the volumetric fraction of particles occupied in each fluid cell. The volume of a spherical particle with radius r_p, located at distance $|\mathbf{r}|$ between its centroid to the pipe center, and enclosed between two planes with distances a and b ($a < b$) to the pipe center, corresponding to the inner and outer boundaries of a suspending fluid mesh cell, respectively, can be estimated as follows:

$$V = \pi \left[r_p^2 (b - a) - \frac{(b - |\mathbf{r}|)^3 - (a - |\mathbf{r}|)^3}{3} \right] \qquad (7.108)$$

For simplification, the curvature of the fluid meshes was not taken into account, and it was assumed that particles were enclosed between two straight surfaces.

In this study, the pipe geometry was discretized using 21 cylindrical meshes with identical length of the pipe L_{pipe}. The inner and outer boundaries of the ir^{th} mesh cell (ir starting from 0 to 20) are distanced by $(ir - 0.5)\Delta r$ and $(ir + 0.5)\Delta r$ to the pipe center ($\Delta r = R_{pipe}/20$). Accordingly, the 0th mesh cell refers to a cylindrical mesh of $D_{pipe}/20$ in diameter centered at the pipe axis. Also, the inner and outer radii of the 20th mesh cell measure $19.5 R_{pipe}/20$ and R_{pipe}, respectively. Considering the ir_{first}^{th} and ir_{last}^{th} cells, referring to the mesh cells which contain the points on the particle surface with the shortest ($|\mathbf{r}| - r_p$) and longest ($|\mathbf{r}| + r_p$) distances to the pipe center, respectively, as shown in Fig. 7.3, the particle is split in total N_{split} times ($N_{split} = ir_{last} - ir_{first}$). Therefore, four different scenarios can then happen depending on the size and location of the particles within the fluid mesh cells, as follows:

Scenario A: if $ir_{first} = ir_{last} = ir$, therefore the particle does not need to be split ($N_{split} = 0$). Therefore, the particle concentration in the ir^{th} mesh cell equals $\frac{4}{3}\pi r_p^3$.

Scenario B: The partial volume of the particle, enclosed in the ir_{first}^{th} mesh cell can be estimated by setting $a = |\mathbf{r}| - r_p$ and $b = (ir_{first} + 0.5)\Delta r$ in Eq. (7.18).

Scenario C: The partial volume of the particle, enclosed in each of the ir^{th} mesh cell ($ir_{first} < ir <$ ir_{last}) can be estimated by setting $a = (ir - 0.5)\Delta r$ and $b = (ir + 0.5)\Delta r$ in Eq. (7.18).

Scenario D: The partial volume of the particle, enclosed in the $ir_{last}{}^{th}$ mesh cell can be estimated by setting $a = (ir_{last} - 0.5)\Delta r$ and $b = |\mathbf{r}| + r_p$ in Eq. (7.18).

The abovementioned splitting scenario were examined for all the particles in each time step to calculate the total concentration of particles and volumetric fraction of the suspending fluid (c_v) in each fluid mesh cell. A similar procedure was used to partition the particle drag force between the various radial bands overlapped by the particle in proportion to the volume of the particle in that radial band.
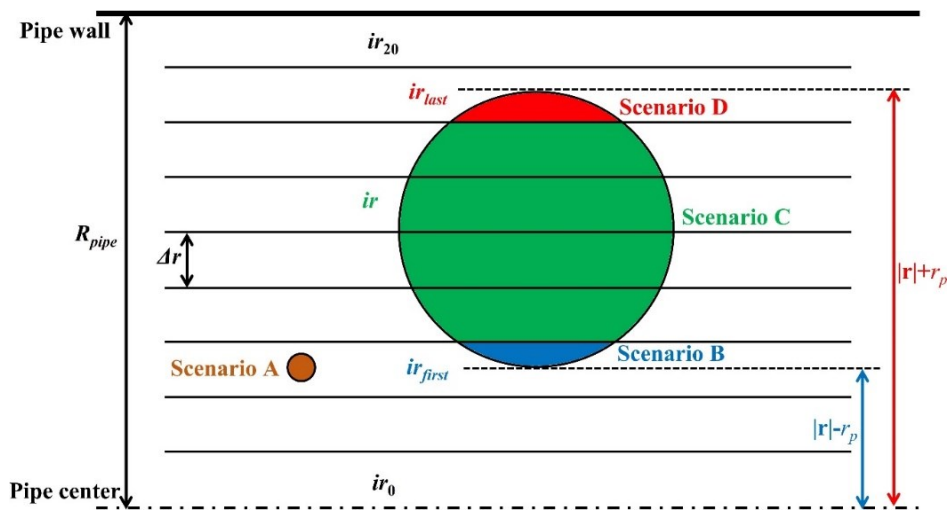
Fig. 7.3. Schematics of splitting method used to calculate the local particle concentration.

7.2.2.2 Smoothing algorithm

A Fourier spectral filtering [44] was used to smooth the distribution of particle concentration and body force on the flow following the homogenization procedure. In this procedure, the concentration and body force were fit to a Fourier series in the radial coordinate r using a half-range expansion over the pipe centerline to make the functions periodic. The Fourier coefficients were then multiplied by a factor g_n to suppress the high-wavenumber modes, where n is the Fourier mode number and

$$g_n = \cfrac{1 - \cfrac{1}{\exp\left(\cfrac{N_F^2 - n^2}{N_0^2}\right)}}{1 - \cfrac{1}{\exp\left(\cfrac{N_F^2}{N_0^2}\right)}}$$

(7.119)

Here N_F and N_0 are the total number of Fourier modes and an adjustable parameter associated with the spectral filter, respectively. For the current paper, we selected N_0 as twice N_F, as was also done by Ghazi et al. [45]. An example for the pipe flow of a highly concentrated suspension (40%) across a 100-mm diameter pipe ($R_{pipe} = 50$ mm) is presented in Fig. 7.4. As shown for the original particle concentration profile obtained from the splitting algorithm, namely "Raw data", high wavenumber noise can be observed in the central zone close to the pipe center, which can have a negative effect on the velocity computation. The concentration field was smoothed using two different N_F values of 10 and 20 in the employed spectral-filter method. As can be observed in Fig. 7.4, the choice $N_F = 20$ led to higher precision compared to smoothing with 10 Fourier nodes, especially in the pipe center and the vicinity of the pipe wall, which are important to characterize the plug flow and LL, respectively. Therefore, in the remainder of this study, $N_F = 20$ Fourier modes was used for the spectral filter.
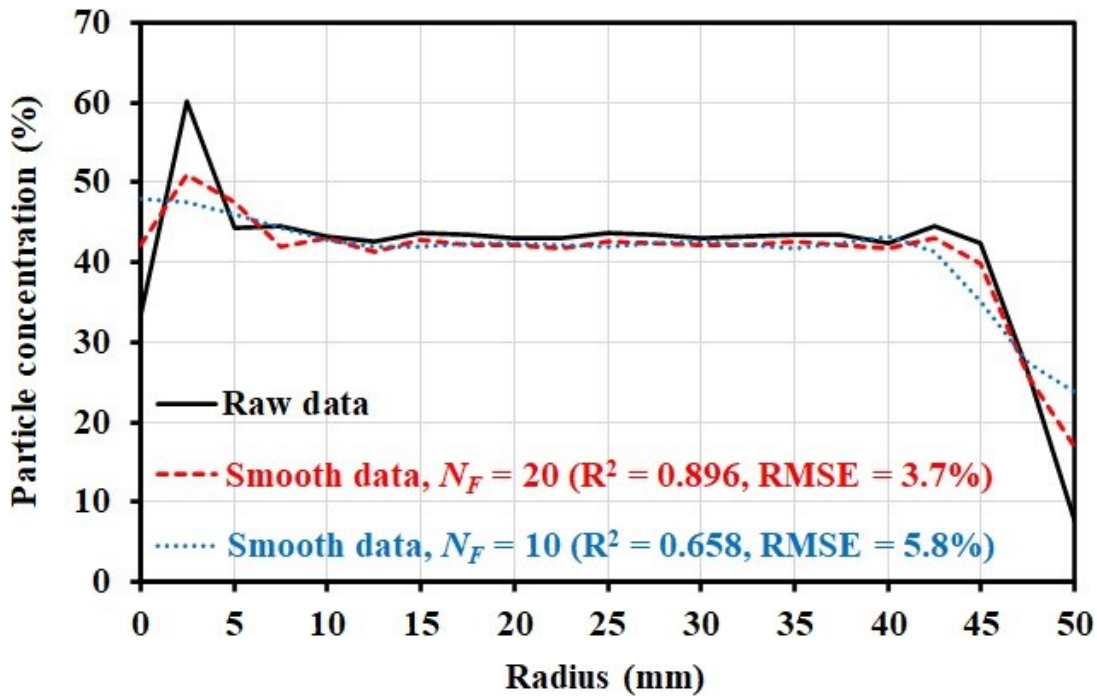

Fig. 7.4. Comparison between the smooth concentration profiles obtained using the spectral filter method with different N_F of 10 and 20 and those originally obtained from the splitting algorithm (Raw data).

7.3 Concrete pipe flow models

As shown in Table 7.3, the model-granular mixtures were proportioned using three PSDs (fine, medium, and coarse) of five spherical particles P1 (1 mm), P2 (3.5 mm), P3 (7.5 mm), P4 (12 mm), and P5 (17 mm), representing the ASTM standard sieve-size ranges of 0-2.5, 2.5-5, 5-10, 10-14, and 14-20 mm, respectively. As reported by Tavangar et al. [32], the modeled PSDs were designed to produce fine and coarse aggregate recommended for concrete production [53].

Table 7.3. Proportioning of different PSDs of the investigated granular mixtures, in terms of volumetric fractions (vol.%) of 5 particle classes (P1-5) in unit volume of aggregate

| PSD #	Particle subclasses (vol.%)				
	P1: 1 mm	P2: 3.5 mm	P3: 7.5 mm	P4: 12 mm	P5: 17 mm
Fine	38	10	38	11	3
Medium	25	8	43	17	8
Coarse	12	7	47	23	12

As summarized in Table 7.4, six different suspensions were proportioned using three total particle concentrations (φ) of 10% (low: LC), 25% (medium: MC), and 40% (high: HC) of fine (FPSD), medium (MPSD), and coarse (CPSD) PSDs. The number of each particle classes of P1-5 and total number of particles (n) dispersed in a cylindrical pipe, measuring 100 mm in diameter (D_{Pipe}) or 50 mm in radius (R), and 500 mm in length (L_{Pipe}), as well as the average diameter (D_{avg}) and packing density (φ_{max}) of particles in each suspension are also presented in Table 7.4. The D_{avg} values of the investigated particle mixtures were calculated using the volumetric-weighted arithmetic average of diameter of their corresponding particles. Moreover, as reported by Tavangar et al. [32], the φ_{max} values of the investigated granular mixtures were calculated using the linear-packing model proposed by Stovall et al. [54] and de Larrard [55]. Two different suspending fluid flow Reynolds numbers Re of 100 and 500, reflecting two viscosity levels of the suspending fluid, were considered for each suspension.

Table 7.4. Proportioning of different PSDs of the investigated granular mixtures, in terms of volumetric fractions (vol.%) of 5 particle classes (P1-5) in unit volume of aggregate.

Model #	PSD	Concentration level	Number of particles						D_{avg} (mm)	φ_{max}
			P1	P2	P3	P4	P5	n		
FPSD-LC	Fine		286875	1706	680	47	5	289313	5.429	0.847
MPSD-LC	Medium	Low ($\varphi = 10\%$)	187500	1421	756	73	11	189761	6.990	0.858
CPSD-LC	Coarse		88125	1137	831	100	18	90211	8.635	0.868
MPSD-MC	Medium	Medium ($\varphi = 25\%$)	468750	3553	1889	183	29	474404	7.030	0.857
CPSD-MC	Coarse		220313	2843	2078	250	46	225530	8.657	0.868
CPSD-HC	Coarse	High ($\varphi = 40\%$)	352500	4548	3324	399	73	360844	8.646	0.868

7.3.1 Evaluation of radial particle migrations

The evolution of the concentrations of each particle classes P1-5, total particle concentrations, D_{avg}, and φ_{max} of particles in four different radial zones of Z1, Z2, Z3, and Z4, corresponding to the radial ranges of 0-0.5R, 0.5R-0.75R, 0.75R-0.875R, and 0.875R-R (Fig. 7.5), respectively, was investigated for the whole pipe-flow period (t = 0 - 20). It is worth mentioning that the bulk concrete (BC) and lubrication layer (LL) zones were assigned to the radial ranges of 0-0.875R (Z1-3) and 0.875R-R (Z4), respectively.
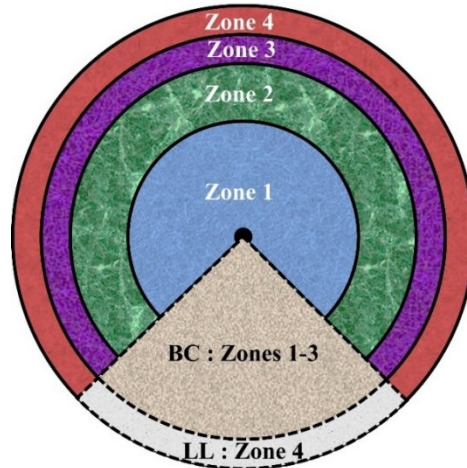
Fig. 7.5. Radial zones Z1, Z2, Z3, and Z4, corresponding to the radial ranges of 0-0.5R, 0.5R-0.75R, 0.75R-0.875R, and 0.875R-R, respectively, as well as the bulk concrete BC (Z1-3: 0-0.875R) and lubrication layer LL (Z4: 0.875R-R).

The following measures were proposed to evaluate the radial SIPM and rheological heterogeneities of the investigated suspensions across the pipe.

7.3.1.1 Shear-induced particle migration index (SIPMI)

The SIPM phenomenon is expected to result in a radial variation in total particle concentration in different zones in a descending order of their radial distance to the pipe center (i.e., $\varphi_{Z1} > \varphi_{Z2} > \varphi_{Z3} > \varphi_{Z4}$). Therefore, in order to evaluate the pumping-induced migration of particles, not only the radial heterogeneity of particle concentrations, but also the order of particle concentrations in different radial zones should be considered. Accordingly, a SIPM index (*SIPMI*) was defined as:

$$SIMPI = [COV(\varphi)_{Z1-4} \times r_s(\varphi)_{Z1-4}]_{t=20} - [COV(\varphi)_{Z1-4} \times r_s(\varphi)_{Z1-4}]_{t=0} \qquad (7.20)$$

where $COV(\varphi)_{Z1\text{-}4}$ is the coefficient of variation of particle concentrations (φ) in different radial zones Z1-4 and $r_s(\varphi)_{Z1\text{-}4}$ is Spearman's rank correlation coefficient [56] between the descending rankings of the particle concentrations ($rank(\varphi)_{Z_i}$) and radial distances ($rank(r)_{Z_i}$) of zones Z1-4 to the pipe center, calculated at the beginning ($t = 0$) and end ($t = 20$) of flow period, given by:

$$COV(\varphi)_{Z1\text{-}4} = \frac{\sigma(\varphi)_{Z1\text{-}4}}{Avg(\varphi)_{Z1\text{-}4}} \times 100\% \tag{7.21}$$

$$r_s(\varphi)_{Z1\text{-}4} = 1 - \frac{6\sum_{i=1}^{4}\left[rank(\varphi)_{Z_i} - rank(r)_{Z_i}\right]^2}{n_Z(n_Z^2 - 1)} \tag{7.22}$$

where $\sigma(\varphi)_{Z1\text{-}4}$, $Avg(\varphi)_{Z1\text{-}4}$, and $n_Z = 4$ are the standard deviation and average of the total particle concentrations in zones Z1-Z4 and number of radial zones Z1-Z4, respectively. It is worth mentioning that $r_s(\varphi)_{Z1\text{-}4}$ values range between 0 and 1 for the worst-case scenario, where $\varphi_{Z1} < \varphi_{Z2} < \varphi_{Z3} < \varphi_{Z4}$, and the expected one from the SIPM phenomenon, i.e., $\varphi_{Z1} > \varphi_{Z2} > \varphi_{Z3} > \varphi_{Z4}$, respectively.

7.3.1.2   *Rheological heterogeneity of the investigated pipe flows*

The yield stress ($\tau_0(\varphi_i)$) and plastic viscosity ($\mu_p(\varphi_i)$) of the suspensions of different radial zones at the end of flow period ($t = 20$), relative to those of the suspending fluid (i.e., $\tau_0(0)$ and $\mu_p(0)$), were calculated as functions of concentrations (φ_i) and packing density ($\varphi_{max\text{-}i}$) of the spherical particles in the given radial zone "*i*" ($i = 1$ to 4) using the models proposed by Chateau et al. [57] (Eq. (7.23)) and Krieger and Dougherty [58] (Eq. (7.24)), respectively, as follows:

$$\tau_{0\text{-}r\text{-}i} = \frac{\tau_0(\varphi_i)}{\tau_0(0)} = \sqrt{(1 - \varphi_i)\left(1 - \frac{\varphi_i}{\varphi_{max\text{-}i}}\right)^{-2.5\varphi_{max\text{-}i}}} \tag{7.23}$$

$$\mu_{p\text{-}r\text{-}i} = \frac{\mu_p(\varphi_i)}{\mu_p(0)} = \left(1 - \frac{\varphi_i}{\varphi_{max\text{-}i}}\right)^{-2.5\varphi_{max\text{-}i}} \tag{7.24}$$

The yield stress- (*YSHI*) and viscosity-heterogeneity (*VHI*) indices were then proposed to evaluate the radial heterogeneity of the rheological properties of the suspensions across the pipe, given by:

$$YSHI\ (\%) = \left[COV(\tau_{0\text{-}r})_{Z1\text{-}4} \times r_s(\tau_{0\text{-}r})_{Z1\text{-}4}\right]_{t=20} \tag{7.25}$$

$$VHI\ (\%) = \left[COV(\mu_{p\text{-}r})_{Z1\text{-}4} \times r_s(\mu_{p\text{-}r})_{Z1\text{-}4}\right]_{t=20} \tag{7.26}$$

where $COV(\tau_{0\text{-}r})_{Z1\text{-}4}$ and $COV(\mu_{p\text{-}r})_{Z1\text{-}4}$ are the coefficients of variation of relative yield stress and plastic viscosity values in different radial zones Z1-4, respectively, and $r_s(\tau_{0\text{-}r})_{Z1\text{-}4}$ and $r_s(\mu_{p\text{-}r})_{Z1\text{-}4}$ are Spearman's rank correlation coefficients between the descending rankings of the relative yield stress and plastic viscosity values, respectively, and radial distances $(rank(r)_{Z_i})$ of zones Z1-4 to the pipe center, calculated at the end of flow period ($t = 20$), similarly to Eqs. (21) and (22).

7.4 Results and discussion

This section presents results of simulations for the DEM one-way coupled and the CFD-DEM four-way coupled simulations, including the effect of particle-fluid coupling on evolution of concentration of particle classes P1-5 and total concentration of particles in different radial zones Z1-4 over the flow period ($t = 0$ - 20). The effect of particle-fluid coupling on the *SIPMI*, *YSHI*, and *VHI* indices is examined, reflecting the pumping-induced heterogeneities across the pipe at the end of the pipe flow period ($t = 20$). The effect of particle-fluid coupling on the rheological properties of the suspending fluid, as well as the PSD, volumetric content, and packing density of the aggregate on the pumping flow rate and rheological heterogeneity of the investigated suspensions were evaluated:

7.4.1 Radial evolution of concentration of different particle classes

As shown in Fig. 7.6 for high concentration (40%) of coarse PSD (CPSD-HC suspension) and both suspending fluid Reynolds numbers 100 and 500, and in Figs. 7.A1-5 in the Appendix for other suspensions, the concentrations of different particle classes Pj (j = 1 to 5) in different radial zones Zi (i = 1 to 4), obtained using both DEM and coupled CFD-DEM approaches vary over the pipe flow period. As can be observed for all the cases, the finest particles P1 (1 mm) migrated to the LL zone, reflected by rising concentration over time in Z4 ($0.875R$-R). Moreover, the P1 concentration significantly decreased in zone Z3 ($0.75R$-$0.875R$). This confirms that larger portion of the P1 particles forming the LL originally migrated from its vicinity (Z3), rather than from the other central zones Z1-Z2. On the other hand, lowering the concentration of all the larger particles

P2-P5 in the LL zone confirm their migration to the central zones over time. The results revealed that packing density of all the particle classes increased in the central zones Z1-Z2 (0-0.75R), as indicated by increasing concentrations over time.

The concentrations of the largest particles P4 (12 mm) and P5 (17 mm) decreased in the vicinity of the pipe walls; i.e., Z3-Z4 (0.75R-R), for all the cases. It is worth mentioning that depending on the concentration levels of the investigated mixtures, the median particles P2 (3.5 mm) and P3 (5 mm) showed opposite concentration rates in zone Z3 (0.75R-0.875R). As can be observed, the P3 concentrations in Z3 increased for medium and high concentration suspensions, while decreased for low concentration suspensions over time. On the other hand, P2 particles experienced positive and negative concentration rates over time for the suspensions containing 10% and 25%-40% particle concentrations, respectively. Different trends can be observed through the evolution of the concentrations of different particles in suspensions with different *Re* numbers and simulated using DEM and coupled CFD-DEM approaches, as further discussed in the next sections.

7.4.2 Evolution of total particle concentration across pipe

The radial evolutions of the total concentrations of particles across the radial zones Z1-Z4 for the various investigated suspensions that are simulated using the DEM and the four-way coupled CFD-DEM approaches are presented in Figs. 7.7 and 8, respectively. The lowest initial concentration of particles in Z4 (LL: 0.875R-R) in the beginning of the flow period (at t = 0) for all simulated cases can be attributed to the wall effect (WE) that affects the distribution of particles in vicinity of the pipe wall, even prior to applying any pumping shear. Having an unceasing lowering rate, Z4 also showed the lowest total concentration values over time, compared to other radial zones, for all simulated cases, which can confirm the formation of the LL in vicinity of the pipe wall.

In the case of the low- (LC: 10%) and medium- (MC: 25%) concentration suspensions, the total particle concentrations increased in the central zones Z1 and Z2 (0-0.75R) and decreased in the outer Z3 and Z4 zones (0.75R-R) in the vicinity of the pipe wall. Increasing the radial distance from the pipe center led to a continuous lowering of total particle concentrations across the pipe for all the LC and MC suspensions. Accordingly, the central zone Z1 (0-0.5R) showed the highest particle concentration, followed by Z2 (0.5R-0.75R), and Z3 (0.75R-0.875R) at the end of flow period (t = 20) which is in accordance with the expected order of SIPM in pipes.
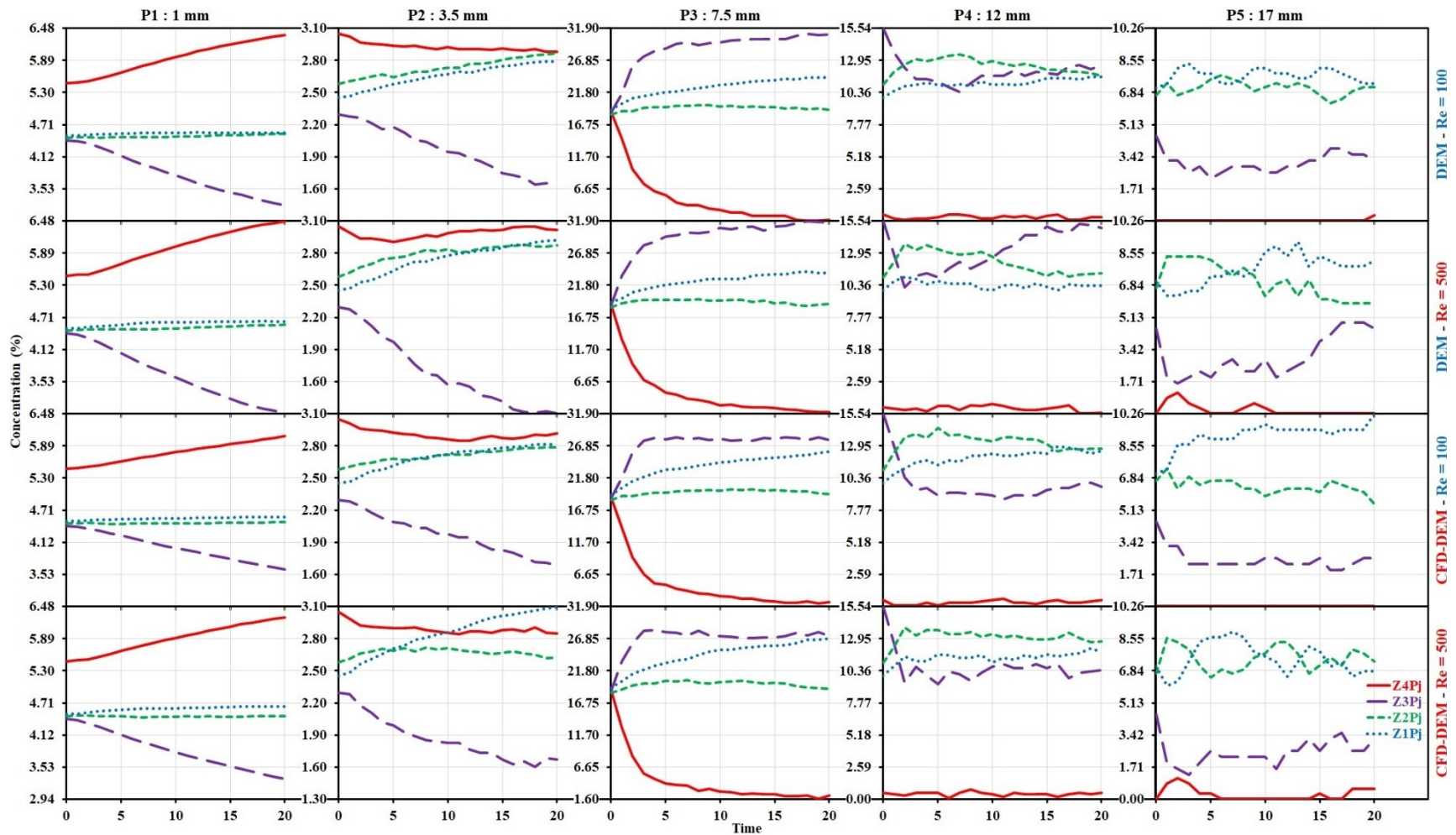
Fig. 7.6. Evolution of concentrations of P1-5 particles in four different radial zones Z1-4 for the mixture containing coarse PSD and high (40%) concentration of particles (CPSD-HC) versus flow time.

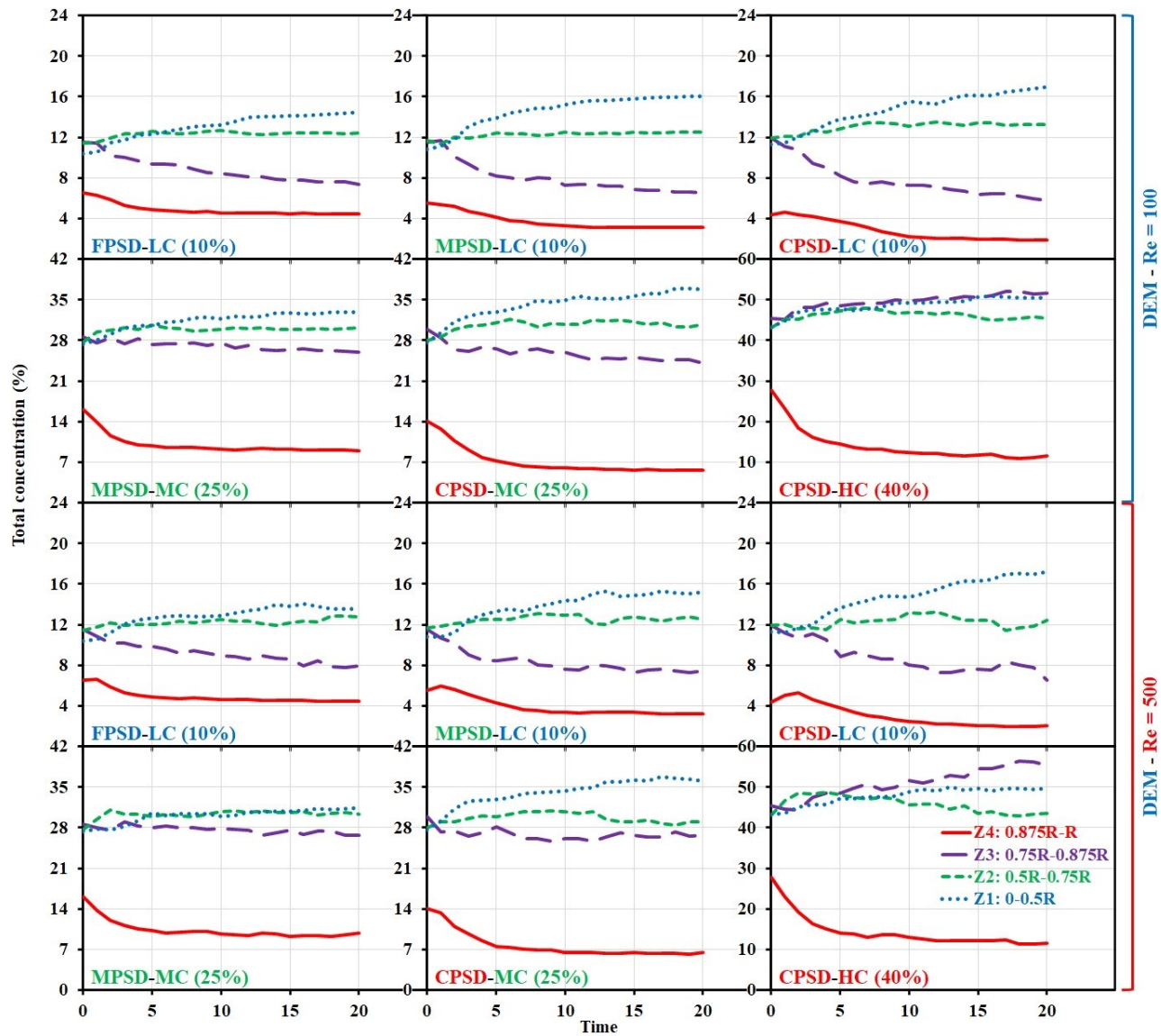**Fig. 7.7.** Total concentrations of particles in four different radial zones Z1 to Z4 over time obtained using the DEM approach.
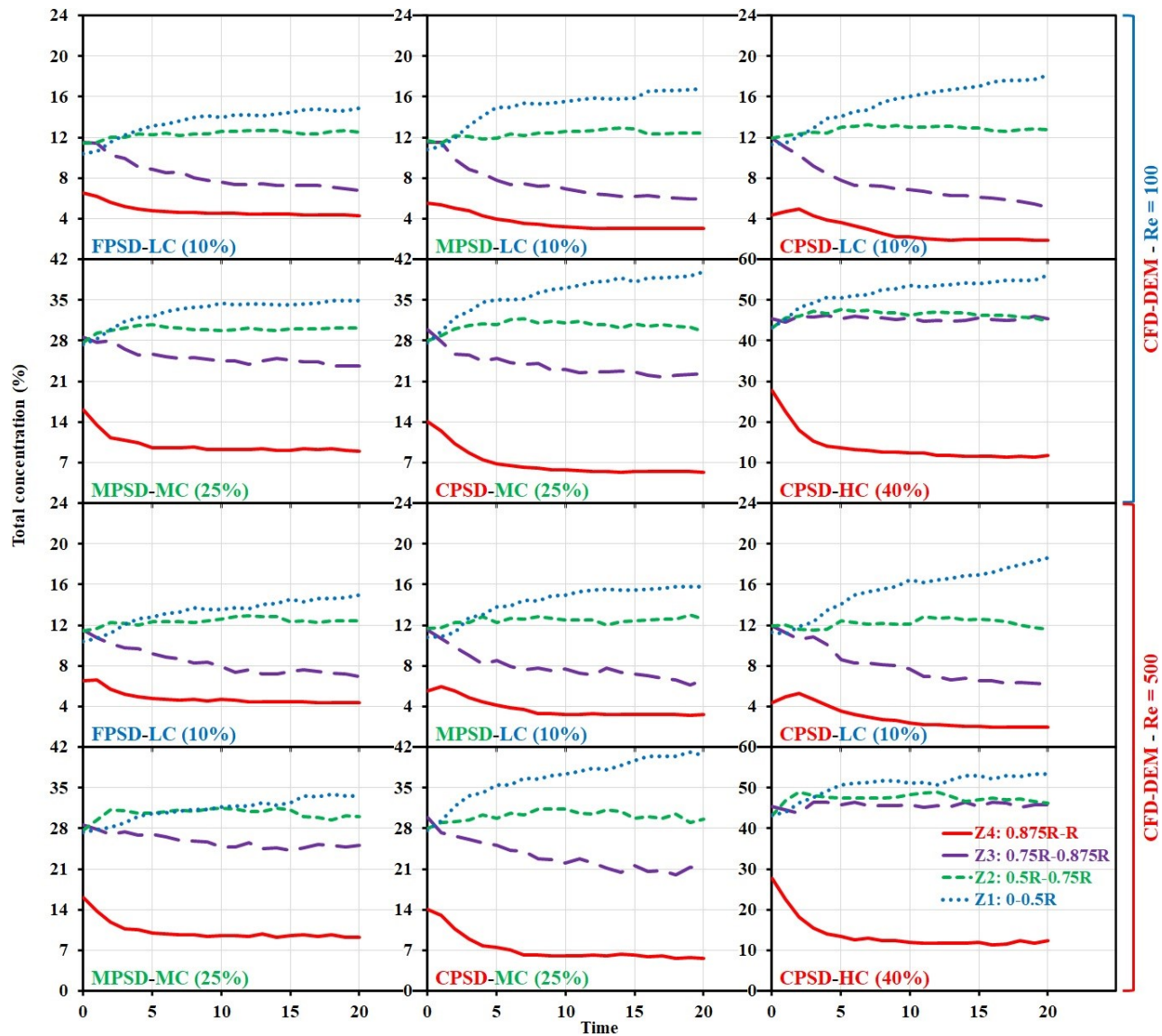
Fig. 7.8. Total concentrations of particles in four different radial zones Z1 to Z4 over time obtained using the four-way coupling CFD-DEM approach.

In the case of the high concentration suspension CPSD-HC, the total particle concentration increased in Z3 (0.75R-0.875R) over time. In the case of the DEM simulation results (Fig. 7.7), the total concentrations in Z3 overpassed those of the central zones Z1 and Z2 near the end of flow period (t = 20) which does not conform to the expected order in typical SIPM in pipes. As can be observed in Fig. 7.8, considering the fully coupling of the suspending fluid flow and particle dynamics by means of the four-way CFD-DEM approach led to more accurate simulation of the pipe flow of the high concentration suspension CPSD-HC, where the highest total concentration was obtained in the central zone Z1 (0-0.5R) rather than the zones Z2 and Z3. Moreover, the CFD-DEM approach led to wider radial variations between the total particles' concentrations across the pipe for all the cases compared to those obtained using the DEM approach. This can reflect that fully fluid-particle coupling allows capturing higher degrees of SIPM across the pipe than the DEM approach which only considers the particle collisions and 1-way effect of suspending fluid on particles. This is further discussed and analyzed in the next section.

Furthermore, as can be observed for both DEM and CFD-DEM simulations, for a given PSD and concentration of particles, the evolution of the total particles' concentrations in the LL (Z4) zone exhibited comparable trends for different suspending fluid *Re* numbers. It can thus be concluded that LL composition in terms of particle concentration mostly depends on the granular skeleton characteristics (concentration and PSD) rather than the rheology and flow properties of the suspending fluid. On the other hand, the variation of the *Re* number mostly influenced the evolution of the particle concentrations in other zones Z1-Z3. It can thus be concluded that SIPM across the BC zone (Z1-Z3: 0-0.875R) is a consequence of the coupled effect of both particulate characteristics and suspending fluid rheology, which is further discussed in the next section.

7.4.3 Shear-induced particle migration (SIPM) across pipe

The SIPM across the simulated pipe flows was evaluated using the *SIPMI* index (Eq. (7.20). The index is presented in Fig. 7.9 for all the investigated suspensions, simulated using both one-way coupled DEM and four-way coupled CFD-DEM approaches. For a given suspension, the full coupling of the particle dynamics and suspending fluid flow through the CFD-DEM simulations led to more accurate simulation of the SIPM compared to the DEM approach, which is reflected by higher *SIMPI* values. The difference is particularly apparent at higher concentrations.
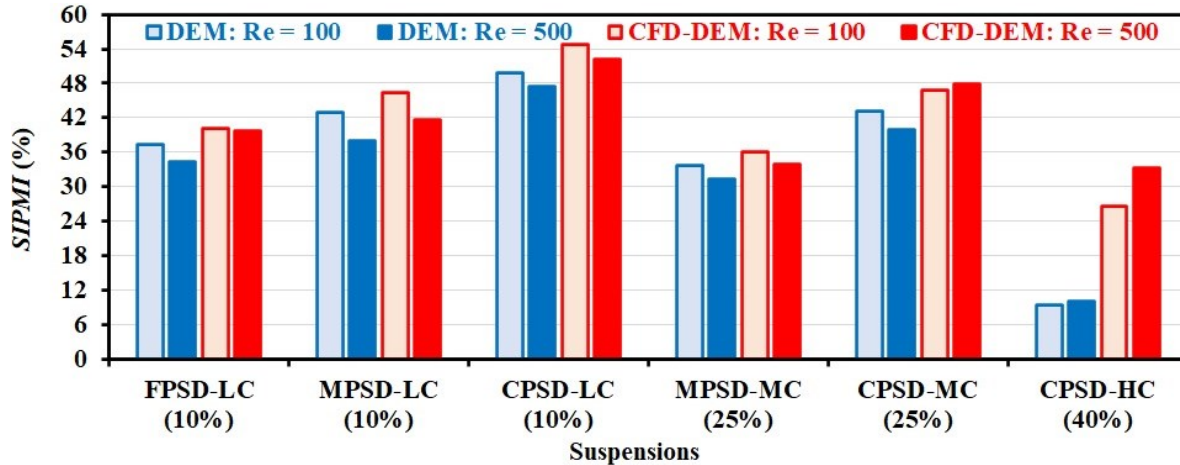
Fig. 7.9. *SIPMI* indices of investigated suspension pipe flows simulated using the one-way coupled DEM and four-way coupled CFD-DEM approaches

As can be observed, for a given concentration of particles and suspending fluid flow *Re* number, coarser PSD of particles led to higher *SIPMI* indices, which is well conformed with the spatially varying particle interaction frequency described by Phillips et al. [39]. Specifically, according to [39], for a given particle concentration and shear rate, the SIPM is directly proportional to the particle size. Moreover, for a given PSD of particles, suspensions with higher concentration exhibited lower *SIMPI* indices. This can be attributed to the lower pipe wall effect (WE) on the initial heterogeneity of higher concentration of particles across the pipe in the beginning of the flow period ($t = 0$), reported by Tavangar et al. [32]. According to Phillips et al. [39], for a given particle size and shear rate, lower gradient in the particle concentrations across the pipe results in lower spatial variation in the frequency of particle interactions and, consequently, lower SIPM is expected.

As can be observed in Fig. 7.9 for the CFD-DEM simulations, a lower *Re* of the suspending fluid led to higher *SIMPI* values for all the LC (10%) suspensions, in addition to MPSD-MC, proportioned with medium PSD and medium concentration (25%) of particles. This can be explained by the fact that in the case of LC and MPSD-MC suspensions, the collision-induced velocity of particles are lower than the suspending fluid flow velocity. This is due to lower possibility of collisions in LC suspensions and smaller collision forces within medium-size distribution of particles (MPSD) compared to HC and CPSD suspensions, respectively. Therefore, lower *Re* value (higher viscosity) of the suspending fluid led to higher drag forces to push forward the particles (Eq. (7.3)). This can increase the collision frequency of particles and consequently increase the possibility of SIPM for LC and MPSD-MC suspensions.

However, in the case of suspensions of medium (MC: 25%) and high (HC: 40%) concentrations of coarse PSD (CPSD) of particles, increasing the *Re* of the suspending fluid resulted in higher *SIMPI* values. This can be attributed to the fact that particles gained greater forces than the suspending fluid due to higher interparticle collision forces in medium and high concentrations of coarse PSD of particles. Indeed, increasing the concentration and size differences between two colliding particles can increase the possibility of collision and magnitude of the collision forces, respectively. Therefore, lower drag forces, exerted by the suspending fluid with higher *Re* (or lower viscosity), can resist less against the collision forces on particles, hence leading the particles to migrate more freely to the other radial zones and, consequently, obtain higher *SIPMI* values.
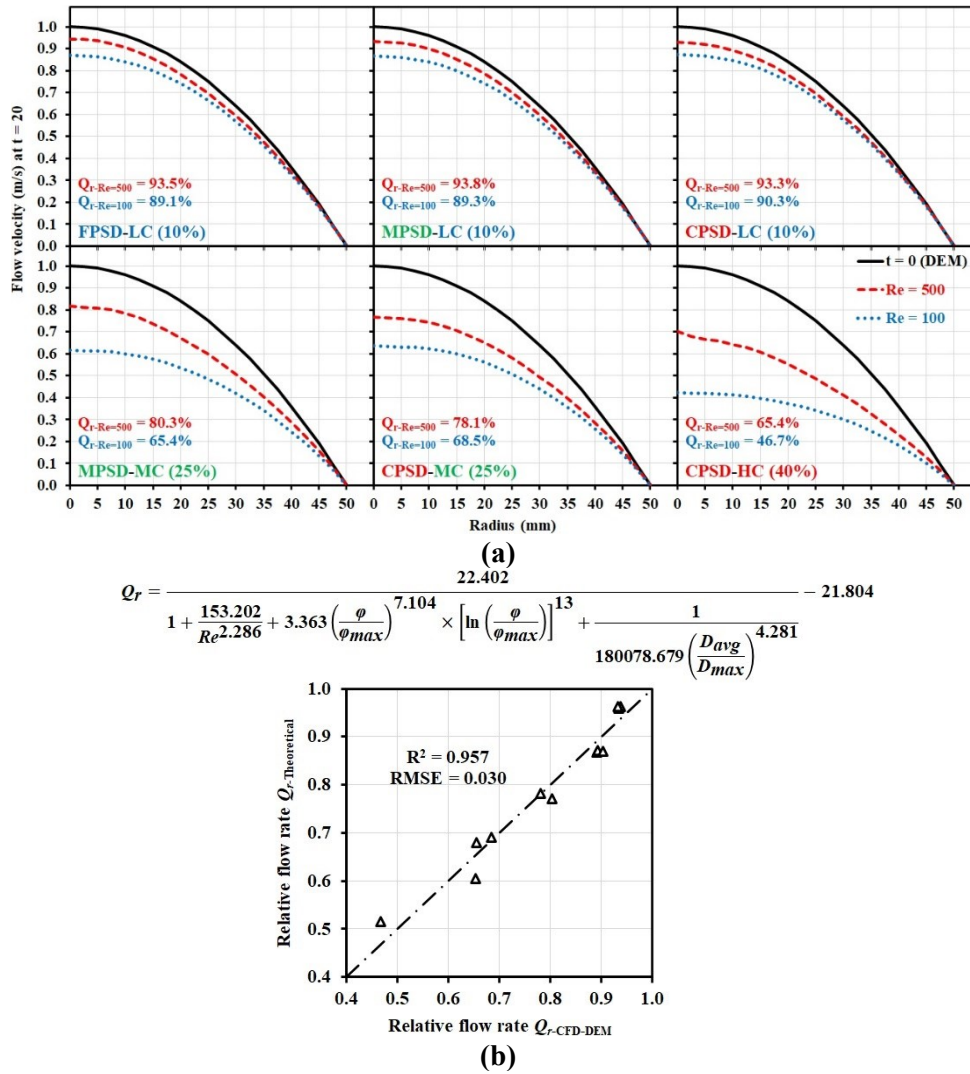
Fig. 7.10a compares the flow velocity profiles of the suspending fluids of the investigated suspensions across the pipe, obtained using the four-way coupling CFD-DEM simulations at the end of flow period ($t = 20$) with their initial profiles at the beginning of the computation ($t = 0$), as assumed fixed through the DEM simulations. As can be observed in Fig. 7.10a, considering the effect of presence of particles on suspending fluid flow using the employed four-way coupling CFD-DEM approach decreased the suspending flow velocity magnitudes across the pipe at the end of the computation ($t = 20$) and, therefore, it led to lower flow rates than their initial values. The relative flow rate Q_r values, illustrated in Fig. 7.10a, were calculated as the ratio of the flow rates and the end of the computation ($t = 20$) to their initial values (at $t = 0$), as:

$$Q_r(\%) = \frac{Q_{t=20}}{Q_{t=0}} \text{ where } Q = \int u_f \, dA = \int 2\pi r \, u_f(r) \, dr \tag{7.27}$$

where A is the surface area of the pipe cross section and $u_f(r)$ is the suspending fluid velocity at the radial distance r to the pipe center. As can be observed in Fig. 7.10a, for a given concentration and PSD of particles, higher *Re* of the suspending fluid resulted in higher Q_r values which can be attributed to its lower plastic viscosity. Accordingly, the Q_r values for the suspending fluid flow's Reynolds numbers *Re* of 100 and 500 ranged from 46.7% to 90.3% and 65.4% to 93.8% respectively. The coupled effect of the relative-solid packing-fraction (φ/φ_{max}) and PSD (D_{avg} (mm)) of particles and *Re* of the suspending fluid flow on relative flow rates Q_r of the investigated pipe flow simulations was evaluated, as shown in Fig. 7.10b. As can be observed, for a given PSD of particles (i.e., given D_{avg} and φ_{max}), increasing the particle concentration results in lower flow rate at the end of the pipe flow computation. This is due to higher

resistance of the particles with higher relative-solid packing fractions (φ/φ_{max}) against the suspending fluid flow. According to the adjusting factors of the established correlation in Fig. 7.10b, it can be concluded that the relative flow rate magnitudes are more controlled by the concentration and PSD of particles rather than the suspending fluid's flow Reynolds number.

$$Q_r = \frac{22.402}{1 + \dfrac{153.202}{Re^{2.286}} + 3.363\left(\dfrac{\varphi}{\varphi_{max}}\right)^{7.104} \times \left[\ln\left(\dfrac{\varphi}{\varphi_{max}}\right)\right]^{13}} + \frac{1}{180078.679\left(\dfrac{D_{avg}}{D_{max}}\right)^{4.281}} - 21.804$$

Fig. 7.10 (a) Flow velocity profiles of the investigated pipe flows at the end of the flow period ($t = 20$), obtained using the four-way coupled CFD-DEM approach and **(b)** the coupled effect of the relative-solid packing-fraction (φ/φ_{max}), mean diameter (D_{avg}), and maximum diameter ($D_{max} = 17$ mm for P5) of particles and Re of the suspending fluid's flow on relative flow rate (Q_r) values of the investigated suspension pipe flows.

7.4.4 Changes in rheology of investigated suspensions induced by pipe flow

7.4.4.1 Rheological heterogeneity of investigated pipe flows

The yield stress- (*YSHI*) and viscosity-heterogeneity (*VHI*) indices of the investigated suspension pipe flows were evaluated using Eqs. (25) and (26) and presented in Figs. 7.11a and 7.12a, respectively. As can be observed, the four-way coupled CFD-DEM simulations showed higher rheological heterogeneity indices than those obtained using the one-way coupled DEM approach due to greater *SIPMI* values captured using the CFD-DEM modeling approach. As can be observed, the SIPM led to larger *VHI* indices (13.7%-54.6%) compared to the *YSHI* values (4.2%-21.6%) for the investigated suspension pipe flow simulations obtained using the CFD-DEM approach. This can be due to more significant influence of the relative-solid packing fraction (φ/φ_{max}) values on the viscosity values (Eq. (7.24)) than the yield stress values (Eq. (7.23)) of suspensions. As explained earlier in section 4.3 for the *SIPMI* indices, increasing the *Re* of the suspending fluid flow led to lower rheological heterogeneities for the pipe flows of the LC and MPSD-MC suspensions while higher *YSHI* and *VHI* values were achieved for the suspensions proportioned with medium (MC) and high (HC) concentrations of coarse PSD (CPSD) of particles.

The coupled effect of the relative-solid packing-fraction (φ/φ_{max}) and PSD (D_{avg} (mm)) of particles and *Re* of the suspending fluid flow on the *YSHI* and *VHI* indices of the investigated suspension pipe flows was evaluated in Figs. 7.11b and 7.11b, respectively. As can be observed, the rheological heterogeneities are in good agreements with the granular skeleton characteristics and suspending fluid Reynolds number. Accordingly, increasing the φ/φ_{max} and D_{avg} of particles led to higher pumping-induced rheological heterogeneities across the pipe. The maximum and minimum rheological heterogeneity indices among the investigated suspensions were thus obtained for the FPSD-LC and CPSD-HC suspension pipe flows, respectively. According to the established correlations in Figs. 7.11b and 7.12b, the *YSHI* and *VHI* indices are more controlled by the characteristics of the granular skeleton, in terms of concentration, packing density, and PSD of particles, rather than the suspending fluid rheology and pumping flow rate, reflected by the flow Reynolds number *Re.*

7.4.4.2 *Rheological characterization of the lubrication layer and bulk concrete after pumping*

The rheological properties of the investigated reference suspensions and their corresponding LL (Z4: 0.875R-R) and BC (Z1-3: 0-0.875R) zones were characterized in terms of the yield stress and plastic viscosity values relative to those of their corresponding suspending fluids using Eqs. (23) and (24), respectively, at the end of the pipe flow period (t = 20) of the CFD-DEM simulations and presented in Fig. 7.13.

(a)

$$YSHI\,(\%) = \cfrac{1}{1 - 0.019Re^{0.074} - 0.007\,\cfrac{\ln\left(\frac{\varphi}{\varphi_{max}}\right)}{\left(\frac{\varphi}{\varphi_{max}}\right)^{0.959}} - 1.020\left(\frac{D_{avg}}{D_{max}}\right)^{0.148}} - 1.820$$
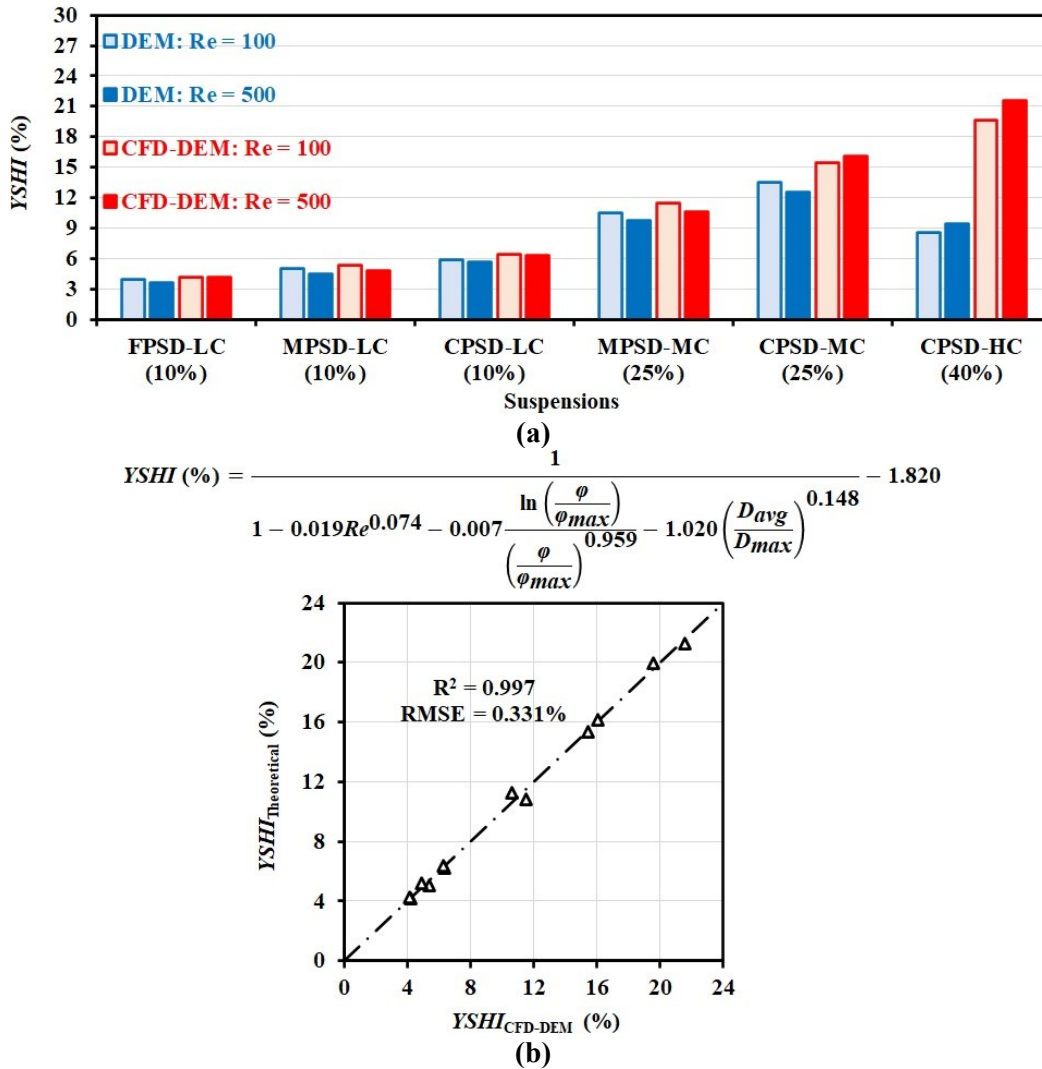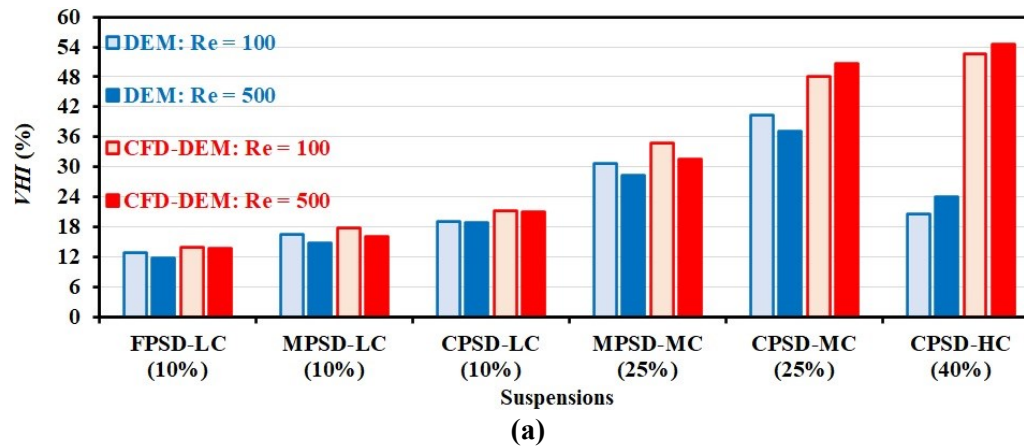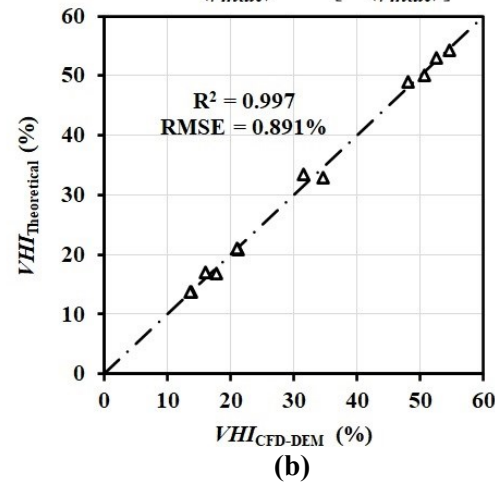

(b)

Fig. 7.11 (a) Yield-stress heterogeneity indices (*YSHI*) of the investigated suspension pipe flows and **(b)** the coupled effect of the relative-solid packing-fraction (φ/φ_{max}), mean diameter (D_{avg}), and maximum diameter (D_{max} = 17 mm for P5) of particles and *Re* of the suspending fluid flow on *YSHI* indices of the investigated suspension pipe flows.

$$VHI\ (\%) = \cfrac{1}{1 - 0.006Re^{0.031} - 0.0005\left(\cfrac{\varphi}{\varphi_{max}}\right)^{0.058}\left[\ln\left(\cfrac{\varphi}{\varphi_{max}}\right)\right]^{5} - 1.003\left(\cfrac{D_{avg}}{D_{max}}\right)^{0.037}} - 3.546$$

Fig. 7.12 (a) Viscosity heterogeneity indices (*VHI*) of the investigated suspension pipe flows and **(b)** the coupled effect of the relative-solid packing-fraction (φ/φ_{max}), mean diameter (D_{avg}), and maximum diameter (D_{max} = 17 mm for P5) of particles and *Re* of the suspending fluid flow on *VHI* indices of the investigated suspension pipe flows.
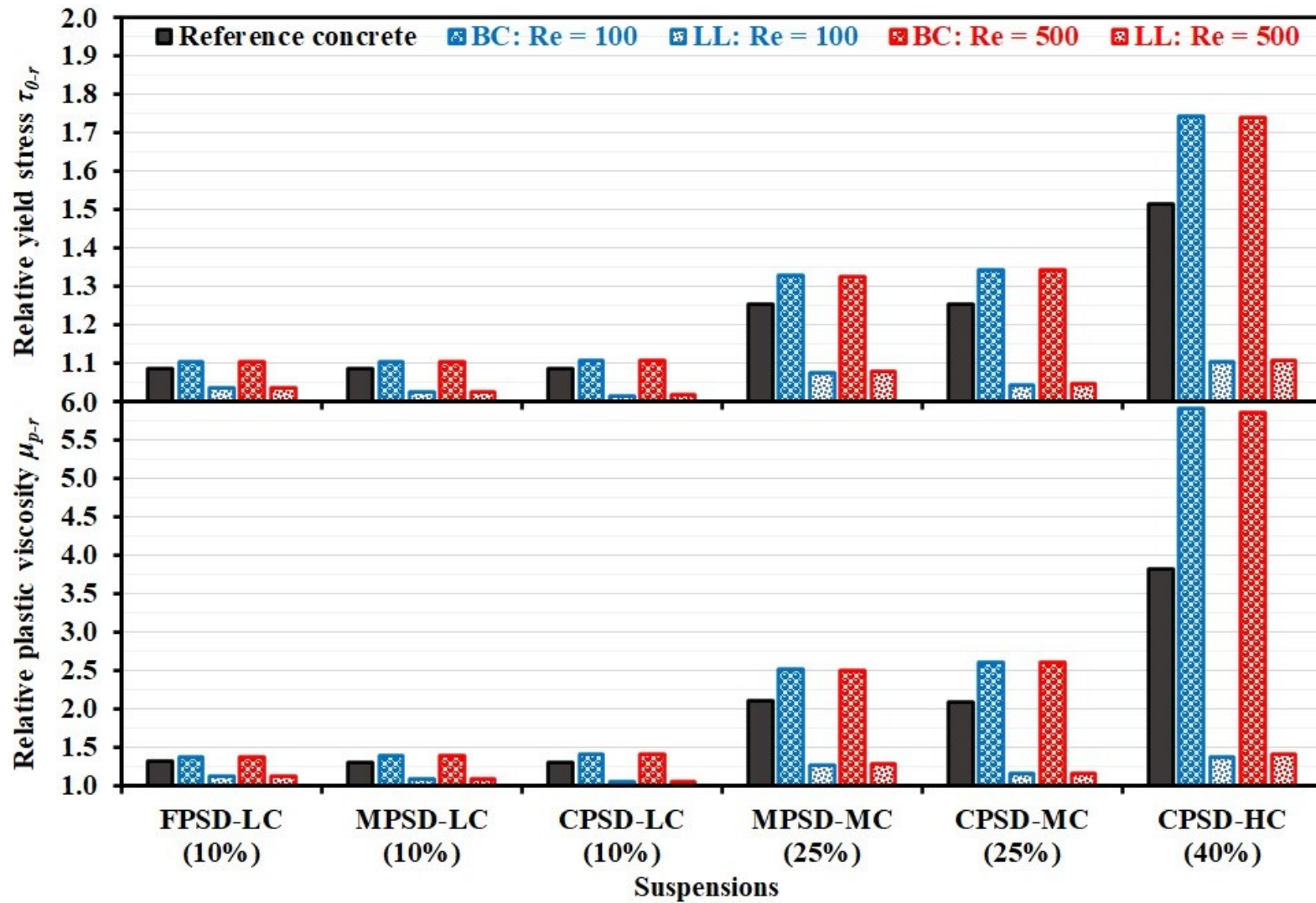
Fig. 7.13. Relative yield stress and plastic viscosity values of investigated reference suspensions and their corresponding LL and BC zones obtained using the CFD-DEM simulations.

As can be observed, the BC and LL zones showed significantly higher and lower rheological properties compared to the reference concrete models, respectively. Accordingly, the relative yield stress values of the reference mixtures and their corresponding BC and LL zones ranged from 1.08 to 1.51, 1.10 to 1.74, and 1.01 to 1.11, respectively. Moreover, the μ_{p-r} values of 1.30-3.82, 1.37-5.92, and 1.05-1.40 were obtained for the investigated reference suspensions and their corresponding BC and LL zones, respectively. As discussed in section 4.4.1, the rheological properties of the BC and LL zones are more influenced by the PSD and concentration of the particles rather than the suspending fluid's flow Reynolds number. The maximum and minimum relative rheological properties of the BC zones of the investigated pipe flows were obtained for the highest and lowest concentrations of the coarse and fine PSDs of particles (i.e., CPSD-HC and FPSD-LC mixtures) and suspending fluid' *Re* values of 100 and 500, respectively. On the other hand, the maximum and minimum τ_{0-r-LL} and μ_{p-r-LL} values were obtained for the LL zones of the pipe flows of the highest and lowest concentrations of the coarse PSD (i.e., CPSD-HC and CPSD-LC) of particles and suspending fluid *Re* values of 500 and 100, respectively.

7.5 Validation of LL thickness estimations

(DIP) of the cut sections of hardened concrete in pipes [20]. A maximum particle-size threshold, generally finer than 2 mm, is selected according to the literature for typical particle size in the LL for concrete pipe flow [1,9,12,13]. The LL thickness then corresponds to the zone in the vicinity of the pipe wall where no particle coarser than the selected threshold can be detected through the pipe cross section images. Although, an initial fixed assumption of $0.125R$ (6.25 mm) has been made for the LL zones (Z4: $0.875R$-R) of all the investigated pipe flows to facilitate the SIPM analyses; in order to validate the results of the carried-out CFD-DEM simulations, the LL thicknesses of the simulated pipe flows was accurately measured at the final time step ($t = 20$) similarly to the abovementioned DIP technique.

For DEM simulations, the LL thickness referred to the zone in the vicinity of the pipe walls where no particle coarser than the finest particle P1 (1 mm) can be observed through the pipe cross section images [32]. These images were captured using the post-processing results at the middle of the pipe length for all the simulated pipe flows. As shown in Fig. 7.14, in order to easier identification of the LL thickness, only the finest particles P1 (1 mm) were colored in black while all the other particles P2-5 (3.5-17 mm) were illustrated in white color. As can be observed in Fig. 7.14, the evaluated LL thicknesses (e_{LL}) of the investigated pipe flows ranged from 0.8 to 1.7 mm and 1.3 to 2.7 mm for suspending fluid's flow *Re* of

100 and 500, respectively. The predicted LL thicknesses are in general accordance with the typically reported values for experimental measurements of the LL thickness in the literature (1-3 mm) [1,9,12,13].

7.6 Limitations and further applications of numerical approach

The four-way CFD-DEM coupling approach used in this study could accurately simulate the SIPM mechanism leading to rheological heterogeneity across the pipe and formation of LL during concrete pumping process. In addition to its higher precision, it was revealed that the developed CFD-DEM coupling approach required comparable calculation times with the DEM approach. This is due to the fact that the calculation time is mostly controlled by the computation of particle collisions through the DEM algorithm, which is common within both methods, rather than the short CFD algorithm. The following limitations can be addressed for the further applications of the employed approach for concrete pumping simulation.

- A spherical form was assumed for the particles to simplify the computations of the interparticle collisions. Taking into account the longer calculation time required, the use of the irregularly shaped particles can result in more realistic simulations.
- The role of yield stress was neglected in the CFD model used to simplify the computation of the suspending fluid flow. The yield-stress term can be added to the CFD algorithm to enable the numerical solution to simulate the plug flow formation in the pipe center under lower shear rates.
- The viscosity of the suspending fluid was assumed fixed over the whole pipe flow period by means of the limited *Re* values of 100 and 500. The use of a wider range of rheological properties, in addition to take into account the pumping-induced and time-dependent variations in rheological properties of concrete [23,59,60] can enhance the generalizability of the employed approach for different types of concrete and pumping conditions.

(a) FPSD-LC - *Re* = 100   **(b) MPSD-LC - *Re* = 100**   **(c) CPSD-LC - *Re* = 100**

(d) MPSD-MC - *Re* = 100   **(e) CPSD-MC - *Re* = 100**   **(f) CPSD-HC - *Re* = 100**

(g) FPSD-LC - *Re* = 500   **(h) MPSD-LC - *Re* = 500**   **(i) CPSD-LC - *Re* = 500**

(j) MPSD-MC - *Re* = 500   **(k) CPSD-MC - *Re* = 500**   **(l) CPSD-HC - *Re* = 500**
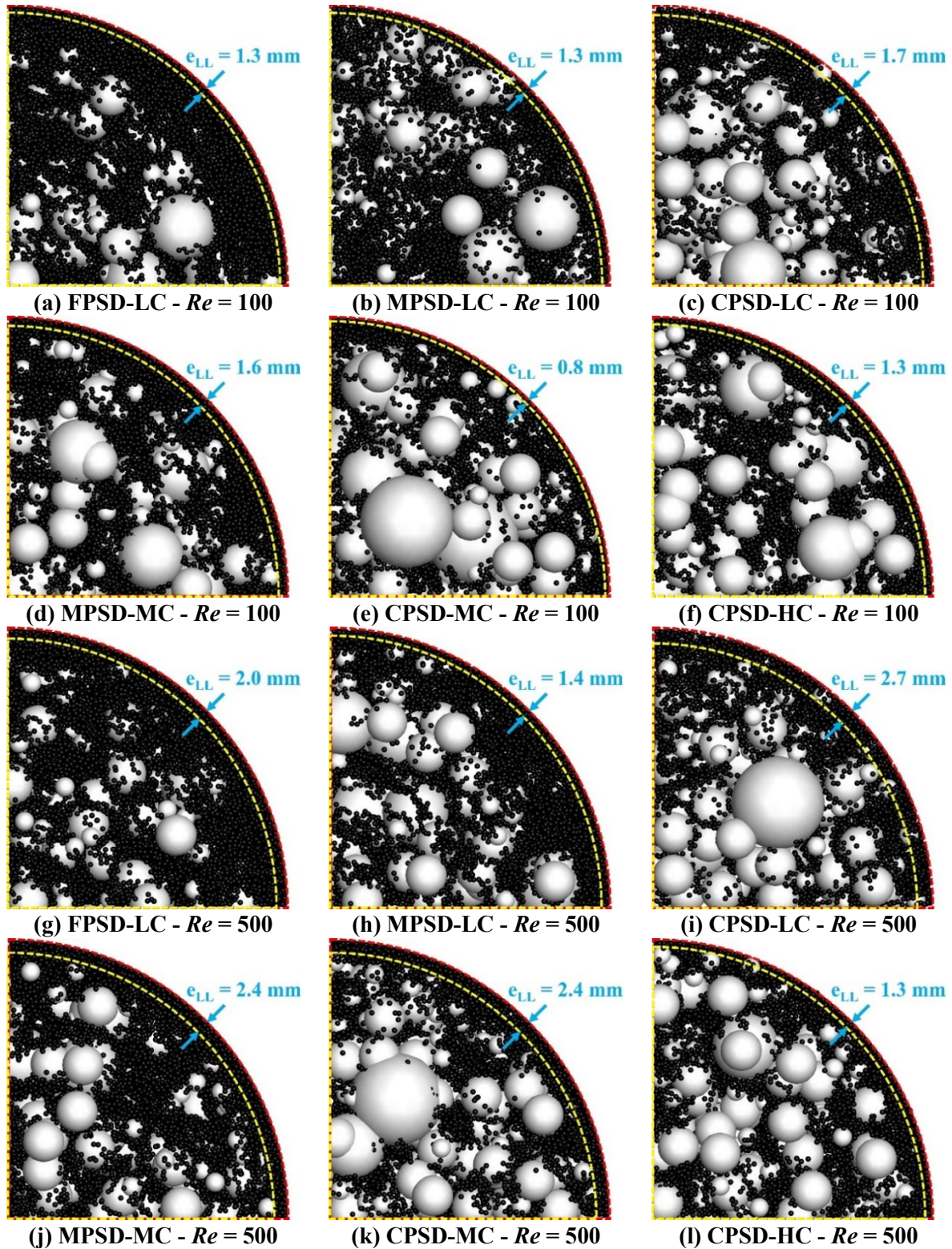
Fig. 7.14 Estimation of LL thicknesses of **(a** and **g)** FPSD-LC, **(b** and **h)** MPSD-LC, **(c** and **i)** CPSD-LC, **(d** and **j)** MPSD-MC, **(e** and **k)** MPSD-HC, and **(f** and **l)** CPSD-HC mixtures with suspending fluid's flow *Re* values of 100 and 500, respectively, using image-analysis technique.

7.7 Conclusions

In this study, a four-way CFD-DEM coupling approach was used to simulate the mechanism of shear-induced particle migration (SIPM) that can cause rheological heterogeneity across the pipe and formation of the lubrication layer (LL) during concrete pumping. The simulated mixtures included 12 biphasic suspensions made with 10%-40% concentrations of different wide PSDs of five spherical-particle classes ranging from 1 to 17 mm in diameter. Suspending fluids of different viscosity levels resulting in different suspending fluid Reynolds number (Re) were considered. The concentration of particles was tracked over time at four radial zones to evaluate the SIPM and pumping-induced rheological heterogeneities and characterize the LL after pumping. The results of the CFD-DEM simulations were compared with those of a one-way coupled DEM approach for a 100-mm diameter pipe to highlight the significance of the fully coupling of suspending fluid-particles forces and vice versa for multiphasic modeling of concrete pipe flow. The simulation results lead to the following concluding remarks.

- Unlike the single-phase modeling approach, the developed multiple time-scale four-way CFD-DEM coupling model proved effective to evaluate the coupled effect of the PSD and concentration of aggregate and rheology of the suspending mortar on shear-induced heterogeneities during multiphasic concrete pipe flow. Moreover, the developed CFD-DEM coupling approach led to higher precision and comparable calculation time to model SIPM compared to the one-way coupled DEM approach.

- The SIPM mechanism of the formation of the LL containing the lowest total particle concentration across the pipe was successfully simulated using the numerical simulations. The formation of the LL was reflected by the migration of the finest particle (1 mm) towards the vicinity of the pipe wall while concentration of the larger particles (3.5-17 mm) increased in the central zones Z1-Z2 over time.

- Unlike the one-way coupled DEM approach, the four-way coupling of particles and suspending fluid flow through the CFD-DEM simulations successfully led to the highest total particle concentration in the central zone Z1 (0-0.5R), followed by Z2 (0.5R-0.75R), Z3 (0.75R-0.875R), and Z4 (LL: 0.875R-R), specially for the high-concentration suspension CPSD-HC (40%). The use

of CFD-DEM approach resulted in wider variations between the particle concentrations across the pipe compared to the DEM results for all the suspensions.

- The composition of the LL was found mostly controlled by the characteristics of the granular skeleton rather than the rheology of the suspending fluid. The numerical approach used and the suspending fluid's *Re* mostly affected the evolutions of particle concentration in zones Z1-3 rather than the LL.

- The four-way CFD-DEM coupling approach led to capture greater degrees of SIPM during concrete pipe flow compared to the DEM simulations. Moreover, for a given *Re* of the suspending fluid flow, coarser PSD and lower concentration of particles resulted in higher *SIPMI* indices. Furthermore, unlike the mixtures containing the medium and high concentration of coarse PSD of particles, increasing the *Re* resulted in lower *SIPMI* indices for the LC and MPSD-MC suspensions.

- The relative pumping flow rates of the investigated pipe flow simulations at the end of the pipe flow period to their initial value (Q_r) was found in good agreement with the relative-solid packing-fraction (φ/φ_{max}) and mean diameter (D_{avg}) of particles and suspending-fluid *Re*. According to the established correlation, for a given PSD, higher concentration of particles led to lower Q_r values. Moreover, higher *Re* values resulted in higher Q_r values. However, the pumping flow rate was found more controlled by the characteristics of the granular skeleton rather than the suspending-fluid rheology, reflected by *Re* values.

- Yield stress (*YSHI*) and viscosity (*VHI*) heterogeneity indices ranged from 4.2% to 21.6% and 13.7% to 54.6%, respectively. These values are mostly controlled by the φ/φ_{max} and D_{avg} of particles rather than the suspending fluid *Re*. Increasing the concentration and mean diameter of particles led to higher *YSHI* and *VHI* indices across the pipe. Moreover, increasing the suspending fluid *Re* led to lower rheological dissimilarity across the pipe for all the LC suspensions and MC-MPSD mixture, which resulted in higher *YSHI* and *VHI* for CPSD-MC and CPSD-HC suspensions.

- The relative yield stress (τ_{0-r}) and plastic viscosity (μ_{p-r}) of the bulk concrete (BC) and LL to their suspending fluid were successfully evaluated using the CFD-DEM simulation results at the end of pipe flow computation. The rheological properties of the BC (τ_{0-r-BC}: 1.10-1.74 and μ_{p-r-BC}: 1.37-5.92) and LL (τ_{0-r-LL}: 1.01-1.11 and μ_{p-r-LL}: 1.05-1.40) were found to be controlled primarily by the characteristics of the suspended particles, rather than the suspending fluid *Re*.

- The LL thickness (e_{LL}) of the investigated pipe flows was successfully estimated using digital image processing (DIP) of the pipe cross sections using the post-processing results of the CFD-DEM simulations at the end of flow computation. The estimated e_{LL} values ranged from 0.8 to 2.7 mm is comparable with values typically reported in the literature for concrete pumping experiments (1-3 mm).

7.8 Acknowledgement

APPENDIX

The evolution of the volumetric concentration of different particle subclasses P1-5 in different radial zones Z1-4 are presented in Figs. 7.A1-7.A5 for LC (10%) and MC (25%) suspensions.

Fig. 7.A1. Evolution of concentrations of P1-5 particles in four different radial zones Z1-4 for the mixture containing fine PSD and low (10%) concentration of particles (FPSD-LC) versus flow time.

Fig. 7.A2. Evolution of concentrations of P1-5 particles in four different radial zones Z1-4 for the mixture containing medium PSD and low (10%) concentration of particles (MPSD-LC) versus flow time.

Fig. 7.A3. Evolution of concentrations of P1-5 particles in four different radial zones Z1-4 for the mixture containing coarse PSD and low (10%) concentration of particles (CPSD-LC) versus flow time.

Fig. 7.A4. Evolution of concentrations of P1-5 particles in four different radial zones Z1-4 for the mixture containing medium PSD and medium (25%) concentration of particles (MPSD-MC) versus flow time.
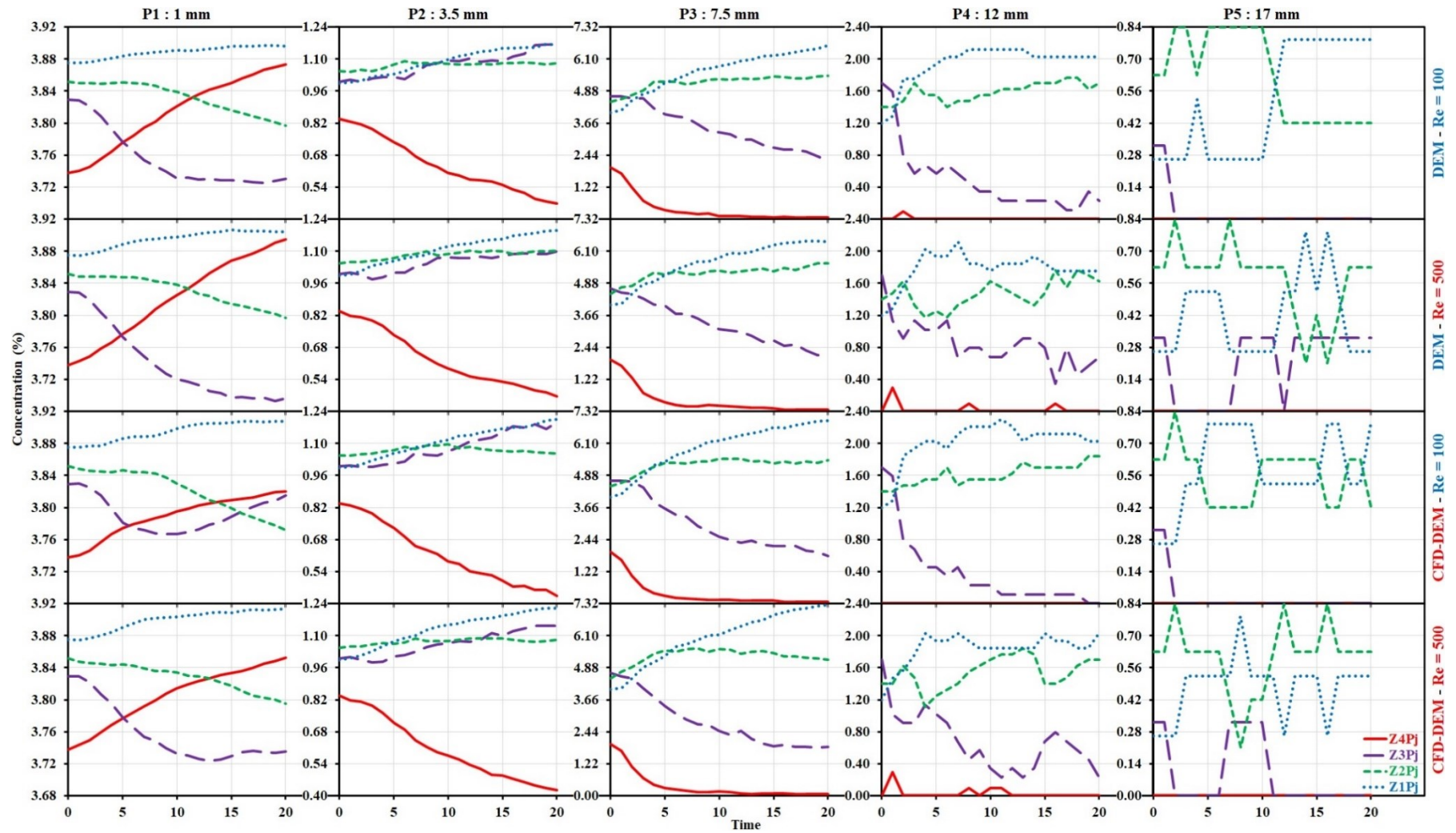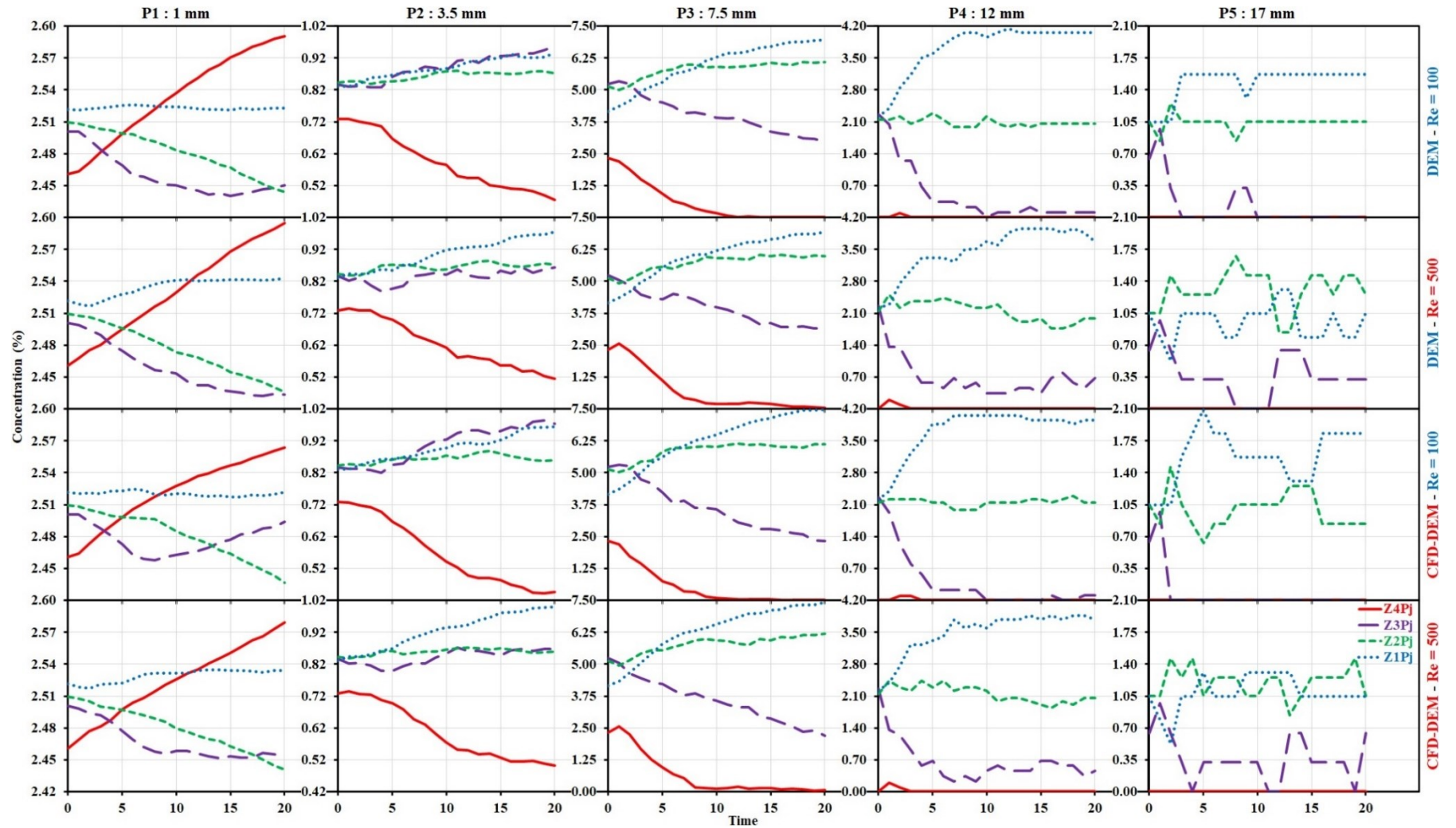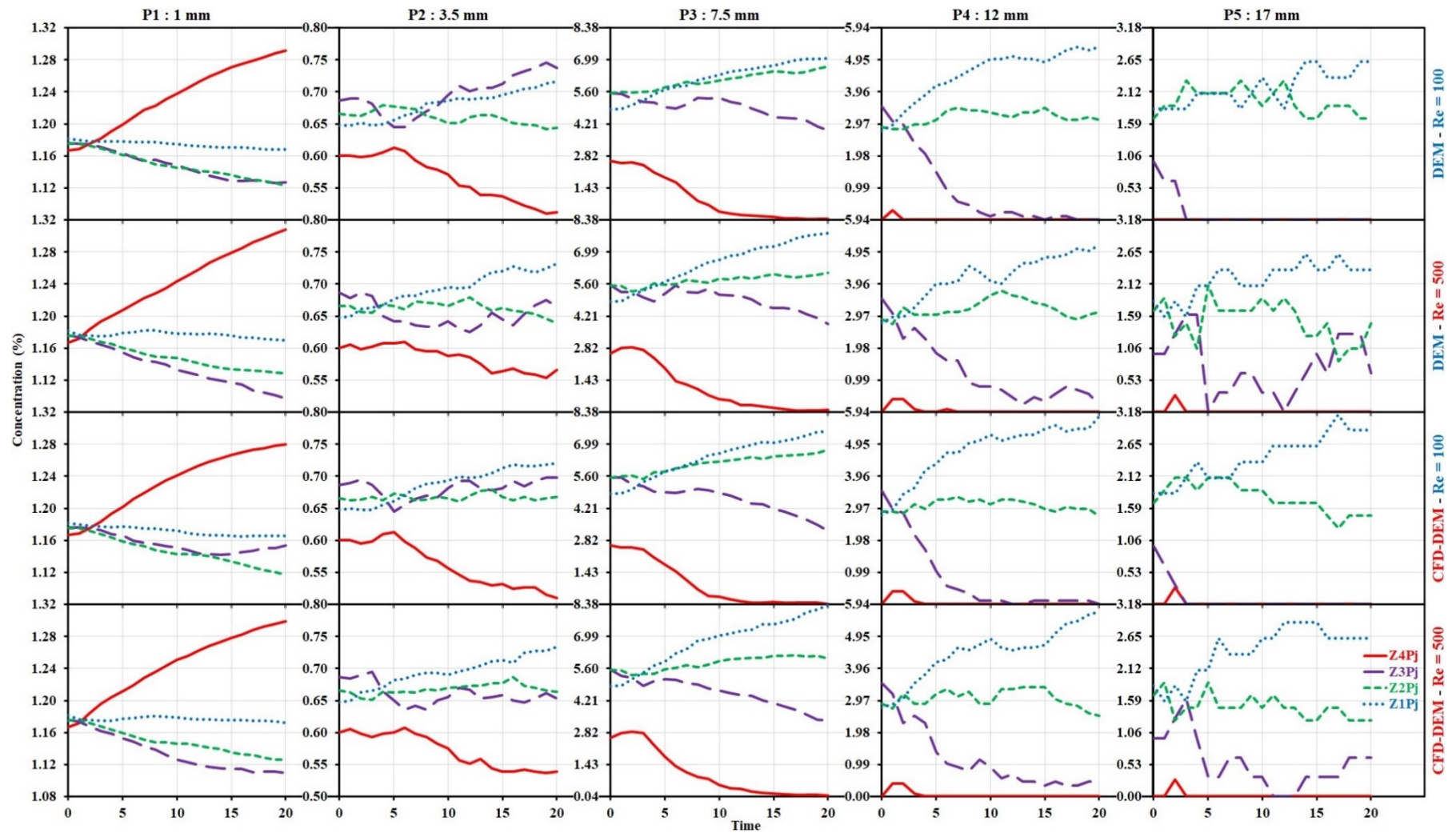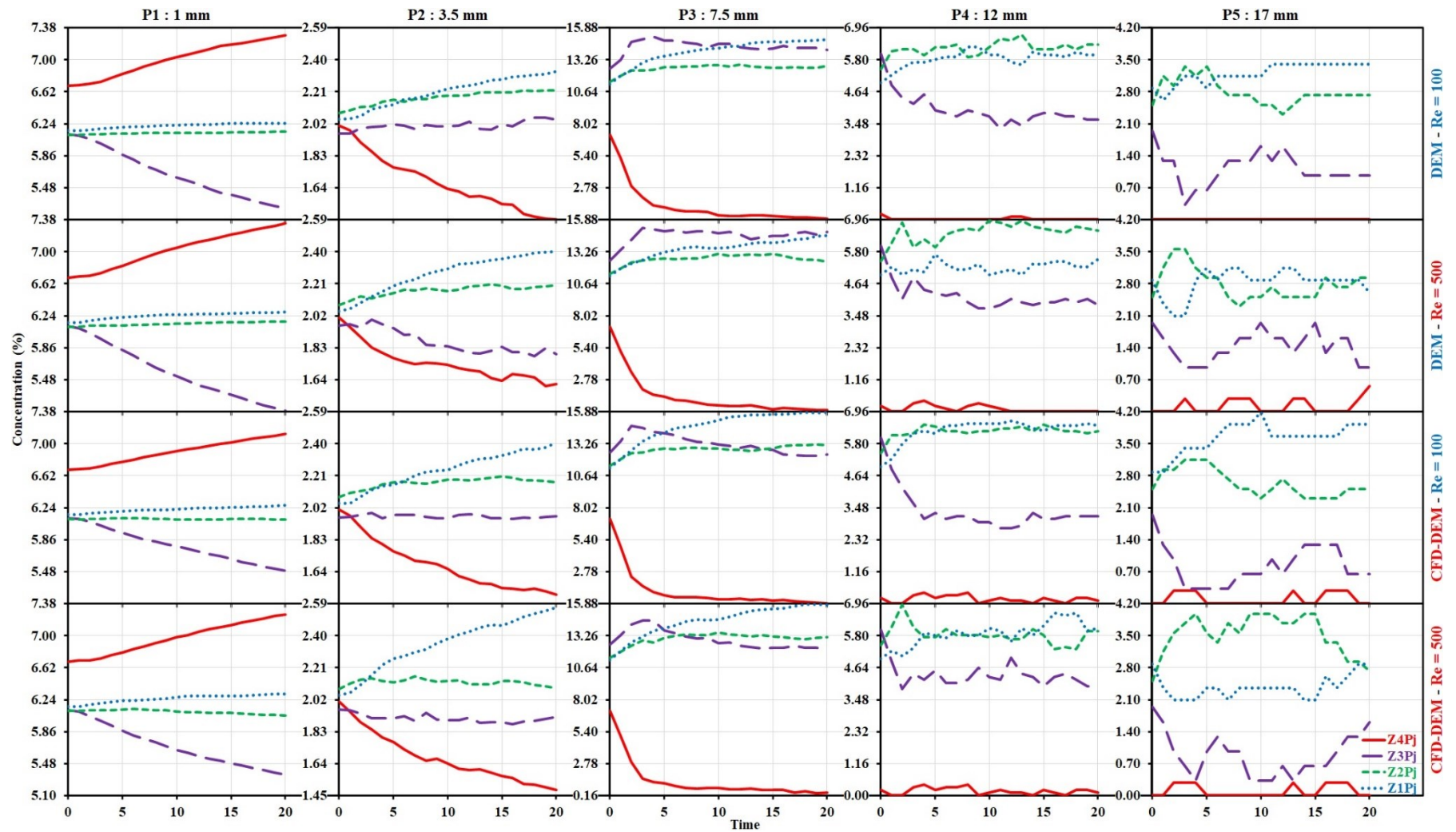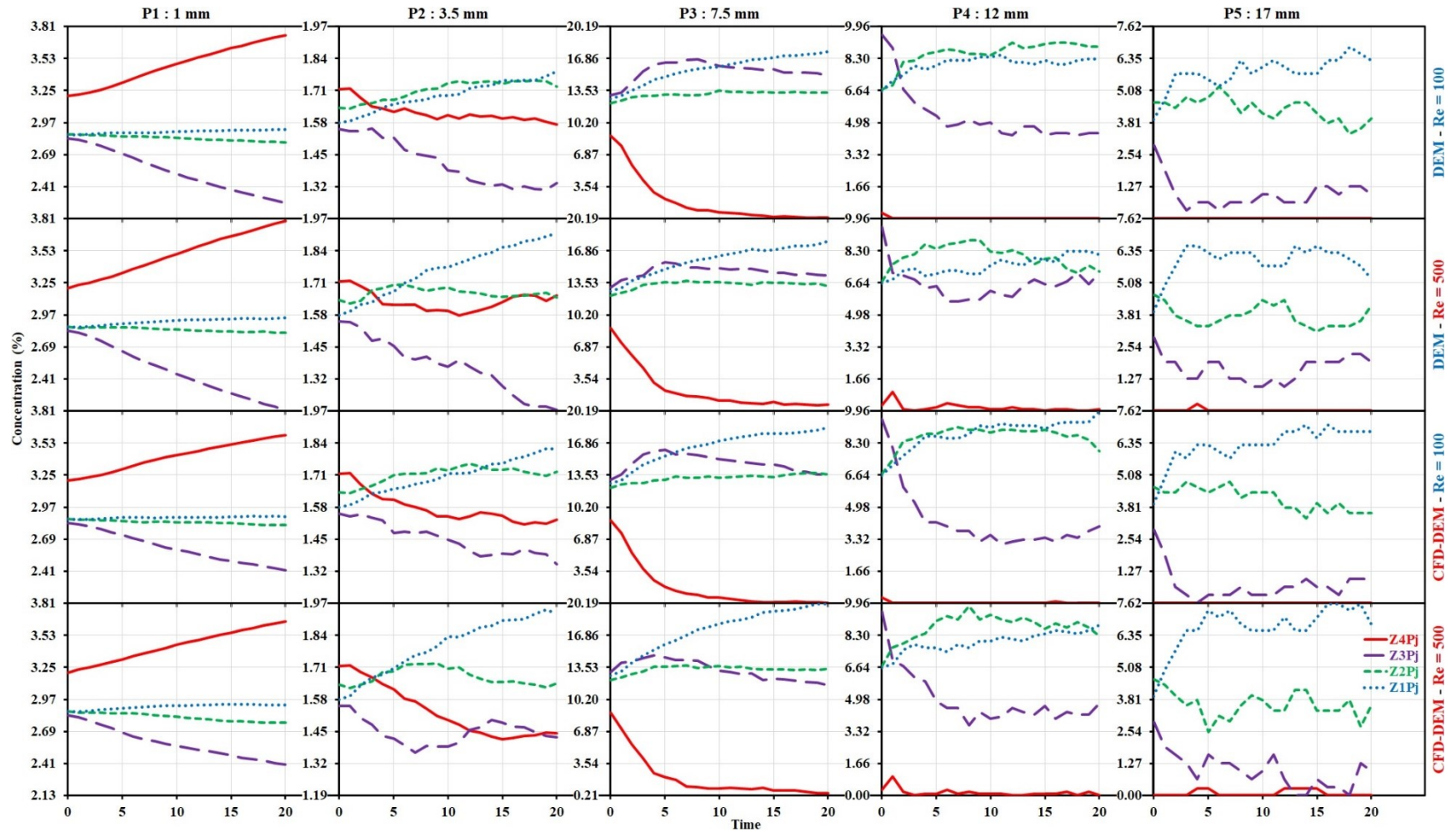
Fig. 7.A5. Evolution of concentrations of P1-5 particles in four different radial zones Z1-4 for the mixture containing coarse PSD and medium (25%) concentration of particles (CPSD-MC) versus flow time.

REFERENCES

[1]   T. Tavangar, M. Hosseinpoor, A. Yahia, K.H. Khayat, Computational investigation of concrete pipe flow: Critical review, ACI Materials Journal, 118 (6) (2021) 203-215. https://dx.doi.org/10.14359/51733124.

[2]   P.V.P. Moorthi, A. Gopinath, P. Nanthagopalan, Mechanistic origins of concrete pumping: a comprehensive outlook and way forward, Magazine of Concrete Research, In Press (2022). https://doi.org/10.1680/jmacr.21.00278.

[3]   V. Vand, Viscosity of solutions and suspensions. I. Theory, The Journal of Physical and Colloid Chemistry, 52 (2) (1948) 277-299. https://doi.org/10.1021/j150458a001.

[4]   A. Karnis, H.L. Goldsmith, S.G. Mason, The kinetics of flowing dispersions: I. Concentrated suspensions of rigid particles, Journal of Colloid and Interface Science, 22 (6) (1966) 531-553. https://doi.org/10.1016/0021-9797(66)90048-8.

[5]   F. Gadala-Maria, A. Acrivos, Shear-induced structure in a concentrated suspension of solid spheres, Journal of Rheology, 24 (6) (1980) 799-814. https://doi.org/10.1122/1.549584.

[6]   D. Leighton, A. Acrivos, The shear-induced migration of particles in concentrated suspensions, Journal of Fluid Mechanics, 181 (1987) 415-439. https://doi.org/10.1017/S0022112087002155.

[7]   J.R. Abbott, N. Tetlow, A.L. Graham, S.A. Altobelli, E. Fukushima, L.A. Mondy, T.S. Stephens, Experimental observations of particle migration in concentrated suspensions: Couette flow, Journal of Rheology, 35 (5) (1991) 773-795. https://doi.org/10.1122/1.550157.

[8]   S. Jacobsen, L. Haugan, T.A. Hammer, E. Kalogiannidis, Flow conditions of fresh mortar and concrete in different pipes, Cement and Concrete Research, 39 (11) (2009) 997-1006. https://doi.org/10.1016/j.cemconres.2009.07.005.

[9]   T.T. Ngo, E.H. Kadri, R. Bennacer, F. Cussigh, Use of tribometer to estimate interface friction and concrete boundary layer composition during the fluid concrete pumping, Construction and Building Materials, 24 (7) (2010) 1253-1261. https://doi.org/10.1016/j.conbuildmat.2009.12.010.

[10]   M.S. Choi, Y.J. Kim, S.H. Kwon, Prediction on pipe flow of pumped concrete based on shear-induced particle migration, Cement and Concrete Research, 52 (2013) 216-224. https://doi.org/10.1016/j.cemconres.2013.07.004.

[11]   H.D. Le, E.H. Kadri, S. Aggoun, J. Vierendeels, P. Troch, G. De Schutter, Effect of lubrication layer on velocity profile of concrete in a pumping pipe, Materials and Structures, 48 (2015) 3991-4003.

https://doi.org/10.1617/s11527-014-0458-5.

[12]   E. Secrieru, Pumping behaviour of modern concretes - Characterisation and prediction, Ph.D. Dissertation, Technische Universität Dresden (2018). https://nbn-resolving.org/urn:nbn:de:bsz:14-qucosa-234912.

[13]   A. Salinas, D. Feys, Estimation of lubrication layer thickness and composition through reverse engineering of interface rheometry tests, Materials, 13 (8) (2020) 1799. https://doi.org/10.3390/ma13081799.

[14]   M.S. Choi, Y.J. Kim, S.H. Kwon, Prediction on pipe flow of pumped concrete based on shear-induced particle migration, Cement and Concrete Research, 52 (2013) 216-224. https://doi.org/10.1016/j.cemconres.2013.07.004.

[15]   M.S. Choi, Numerical prediction on the effects of the coarse aggregate size to the pipe flow of pumped concrete, Journal of Advanced Concrete Technology, 12 (8) (2014) 239-249. https://doi.org/10.3151/jact.12.239.

[16]   X. Xie, L. Zhang, C. Shi, X. Liu, Prediction of lubrication layer properties of pumped concrete based on flow induced particle migration, Construction and Building Materials, 322 (7) (2022) 126115. https://doi.org/10.1016/j.conbuildmat.2021.126115.

[17]   D. Kaplan, Pumping of Concrete. Ph.D. Thesis, LCPC, Paris, France (1999) (In French). https://tel.archives-ouvertes.fr/tel-01310219/

[18]   D. Kaplan, T. Sedran, F. De Larrard, M. Vachon, G. Machese, Forecasting pumping parameters, In: Proc. of the 2nd International RILEM symposium on self-compacting concrete, Tokyo, 2001, 556-564.

[19]   S.H. Kwon, K.P. Jang, J.H. Kim, S.P. Shah, State of the art on prediction of concrete pumping, International Journal of Concrete Structures and Materials, 10 (3) (2016) 75-85. https://doi.org/10.1007/s40069-016-0150-y.

[20]   L. Chen, G. Liu, W. Cheng, G. Pan, Pipe flow of pumping wet shotcrete based on lubrication layer, SpringerPlus 5, 945 (2016). https://doi.org/10.1186/s40064-016-2633-3.

[21]   D. Kaplan, F. De Larrard, T. Sedran, Design of concrete pumping circuit, ACI Materials Journal, 102 (2) (2005) 110-117. https://doi.org/10.14359/14304.

[22]   D. Feys, K.H. Khayat, A. Perez-Schell, R. Khatib, Development of a tribometer to characterize lubrication layer properties of self-consolidating concrete, Cement & Concrete Composites, 54

(2014) 40-52. https://doi.org/10.1016/j.cemconcomp.2014.05.008.

[23]   R D. Feys, G. De Schutter, S. Fataei, N.S. Martys, V. Mechtcherine, Pumping of concrete: Understanding a common placement method with lots of challenges, Cement and Concrete Research, 154 (2022) 106720. https://doi.org/10.1016/j.cemconres.2022.106720.

[24]   M. Choi, C.F. Ferraris, N.S. Martys, D. Lootens, V.K. Bui, H.R.T. Hamilton, Metrology needs for predicting concrete pumpability, Advances in Materials Science and Engineering, (2015) 456238. http://dx.doi.org/10.1155/2015/456238.

[25]   E. Secrieru, W. Mohamed, S. Fataei, V. Mechtcherine, Assessment and prediction of concrete flow and pumping pressure in pipeline, Cement and Concrete Composites, 107 (2020) 103495. https://doi.org/10.1016/j.cemconcomp.2019.103495.

[26]   T. Tavangar, M. Hosseinpoor, A. Yahia, K.H. Khayat, Novel tri-viscous model to simulate pumping of flowable concrete through characterization of lubrication layer and plug zones, Cement and Concrete Composites, 126 (2022) 104370. https://doi.org/10.1016/j.cemconcomp.2021.104370.

[27]   A.A. Mahmood, M. Elektorowicz, A review of discrete element method research on particulate systems, Soft Soil Engineering International Conference 2015 (SEIC2015), IOP Conference Series: Materials Science and Engineering, 136 (2016) 012034. https://www.dx.doi.org/10.1088/1757-899X/136/1/012034.

[28]   G. Cao, H. Zhang, Y. Tan, J. Wang, R. Deng, X. Xiao, B. Wu, Study on the effect of coarse aggregate volume fraction on the flow behavior of fresh concrete via DEM, Procedia engineering, 102 (2015) 1820-1826. https://doi.org/10.1016/j.proeng.2015.01.319.

[29]   M.A. Haustein, G. Zhang, R. Schwarze, Segregation of granular materials in a pulsating pumping regime, Granular Matter, 21 (2019) 111. https://doi.org/10.1007/s10035-019-0967-6.

[30]   Y. Zhan, J. Gong, Y. Huang, C. Shi, Z. Zuo, Y. Chen, Numerical study on concrete pumping behavior via local flow simulation with discrete element method, Materials, 12 (9) (2019) 1415. https://doi.org/10.3390/ma12091415.

[31]   J. Hao, C. Jin, Y. Li, Z. Wang, J. Liu, H. Li, Simulation of motion behavior of concrete in pump pipe by DEM, Advances in Civil Engineering, (2021) 3750589. https://doi.org/10.1155/2021/3750589.

[32]   T. Tavangar, M. Hosseinpoor, J.S. Marshall, A. Yahia, K.H. Khayat, Discrete-element modeling of shear-induced particle migration during concrete pipe flow: Effect of size distribution and concentration of aggregate on formation of lubrication layer, Cement and Concrete Research,2023,

Chapter 7. Four-way CFD-DEM coupling to simulate concrete pipe flow Mechanism of
formation of lubrication layer
284

107113. https://doi.org/10.1016/j.cemconres.2023.107113.

[33]   Y. Tan, H. Zhang, D. Yang, S. Jiang, J. Song, Y. Sheng, Numerical simulation of concrete pumping process and investigation of wear mechanism of the piping wall, Tribology International, 46 (1) (2012) 137-144. https://doi.org/10.1016/j.triboint.2011.06.005.

[34]   M. Zhou, S. Wang, S. Kuang, K. Luo, J. Fan, A. Yu, CFD-DEM modelling of hydraulic conveying of solid particles in a vertical pipe, Powder Technology, 354 (2019) 893-905. https://doi.org/10.1016/j.powtec.2019.07.015.

[35]   P. Kieckhefen, S. Pietsch, M. Dosta, S. Heinrich, Possibilities and limits of computational fluid dynamics-discrete element method simulations in process engineering: A review of recent advancements and future trends, Annual Review of Chemical and Biomolecular Engineering, 11 (2020) 397-422. https://doi.org/10.1146/annurev-chembioeng-110519-075414.

[36]   S. Jiang, X. Chen, G. Cao, Y. Tan, X. Xiao, Y. Zhou, S. Liu, Z. Tong, Y. Wu, Optimization of fresh concrete pumping pressure loss with CFD-DEM approach, Construction and Building Materials, 276 (2021) 122204. https://doi.org/10.1016/j.conbuildmat.2020.122204.

[37]   S. Jiang, W. Zhang, X. Chen, G. Cao, Y. Tan, X. Xiao, X., S. Liu, Q. Yu, Z. Tong, CFD-DEM simulation research on optimization of spatial attitude of concrete pumping boom based on evaluation of minimum pressure loss, Powder Technology, 403 (2022) 403, 117365. https://doi.org/10.1016/j.powtec.2022.117365.

[38]   Z.S. Ali, M. Hosseinpoor, A. Yahia, New aggregate grading models for low-binder self-consolidating and semi-self-consolidating concrete (Eco-SCC and Eco-semi-SCC), Construction and Building Materials, 265 (2020) 120314. https://doi.org/10.1016/j.conbuildmat.2020.120314.

[39]   R.J. Phillips, R.C. Armstrong, R.A. Brown, A.L. Graham, J.R. Abbott, A constitutive equation for concentrated suspensions that accounts for shear-induced particle migration, Physics of Fluids A: Fluid Dynamics, 4 (1) (1992) 30-40. https://doi.org/10.1063/1.858498.

[40]   F.F. Dizaji, J.S. Marshall, J.R. Grant, Collision and breakup of fractal particle agglomerate in a shear flow, Journal of Fluid Mechanics, 862 (2019) 592-623. https://doi.org/10.1017/jfm.2018.959.

[41]   J.S. Marshall, Discrete-element modeling of particulate aerosol flows, Journal of Computational Physics, 228 (5) (2009) 1541-1561. https://doi.org/10.1016/j.jcp.2008.10.035.

[42]   R. Di Felice, The voidage function for fluid-particle interaction systems, International Journal of Multiphase Flow, 20 (1) (1994) 153-159. https://doi.org/10.1016/0301-9322(94)90011-6.

[43]   R.O. Chhabra, P.H.T. Uhlherr, D.V. Boger, The influence of fluid elasticity on the drag coefficient for creeping flow around a sphere, Journal of Non-Newtonian Fluid Mechanics, 6 (3-4) (1980) 187-199. https://doi.org/10.1016/0377-0257(80)80002-4.

[44]   S.A. Orszag, D. Gottlieb, High resolution spectral calculations of inviscid compressible flows, In: Rautmann, R. (eds) Approximation Methods for Navier-Stokes Problems. Lecture Notes in Mathematics, vol 771. Springer, Berlin, Heidelberg (1980) 381-398. https://doi.org/10.1007/BFb0086919.

[45]   C.J. Ghazi, J.S. Marshall, A CO2 tracer-gas method for local air leakage detection and characterization, Flow Measurement and Instrumentation, 38 (2014) 72-81. https://doi.org/10.1016/j.flowmeasinst.2014.05.015.

[46]   B. Blais, F. Bertrand, CFD-DEM investigation of viscous solid-liquid mixing: Impact of particle properties and mixer characteristics, Chemical Engineering Research and Design, 118 (2017) 270-285. https://doi.org/10.1016/j.cherd.2016.12.018.

[47]   L. Schiller, A. Naumann, Über die grundlegenden Berechnungen bei der Schwerkraftaufbereitung, Zeitschrift des Vereines Deutscher Ingenieure, 77 (1933) 318-320.

[48]   M. Fourmentin, P. Faure, S. Rodts, U. Peter, D. Lesueur, D. Daviller, P. Coussot, NMR observation of water transfer between a cement paste and a porous medium, Cement and Concrete Research, 95 (2017) 56-64. https://doi.org/10.1016/j.cemconres.2017.02.027.

[49]   H. Hertz, Ueber die Berührung fester elastischer Körper, Journal für die reine und angewandte Mathematik 92, (1882) 156-171. https://doi.org/10.1515/9783112342404-004.

[50]   P.A. Cundall, O.D.L. Strack, A discrete numerical model for granular assembles, Géotechnique, 29 (1) (1979) 47-65. https://doi.org/10.1680/geot.1979.29.1.47.

[51]   J.S Marshall, S. Li, (2014), Adhesive Particle Flow: A Discrete-Element Approach, Cambridge: Cambridge University Press, (2014) ISBN 9781139424547.

[52]   J.S. Marshall, Comparison of methods for computing the concentration field of a particulate flow, International Journal of Multiphase Flow, 56 (2013) 4-14. https://doi.org/10.1016/j.ijmultiphaseflow.2013.05.009.

[53]   Canadian Standards Association CSA A23.1:19/CSA A23.2:19 standard, Concrete materials and methods of concrete construction/Test methods and standard practices for concrete, CSA Group (2019) SKU: 2425145.

[54]   T. Stovall, F. de Larrard, M. Buil, Linear packing density model of grain mixtures, Powder Technology, 48 (1) (1986) 1-12. https://doi.org/10.1016/0032-5910(86)80058-4.

[55]   F. de Larrard, Concrete mixture proportioning — a scientific approach, in: S. Mindess, A. Bentur (Eds.), Modern Concrete Technology Series No. 7, E&FN SPON, London (1999) ISBN 9780419235002.

[56]   W.W. Daniel, (1990) Applied Nonparametric Statistics (2nd ed.), Boston: PWS-Kent, ISBN 978-0-534-91976-4, 358-365.

[57]   X. Chateau, G. Ovarlez, K.L. Trung, Homogenization approach to the behavior of suspensions of noncolloidal particles in yield stress fluids, Journal of Rheology, 52 (2) (2008) 489-506. https://doi.org/10.1122/1.2838254.

[58]   I.M. Krieger, T.J. Dougherty, A mechanism for non-Newtonian flow in suspensions of rigid spheres, Transaction of the Society of Rheology, 3 (1959) 137-152. https://doi.org/10.1122/1.548848.

[59]   D. Feys, G. De Schutter, K.H. Khayat, R. Verhoeven, Changes in rheology of self-consolidating concrete induced by pumping, Materials and Structures, 49 (2016) 4567-4677. https://doi.org/10.1617/s11527-016-0815-7.

[60]   J. Vosahlik, K. Riding, D. Feys, W. Lindquist, K. Keller, S. Van Zetten, B. Schulz, Concrete pumping and its effect on the air void system, Materials and Structures, 51 (4) (2018) 94. https://doi.org/10.1617/s11527-018-1204-1

CHAPTER 8. Conclusions and perspectives

8.1 Conclusions

Accurately estimating the pumpability of concrete is crucial for designing effective pumping systems and selecting appropriate pumps to ensure successful processing of the concrete. The pressure required to pump concrete is significantly affected by the characteristics of the lubrication layer formed during pumping, which is caused by the shear-induced particle migration. Predicting the variation in heterogeneity of concrete mixtures during pipe flow is very challenging due to the complex physics involved in the migration of aggregates in concrete mixtures. In order to prevent some failures, such as pipe blockage, numerical approaches based on CFD, DEM, and coupled CFD-DEM were proposed in this study.

The main objectives of this study were to (1) predict the pressure required to pump concrete at large scale; (2) identify the influencing parameters in designing pumping circuit using computational fluid dynamics; (3) characterize lubrication layer based in terms of rheological properties and thickness; and (4) investigate the main mechanism of lubrication layer formation. These main four objectives were investigated through two simulation phases of this thesis. Following the literature review on advantages and disadvantages of various computational approaches, the following phases were carried out:

In the **Phase 1**, new viscosity models were proposed to predict and characterize LL in large scale. The thickness and rheological properties of the lubrication layer and plug flow zones along were successfully evaluated using the proposed viscosity models. The coupled effect of main influencing parameters on pumpability of concrete, including the rheological properties of plug flow, BC, and LL, as well as flow rate magnitude and pipe diameter, was evaluated.

In the **Phase 2**, a muti-scale DEM and coupled CFD-DEM approaches were proposed to achieve better understanding of the shear-induced particle migration leading to the formation of the LL. The coupled effect of influencing parameters, such as wide PSD and concentration of particles, as well as mortar rheology on rheological heterogeneities across the pipe was investigated.

Based on the results obtained in this study, the following conclusions can be pointed out:

8.1.1 *Phase 1: Homogenous modeling of concrete flow*

- The tri-viscous approach was effectively developed and utilized to characterize various flow zones in pipes, such as the thickness and viscous constant of the lubrication layer, as well as the viscosity and radius of the plug flow zone. These parameters cannot be determined through empirical or analytical methods.

- Using the tri-viscous model I, the simulated viscous constants were found to vary between 30% to 200% compared to the values obtained through tribological measurements. Increasing the pipe diameter and reducing the flow rate tended to result in the formation of thicker lubrication layers.

- The frequency distribution analysis of the simulated lubrication layer thicknesses indicated that at low flow rates, the majority of the thicknesses for 100- and 125-mm diameter pipes were between 1.5 to 2 mm (80.2%) and 3 to 3.5 mm (63.3%), respectively. However, increasing the flow rate resulted in a higher frequency of lubrication layer thicknesses between 1.5 to 2 mm in both the 100 (85.4%) and 125-mm (63.3%) diameter pipes.

- The tri-viscous model I led to evaluate the combined effect of plug flow, sheared concrete, and lubrication layer zones properties on pumping pressure loss using the tri-viscous simulations. The established correlation demonstrated a higher level of accuracy in predicting pumping pressure drop compared to the Kaplan et al. model, as evidenced by a higher R^2 (0.98 vs. 0.88) and a closer estimation index (0.98 vs. 1.08) to unity. The correlation revealed that an increase in the rheological properties of the plug, sheared concrete, and lubrication layer zones, as well as higher flow rates and smaller pipe diameters, could increase the pumping pressure loss. The plastic viscosity of the concrete and the viscous constant of the lubrication layer were found to have the most significant effect on pressure loss compared to the viscosity and radius of the plug flow. Additionally, pipe diameter was found to have a greater influence on pressure loss than flow rate magnitude in pumping specifications.

- For flow rates ranging from 8.1-16.4 l/s, the simulated maximum flow velocity (V_{max}), Reynolds number (Re), and critical shear rate ($\dot{\gamma}_{c-LL}$) values of the studied mixtures varied

between 0.8-2.4 m/s, 1.4-18.8, and 80-430 s^{-1}, respectively. The investigated mixtures showed a 44% higher V_{max}, 14% higher Re, and 30% higher $\dot{\gamma}_{c-LL}$ values when flowing through a 100-mm diameter pipe compared to a 125-mm diameter pipe.

- The shear-rate dependent tri-viscous model II successfully led to evaluate the combined effect of critical shear rate, rheological properties, thickness of different pipe-flow zones, flow rate, and pipe diameter on pumping pressure loss. This resulted in higher precision of pressure-drop prediction compared to the analytical Kaplan et al. model. The critical shear rate ($\dot{\gamma}_{c-LL}$) was found to have the most dominant effect on pressure drop compared to the rheological characteristics and thickness of different pipe flow zones. Among the various rheological properties, pressure loss was more influenced by the viscosities of the sheared-BC and plug-flow zones rather than the viscous constant of the LL.

8.1.2 *Phase 2: Heterogeneous modelling of concrete flow - Coupling fluid and solid phases*

- A soft-sphere - multi-time scale DEM approach was successfully used to model the effects of pipe-wall and shear-induced particle migration on the formation of the lubrication layer during concrete pumping. A total of nine different concrete suspensions were studied, each containing spherical particles of various sizes ranging from 1 to 17 mm. The study examined how the concentration of particles (ranging from 10% to 40%) and the particle size distribution (classified as fine, medium, or coarse) affected the variation of rheological properties across a pipe.

- The outermost zone Z4 had the lowest concentration and smallest average particle diameter (D_{avg}), indicating the presence of a low concentration layer (LL) near the pipe wall. The average particle diameter within the simulated LLs ranged from 1.4 to 2.8 mm.

- Over time, the volume of particles in all subclasses increased gradually in the central zone (Z1), resulting in greater packing of particles at the center of the pipe. This was more noticeable for larger particles (3.5-17 mm) than for the smallest particle size (1 mm), resulting in a relatively coarser particle size distribution (PSD) at the pipe center compared to the outer radial zones and the reference mixture.

- The concrete suspensions that contained lower concentrations and coarser particle size distributions had higher coefficients of variation (COV) of particle concentrations in various radial zones over time. Among suspensions with the same concentration, those with coarser particle size distributions experienced higher SIPM. However, for fine-particle size distributions, higher particle concentrations resulted in lower SIPM.

- In low-concentration (LC = 10%) and medium-concentration (MC = 25%) suspensions, the total concentration of particles decreased continuously from the center of the pipe towards the LL zone. However, in high-concentration (HC = 40%) suspensions simulated using the DEM approach, the highest particle concentration was observed in zone Z3 (0.75R-0.875R), followed by the central zones Z1 and Z2 (0-0.75R). Therefore, to achieve more accurate simulations of highly concentrated suspension pipe flows, a fully fluid-particle coupling approach (4-way CFD-DEM) was then applied.

- The coupled effect of the PSD and concentration of aggregate, as well as rheology of the suspending mortar on shear-induced heterogeneities during multiphasic concrete pipe flow was successfully investigated using the coupling approach.

- The use of a four-way CFD-DEM coupling approach improved the ability to capture higher degrees of SIPM during concrete pipe flow, compared to DEM simulations alone. At a given Reynolds number of the suspending fluid flow, suspensions with coarser particle size distributions and lower particle concentrations had higher SIPMI indices. Additionally, unlike mixtures containing medium and high concentrations of coarse particles, increasing the Reynolds number resulted in lower SIPMI indices for low-concentration and medium-particle size distribution-medium-concentration suspensions.

- Various methods were proposed to assess the pumping-induced heterogeneity of the suspensions investigated in terms of the wall effect (WEI), yield stress heterogeneity index (YSHI), and viscosity heterogeneity index (VHI) across the pipes. It was observed that the proposed WEI, YSHI, and VHI indices were highly correlated with the mean diameter (D_{avg}) and the relative-solid packing fraction (φ/φ_{max}) of the particles.

- The simulated YSHI and VHI indices ranged from 4.2% to 21.6% and 13.7% to 54.6%, respectively. The values of these indices were mainly influenced by the particle volume fraction (φ/φ_{max}) and mean diameter (D_{avg}), rather than the Reynolds number of the

suspending fluid flow. Increasing the particle concentration and mean diameter resulted in higher YSHI and VHI indices across the pipe. Increasing the Reynolds number of the suspending fluid flow led to lower rheological dissimilarity across the pipe for LC suspensions and MC-MPSD mixture, which resulted in higher YSHI and VHI for CPSD-MC and CPSD-HC suspensions.

- The CFD-DEM simulations allowed to evaluate the relative yield stress (τ_{0-r}) and plastic viscosity (μ_{p-r}) of the bulk concrete (BC) and LL to their suspending fluid. The results of the simulation showed that the rheological properties of both the BC and LL were mainly influenced by the characteristics of the suspended particles, such as their concentration, mean diameter, and particle size distribution, rather than the Reynolds number of the suspending fluid. The values of τ_{0-r} for the BC ranged from 1.10 to 1.74, while the values of μ_{p-r} for the BC ranged from 1.37 to 5.92. On the other hand, the values of τ_{0-r} for the LL ranged from 1.01 to 1.11, while the values of μ_{p-r} for the LL ranged from 1.05 to 1.40.

- The thickness of the LL (e_{LL}) in the pipe flows was estimated using digital image processing (DIP) of the pipe cross sections after the CFD-DEM simulations were completed. The estimated e_{LL} values ranged from 0.8 to 2.7 mm, which is consistent with experimental values reported in the literature, which are typically in the range of 1-3 mm.

8.2 Future works

This study focused on developing numerical simulation and investigating the influencing parameters on concrete pipe flow behavior. According to the achievements of this study, further investigations may be necessary for better understanding the complex behavior of concrete suspension during pipe flow, such as:

o In this study, aggregates were considered as spherical particles for the simplification. It is suggested that using aggregates with various shapes into the model can lead to reach more realistic results.

o The study assumed a fixed viscosity for the suspending fluid throughout the entire pipe flow period, with limited Reynolds numbers of 100 and 500. Using a wider range of rheological properties, as well as considering the time-dependent variations in rheological

properties of concrete due to pumping-induced effects, can improve the applicability of the approach for various types of concrete and pumping conditions. This can lead to more accurate predictions of concrete flow behavior.

o A coupling of DEM (Discrete Element Method), CFD (Computational Fluid Dynamics), and AI (Artificial Intelligence) can lead to more realistic and accurate results compared to traditional computational methods. DEM can simulate the behavior of individual particles, while CFD can simulate the fluid flow around those particles, and AI can optimize the parameters and improve the accuracy of the simulations. This coupled approach can provide more detailed and realistic insights into the behavior of complex systems, such as concrete pipe flows, and help to improve the design and operation of such systems.

o Incorporating adhesive forces in the modelling of aggregate agglomeration can lead to more realistic results. This is due to the fact that aggregates are not perfectly smooth and can stick together due to various adhesive forces, such as van der Waals, electrostatic, and capillary forces. By including these forces in the model, the simulation can better capture the behavior of aggregates and their tendency to agglomerate.

CHAPTER 8. Conclusions et perspectives *(Français)*

8.3 Conclusions

Estimer avec précision la pompabilité du béton est crucial pour concevoir des systèmes de pompage efficaces et sélectionner des pompes appropriées pour assurer le traitement réussi du béton. La pression requise pour pomper du béton est significativement affectée par les caractéristiques de la couche de lubrification formée par la migration des particules induite par le cisaillement. Prédire la variation d'hétérogénéité des mélanges de béton lorsqu'ils circulent dans les tuyaux de pompage est très difficile en raison de la physique complexe impliquée dans la migration des granulats dans les mélanges de béton. Afin de prévenir certains échecs tels que les blocages dans le circuit de pompage, des approches numériques basées sur la CFD, la DEM et la CFD-DEM couplée ont été proposées.

Les principaux objectifs de cette étude étaient de (1) prédire la pression requise pour pomper du béton à grande échelle ; (2) identifier les paramètres influents dans la conception du circuit de pompage à l'aide de la dynamique des fluides numérique ; (3) caractériser la couche de lubrification en fonction de ses propriétés rhéologiques et de son épaisseur ; (4) étudier le mécanisme principal de la formation de la couche de lubrification. Ces quatre objectifs principaux ont été examinés à travers deux phases de simulation de cette thèse. Suite à l'examen de la littérature sur les avantages et les inconvénients des différentes approches numériques, les phases suivantes ont été réalisées :

À la **Phase 1**, de nouveaux modèles de viscosité ont été proposés pour prédire et caractériser la couche de lubrification à grande échelle. L'épaisseur et les propriétés rhéologiques de la couche de lubrification et des zones d'écoulement par bouchon le long des différentes sections du tuyau ont été évaluées avec succès à l'aide des modèles de viscosité proposés. Les principaux paramètres influents sur la pompabilité du béton ont été définis, notamment les propriétés rhéologiques de l'écoulement par bouchon, les conditions aux limites et la couche de lubrification, ainsi que le débit et le diamètre du tuyau.

À la **Phase 2**, des approches DEM multi-échelle et CFD-DEM couplées ont été proposées pour atteindre une compréhension plus réaliste de la migration des particules induite par le cisaillement

conduisant à la formation de la couche de lubrification. L'effet couplé des paramètres influents telles que la concentration en particules et la distribution de taille des particules sur la variation d'hétérogénéité de l'écoulement de suspension de béton a été étudié.

En se basant sur les résultats obtenus et présentés dans ce manuscrit, les conclusions suivantes peuvent être soulignées :

8.3.1 Phase 1 : Modélisation homogène de l'écoulement du béton

- L'approche tri-visqueuse a été développée et utilisée de manière efficace pour caractériser diverses zones d'écoulement dans les tuyaux, telles que l'épaisseur et la constante visqueuse de la couche de lubrification, ainsi que la viscosité et le rayon de la zone d'écoulement en bouchon. Ces paramètres ne peuvent pas être déterminés par des méthodes empiriques ou analytiques.

- En utilisant le modèle tri-visqueux I, les constantes visqueuses simulées peuvent varier entre 30% et 200% par rapport aux valeurs obtenues par des mesures tribologiques. Les différences les plus significatives entre les deux ont été trouvées dans les essais de pompage avec des débits maximum et minimum dans des tuyaux de diamètres de 100 mm et 125 mm. L'augmentation du diamètre du tuyau et la réduction du débit avaient tendance à entraîner la formation de couches de lubrification plus épaisses.

- L'analyse de la distribution de fréquences des épaisseurs de couche de lubrification simulées a indiqué qu'à faible débit, la majorité des épaisseurs pour les tuyaux de diamètres de 100 mm et 125 mm étaient comprises entre 1,5 et 2 mm (80,2%) et entre 3,0 et 3,5 mm (63,3%), respectivement. Cependant, l'augmentation du débit a entraîné une fréquence plus élevée de couche de lubrification ayant une épaisseur comprise entre 1,5 et 2 mm dans les tuyaux de diamètres de 100 mm (85,4%) et 125 mm (63,3%).

- L'étude a évalué l'effet combiné des propriétés des zones d'écoulement de type bouchon, de béton cisaillé et de la couche de lubrification sur la perte de pression de pompage en utilisant des simulations tri-visqueuses. La corrélation établie a démontré un niveau de précision supérieur dans la prédiction de la chute de pression de pompage par rapport au modèle de Kaplan et al., comme en témoigne un R^2 plus élevé (0,98 contre 0,88) et un

indice d'estimation plus proche de l'unité (0,98 contre 1,08). La corrélation a révélé qu'une augmentation des propriétés rhéologiques des zones d'écoulement de type bouchon, de béton cisaillé et de la couche de lubrification, ainsi que des débits plus élevés et des diamètres de tuyaux plus petits, pouvaient augmenter la perte de pression de pompage. La viscosité plastique du béton et la constante visqueuse de la couche de lubrification ont l'effet le plus significatif sur la perte de pression par rapport à la viscosité et au rayon d'écoulement de type bouchon. De plus, le diamètre du tuyau a présenté une plus grande influence sur la perte de pression que le débit dans les spécifications de pompage.

- Pour des débits allant de 8,1 à 16,4 l/s, les valeurs simulées de la vitesse maximale d'écoulement (Vmax), du nombre de Reynolds (Re) et du taux de cisaillement critique ($\dot{\gamma}_{c\text{-LL}}$) des mélanges étudiés variaient respectivement entre 0,8 et 2,4 m/s, 1,4 et 18,8 et 80 et 430 s^{-1}. Les mélanges étudiés ont montré une Vmax supérieure de 44 %, un Re supérieur de 14 % et des valeurs de $\dot{\gamma}_{c\text{-LL}}$ supérieures de 30 % lorsqu'ils s'écoulent dans un tuyau de 100 mm de diamètre par rapport à un tuyau de 125 mm de diamètre.

- L'étude a permis d'évaluer avec succès l'effet combiné du taux de cisaillement critique, des propriétés rhéologiques, de l'épaisseur des différentes zones d'écoulement, du débit et du diamètre du tuyau sur la perte de pression de pompage en utilisant un nouveau modèle tri-visqueux dépendant du taux de cisaillement. Cela a entraîné une précision supérieure de la prédiction de la chute de pression par rapport au modèle analytique de Kaplan et al. Le taux de cisaillement critique ($\dot{\gamma}_{c\text{-LL}}$) a montré l'effet le plus dominant sur la chute de pression par rapport aux caractéristiques rhéologiques et à l'épaisseur des différentes zones d'écoulement. Parmi les différentes propriétés rhéologiques, la perte de pression était plus influencée par les viscosités des zones de BC cisaillées et d'écoulement de bouchon plutôt que par la constante visqueuse des LL.

8.3.2 *Phase 2 : Modélisation hétérogène de l'écoulement du béton - Couplage des phases fluides et solides*

- Une approche DEM à échelles de temps multiples avec sphères douces a été utilisée avec succès pour modéliser les effets de la paroi du tuyau, de la migration des particules induite par le cisaillement et de la formation de la couche de lubrification dans le pompage du béton. Neuf suspensions de béton différentes ont été étudiées, chacune contenant des particules sphériques de tailles variées allant de 1 à 17 mm. L'étude a montré comment la concentration de particules (allant de 10% à 40%) et la distribution de taille de particules (classée comme fine, moyenne ou grossière) ont affecté les variations de la distribution radiale à travers un tuyau.

- La zone la plus externe Z4 avait la concentration la plus basse et le diamètre moyen de particules (D_{avg}) le plus petit, ce qui indiquait la présence d'une couche à faible concentration (LL) près de la paroi du tuyau. Le diamètre moyen des particules dans les LL simulées variait de 1,4 à 2,8 mm.

- Au fil du temps, le volume de particules dans toutes les sous-classes a augmenté progressivement dans la zone centrale (Z1), entraînant un compacité plus important des particules au centre du tuyau. C'était plus perceptible pour les particules plus grandes (3,5-17 mm) que pour la plus petite taille de particules (1 mm), ce qui a entraîné une distribution de taille de particules relativement plus grossière (PSD) au centre du tuyau par rapport aux zones radiales extérieures et au mélange de référence.

- Les suspensions de béton qui contenaient des concentrations plus faibles et des distributions granulométriques plus grossières présentaient des coefficients de variation (COV) plus élevés des concentrations de particules dans diverses zones radiales au fil du temps. Parmi les suspensions ayant la même concentration, celles dont la distribution granulométrique était plus grossière présentaient un SIPM plus élevé. Cependant, pour les distributions de taille de particules fines, des concentrations de particules plus élevées ont entraîné un SIPM plus faible

- Dans les suspensions à faible concentration (LC = 10%) et à concentration moyenne (MC = 25%), la concentration totale de particules a diminué de façon continue du centre du tuyau

vers la zone LL. Cependant, dans les suspensions à forte concentration (HC = 40 %), la plus forte concentration de particules a été observée dans la zone Z3 (0,75R-0,875R), suivie des zones centrales Z1 et Z2 (0-0,75R). Par conséquent, pour obtenir des simulations plus précises des écoulements de suspensions hautement concentrées, une approche de couplage complet fluide-particules (CFD-DEM à 4 voies) a été appliquée.

- L'effet couplé de la DSP, de la concentration des agrégats et de la rhéologie du mortier de suspension sur les hétérogénéités induites par le cisaillement pendant l'écoulement multiphasique d'un tuyau en béton a été étudié avec succès en utilisant les approches de couplage.

- L'utilisation d'une approche de couplage CFD-DEM 'Four-way' a amélioré la capacité à capturer des degrés plus élevés de SIPM pendant l'écoulement de béton dans un conduite, par rapport aux simulations DEM seules. À un nombre de Reynolds donné de l'écoulement du fluide, les suspensions avec des distributions granulométriques plus grossières et des concentrations de particules plus faibles présentaient des indices SIPMI plus élevés. De plus, contrairement aux mélanges contenant des concentrations moyennes et élevées de particules grossières, l'augmentation du nombre de Reynolds a entraîné des indices SIPMI plus faibles pour les suspensions à faible concentration et à distribution granulométrique moyenne et à concentration moyenne.

- Diverses méthodes ont été proposées pour évaluer l'hétérogénéité induite par le pompage des suspensions étudiées en termes d'effet de paroi (WEI), d'indice d'hétérogénéité de la contrainte d'écoulement (YSHI) et d'indice d'hétérogénéité de la viscosité (VHI) à travers les tuyaux. Il a été observé que les indices WEI, YSHI et VHI proposés étaient fortement corrélés avec le diamètre moyen (D_{avg}) et la fraction de tassement solide relative (φ/φ_{max}) des particules.

- Les indices YSHI et VHI ont été mesurés et se situent dans une fourchette de 4,2 % à 21,6 % et de 13,7 % à 54,6 %, respectivement. Les valeurs de ces indices étaient principalement influencées par la fraction volumique des particules (φ/φ_{max}) et le diamètre moyen (D_{avg}), plutôt que par le nombre de Reynolds de l'écoulement du fluide en suspension. L'augmentation de la concentration de particules et du diamètre moyen a entraîné une augmentation des indices YSHI et VHI dans le tuyau. L'augmentation du nombre de

Reynolds de l'écoulement du fluide de la suspension a entraîné une moindre dissimilarité rhéologique à travers le tuyau pour les suspensions LC et le mélange MC-MPSD, ce qui a donné lieu à des indices YSHI et VHI plus élevés pour les suspensions CPSD-MC et CPSD-HC.

- Les simulations CFD-DEM ont permis d'évaluer la limite d'élasticité relative (τ_0-r) et la viscosité plastique (μ_{p-r}) du béton en vrac (BC) et du LL par rapport à leur fluide de suspension. Les résultats de la simulation ont montré que les propriétés rhéologiques du BC et du LL étaient principalement influencées par les caractéristiques des particules en suspension, telles que leur concentration, leur diamètre moyen et leur distribution granulométrique, plutôt que par le nombre de Reynolds. Les valeurs de τ_{0-r} pour le BC étaient comprises entre 1,10 et 1,74, tandis que les valeurs de μ_{p-r} pour le LL étaient comprises entre 1,37 et 5,92. D'autre part, les valeurs de τ_{0-r} pour le LL varient de 1,01 à 1,11, tandis que les valeurs de (μ_{p-r}) pour le LL varient de 1,05 à 1,40.

- L'épaisseur du LL (e_{LL}) dans les écoulements des tuyaux a été estimée en utilisant le traitement d'image numérique (DIP) des sections transversales des tuyaux après la fin des simulations CFD-DEM. Les valeurs estimées de l'e_{LL} variaient de 0,8 à 2,7 mm, ce qui est cohérent avec les valeurs généralement rapportées dans la littérature pour les expériences de pompage du béton, qui sont généralement comprises entre 1 et 3 mm.

8.4 Travaux futurs

Le pompage du béton est une technique de construction émergente qui devrait être étudiée par les chercheurs travaillant sur la pompabilité du béton. Cette thèse s'est concentrée sur le développement d'une simulation numérique et sur l'étude des paramètres influençant le comportement d'écoulement de béton. Ainsi dans une conduite, les sujets peuvent être mis en avant pour des travaux futurs, comme suit :

- Dans cette étude, les granulats ont été considérés comme des particules sphériques par souci de simplification. Il est suggéré que l'utilisation de granulats de différentes formes dans le modèle peut conduire à des résultats plus réalistes. Les résultats peuvent alors être comparés à ceux de l'étude actuelle.

o L'étude a supposé une viscosité fixe pour le fluide en suspension pendant toute la période d'écoulement dans la conduite, avec des nombres de Reynolds limités à 100 et 500. Cependant, il est suggéré que l'utilisation d'une gamme plus large de propriétés rhéologiques, ainsi que la prise en compte des variations dans le temps des propriétés rhéologiques du béton dues aux effets induits par le pompage, peuvent améliorer l'applicabilité de l'approche pour divers types de béton et de conditions de pompage. Cela peut conduire à des prédictions plus précises du comportement d'écoulement du béton.

o Le couplage de la DEM, de la CFD et de l'IA (intelligence artificielle) peut donner des résultats plus réalistes et plus précis que les méthodes de calcul traditionnelles. En effet, la méthode des éléments discrets peut simuler le comportement des particules individuelles, la CFD peut simuler l'écoulement des fluides autour de ces particules et l'IA peut optimiser les paramètres et améliorer la précision des simulations. Cette approche couplée peut donner un aperçu plus détaillé et plus réaliste du comportement de systèmes complexes, tels que les écoulements de tuyaux en béton, et contribuer à améliorer la conception et le fonctionnement de ces systèmes.

o L'incorporation des forces adhésives dans la modélisation de l'agglomération des agrégats peut conduire à des résultats plus réalistes. En effet, dans les situations réelles, les agrégats ne sont pas parfaitement lisses et peuvent se coller les uns aux autres en raison de diverses forces adhésives telles que les forces de van der Waals, les forces électrostatiques et les forces capillaires. En incluant ces forces dans le modèle, la simulation peut mieux saisir le comportement des agrégats et leur tendance à s'agglomérer.